

University of Alberta

**Thermal Cracking Reactions of Model
Compounds of Asphaltenes**

by

Ali Haider Alshareef

A thesis submitted to the Faculty of Graduate Studies and Research
in partial fulfillment of the requirements for the degree of

Doctor of Philosophy

in

Chemical Engineering

Department of Chemical and Materials Engineering

©Ali Haider Alshareef

Spring 2012

Edmonton, Alberta

Permission is hereby granted to the University of Alberta Libraries to reproduce single copies of this thesis and to lend or sell such copies for private, scholarly or scientific research purposes only. Where the thesis is converted to, or otherwise made available in digital form, the University of Alberta will advise potential users of the thesis of these terms.

The author reserves all other publication and other rights in association with the copyright in the thesis and, except as herein before provided, neither the thesis nor any substantial portion thereof may be printed or otherwise reproduced in any material form whatsoever without the author's prior written permission.

ABSTRACT

Resolution of reaction pathways to coke formation during the upgrading of heavy resources, such as the vacuum residue fraction of bitumen, is hampered by the extreme complexity of these materials. Alternatively, probing the molecular-level reactions and cracking kinetics of model compounds that incorporate structures known to be present in the asphaltenes was shown to provide more quantitative information. The objective of this research is to investigate the thermal cracking and coking reactions in the condensed liquid phase of especially synthesized model compounds of asphaltenes.

The model compounds used in this study are of three distinct chemical structures: archipelago structures made of three aromatic systems linked by two ethano bridges, alkylpyrene compounds with different side-chain lengths, and cholestane-benzoquinoline compounds substituted with different aromatic groups. All of the compounds have high molecular weights, within a range of 530–770 g/mol, to ensure they remain in the liquid phase at the reaction conditions.

The pure compounds and binary mixtures of them were thermally cracked using thermogravimetric analysis to obtain cracking kinetics and coke yields. Microreactor experiments on selective samples provided the conversion of parents, and nature and selectivity of products. Analysis using a number of chromatographic and spectroscopic techniques showed that initial fragments from

the model compounds add to other fragments and to the parent via alkyl–alkyl and alkyl–aryl addition reactions to build larger archipelago structures. In addition to the labile bonds that were expected to crack, strong bonds such as alkyl–pyrene bonds also cracked, likely facilitated by unimolecular rearrangement processes. The archipelago compounds formed much more addition products, and subsequently more coke, than the other two families of compounds or their phenyl analogs. Within each family, minor structural changes were found to greatly influence the coke yield, with the reactivity of the parent and its initially formed products, as well as the intermolecular associations, as observed with polarized light microscopy, as the main controlling factors. The activation energy of the cracking reactions, on the other hand, fell within a narrow range for each family of compounds suggesting that similar bonds dominate cracking.

ACKNOWLEDGEMENTS

All praise is due to the Lord for the countless blessings that have been showered upon me ever since I can remember.

None of this work would have been possible without the guidance, mentoring, and invaluable feedback offered by my supervisor, teacher, and role model: Dr. Murray Gray. My experience with you was eye-opening, life-changing, and with an impact warranted for a lifetime. For all that, thank you.

I thank Dr. Stryker and Dr. Tykwinski for their comments, ideas, questions, and suggestions. I also thank you and your team members for working hard in making the fabulous model compounds destroyed in this research (sorry for that!).

I thank Tuyet Le and Kavithaa Loganathan for the technical assistance and training on the various instruments. I thank Arash Karimi for training on the TGA, Xiaoli Tan for doing all the NMR tests, Reza Bagheria for the polarized light microscopy, and Alison Salmon for helping with some experiments.

I gratefully acknowledge the financial support by Saudi Aramco, Syncrude Canada, COSI, and NSERC.

I thank my mom (Layla), dad (Haider), and all my family for their care, support, love and affection. I thank all my friends, both those I was blessed to know in Edmonton, and my dear ones back home in Qatif.

Lastly, I thank my lovely wife Eman for her patience, care, help and support. You and our boys, Haider and Mohammad, your love and smiles are what keep me going through difficult times. For all that, I'm indebted for the rest of my life.

TABLE OF CONTENTS

<i>1. INTRODUCTION.....</i>	<i>1</i>
1.1 RESEARCH OBJECTIVES	4
1.2 THESIS OUTLINE.....	5
1.3 REFERENCES	8
<i>2. LITERATURE BACKGROUND</i>	<i>9</i>
2.1 THE ASPHALTENES	9
2.1.1 Definition of the Asphaltenes	9
2.1.1.1 <i>Effect of Solvent Type.....</i>	<i>11</i>
2.1.1.2 <i>Effect of Degree of Dilution.....</i>	<i>11</i>
2.1.1.3 <i>Effect of Temperature</i>	<i>12</i>
2.1.1.4 <i>Effect of Contact Time</i>	<i>12</i>
2.1.2 Origin of Petroleum and the Asphaltenes	13
2.1.3 Canonical Properties of the Petroleum Asphaltenes	15
2.1.3.1 <i>The Basics</i>	<i>15</i>
<u>2.1.3.1.1 <i>Elemental Composition.....</i></u>	<i>15</i>
<u>2.1.3.1.2 <i>Aromaticity.....</i></u>	<i>16</i>
<u>2.1.3.1.3 <i>Density, Viscosity, and Melting Point.....</i></u>	<i>17</i>
2.1.3.2 <i>Molecular Weight.....</i>	<i>18</i>
2.1.3.3 <i>Molecular Structure</i>	<i>20</i>
2.1.3.4 <i>Self-Association.....</i>	<i>24</i>

2.1.4 Modeling the Asphaltene Molecules	25
2.2 THERMAL CONVERSION OF VACUUM RESIDUE AND THE ASPHALTENES.....	27
2.2.1 Cracking Reactions	28
2.2.2 Coking Reactions	30
2.3 THERMAL REACTIONS OF MODEL COMPOUNDS	33
2.3.1 Vapor– vs. Liquid–Phase Reactions	33
2.3.2 Reactions of Benzene–Based Compounds.....	35
2.3.3 Reactions of Polycyclic Aromatics	38
2.3.4 Reactions of Biomarkers.....	43
2.4 REFERENCES	47
3. FORMATION OF ARCHIPELAGO STRUCTURES DURING THERMAL REACTIONS	61
3.1 INTRODUCTION	61
3.2 MATERIALS AND METHODS.....	62
3.3 RESULTS AND DISCUSSION	65
3.4 CONCLUSIONS.....	76
3.5 REFERENCES	77
4. MEASUREMENT OF CRACKING KINETICS OF PURE MODEL COMPOUNDS BY THERMOGRAVIMETRIC ANALYSIS.....	79
4.1 INTRODUCTION	79
4.2 KINETICS ESTIMATION METHODS IN TGA	81
4.2.1 The Peak Temperature Method.....	81
4.2.2 The Isoconversional Methods	83

4.2.3 The Differential Method	84
4.3 MATERIALS AND METHODS.....	85
4.4 RESULTS AND DISCUSSION.....	88
4.5 CONCLUSIONS.....	100
4.6 REFERENCES	102
5. EFFECTS OF CHEMICAL STRUCTURE ON CRACKING AND COKING OF ARCHIPELAGO MODEL COMPOUNDS OF ASPHALTENES	104
5.1 INTRODUCTION	104
5.2 MATERIALS AND METHODS.....	105
5.3 RESULTS	111
5.3.1 TGA Results.....	111
5.3.2 Microreactor Experiments	114
5.3.2.1 Cracked Products.....	116
5.3.2.2 Addition Products	120
5.3.2.3 Binary Experiments with Benzo[a]pyrene (BP) ..	123
5.3.3 Cross-Polarized Light Microscopy.....	130
5.4 DISCUSSION.....	132
5.4.1 Cracking Reactions	133
5.4.1.1 Initiation.....	133
5.4.1.2 Aryl-Alkyl Bond Cleavage.....	135
5.4.1.2.1 <u>Uni- vs. Bi-Molecular Cracking Mechanism</u>	135
5.4.1.2.2 <u>Rearrangement Reactions</u>	138
5.4.2 Coking Reactions	143

5.5 CONCLUSIONS.....	149
5.6 REFERENCES	150
6. THERMAL CRACKING OF SUBSTITUTED CHOLESTANE– BENZOQUINOLINE MODEL COMPOUNDS.....	154
6.1 INTRODUCTION	154
6.2 MATERIALS AND METHODS.....	155
6.3 RESULTS AND DISCUSSION	159
6.3.1 Thermogravimetric Analysis (TGA).....	159
6.3.2 Decomposition in Batch Reactions.....	163
6.3.3 Addition Reactions and Coking.....	170
6.3.4 Dealkylation and Aromatization Reactions	173
6.3.5 Summary of Decomposition Pathways.....	185
6.4 CONCLUSIONS.....	187
6.5 REFERENCES	188
7. THERMOGRAVIMETRIC ANALYSIS OF BINARY MIXTURES OF MODEL COMPOUNDS	191
7.1 INTRODUCTION	191
7.2 MATERIALS AND METHODS.....	193
7.3 RESULTS AND DISCUSSION	195
7.3.1 Coke Reduction Behavior	197
7.3.1.1 <i>P</i> -3,5-pyr- <i>P</i> / <i>P</i> -mPhP- <i>P</i> Experiments.....	198
7.3.1.2 <i>P</i> -3,5-pyr- <i>P</i> / THP Experiments.....	201
7.3.1.3 <i>P</i> -2,5-pyr-3-Me- <i>P</i> / <i>P</i> -mPhP- <i>P</i> Experiments	204
7.3.2 Simple Additive Behavior.....	205

7.3.2.1 <i>P-BiTh-P / P-mPhP-P Experiments</i>	205
7.3.2.2 <i>P-BiTh-P / P-Th-P Experiments</i>	208
7.4 CONCLUSIONS.....	209
7.5 REFERENCES	210
8. SYNTHESIS AND CONCLUSIONS.....	212
8.1 SYNTHESIS	212
8.1.1 Implications to Practical Issues.....	213
8.1.2 Sources of Uncertainties	213
8.2 CONCLUSIONS.....	216
8.3 RECOMMENDATIONS.....	217
APPENDIX A: CALIBRATION CURVES AND OPTIMIZATION OF ANALYTICAL INSTRUMENTS	219
A.1 THERMOGRAVIMETRIC ANALYSIS (TGA)	219
A.1.1 Performance Tests with CaOx.....	220
A.1.2 Leak Test	223
A.2 SAND BATH PERFORMANCE	224
A.3 GAS CHROMATOGRAPHY	227
A.3.1 Optimization of the Main Controlling Factors.....	229
A.3.2 Calibration Curves for the Quantification of Cracked Products in GC	233
A.3.2.1 <i>Calibration for P-3,5-pyr-P</i>	233
A.3.2.2 <i>Calibration for P-BiTh-P</i>	235
A.3.2.3 <i>Calibration for BP</i>	236
A.4 HIGH PERFORMANCE LIQUID CHROMATOGRAPHY	238

A.4.1 Main Controlling Factors in HPLC Analysis.....	238
A.4.2 Calibration Curves for the Model Compounds in HPLC...	241
<i>A.4.2.1 Calibration for P-BiTh-P</i>	<i>242</i>
<i>A.4.2.2 Calibration for P-3,5-pyr-P.....</i>	<i>244</i>
<i>A.4.2.3 Calibration for P-2,6-pyr-P.....</i>	<i>247</i>
<i>A.4.2.4 Calibration for P-mPh-P</i>	<i>248</i>
<i>A.4.2.5 Calibration for P-pPh-P</i>	<i>249</i>
<i>A.4.2.6 Calibration for P-Th-P</i>	<i>250</i>
<i>A.4.2.7 Calibration for BP</i>	<i>251</i>
<i>A.4.2.8 Calibration for TDP</i>	<i>252</i>
<i>A.4.2.9 Calibration for Chol-Ph</i>	<i>253</i>
<i>A.4.2.10 Calibration for Chol-BB.....</i>	<i>254</i>
<i>A.4.2.11 Calibration for Chol-Py</i>	<i>255</i>

LIST OF TABLES

Table 2.1:	Examples of bonds that crack at elevated temperatures with their bond dissociation energies (BDE) from McMillen and Golden.....	29
Table 3.1:	Estimated yield of addition products from thermal cracking of model compounds	63
Table 4.1:	Summary of the differential calculation of kinetics of P- <i>m</i> Ph-P at various heating rates.....	96
Table 4.2:	Kinetic parameters from the three methods for P-Th-P	98
Table 5.1:	The archipelago model compounds, molecular weights, and estimated boiling points	107
Table 5.2:	List of microreactor experiments, with conversion, and HPLC recovery.....	115
Table 5.3:	Moles of major cracked products per 100 moles of converted model compound.....	118
Table 5.4:	Binary experiments of Benzo[a]Pyrene (BP) plus P- <i>m</i> Ph-P and P- <i>p</i> Ph-P model compounds at 400 °C – 15 min Reactions.....	126
Table 5.5:	Thermochemical estimates for P- <i>m</i> Ph-P fragments.....	139
Table 6.1:	TGA results for the six model compounds	161
Table 6.2:	Microreactor experiments and conversion of the parent compounds	164
Table 7.1:	List of all TGA binary experiments	196
Table A.1:	Comparing the parameters of the CaOx pyrolysis in the TGA with the average (Avg) and standard deviation (StD).	222
Table A.2:	GC calibration data for Pyrene with P-3,5-pyr-P in MC	233
Table A.3:	GC calibration data for pyrene with P-BiTh-P in MC	235

Table A.4:	GC calibration data for BP with Phen in MC	236
Table A.5:	HPLC optimization runs with P, Phen, and P-BiTh-P in MC	239
Table A.6:	HPLC calibration data for P-BiTh-P to Phen, with P in MC.....	242
Table A.7:	HPLC calibration data for P to Phen, with P-BiTh-P in MC.....	243
Table A.8:	HPLC calibration data for P to Phen, with P-3,5-pyr-P in MC	244
Table A.9:	HPLC calibration data for P-3,5pyr-P to Phen, with P in MC.....	246
Table A.10:	HPLC calibration data for P-2,6pyr-P	247
Table A.11:	HPLC calibration data for P- <i>m</i> Ph-P.....	248
Table A.12:	HPLC calibration data for P- <i>p</i> Ph-P.....	249
Table A.13:	HPLC calibration data for P-Th-P	250
Table A.14:	HPLC calibration data for Benzo[a]pyrene	251
Table A.15:	HPLC calibration data for TDP	252
Table A.16:	HPLC calibration data for Chol-Ph.....	253
Table A.17:	HPLC calibration data for Chol-BB with pyrene (P) as standard...	254
Table A.18:	HPLC calibration data for Chol-Py.....	255

LIST OF FIGURES

Figure 2.1:	Kerogen chemical structure, after Freund et al. The positions where the structure continues to propagate are marked as ‘link’	14
Figure 2.2:	Representative asphaltene structure following the archipelago model, after Sheremata et al. with reduced molecular weight to fit the ~500–2000 Da range	22
Figure 2.3:	Chemical structures suggested by Mullins to be dominant in the asphaltenes	23
Figure 2.4:	Examples of three important propagation reactions of free radicals	30
Figure 2.5:	Hydrogen transfer mechanisms: H-atom addition (HA), concerted hydrogen transfer, reverse radical disproportionation (RRD), multistep mechanism, and radical hydrogen transfer (RHT).....	38
Figure 2.6:	RHT and the stable radical that forms after hydrogen transfer, after Freund et al.	42
Figure 2.7:	Cholestane with ring designation and carbon numbering. The (X) mark shows the most likely linkage point of similar steroids to the macromolecule of kerogen or the asphaltenes	45
Figure 3.1:	MALDI–MS of products from cracking of compound 1	66
Figure 3.2:	MALDI–MS of products from cracking of compound 2	67
Figure 3.3:	MALDI–MS of products from cracking of compound 3	68
Figure 3.4:	MALDI–MS of products from cracking of compound 4	69
Figure 3.5:	¹ H-NMR spectrum of products from compound 2 after pyrolysis at 400 °C for 15 min. The aliphatic region is enlarged, showing new resonances consistent with the product shown, where Ph is phenyl and P is pyrene. The assignments were made by simulating the ¹ H-NMR spectrum of the compound in Figure 3.7 (b) (see Figure 3.6).....	70
Figure 3.6:	Comparison of the simulated and experimentally measured ¹ H-NMR spectra of the two “benzylic” protons between the methine	

and pyrene groups labeled A in Figure 3.5 . The top spectrum is simulated with MestReNova. The bottom spectrum was experimentally measured	71
Figure 3.7: Suggested structures of major addition products	72
Figure 4.1: Chemical structure of P- <i>m</i> Ph-P and P-Th-P	85
Figure 4.2: Weight loss and rate of weight loss curves for P- <i>m</i> Ph-P pyrolysis in the TGA at a heating rate of 10 °C/min	89
Figure 4.3: Rate of weight loss vs. T for P- <i>m</i> Ph-P at various heating rates. All the curves are enlarged by the shown value except the one at 50 °C/min	89
Figure 4.4: Peak temperature plots using equations (4.2) and (4.3). The shown apparent activation energies of cracking of P- <i>m</i> Ph-P are lower than expected for such a chemical structure	90
Figure 4.5: Peak temperature plot using equation (4.5)	91
Figure 4.6: Isoconversional methods at 0.3 conversion using OFW and Friedman correlations for P- <i>m</i> Ph-P runs at 1, 5, 10, and 50 °C/min	92
Figure 4.7: Isoconversional methods at 0.3 conversion using KAS/V and Starink correlations for P- <i>m</i> Ph-P runs at 1, 5, 10, and 50 °C/min	92
Figure 4.8: The change of activation energy with conversion for the four isoconversional methods	93
Figure 4.9: Friedman method at various conversion levels for P- <i>m</i> Ph-P experiments at 1, 5, 10, and 50 °C/min	94
Figure 4.10: Plotting the differential calculations of $k (-dw/dt/w)$ vs $1/T$ (K ⁻¹) for the 10 °C/min run of P- <i>m</i> Ph-P. The regression line is not visible due to the high linearity and the many points used and hence was extended to the axes	95
Figure 4.11: Average E for a series of pyrene-based model compounds. The central groups in these compounds in terms of increasing estimated boiling points are: 1,4- <i>n</i> Butyl, 2,5-thiophene, 1,3-benzene, 1,4-benzene, 5,5'-(2,2'-bithiophene), 2,8-dibenzofuran, 1,1'-(4,4'-biphenyl), 4,4'-(2,2'-bipyridine), and 2,7-(9,9-diethyl-9H-flourene)	99
Figure 5.1: The general structure of the pyrene-based model compounds	

(top) with one specific example (bottom)	106
Figure 5.2: Typical curves of weight loss and temperature versus time in the TGA experiments showing the high stability of these model compounds before the onset of cracking. This curve is for P-BiTh-P after 5 min hold up at ambient temperature followed by a 10 °C/min ramp to 500 °C and a final isothermal hold up for 15 min	112
Figure 5.3: Coke yield for all the model compounds versus the estimated boiling points	113
Figure 5.4: The three major pairs, A , B , and C , of cracked products formed by the tested archipelago compounds in the microreactor experiments	116
Figure 5.5: The molar yields for P-3,5-pyr-P experiments at different conversion levels.....	119
Figure 5.6: Molar yields for P-BiTh-P experiments at different conversion levels. Parent-minus-P was not detected and hence is not shown in the figure	120
Figure 5.7: MALDI–MS spectra for P-3,5-pyr-P showing the addition product region as the conversion increases.....	121
Figure 5.8: MALDI–MS spectra for P-BiTh-P at various conversion levels....	122
Figure 5.9: The normalized molar yields (moles formed with BP/ moles formed without BP) of major cracking products by P- <i>m</i> Ph-P with BP as a diluents	127
Figure 5.10: MALDI–MS of P- <i>m</i> Ph-P with and without BP at two different molar ratios. New peaks, such as the one at <i>m/z</i> 584, result from addition reactions between major cracked products of P- <i>m</i> Ph-P and BP	128
Figure 5.11: MALDI-MS/MS of the <i>m/z</i> 584 signal shown in Figure 5.10 . The splitting pattern indicate methybenzopyrene and methylpyrene ions as the major fragments, consistent with an alkyl–aryl addition between BP and <i>m/z</i> 333 fragment (Parent-minus-P), consistent with the drawn structure	129
Figure 5.12: A negative correlation is apparent between the isotropic temperature (the temperature of liquid crystals disappearance) and the coke yield of the archipelago model compounds	130

- Figure 5.13:** The liquid crystals formed by P-3,5-pyr-P during the hot stage microscopy under cross-polarized light. These LC started to form at ~70–80 °C and disappeared at ~260 °C131
- Figure 5.14:** Estimated bond dissociation energies (BDE) of C–C and C–H bonds in P-*m*Ph-P, as well as standard heat of formation values (ΔH_f°) at 298 K. ^aEstimated by Marrero and Gani group additivity method. ^bFrom Smith and Savage. ^cFrom McMillen and Golden. All values are given in kcal/mol134
- Figure 5.15:** Cracking pathways via β -scission of the rearranged radical in P-*m*Ph-P. The addition through pyrene is expected to be the major pathway as the resultant radical can be delocalized over many atoms in pyrene. Numbers on arrows are enthalpy changes while those next to the structures are the standard heats of formation at 298 K in kcal/mol, as estimated and summarized in **Table 5.5**140
- Figure 5.16:** (a) The transition state resulting from the benzene–pyrene ring addition after the initial alkyl–pyrene or alkyl–benzene ring closure. The resulting radicals are marked differently to easily follow their resonance steps (not both in the same molecule). (b) If the radical in (a) formed by 1,2-aryl shift through benzene followed by benzene–pyrene closure, the resulting radical at the ipso position in pyrene could abstract hydrogen then rapidly rearomatize to pyrene and Parent-minus-EtP olefin.....141
- Figure 5.17:** The rapid cleavage of P-BiTh-P to a diolefin and two radicals build the radicals and olefins pool quickly and engage in addition reactions at a higher rate and more effectively than in hydrocarbons143
- Figure 5.18:** A simplified reaction network for coke formation. The indices *i*, *j*, *k*, and *m* represent the number of ring groups. Experimental results for the largest detected products from MALDI–MS suggest that for $j > 10$ in this family of pyrene compounds, the solubility is insignificant. Termination reactions by radical combinations can take place at any point of the reaction148
- Figure 6.1:** Structure of cholestane with ring designation and carbon numbering155
- Figure 6.2:** Structure, molecular weight, and short name notation (in parentheses) of the six model compounds156

- Figure 6.3:** Two TGA runs of Chol-Thio show very good repeatability. The derivative curves are used to calculate the kinetics shown in **Table 6.1**. The temperature profile curve is also shown162
- Figure 6.4:** Rate of weight loss versus temperature for the six cholestane-based model compounds as measured in the TGA. Chol-Py has the highest temperature at the maximum rate of weight loss in this family of compounds.....163
- Figure 6.5:** MALDI-MS of Chol-Ph reaction products at 375 °C–20 min. Two major products are observed only that are 16 m/z from the parent.....167
- Figure 6.6:** MALDI-MS of Chol-Ph reaction products at 420 °C–20 min167
- Figure 6.7:** MALDI-MS of Chol-Py reaction products at 420 °C–20 min.168
- Figure 6.8:** MALDI-MS of Chol-BB products of reactions at 34 and 84% conversion. Cracked products on the top spectra dehydrogenate and dealkylate to give the observed peaks in the bottom.....170
- Figure 6.9:** MALDI-MS/MS of the major product of m/z 679 from Chol-BB reaction at 420 °C–40 min. The cleavage pattern indicates that this product still has the alkyl chain and the bibenzyl group attached173
- Figure 6.10:** (A) Estimation of the BDE of the C10–C19 bond in cholestane using 9-methyldecalin as an approximation. (B) Estimation of the heat of reaction for the β -scission to expel a methyl group and form a double bond at the C1–C10 position in the cholestane part of the molecules176
- Figure 6.11:** The aliphatic region in the ^1H -NMR of Chol-BB before reaction (top), at 34% conversion (middle), and at 84% conversion (bottom).....179
- Figure 6.12:** Comparison of the experimentally measured ^1H -NMR spectrum for Chol-BB (top) and the calculated or simulated spectrum using MestReNova (bottom). The arrows show the position of corresponding resonances in the experimental spectrum for some protons.....180
- Figure 6.13:** Enlarged region around the benzylic position of the NMR spectra of Chol-BB at 34% and 84% conversion along with the simulation of the two possible structures of the major cracked

product of 679 m/z shown in Figure 6.14 . BB denotes the resonance arising from the benzylic protons in bibenzyl (protons e in Figure 6.12)	182
Figure 6.14: Suggested decomposition pathway for Chol-BB to form the major cracked products of m/z 679 ((a) and (b)). Subsequent aromatization of A, B, and C rings with loss of the 8-carbon side chain (after methyl migration in (a)) would give the (c) product of m/z 563 from both (a) and (b)	183
Figure 6.15: The aromatic region in the ^1H -NMR of Chol-BB before reaction (top), at 34% conversion (middle), and at 84% conversion (bottom). The resonances marked with an asterisk are from a known contaminant (diethylphthalate, also the ones at $\delta \sim 1.4$ in Figure 6.11)	184
Figure 7.1: The molecular structures of the model compounds used in this study	194
Figure 7.2: Comparison of the TGA trends for P- <i>m</i> Ph-P, P-3,5-pyr-P, and a 1:1 mixture of the two compounds, all following the same temperature profile shown on the figure	198
Figure 7.3: Coke yield as a function of P-3,5-pyr-P weight fraction, in mixtures with P- <i>m</i> Ph-P	199
Figure 7.4: E versus the weight fraction of P-3,5-pyr-P mixed with P- <i>m</i> Ph-P	201
Figure 7.5: TGA results of THP, P-3,5-pyr-P, and a 1:1 mixture of the two compounds	202
Figure 7.6: Total coke yield from THP and P-3,5-pyr-P mixtures shown against the weight fraction of P-3,5-pyr-P	203
Figure 7.7: The apparent activation energy of cracking (E) values from the separate peaks observed in TGA (Figure 7.5) for P-3,5-pyr-P and THP mixtures. Black circles are from the first peak (mainly THP mixture) and white circles are calculated from the second peak (mainly P-3,5-pyr-P mixtures)	204
Figure 7.8: The coke yield by a mixture of P-BiTh-P and P- <i>m</i> Ph-P. The sample mixed using MC solvent is shown as a white circle	206
Figure 7.9: The apparent activation energy of cracking for a mixture of P-BiTh-P and P- <i>m</i> Ph-P model compounds as a function of the weight fraction of P-BiThP	207

Figure A.1: TGA experiment with CaOx performed on Oct 09	220
Figure A.2: Six experiments on CaOx typically performed after instrument maintenance	221
Figure A.3: Oxygen leak test with copper powder.....	223
Figure A.4: Temperature curve for the LHS SB	224
Figure A.5: The temperature profile for heating a microreactor in the RHS SB. After reaching the final temperature, the reactor was removed and was allowed to cool in air followed by immersion in cool water.....	225
Figure A.6: Two experiments of heating the microreactor with a glass liner inside followed by two different cooling profiles.....	226
Figure A.7: The integrated area of GC peaks as a function of the concentration of BB in MC. The line shown is the regression line	228
Figure A.8: Response factor of the GC experiments of BB with NP as the calibration standard (equals the slope). The line shown is the regression forced through the origin point giving the shown equation.....	228
Figure A.9: Effect of ramping temperature while fixing the oven starting temperature at 40 °C and the carrier gas flow rate at 0.2 mL/min..	229
Figure A.10: Effect of helium gas flow rate on the GC results. The oven ramping and starting temperatures are fixed at 6 °C and 40 °C, respectively.....	230
Figure A.11: Effect of oven starting temperature on the retention time and peak shapes. FR and RT fixed at 0.2 mL/min and 6 °C/min, respectively.....	231
Figure A.12: A linear relationship exists between the area/concentration ratio of BB to NP in spite of the variable RT, FR, or ST used in obtaining the above data points	232
Figure A.13: Integrated area of the pyrene peak in GC as a function of C	234
Figure A.14: Response factor calculation of pyrene to phenanthrene in solution with P-3,5-pyr-P	234
Figure A.15: Area of P in GC as a function of C with P-BiTh-P in MC.....	235

Figure A.16: Response factor calculation of pyrene to phenanthrene in solution with P-BiTh-P	236
Figure A.17: Area of BP in GC as a function of concentration in MC	237
Figure A.18: Response factor calculation of BP to Phen dissolved in MC	237
Figure A. 19: Effect of flow method. The order of eluting peaks corresponds to Phen, P, and P-BiTh-P, respectively	240
Figure A. 20: Effect of detector settings. The order of eluting peaks is similar to Figure A.19	241
Figure A.21: Response factor calculations for P-BiTh-P to Phen dissolved in MC in HPLC	242
Figure A.22: Integrated area of P-BiTh-P in HPLC as a function of C	243
Figure A.23: Area of P in HPLC as a function of C . P is in MC solution with Phen and P-BiTh-P	244
Figure A.24: Area of P in HPLC as a function of C . P is in MC solution with Phen and P-3,5-pyr-P	245
Figure A.25: Area of P-3,5-pyr-P in HPLC as a function of C	246
Figure A.26: Area of P-2,6-pyr-P in HPLC as a function of C	247
Figure A.27: Integrated area of P- <i>m</i> Ph-P in HPLC as a function of C . In this sample, P- <i>m</i> PhP, P, Phen, and BP were dissolved in MC.....	248
Figure A.28: Area of P- <i>p</i> Ph-P in HPLC as a function of C	249
Figure A.29: Area of P-Th-P in HPLC as a function of C	250
Figure A.30: Area of BP in HPLC as a function of C in MC with Phen	251
Figure A.31: Area of TDP in HPLC as a function of C	252
Figure A.32: Area of Chol-Ph in HPLC as a function of C	253
Figure A.33: Area of Chol-BB in HPLC as a function of C	254
Figure A.34: Integrated area of Chol-Py in HPLC as a function of C	255

NOMENCLATURE

ABBREVIATIONS

OPEC	Organization of the Petroleum Exporting Countries
ASTM	American Society for Testing and Materials
VR	Vacuum Residue
PAH	Polycyclic Aromatic Hydrocarbons
Da	Dalton
MCR	Micro–Carbon Residue
RD	Radical Disproportionation
RRD	Reverse Radical Disproportionation
RHT	Radical Hydrogen Transfer
HA	Hydrogen Atom
DN	Dewar Reactivity Number
BDE	Bond Dissociation Energy
VPO	Vapor Pressure Osmometry
NMR	Nuclear Magnetic Resonance
MALDI	Matrix–Assisted Laser Desorption / Ionization
TGA	Thermogravimetric Analysis
HPLC	High Performance Liquid Chromatography
GC	Gas Chromatography
FID	Flame Ionization Detector

XPS	X-ray Photoelectron Spectroscopy
OFW	Ozawa-Flyn-Wall
KAS/V	Kissinger-Akahira-Sunose/Vyazovkin
MS	Mass Spectrometry
ΔH_f°	Standard heat of formation
UV	Ultraviolet
m/z	Mass / Charge Ratio
LC	Liquid Crystals
LHS	Left Hand Side
RHS	Right Hand Side
SB	Sand Bath
RT	Ramping Temperature
FR	Flow Rate
ST	Oven Starting Temperature

CHEMICAL ABBREVIATIONS

P	Pyrene
Phen	Phenanthrene
BP	Benzo[a]pyrene
Ph	Phenyl
P-<i>n</i>But-P	1,4-dipyren-1-yl-butane
P-Th-P	2,5-Bis(2-pyren-1-yl-ethyl)-thiophene
P-<i>m</i>Ph-P	1,3-Bis(2-pyren-1-yl-ethyl)-benzene
P-<i>p</i>Ph-P	1,4-Bis(2-pyren-1-yl-ethyl)-benzene

P-2,6-Pyr-P	2,6-Bis(2-pyren-1-yl-ethyl)-pyridine
P-3,5-Pyr-P	3,5-Bis(2-pyren-1-yl-ethyl)-pyridine
P-2,5-Pyr-3-Me-P	2,5-Bis(2-pyren-1-yl-ethyl)-3-methyl-pyridine
P-BiTh-P	5,5'-Bis(2-pyren-1-yl-ethyl) -2,2'-bithiophene
P-DBF-P	2,8-Bis(2-pyren-1-yl-ethyl)- dibenzofurane
P-BiPh-P	1,1'-Bis(2-pyren-1-yl-ethyl) -4,4'-biphenyl
P-B-P	4,4'-Bis(2-pyren-1-yl-ethyl) -2,2'-bipyridine
P-F-P	2,7-Bis(2-pyren-1-yl-ethyl)- 9,9-diethyl-9H-fluorene
<i>n</i>-C7	Normal heptane
<i>n</i>-C16	Normal hexadecane
DDP	1-dodecylpyrene
DPE	1,20-di(1-pyrenyl)eicosane
DCTB	2-[(2E)-3-(4-tert-butylphenyl)-2-methylprop-2-enylidene] malononitrile
MC	Methylene Chloride (Dichloromethane)
MeP	1-methylpyrene
EtP	1-ethylpyrene
BB, bibenzyl	1,2-diphenylethane
Chol-Ph	Cholestane–benzoquinoline substituted with phenyl
Chol-BB	Cholestane–benzoquinoline substituted with bibenzyl
Chol-Thio	Cholestane–benzoquinoline substituted with thiophene
Chol-NP	Cholestane–benzoquinoline substituted with naphthalene
Chol-Ph-<i>n</i>But	Cholestane–benzoquinoline substituted with phenyl-4- <i>n</i> butyl
Chol-Py	Cholestane–benzoquinoline substituted with pyrene
MeOH	Methanol
THP	1,3,6,8-tetrahexylpyrene

TDP	1,3,6,8-tetradecylpyrene
CaOx	Calcium Oxalate
NP	Naphthalene

SYMBOLS

δ	NMR chemical shift, measured in ppm
E	Activation energy of cracking
A	Pre-exponential factor
A	Integrated area under peak
n	Reaction order
k	The rate constant = $-dW/dt/W$
T	Temperature
T_P	Peak Temperature (T at maximum rate of weight loss)
$(-dW/dt/W)_P$	Normalized rate of weight loss at the maximum point
W_P	Weight at the maximum rate of weight loss
T_f	Temperature at which an extent of conversion is reached
t	Time
X	Conversion
F	Response Factor
C	Concentration
W, Wt, wt	Weight
R	Universal gas constant
β	Heating rate in TGA

CHAPTER 1

INTRODUCTION

As the world economy recovers from the recession of 2008/2009, both the oil prices and energy demand are increasing rapidly worldwide to pre-recession levels and higher. The average OPEC basket price for conventional oils in July of 2011 was \$112, which is over 60% higher than the \$69 price for the same month five years ago.¹ These higher prices for conventional oil coupled with the ever-increasing global demand make unconventional resources, such as heavy oils and bitumen, more attractive and their exploitation economically feasible. The Canadian province of Alberta currently has the third largest oil reserves, after Saudi Arabia and Venezuela, with 171.3 billion barrels of oil, over 99% of which is bitumen, making Canada an important global hub for unconventional oils.² Unfortunately, the heavy oils and bitumen have many difficulties and challenges in extraction, transportation, and refining such that most refineries that use conventional oils cannot process them as they are produced.

Heavy oils and bitumen have high density, hence the term heavy, high viscosity, high heteroatom content, such as nitrogen and sulfur, as well as high metal content such as nickel and vanadium.³ These heteroatoms and metals have to be dealt with to meet the environmental restrictions and prevent fouling of catalysts in downstream upgrading processes. Moreover, the vacuum residue

(VR), which is the material that remains non-distillable after vacuum distillation, typically accounts for up to 50% of the whole bitumen.⁴ Therefore, any economically profitable processing for bitumen must successfully utilize this fraction by thermally cracking the VR into distillable liquids.

The asphaltenes is a solubility class, by definition, that comprises a significant portion of bitumen, heavy oils, and VR. The asphaltenes have higher heteroatom content than the parent VR or bitumen, and higher tendency of forming large amounts of solid residue, or coke, during thermal upgrading processes.^{4, 5} Commercial processes that thermally crack VR deal with the above two problems but they are either expensive to operate due to the high cost of hydrogen and catalyst, such as in hydroconversion processes, or yield lower amounts of liquids due to high levels of coke formation, such as in delayed or fluid coking. The improvement of existing technologies in terms of increasing the liquid yield, reducing the coke formation, and sustaining longer operational cycles, or even the development of new technologies for the thermal cracking of VR and the asphaltenes, require full understanding of the coking and cracking pathways of the different constituents of these materials.

Attempts to unravel the properties and constituents of the asphaltenes have been hampered by the extreme complexity of this fraction, giving controversial results, as will be outlined briefly in Chapter 2. The VR and asphaltenes, and petroleum in general, are complex mixtures of hundreds of thousands of components.⁶ The asphaltenes typically contain any compounds within the VR with low solubility in *n*-alkane solvents, due to high molecular weight, high

aromaticity, high polarity, or any combination of these features. Therefore, the identification, separation, and quantitative analysis of the different components and their behavior under thermal conditions are nearly impossible. Alternatively, one could investigate the properties and the behavior under thermal cracking conditions of certain functional groups that are known to be present in the asphaltenes or VR in appropriate model compounds. This approach has been long applied in the literature, as will be shown in the next chapter, and has proven to yield much more quantitative information about the behavior of different groups such as alkanes, alkylaromatics, and naphthenoaromatic moieties in model compounds. Following this approach, the subject of this thesis is the thermal behavior of specially synthesized model compounds containing different functionalities to mimic groups known to be present in the asphaltenes and VR. The difference between this research and the previous studies lies in the emphasis on the liquid phase reactions with large and complex model compounds that are custom-made, with molar masses over 530 Da.

The terms VR and asphaltenes could be used interchangeably in this introduction since the asphaltenes are a significant sub-class of the VR. The continuity of the petroleum mixture, as described excellently by Boduszynski⁷, suggests that molecules in the asphaltenes should not look very different from those in the VR. The range of the molar masses in these complex mixtures is quite wide, suggesting that any VR component could possibly be present in the asphaltenes too.⁷ Although the discussion in this work focuses on the asphaltenes,

all the results, discussion, and findings are equally applicable to the VR, which is more important industrially.

1.1 RESEARCH OBJECTIVES

The most important objective of this research is to acquire a better understanding of the thermal cracking and coking behavior in the condensed liquid phase, using especially synthesized model compounds. The emphasis on performing the reactions in a condensed or liquid phase is to mimic most of the commercial processes, in which the thermal cracking reactions are carried out in the liquid phase. Therefore, the model compounds were synthesized with high molecular weights, but within the established range reported in the literature, to ensure they remain liquid at the reaction conditions. In addition, these model compounds incorporate structures known to be present in the asphaltenes such as polycyclic aromatics, alkyl bridges and side-chains, pyridinic, thiophenic, and biomarker-like entities, among others. The model compounds are grouped in three different families based on their distinct chemical structures: archipelago, island, and substituted cholestane-benzoquinoline compounds. Because these model compounds are especially synthesized and are not commercially available, techniques that use milligram quantities are necessary to obtain as much information on the thermal behavior with the least amount of samples. Some of the thermal characteristics of the model compounds that were investigated in this research include: the kinetics of cracking, yield of coke, the nature and selectivity of cracked and addition products, and the effect of the chemical structure on the cracking and coking pathways.

1.2 THESIS OUTLINE

The thesis is organized in eight chapters, including this introduction as the first chapter. The second chapter gives background on the relevant literature. A brief overview of the asphaltenes, including their definition, origin, main properties, and thermal reactions, is presented in this chapter. In addition to the thermal reactions of the asphaltenes and VR, a few important studies on the thermal reactions of model compounds will be reviewed.

The third chapter reports the formation of archipelago structures during the thermal cracking of different families of model compounds. The reaction conditions were chosen to simulate catagenesis over a very short time scale as well as the thermal conditions in commercial upgrading processes. The objective was to investigate how the heavy components may form during catagenic reactions of petroleum and in thermal upgrading processes, such as coking. This study revealed the importance of the addition reactions in the liquid phase by quantitatively determining the yields and identifying structures of the addition products.

In the fourth chapter, the cracking kinetics of the archipelago model compounds are investigated. To accurately measure the cracking kinetics for these model compounds, as well as the other families of compounds, a new method for calculating the kinetics was established. This differential method to calculate the Arrhenius kinetics from thermogravimetric analysis data is compared against peak temperature and isoconversional methods, which are the most common methods reported in the literature. The differential analysis is shown to give the most

consistent and accurate measurements of the cracking kinetics with the least amounts of samples.

Chapter five gives a comprehensive discussion on the effect of the chemical structure on the cracking and coking pathways within the archipelago family of compounds. The model compounds in this homologous series are pyrene-based with the motif *pyrene*–(C_2H_4)–*A*–(C_2H_4)–*pyrene*, where *A* is an aromatic group that may contain sulfur, nitrogen, or oxygen. The objective of this section is to compare these model compounds against each other to understand the role of hydrocarbon groups versus heterocyclic groups in the cracking and coke formation processes.

Chapter six is dedicated to the thermal reactions of the substituted cholestane–benzoquinoline model compounds. The cholestane part of these molecules is typically employed as a representative of biomarkers. Fusing the cholestane with the aromatic benzoquinoline mimics some naphthenoaromatic groups that are present in the asphaltenes. The thermal reactions of six compounds, that differ only on the substituent on benzoquinoline, are reported in this chapter. The results give insights on possible reactions experienced by naphthenoaromatic groups and imply structural aspects on how biomarkers are present in kerogen, VR, and the asphaltenes.

Chapter seven is a short report on the thermogravimetric analysis experiments of binary mixtures of model compounds. Hypotheses on the effect of

mixing two model compounds on the coke yield and cracking kinetics are examined and briefly presented in this chapter.

The last chapter of this thesis, chapter eight, gives an overall synthesis of the previous chapters and outlines the significance of the work to practical issues, in addition to the gaps and possible sources of errors and uncertainties in this research. The major conclusions drawn from the previous chapters are also summarized followed by recommendations for future research.

1.3 REFERENCES

1. OPEC Basket Price. www.opec.org (August 1, **2011**),
2. Government of Alberta. www.oilsands.alberta.ca (August 1, **2011**),
3. Strausz, O. P.; Lown, E. M., *The Chemistry of Alberta Oil Sands, Bitumens, and Heavy Oils*. AERI: Calgary, AB, **2003**.
4. Speight, J. G., *The Chemistry and Technology of Petroleum*. Fourth ed.; CRC Press: Boca Raton, FL, **2007**.
5. Siskin, M.; Kelemen, S. R.; Eppig, C. P.; Brown, L. D.; Afeworki, M., Asphaltene molecular structure and chemical influences on the morphology of coke produced in delayed coking. *Energy Fuels* **2006**, 20, 1227-1234.
6. Hughey, C. A.; Rodgers, R. P.; Marshall, A. G., Resolution of 11 000 compositionally distinct components in a single Electrospray ionization Fourier transform ion cyclotron resonance mass spectrum of crude oil. *Anal Chem* **2002**, 74, 4145-4149.
7. Boduszynski, M. M., Composition of heavy petroleums. 1. Molecular weight, hydrogen deficiency, and heteroatom concentration as a function of atmospheric equivalent boiling point up to 1400.degree.F (760.degree.C). *Energy Fuels* **1987**, 1, 2-11.

CHAPTER 2

LITERATURE BACKGROUND

2.1 THE ASPHALTENES

The canonical properties and thermal behavior of these compounds must be reviewed to link the behavior of model compounds under thermal cracking conditions to the real asphaltenes. The current understanding of the asphaltenes, their origin, key features and properties, such as the molecular weight and structure, and modeling of the asphaltenes will be summarized in this section.

2.1.1 Definition of the Asphaltenes

Fractionation of petroleum using solvents has been practiced for decades.¹ One of these fractions is termed asphaltenes, which are brownish–black powdery materials precipitated by addition of low–boiling alkane solvents to petroleum, residua, or bitumen.² Hence, the asphaltene fraction is just a solubility class that is soluble in aromatic solvents, such as benzene or toluene, and insoluble in *n*-pentane or *n*-heptane. The definition based on solubility in aromatics and insolubility in alkanes makes the asphaltene the least soluble fraction of petroleum, containing any compounds with low solubility due to high aromaticity, molecular weight, polarity, or any combination of the three. These factors make the asphaltene precipitation from petroleum feedstocks a complex process that is

affected by a number of factors, which are standardized in laboratory determinations to ensure reproducibility. For example, the ASTM method to determine the heptane–asphaltenes in crude petroleum, numbered D6560, recommends using ~30 mL heptane per gram of sample that has an asphaltene content less than 25 wt% and ~50 mL/g if the sample has over 25 wt%. If the material is very heavy and viscous, dissolution in toluene is recommended before adding ~40 volumes of heptane to each volume of sample at room temperature and leaving the sample to precipitate over night before filtering.³ Nevertheless, variations of the precipitating method are adapted from lab to lab and hence one must be cautious when comparing properties and behavior of asphaltenes precipitated using different solvents or techniques.

At the industrial scale, the removal of the asphaltenes from bitumen or heavy oils is used in some cases to reduce the metal and heteroatom contents of the remaining oil. This reduction can be beneficial to protect and prolong the lifecycle of catalysts in the downstream processes. Industry conditions for the precipitation of asphaltenes use many different solvents, such as paraffins, isoparaffins, straight–run naphtha, or other non–aromatic solvents over a range of dilutions and temperatures.⁴ These operating variables are also used to manipulate the yields and rates of precipitation. Such studies are also conducted at the laboratory scale in order to prepare samples with different characteristics and to develop models for phase equilibrium and separation kinetics. These studies demonstrate that the solvent type, dilution degree, temperature, and contact time are the major factors that influence the yield and properties of the asphaltenes from a given crude oil.²

2.1.1.1 Effect of Solvent Type

The solvent used to precipitate asphaltenes plays a major role on the yield. Mitchell and Speight⁴ precipitated the asphaltenes from Athabasca bitumen with many pure non-polar solvents, such as normal paraffins, isoparaffins, cycloparaffins, terminal olefins, aromatics, and blends of different ratios of benzene and *n*-pentane solvents. The amount of asphaltenes precipitated by these solvents correlated linearly with the solubility parameter of these solvents and blends. The solubility parameter, defined by Hildebrand and co-workers^{5, 6}, is a measure of the solvent power, or the energy of the solution, to overcome the association forces of the solute.⁴ Hence, aromatic solvents would have high solution energies due to their higher dispersion forces, while the paraffins would have the least solution energies since they tend to undergo parallel self-association⁴, which translates into lower solvation power. In addition to affecting the yield, the properties of the precipitated asphaltenes using different solvents could also be different.³ Therefore, when comparing asphaltic materials, the precipitating solvents must be identified; for example *n*-heptane asphaltenes or *n*-pentane asphaltenes.

2.1.1.2 Effect of Degree of Dilution

Even when using the same solvent, the yield of asphaltenes is affected by the ratio of solvent to bitumen or other petroleum materials. As the ratio of the precipitating solvent increases, keeping other factors constant, the asphaltenes yield increases until a plateau is reached when the solvent ratio is above circa 25

mL/g of asphaltenes.³ Gawrys et al.⁷ separated the asphaltenes into 20–30 fractions by gradually increasing the added *n*-heptane and examined their chemical compositions. The results suggested that the type of interactions responsible for inducing precipitation is petroleum-dependent. In two crudes examined by Gawrys et al.⁷, the polar and H-bonding interactions were more important, while in another crude oil, dispersion forces were more important. Nitrogen, sulfur, oxygen, and aromaticity were generally distributed normally throughout the asphaltene fraction.

2.1.1.3 Effect of Temperature

The temperature at which the precipitation is performed affects the yield of asphaltenes. Early investigations suggested an increase in the asphaltenes yield as the temperature increases due to the decrease in the solubility parameter of the low molecular weight solvents, such as pentane, as the temperature increases.⁴ But this apparent increase in the asphaltenes yield with increasing temperature is actually added resin materials that now precipitated with the asphaltenes at the elevated temperatures.^{2, 8} For the asphaltenes fraction itself, the increase in temperature increases the solubility of the asphaltenic materials resulting in decreased precipitate yield.^{3, 9} To avoid such complications in the precipitation of the asphaltenes, ambient conditions are typically used.

2.1.1.4 Effect of Contact Time

At fixed solvent ratio and temperature, the amount of asphaltenes precipitated increases with time after adding the solvent, reaching a plateau after

circa 24 hours in *n*-heptane.³ For *n*-pentane, for example, the required contact time is on the order of ~ 8 hours to obtain stable asphaltenes yields.⁸ The long contact time before reaching stable yields is due to the time required by the asphaltene molecules to agglomerate and also due to the time required for the solvent to penetrate the heavy materials, such as bitumen, which is diffusion-controlled.²

2.1.2 Origin of Petroleum and the Asphaltenes

An overview of how petroleum formed serves as an indication of the nature and level of complexity of the asphaltenes, which constitute a significant portion of heavy oils. The prevalent view of the origin of petroleum is that organic material is accumulated in sedimentary deposits and transformed into a polymeric material called kerogen. Although kerogen is typically considered as a precursor to petroleum, it is actually a by-product of the generation and maturation processes of petroleum.² Kerogen is a carbonaceous material that occurs in sedimentary organic matter and consists of a complex mixture of lipids, polymers, and biochemicals cross-linked into a very high molecular weight geopolymer that is insoluble in any organic solvent.^{10, 11} Kerogen is suggested to be composed of a number of aromatic, naphthenic, naphthenoaromatic, heteroaromatic cores that are linked by aliphatic, ester, ether, or thioether chains, in addition to pendant groups present on the cores.¹¹⁻¹³ **Figure 2.1** shows a representative portion, after Freund et al.¹⁰, of kerogen that shows 9 cores of about 10,000 cores that make up the kerogen.

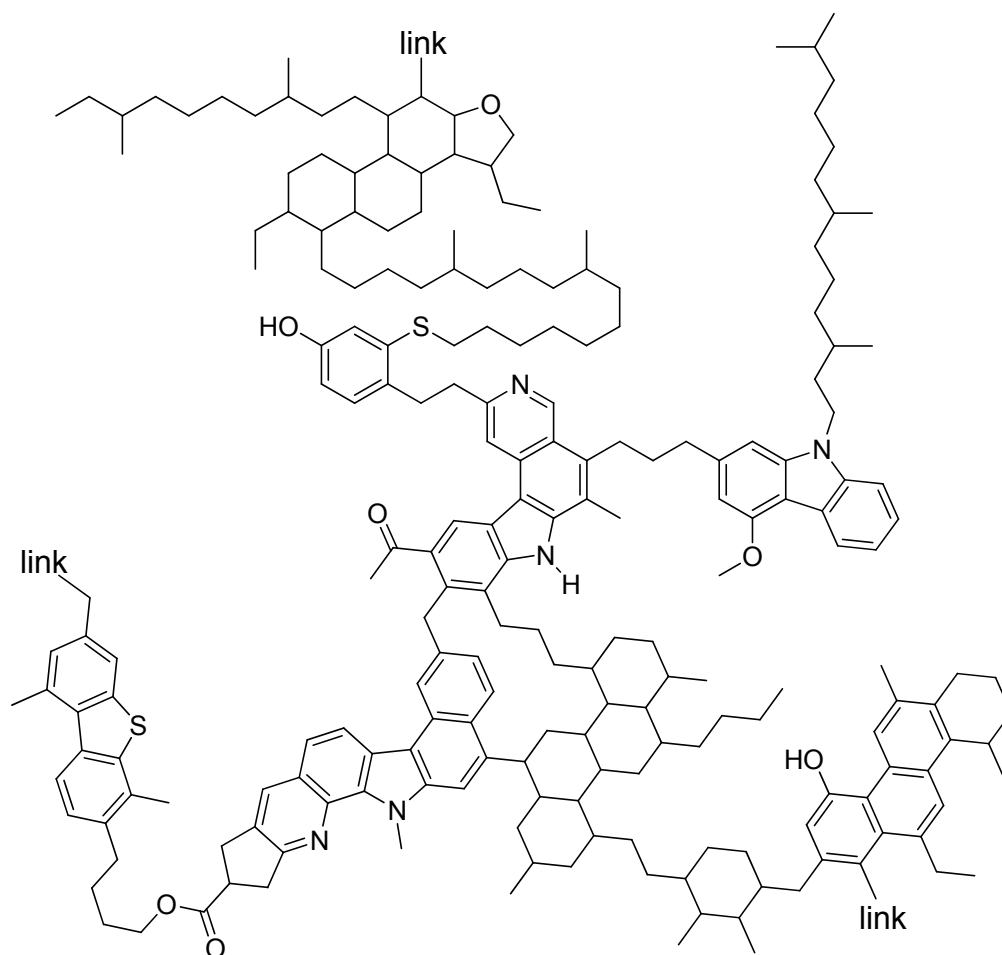


Figure 2.1: Kerogen chemical structure, after Freund et al.¹⁰ The positions where the structure continues to propagate are marked as 'link'.

After forming the kerogen deposits in sedimentary rocks, continued geothermal heating after burial, in addition to the role of anaerobic bacteria² at the early stages, causes the kerogen to undergo catagenesis, or thermal cracking, releasing petroleum¹⁴, which migrates and accumulates in traps to form commercial deposits.¹⁵ The asphaltenes, as a sub-class of oil, could generate directly from the decomposition of the kerogen or form after the formation of petroleum. In any case, the complexity of the kerogen is expected to give hundreds of thousands of molecules with different functional groups upon thermal

cracking, from which any compound could end up as an asphaltene molecule if it meets the low solubility criteria of the asphaltenes.

2.1.3 Canonical Properties of the Petroleum Asphaltenes

2.1.3.1 The Basics

Since the asphaltenes could be isolated from heavy oils and VR relatively easily, they have been the focus of many research studies on their properties and behavior in thermal and catalytic upgrading processes. A full review of the properties of the asphaltenes is beyond the scope of this thesis, but rather review for some basic properties that are relevant to the thermal behavior will be outlined. The elemental composition, aromaticity, density, viscosity, and melting point of the petroleum asphaltenes are briefly described below.

2.1.3.1.1 Elemental Composition

Although the asphaltenes is a complex mixture of different components, the basic building blocks are similar among asphaltenes from different sources; although some extreme ranges exist specially in heteroatom contents.² The asphaltenes are made up of C, H, N, S, O, Ni, and V.¹⁶ For example, the range of C, H, S, N, and O in the asphaltenes from Alberta heavy oils and bitumens are 80.06–86.61, 6.93–8.45, 3.47–8.21, 0.94–2.82, and 0.44–2.61 wt%, respectively.¹⁷ The Ni and V are concentrated in the VR and the asphaltenes, compared to the rest of the bitumen. For example, while the concentration of Ni and V in Athabasca bitumen are measured to be 65 and 196 ppm, respectively, the *n*-pentane asphaltenes from this bitumen contained Ni and V at 312 and 710 ppm,

respectively.¹⁸ These different constituents of the asphaltenes are arranged in different naphthenic, naphthenoaromatic, aromatic, and paraffinic groups, among many other functional groups.¹⁹ The order and type of arrangements of these groups that make up asphaltene molecules are the topics of long-standing debate, which will be highlighted in the molecular weight and structure sections.

2.1.3.1.2 Aromaticity

Consistent with the elemental analysis presented above, the H/C ratio of the *n*-C7 (*n*-heptane) asphaltenes from Alberta heavy oils and bitumens are in the range of 0.98–1.26, which is much less than the ~1.5 H/C ratio for the source from which these asphaltenes were derived.¹⁷ This low H/C ratio is indicative of the highly aromatic nature of the asphaltenes. Supported by ¹³C–NMR (nuclear magnetic resonance) spectroscopy and XPS (X-ray photoelectron spectroscopy), the carbon aromatic content of residue asphaltenes that were derived from different sources were in the range of 36–50%¹⁶, and up to 55% for Athabasca *n*-C7 asphaltenes.²⁰ The high aromaticity of the asphaltenes is linked to their higher tendency for coke formation during thermal upgrading processes. The asphaltenes residue have typically ~50% by weight as MCR (micro-carbon residue) content, while their parent VRs have an MCR content of only ~20 wt%.¹⁶ For this reason, commercial process attempt to increase the H/C ratio to minimize the coke formation and increase the liquid yield by either hydrogen addition or carbon rejection processes.

2.1.3.1.3 Density, Viscosity, and Melting Point

The density and viscosity of heavy oils are important for both the transportation and upgrading of such feedstocks. The density and viscosity of the asphaltenes, which is even higher than the heavy oils and bitumens, show clearly the heavy nature of this fraction and the challenges in handling the asphaltenes after separation from the feedstocks and during upgrading processes. The density of the saturates, aromatics, resins, and asphaltenes from Athabasca bitumen is 900, 1003, 1058, and 1192 kg/m³, respectively.²¹ Asphaltenes from other heavy oils and bitumens have densities in the range of those from Athabasca bitumen, except highly paraffinic oils, such as an Indonesian heavy oil with an asphaltenes density of only 1132 kg/m³.²¹ In addition to the high density, the asphaltenes show an extremely viscous nature when they are in the melt state, before reaching temperatures of significant reactions, such that the *n*-C7 Athabasca asphaltenes are almost 100 times more viscous than the whole VR.²⁰

The measurements of the viscosity of Athabasca asphaltenes by Asprino et al.²⁰ at the temperature range of 312–358 °C indicates that although the asphaltenes are always obtained as solid powders from precipitation, they melt at elevated temperatures. Gray et al.²² measured an average melting point of 224 °C for Athabasca asphaltenes by depositing the asphaltenes on a metal strip and heating it rapidly. As the temperature is increased to where cracking reactions start, the asphaltenes undergo thermal decomposition. These observations indicate that at the operative temperatures in upgrading processes, the asphaltenes are in

the liquid state. Therefore, our emphasis for modeling the thermal reactions in the liquid phase is in-line with the behavior of asphaltenes.

2.1.3.2 Molecular Weight

Since most of the heavy residua or VR are non-distillable, a good alternative to the distillation data is the molecular weight. Generally, as the molecular weight increases, the boiling point increases for a homologous series of compounds.²³ But one must be cautious when using the molecular weights as an indication of boiling points for complex mixtures like VR or the asphaltenes because, as Boduszynski showed and stated “compounds having similar molar masses cover a broad boiling point range and, conversely, a narrow boiling point cut contains a wide molar mass range.”²³ Therefore, for the asphaltenes fraction, a broad boiling point range is expected for such a complex mixture.

In spite of the expected wide range of molar masses for the asphaltene molecules, average values are typically reported in the current literature based on numerous analytical methods. There is hardly an agreement on this ‘average’ value, which by itself could be misleading and not necessarily representative for the whole asphaltenes. The most important reason for the different results obtained for the molecular weights of the asphaltenes from different characterization techniques, sometimes the same technique at different conditions, is due to the complexity and associative behavior of the asphaltene molecules. For example, vapor pressure osmometry (VPO) for Athabasca asphaltenes dissolved in *o*-dichlorobenzene at 120 °C gave a molar mass of the aggregated asphaltenes

of about 4000 g/mol.²⁴ Akbarzadeh et al.²¹ reported a VPO value for Athabasca asphaltenes as 7900 g/mol in toluene, which was attributed to the self-association of asphaltenes, and hence the molar mass results depended on both the temperature and the solvent. Fluorescence depolarization supported the claim of smaller molecular weights in the range of 500–1000 Da^{25, 26} as reported by Mullins and co-workers in many subsequent papers.²⁷⁻²⁹ However, this study was not supported by proper control experiments to demonstrate the ability of the method to measure average molecular weights in complex mixtures of polyfunctional molecules, as pointed out by Strausz et al.³⁰ Laser desorption mass spectroscopy suggested a range of 300–600 Da with a mean of 400 Da for the Maya asphaltenes³¹, but fragmentation was evident in the data presented, calling the results into question. Qian et al.³² applied field desorption mass spectroscopy to VR derived asphaltenes and measured an average molecular weight of 1238 Da, with the range extending from ~300–3000 Da, in a non-Gaussian distribution. Unfortunately, all of these studies lacked appropriate calibration standards to verify the ability of the instruments to properly measure molecular weight distribution of complex polyfunctional molecules. The main reasons for the uncertainty in measuring the molecular weight are size and composition variance among asphaltene molecules as well as the self-association behavior which interfere with measurements and confuse accurate data interpretations.³⁰ Different molar masses for asphaltenes from different sources is very likely, but an overall consensus exists, as observed from the above studies, that individual components

in any asphaltene will have molar masses mainly in the range of 500-2000 Da, with a spectrum tail extending up to ~3000 Da.

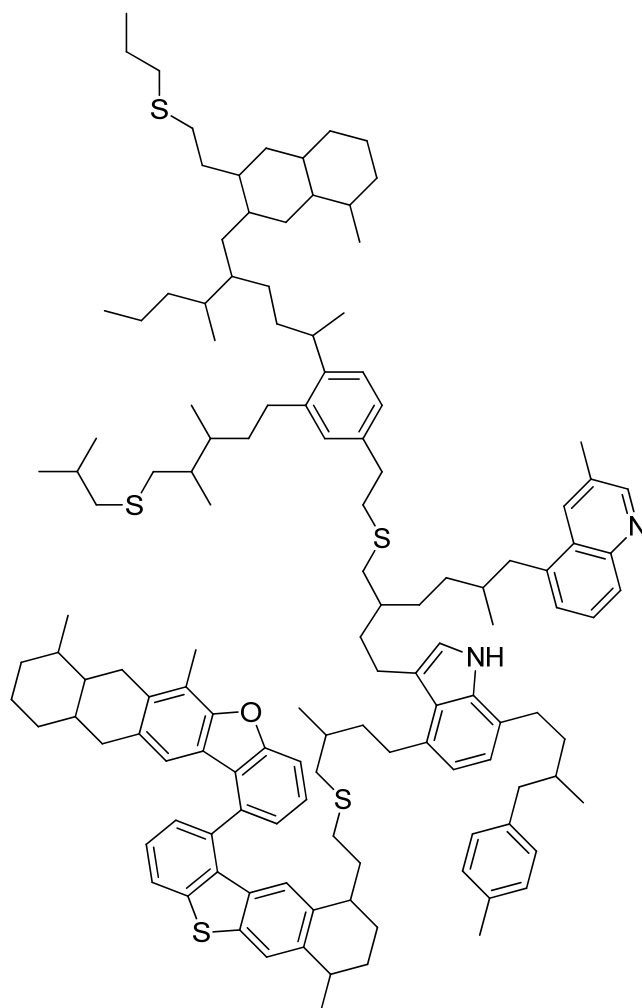
2.1.3.3 Molecular Structure

The molecular structure of petroleum asphaltenes is critical to understanding the origin and migration of these components.^{10, 15, 33} But due to the complexity of the asphaltenes, the debate on a representative chemical structure has not been resolved yet, even after reaching a consensus on the approximate range of molecular weights of the asphaltenes. The main two structural motifs suggested for the asphaltene fraction are the “archipelago” compounds, composed of alkyl-bridged aromatic and cycloalkyl groups linked together mainly with alkyl carbon bridges^{15, 19}, and the “continental” compounds that are based on highly alkylated condensed polycyclic aromatic compounds.^{26, 29}

The archipelago motif was suggested by Strausz and co-workers, starting in the late 1970s, after observing that large quantities of mono-, di-, tri-, and up to pentacyclic aromatic species are released by mild thermolysis of the asphaltenes.³⁴⁻³⁶ Subsequent extensive thermal degradation studies of Alberta asphaltenes resulted in identifying many structural units that appear to be in alkylated homologous series.³⁷ In addition, the selective oxidation of the aromatic rings, using ruthenium ion-catalyzed oxidation (RICO), by which the aromatic carbons are removed as CO₂ and the saturated carbons are left intact, revealed the abundance and importance of alkyl chains and bridges in the asphaltenes.^{37, 38} While the previous work of Strausz and co-workers was directed more towards

the qualitative aspects of the asphaltenes structure, Karimi et al.³⁹ obtained quantitative evidence for the existence of bridged structures in the asphaltenes by using thin film pyrolysis. Their rapid thermal cracking of the asphaltenes at 500 °C generated gases, liquid, and coke with over 91% recovery. Analysis of the liquid products showed the existence of mono– up to tetra–, aromatic and naphthenic rings, paraffins, thiophenes, benzothiophenes, sulfides, and nitrogen–containing molecules.³⁹ The detection and importance of pendent aromatic, alkyl, and cycloalkyl groups to refinery processes^{40, 41}, the characterization of alkyl bridges between aromatic groups^{19, 37}, and the detection of sulphide and ether bridges^{15, 42}, all support a structural paradigm for asphaltenes constructed of polycyclic aromatic and aliphatic groups connected by short alkyl bridges, like an archipelago of islands.

Figure 2.2 shows a representative structure of an archipelago model after Sheremata et al.⁴³ Although the representative structures shown by Sheremata et al. and Strausz et al. are of molecular weights of 4000–6000 Da, which is higher than the current accepted range in the literature, smaller molecules can be represented as portions of this model while preserving the structural aspects. The smaller fragments can agglomerate then to appear at the higher molecular weights detected by VPO experiments²⁴, for example, as will be discussed below in the self–association section.

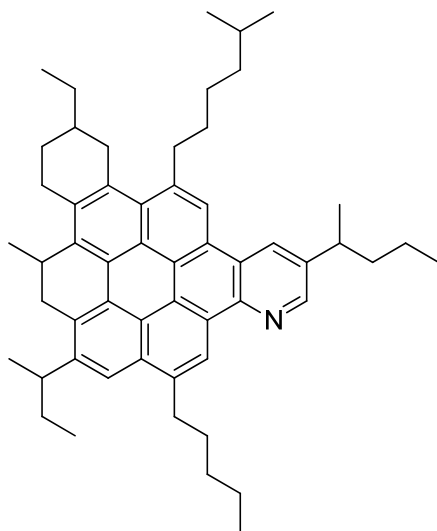


Chemical Formula: $C_{131}H_{178}N_2OS_5$
Molecular Weight: 1957.15

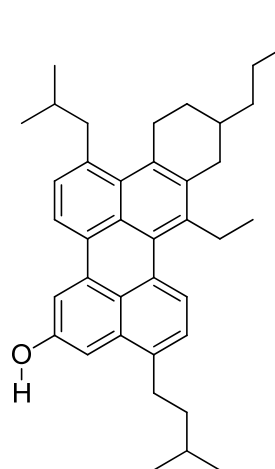
Figure 2.2: Representative asphaltene structure following the archipelago model, after Sheremata et al.⁴³ with reduced molecular weight to fit the ~500–2000 Da range.

An alternate, continental, island, or pericondensed, structural motif has also been posited, consisting of highly condensed polyalkylated aromatic compounds, some with fused saturated rings.^{26, 44, 45} Such a structure can be visualized as a hand with the palm representing the aromatic core and the fingers representing the

alkyl side chains.⁴⁶ **Figure 2.3** shows two representative structures following the island model, after Mullins²⁹.



Chemical Formula: $C_{55}H_{69}N$
Molecular Weight: 744.14



Chemical Formula: $C_{39}H_{48}O$
Molecular Weight: 532.80

Figure 2.3: Chemical structures suggested by Mullins²⁹ to be dominant in the asphaltenes.

The peripheral side-chains are presumably how such structures can be soluble in crude oils. The most recent arguments promulgated in favour of the condensed alkyl aromatic motif rely heavily on either fluorescence spectroscopy²⁶, which cannot be used to determine “average” or most probable structures in a complex mixture of components³⁰, or mass spectrometry without proper calibration by suitable reference compounds.

The complexity of the asphaltenes prevents isolation of single molecules and probing their chemical structure. In such mixtures with considerable heterogeneity where some molecules will be large with metal porphyrins and others are small

with nitrogen, oxygen, or sulfur functionalities, even if the majority of molecules are correctly predicted by one model, other molecules with very different structures cannot be ruled out. But reconciling all the results from accurately-calibrated instruments, the quantitative evidence of pendant groups, the structure of kerogen, along with the behavior of asphaltenes during processing⁴⁷, all support the archipelago motif for the dominant chemical structure of asphaltenes.

2.1.3.4 Self-Association

The self-association of the asphaltene molecules in solution is one of its canonical properties.⁴⁸ Understanding how the molecules associate to build aggregates, then arrange the aggregates into flocs, and finally precipitate, is very important in determining the onset of precipitation in heavy oil and bitumen processing. The ability to model the asphaltenes precipitation can then prevent the deposition of the asphaltenes on hot surfaces and the fouling the catalysts in upgrading processes, and lower the viscosity of the heavy feedstocks to easily process and refine deasphalted oils, as in the paraffinic froth treatment process.²¹

As mentioned in the definition of the asphaltenes, the self-association of the molecules, or the subsequent macroscopic precipitation, is affected by the solvent type, concentration, and temperature. VPO studies showed clearly that as the concentration of asphaltenes increases, the apparent molar mass increases before reaching a plateau while increasing the temperature decreases the measured associated molar mass.⁴⁹ Similar observation on the effect of temperature on the aggregate size was made by the small-angle neutron scattering technique.⁵⁰

The nature of forces that causes the asphaltene molecules to associate strongly is suggested to be mainly π - π stacking by supporters of the island model as the dominant structure of the asphaltenes.^{29, 45} For such a model, the aromatic cores of ~6 molecules form a disordered stack while the side chains are extended in the periphery to form the nanoaggregates, which subsequently cluster together in their path to flocculation.²⁹ But Gray et al.⁵¹ recently challenged this paradigm and suggested instead that the π - π stacking is only a contributing factor, rather than the dominant one, in the aggregation of asphaltene molecules. Mild heating of alkylated hexabenzocoronene in toluene solution resulted in the dissolution of the aggregation of these island-like molecules at only 42 °C. The alternative explanation for the strong association given by Gray et al. was a number of associative forces that act simultaneously in building a supramolecular assembly of the asphaltenes, such as acid-base interaction, hydrogen bonding, axial coordination by metal complexes, van der Waals forces, and π - π stacking.⁵¹ Such forces will form aggregates in line with the recent findings on the aggregate structure of the asphaltenes as being open and flocculated polymer-like materials⁴⁹, and best fit with the evidence for asphaltenes as archipelago molecules that have multiple functional groups.

2.1.4 Modeling the Asphaltene Molecules

As evident from the above brief overview of the definition and most important properties of the asphaltenes, the possible range of molar masses, structural variations, and number of different functionalities is staggering. Such complexity hinders any quantitative characterization of the heaviest components

presents and leads to controversial and uncertain results. One of the best approaches to resolve the behavior of the different constituents of the asphaltenes is by utilizing appropriate model compounds. For example, Akbarzadeh et al.⁴⁸ investigated the nature of associative forces in the asphaltenes by examining the association behavior of pyrene-based model compounds. This work resulted in better understanding of the importance of the polar groups, such as ketones and hydroxyl groups, in enhancing the association.

Tan et al.⁵² synthesized and studied the self-association behavior of a pyrene-based model compound (4,4'-Bis-(2-pyren-1-yl-ethyl)-[2,2'] bipyridinyl), which is composed of two pyrene groups that are linked to bipyridine with two ethano tethers. This compound, which has a molecular weight in the acceptable range of asphaltenes, adsorbed strongly on silica gel, showed emission spectra in the asphaltenes range in steady-state fluorescence spectroscopy, gave an apparent molecular weight in VPO measurements indicative of existing as dimers and monomers in toluene at 75 °C, and finally showed in ¹H-NMR spectroscopy that the association is taking place via π - π stacking of pyridinic and pyrenyl groups.⁵² The similarity of many properties of this compound to the asphaltenes demonstrated the ability of bridged structures, if present in the asphaltenes, to self-associate in solution.⁵² Subsequent work with this model compound, in addition to other compounds based on pyrene, revealed how water could enhance the association in the asphaltenes via hydrogen bonding.⁵³

Dechaine et al.⁵⁴ utilized the same bipyridinyl model of asphaltenes reported by Tan et al.⁵², in addition to vanadyl porphyrins model compounds, to examine

the efficacy of regular solution theories in predicting the solubility behavior of these complex molecules in solutions. Their study showed that these solution theories are incapable of predicting the solubility behavior of such model compounds, raising concerns on the accuracy of the predictions of these theories for the heavy and complex components of the asphaltenes.

Clearly, the amount of information obtained by examining selective properties of well-designed model compounds is quantitatively more instructive and informative than examining the whole asphaltenes. In our work, especially synthesized model compounds will be used to improve the understanding of the thermal behavior of some functional groups that are known to be present in the asphaltenes.

2.2 THERMAL CONVERSION OF VACUUM RESIDUE AND THE ASPHALTENES

Petroleum fractions undergo significant cracking when the temperature is raised above approximately 400 °C. Numerous commercial processes upgrade the heavy fractions of petroleum with variable severities, ranging from mild conditions to decrease the viscosity in visbreaking, to extreme conditions to convert the feed completely to light gases and olefins in the ultrapyrolysis process. Regardless of the upgrading process applied, the underlying chemistry is the same, which involves breaking the chemical bonds of the molecules of the heavy fractions to convert them to liquid fuels, which are typically accompanied by the formation of gases and coke.⁵⁵ Although commercial processes upgrade the

vacuum residues (VR), the asphaltene components crack also to give light oil, a gas mixture with good-burning properties after the removal of by-products, and coke.² For example, while the coke yield from thermal cracking of Athabasca asphaltenes is in the range of 50 wt%, the light oil is in the range of ~35–44 wt%, depending on the heating rate.^{17, 56} The high yield of light oils from the asphaltenes and the VR is the driving incentive for the industrial upgrading of these materials by thermal cracking.

In this section of the literature review cracking and coking reactions, which take place simultaneously during thermal cracking, are briefly highlighted.

2.2.1 Cracking Reactions

The chemical bonds in compounds crack spontaneously without the use of catalyst at elevated temperatures. The energy required to break these bonds depends on the nature of the bond. **Table 2.1** lists the main types of bonds that crack during thermal upgrading processes along with examples of the required energy to dissociate these bonds. At the typical upgrading temperatures of ca. 400–600 °C⁵⁵, the aromatic C–C bonds are not expected to crack because of the high resonance stabilization of the π -electrons.

Because cracking of the chemical bonds is energy intensive and results in the formation of two free radicals that are highly reactive, these free radicals are always present in low concentrations. Although the formation of free radicals requires large amount of energy, they engage quickly after formation in chain reactions with many steps that require minimal or no additional activation energies making such reactions energetically feasible.⁵⁷ Although some reports

suggest simple homolysis followed by stabilization of radical fragments by abstraction and recombination⁵⁸ in the conversion of VR to be the dominant mechanism, a more consistent and thermodynamically favorable mechanism is the free radical chain reactions. Olmstead and Freund⁵⁹ measured the activation energy for the thermal cracking of Arab Heavy VR as 51.5 kcal/mol, which is much lower than any bond in **Table 2.1**, supporting a free radical chain mechanism.

Table 2.1: Examples of bonds that crack at elevated temperatures with their bond dissociation energies (BDE) from McMillen and Golden⁶⁰.

Chemical Bond	Example of cracked bond	BDE at 298 K, kcal/mol
C–C	$n\text{C}_3\text{H}_7\text{--C}_2\text{H}_5$	80.4
	$\text{CH}_3\text{--CH}_3\text{-9-anthracene}$	67.6
C–H	H–Ph; Ph is phenyl	110.9
	H–C ₂ H ₅	98.2
	H–CH ₂ Ph	88.0
C–S	$\text{CH}_3\text{S--C}_2\text{H}_5$	73.3
C–O	$\text{CH}_3\text{O--C}_2\text{H}_5$	81.8
C–N	$\text{CH}_3\text{NH--C}_2\text{H}_5$	79.8

As in the classic Rice-Herzfeld mechanism⁶¹, β -scission and hydrogen abstraction are important propagation steps for the formed radicals. The aromatic groups would also participate in hydrogen donor-acceptor, or shuttling, reactions. Cracking of aliphatic radicals via β -scission leads to the formation of another radical and an olefin product. The most abundant products of cracking reactions typically form starting from the most stable radical or crack to give the most

stable radical.⁵⁷ The formed olefins would also participate in chain reactions such as hydrogenation reactions or radical–addition reactions in the liquid phase or high pressure gaseous phase. Examples of important propagation reactions of free radicals are shown in **Figure 2.4**. The last reaction step of the radicals is termination by radical combinations. From this basic chemistry, cracking will generate smaller products and simultaneously produce larger molecules, and these processes can be incorporated into simple kinetic models.⁶²

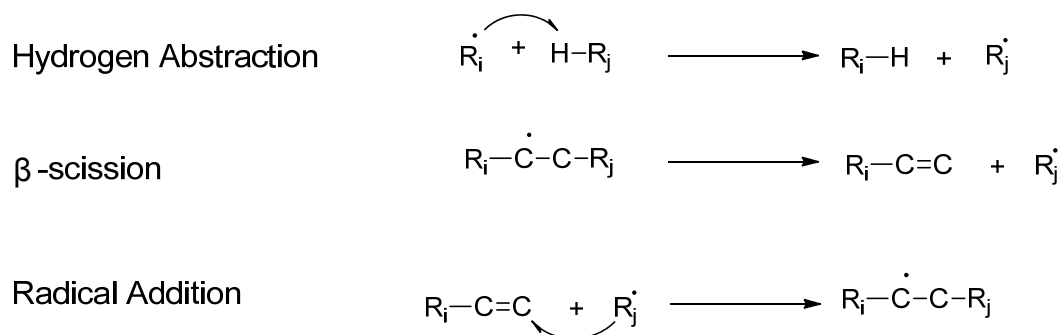


Figure 2.4: Examples of three important propagation reactions of free radicals.

2.2.2 Coking Reactions

As shown above, an important propagation step for free radicals is β -scission to form another free radical and an olefin. Radicals in condensed conditions, such as liquid phase or high pressure gas phase, undergo addition to the formed olefins to build larger structures. One example is the work of Khorasheh and Gray⁶³ where thermally cracking *n*-hexadecane in the liquid phase resulted in the suppression of olefins at higher conversion accompanied by the formation of branched alkanes with carbon atoms higher than *n*-hexadecane. Wu et al.⁶⁴ also observed the formation of these branched alkanes only in the liquid phase

pyrolysis of *n*-hexadecane. At the dilute conditions of gas phase reactions, bimolecular reactions, such as radical addition reactions, are not favorable. Similar addition products were shown recently to form during pyrolysis in the liquid phase of families of model compounds that are more complex than alkanes; giving rise to larger alkyl-bridged structures⁶⁵ (Chapter 3).

For small alkanes, such as ethane and propane, cracking to olefins is performed industrially at very high temperatures since this reaction is thermodynamically unfavorable at low temperatures.⁵⁷ For example, to obtain 95% conversion in the dehydrogenation of propane to propene and hydrogen gas at 1 MPa, a temperature of 1000 °C is required.⁶⁶ On the other hand, the reverse reactions, polymerization, are typically performed at much lower temperatures. For example, to obtain 95% conversion at 1 MPa, the dimerization of propene ($2\text{C}_3\text{H}_6 \leftrightarrow \text{C}_6\text{H}_{12}$) requires a temperature of 240 °C only.⁶⁶ The temperature at which the rate of cracking and rate of polymerization are equal is called the ceiling temperature. For ethylene addition to an ethyl radical, Gray and McCaffrey⁵⁷ calculated the ceiling temperature to be approximately 440 °C. Since most upgrading processes of heavy residues are operating at similar temperatures, in the range of 400–600 °C⁵⁵, and at liquid phase conditions, both cracking and polymerization reactions are important and favorable both kinetically and thermodynamically.^{57, 66}

In the thermal cracking of heavy feedstocks, insoluble carbonaceous materials are usually formed. Wiehe^{67, 68} linked phase behavior with coking, and suggested that coke forms due to phase separation. In this model, aromatic groups

lose hydrogen-rich pendant groups due to cracking. Upon reaching a critical concentration, these large aromatic cores could undergo liquid-liquid phase-separation, followed by rapid cross-linking reactions leading eventually to coke formation. While Wiehe focused only on aromaticity as the driving force for phase separation, oligomerization, as will be shown in Chapter 3, is a second driving force, and any combination of the two may also drive components across the phase boundary suggested by Wiehe.⁶⁹

Resolution of the actual mechanism and reactions during the cracking and coking of residues and asphaltenes is hampered by the extreme complexity of such mixtures, as shown in the asphaltenes section above. One of the best approaches to overcome this complexity is to examine molecular sub-structures in the different constituents of asphaltenes, by choosing appropriate model compounds and investigating their reaction pathways. Although there is considerable uncertainty on the range of structure and molecular weight of asphaltenes, investigating the reactions of polynuclear or polycyclic aromatic compounds with attached alkyl groups is a good representative for the groups dominantly present in the asphaltenes. The importance of using polycyclic aromatic compounds, instead of extrapolating the mechanistic observations from single-ring aromatics, is underscored by many studies that demonstrated the emergence of unexpected reaction pathways, such as the cleavage of strong bonds. The few related studies on the thermal reactions of model compounds are highlighted in the next section.

2.3 THERMAL REACTIONS OF MODEL COMPOUNDS

Thermal reactions in the gaseous phase have been studied for a long time.⁷⁰ Rice and co-workers, for example, examined extensively in the 1920s and 30s the thermal decomposition of small compounds such as methane⁷¹, acetone⁷², and hydrogen peroxide⁷³, which were usually conducted in the gaseous phase. Rice also suggested the free radical mechanism to explain the thermal decomposition of saturated hydrocarbons⁷⁴ and subsequently formalized the famous, and now accepted free radical mechanism, known as Rice and Herzfeld.^{61, 75} This early work is the foundation for understanding thermal decomposition mechanisms for organic compounds. More complex compounds have been studied since then in both gaseous and liquid phase reactions.

In this section, the difference between thermal reactions in the vapor and liquid states is highlighted first. After that, key studies on the thermal decomposition of benzene-based compounds, larger polycyclic aromatics, and biomarker compounds are summarized.

2.3.1 Vapor– Vs. Liquid–Phase Reactions

Wu et al.⁶⁴ examined both liquid– and gas–phase thermal cracking of *n*–hexadecane (*n*-C16) in the mild temperature range of 330–375 °C. Although the overall cracking kinetics were similar in these two phases, the product distribution and selectivity were very different. In the gaseous phase, only cracked or scission products formed with masses equal to or lower than the parent compound. In addition, alkenes or olefins were always formed at higher yields than the saturated

alkanes. On the other hand, cracking *n*-C16 in the liquid phase resulted in the formation of addition products, with masses higher than the parent, and reversing the selectivity of the cracked products such that at higher conversion levels of *n*-C16, the olefins formed at lower yields than the alkanes. The results from the work of Wu et al.⁶⁴ suggest that bimolecular reactions, such as H-abstraction and addition reactions, are favored in the liquid phase due to the higher concentration of molecules. In the dilute gaseous phase, however, unimolecular reactions, such as β -scission to give an olefin and a terminal radical, are dominant.

Similar results were obtained by Khorasheh and Gray⁶³ for the reaction of *n*-C16 at high pressure, 13.9 MPa, where the addition reactions of the cracked radicals to olefins were significant at higher conversions of *n*-C16 resulting in the decrease of the observed yields of olefins. These results are consistent with the suggestions of Gray and McCaffrey⁵⁷ that olefin formation is essential for obtaining significant yields of larger products, as in coking of VR and asphaltenes, via addition reactions. Since the asphaltenes melt prior to reaching the cracking temperatures²², the thermal cracking of the asphaltenes for temperatures higher than 350 °C is taking place predominantly in the liquid-phase. Using the observation noted above for the reactions in the condensed phase, the asphaltenes molecules are expected to crack to give molecules of various sizes that would make up the liquid oil, but also, would undergo addition reactions to form larger products and eventually coke, as observed experimentally.^{39, 56, 76}

2.3.2 Reactions of Benzene-Based Compounds

In the 70s and 80s, extensive research on converting coal into fuel by liquefaction was undertaken to address the predicted fuel oil shortage.⁷⁷ To overcome the complexity of coal, many model compounds were employed to understand the different mechanisms by which the coal decomposes under thermal and catalytic conditions with and without the presence of solvents.⁷⁸ Most of the compounds employed were simple and small in weights that were mainly based on benzene, such as phenylalkanes, diphenylalkanes with different bridge lengths or number of benzene rings, and oxygenated or sulfided compounds that were also small.⁷⁹ Similar to the behavior observed for coal under rapid pyrolysis⁸⁰, ideal model compounds for coal were believed to include bonds that are easily broken under thermal conditions. Therefore, compounds with benzylic bonds, such as 1,2-diphenylethane which is also termed bibenzyl, were the subject of considerable interest because of their facile cleavage to give stable benzylic radicals, which can subsequently abstract hydrogen from other compounds or donor solvents.^{77, 81}

Sekiguchi and Klabunde⁸¹ found that the first step in the pyrolysis of bibenzyl is the homolytic cleavage of the weakest C–C bonds in the bridge to yield two stable benzylic radicals, but they also suggested that approximately 10% of the cleavages are from the alkyl–aryl strong bond to give phenyl and phenylethyl radicals, which subsequently abstract hydrogen to yield benzene and ethylbenzene. But this cleavage of the strong bond is $\sim 10^8$ slower than the cleavage of the benzylic bonds even at 700 °C, suggesting the benzene and

ethylbenzene formed by alternative routes.⁸² The major products of bibenzyl pyrolysis in the gas phase at low temperatures are toluene, stilbene (1,2-diphenylethene), 1,2,3,4-tetraphenylbutane, and 1,2,3-triphenylpropane, with the formation of benzene and styrene being important only at higher temperatures.⁸² Under liquid phase however, Miller and Stein⁸³ found the major products from cracking bibenzyl at temperatures in the range of 350–425 °C to be toluene, *trans*-stilbene, and 1,1-diphenylethane, with all the observed products explained by free-radical chain reactions. The formation of the 1,1-diphenylethane in the condensed phase is likely by a 1,2-aryl shift via the neophyl-like rearrangement.^{82, 83} Cyclization of bibenzyl radicals to yield phenanthrene, as a minor product, seems to be facilitated by the high temperature and high concentration in the liquid phase.⁸³ Indeed, cracking diphenylalkanes at high temperatures resulted in cyclization as an important reaction step, with phenanthrene forming as the second major product after toluene in the case of bibenzyl pyrolysis at 700 °C.⁸⁴

When model compounds containing such benzylic bonds were cracked in the presence of hydrogen donor solvents, such as tetralin or decalin, cleavage of strong bonds was observed to take place. Vernon⁸⁵ examined the reactions of bibenzyl, among other similar compounds, with added tetralin and molecular hydrogen at 450 °C. Vernon⁸⁵ reported the formation of benzene and ethylbenzene by hydrocracking, where a hydrogen atom adds to the benzene ring in bibenzyl leading to cleavage into benzene and ethylbenzene radical. The ethylbenzene radical abstracts then a hydrogen atom from the solvent or the

molecular hydrogen to yield ethylbenzene and another radical or free H-atom that continue the propagation of reaction steps. In addition to the H-atom (HA) addition or elimination, four other mechanisms for transferring hydrogen to the substituted aromatic (or ipso) position, which then leads to cracking of the strong bonds, were examined by McMillen et al.⁸⁶. The additional four mechanisms are the concerted hydrogen transfer, reverse radical disproportionation (RRD), multistep mechanism, and radical hydrogen transfer (RHT). The different hydrogen transfer mechanisms are shown in **Figure 2.5**.

Among these mechanisms McMillen et al.⁸⁶ suggested that RHT is the most consistent mechanism to explain the observed experimental results for the pyrolysis of 1,2'-dinaphthylmethane with hydrogen donor solvents, such as 9,10-dihydro-phenanthrene and anthracene. Arguing against RHT, Autrey and co-workers calculated the energy barrier for RHT to be much higher than previously assumed⁸⁷, which also depended on the structure of the radicals⁸⁸, and showed subsequently⁸⁹ that a combination of HA and RRD, and the change from one pathway to another based on the experimental conditions, are enough to explain the selectivity and experimental results of the pyrolysis of 1,2'-dinaphthylmethane.

Regardless of the mechanism by which hydrogen is transferred, the substituted group at the ipso position in aromatic rings is eliminated only after a hydrogen atom adds at this position. Similar pathways, to a much larger extent, were observed in the reactions of larger polycyclic aromatic compounds, such as pyrene. These results are presented next.

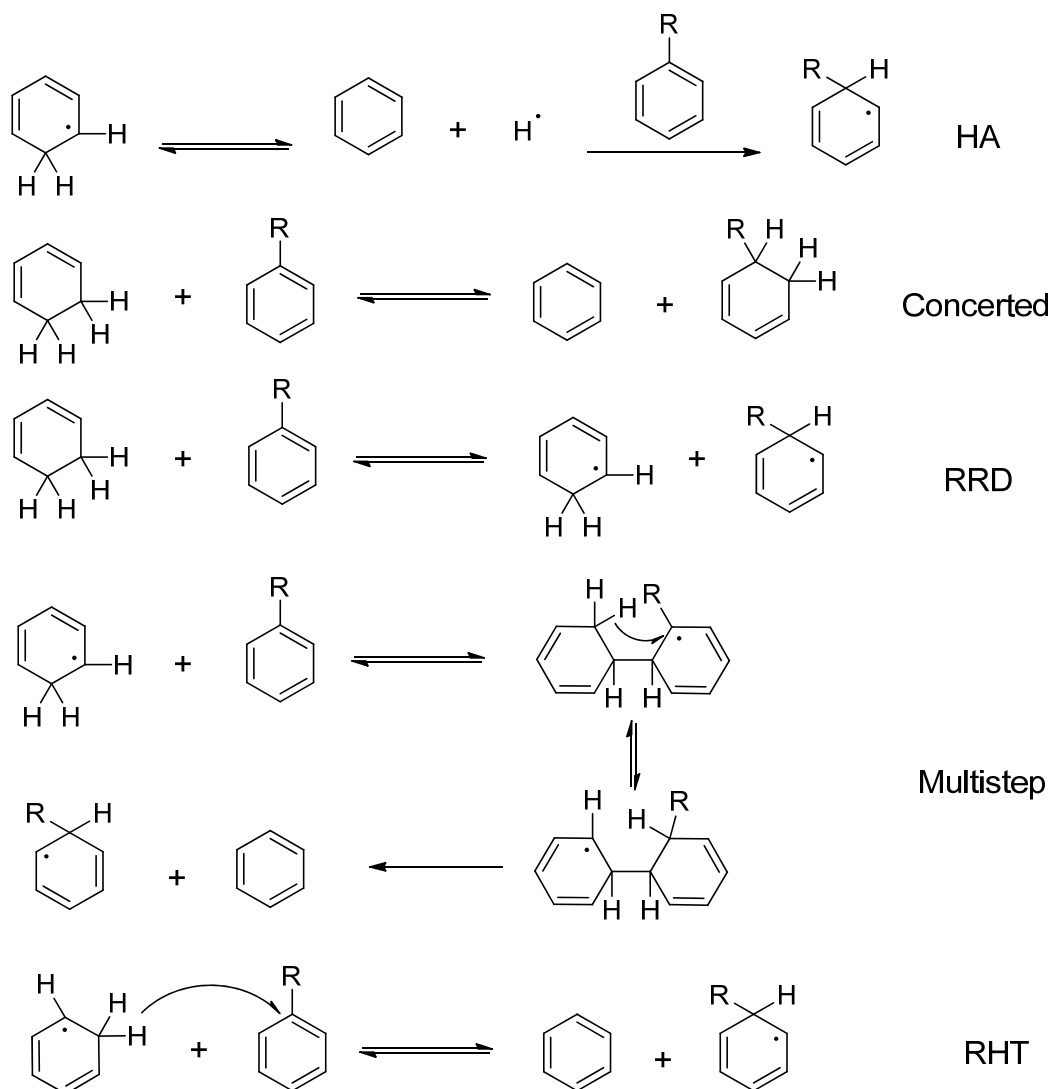


Figure 2.5: Hydrogen transfer mechanisms: H-atom addition (HA), concerted hydrogen transfer, reverse radical disproportionation (RRD), multistep mechanism, and radical hydrogen transfer (RHT).

2.3.3 Reactions of Polycyclic Aromatics

Although the studies on the benzene-based compounds resulted in a wealth of information about the behavior of coals, bitumens, and heavy oils under thermal processing conditions, such heavy resources are also enriched in

polycyclic aromatic compounds, which may not follow the same reaction kinetics and pathways as the single-ring benzene-based compounds.⁹⁰ The work of Savage and co-workers confirmed this possibility as they thermally cracked 1-dodecylpyrene (DDP) at mild conditions, 375–425 °C for 10–180 min, and observed the emergence of new reaction pathway leading to the formation of pyrene and dodecane as major products.⁹¹ The formation of this pair is unusual because it requires the cleavage of the strongest bond, the aryl-alkyl bond, in the alkyl chain. The products from the pyrolysis of alkylbenzenes are entirely explained by free-radical chain reactions and are consistent with bond energies, yielding toluene, an olefin with the same carbon number as the side-chain minus one, styrene, and *n*-alkane with the same carbon number as the side-chain minus two, as the major products.^{92, 93} These apparent differences between the single-ring and multi-ring aromatics in terms of reaction products and kinetics led to an extensive research on the reactions of alkylpyrene compounds by Smith and Savage.⁹⁴⁻⁹⁹

In the work of Savage et al.⁹¹, products from DDP pyrolysis at low conversions were similar to those resulting from the pyrolysis of alkylbenzenes, namely, 1-methylpyrene, 1-undecene, 1-ethylpyrene (from the rapid reduction of vinylpyrene), and *n*-decane. Pyrene and *n*-dodecane were present in low yields at low conversions, but at higher conversion levels their yields increased significantly to become the major products. The formation of these two products is net-hydrogen consuming and was coupled with the formation of H-deficient materials in the form of insoluble char on the reactor walls. Therefore,

hydrogenolysis reactions via either HA or RHT were suggested to be responsible for the cleavage of the strong aryl–alkyl bond to form pyrene and dodecane. To account for the cleavage for the strong aryl–alkyl bond in DDP pyrolysis, Smith and Savage⁹⁴ added an additional term in the rate law previously derived for alkylbenzene decomposition in order to accurately model the experimental reaction kinetics. In addition, they probed the selectivity to cleave the methyl groups in 1,6-dimethylnaphthalene when reacted with DDP (since HA is an exothermic and non–selective reaction as opposed to the more selective RHT) and found that the mechanism responsible for the cleavage is more selective than HA.⁹⁴ Continuing these studies, Smith and Savage⁹⁵ conducted the pyrolysis of 1,3-bis(1-pyrene)propane in the presence of 1,6-dimethylnaphthalene, which resulted in the cleavage of the strong aryl–alkyl bond to give pyrene and 1-propylpyrene by a selective mechanism such as RHT or molecular disproportionation.⁹⁵

To identify the nature of the mechanism responsible for the hydrogenolysis and cleavage of the strong bond, Smith and Savage⁹⁷ examined the reactions of 1-methylpyrene (which cannot undergo RHT) and 1-ethylpyrene at 400–450 °C in a batch reactor for up to 300 min. This study showed that RRD was responsible for the dealkylation in 1-methylpyrene, while a combination of RRD and RHT were the operative mechanisms in the pyrolysis of 1-ethylpyrene. In subsequent kinetic modeling for the pyrolysis of DDP, RHT was found to be the dominant hydrogenolysis mechanism, with RRD being dominant only at the initial stages of the reaction, and that the removal of this step and the use of conventional H–

transfer mechanisms, such as HA and RRD, did not describe all the experimental results.^{99, 100}

To minimize the secondary reactions as much as possible and get a detailed mechanistic interpretation for the cleavage of strong alkyl–pyrenyl bonds as well as to identify the source for the transferred hydrogen, Freund et al.¹⁰¹ pyrolyzed 1,20-di(1-pyrenyl)eicosane (or DPE) at 400-500 °C using flash thermolysis in an open reactor. Significant cracking of the side–chain was observed, similar to other alkylpyrene compounds examined by Savage and co–workers. Using thermochemical analysis, RHT was shown to be the most probable mechanism by which a hydrogen atom is transferred to the ipso position of DPE. The pyrene structure was unique in that a stable phenalenyl–like radical is formed after the addition of the hydrogen atom followed by the rapid elimination of the substituted alkyl group. The structural effect on facilitating the cleavage of the substituted group after hydrogen addition was addressed by Smith and Savage⁹⁶. They correlated the rate of cleavage of the strong bonds in alkylaromatics with their structures using the Dewar reactivity number (DN)¹⁰², which is a measure of the localization energy at the point of substitution. For example, alkylpyrenes with carbon chains less than 16 carbons have a DN of 1.51, in the range where the dealkylation pathway is as important as the reaction pathways of alkylbenzenes. On the other hand, compounds with DN less than 1.33, such as 9-alkylanthracenes which have a DN of 1.26, have the dealkylation pathway as the dominant one.⁹⁶

As for the source that transfers hydrogen to the ipso position, Freund et al.¹⁰¹ identified an internal olefin that is conjugated to the pyrene group using ¹H–NMR

spectroscopy. This olefin was found to form in concert with pyrene, and therefore it was suggested as the possible source of the hydrogen. The RHT step and the formed phenalenyl-like radical is shown in **Figure 2.6** after Freund et al.¹⁰¹ Using the findings of Freund et al.¹⁰¹ for the olefin formation, the char materials that formed in the work of Savage et al.⁹¹ could then rise from addition reaction to the formed olefins, as suggested by Gray and McCaffrey⁵⁷ to take place during coking reactions of VR and the asphaltenes.

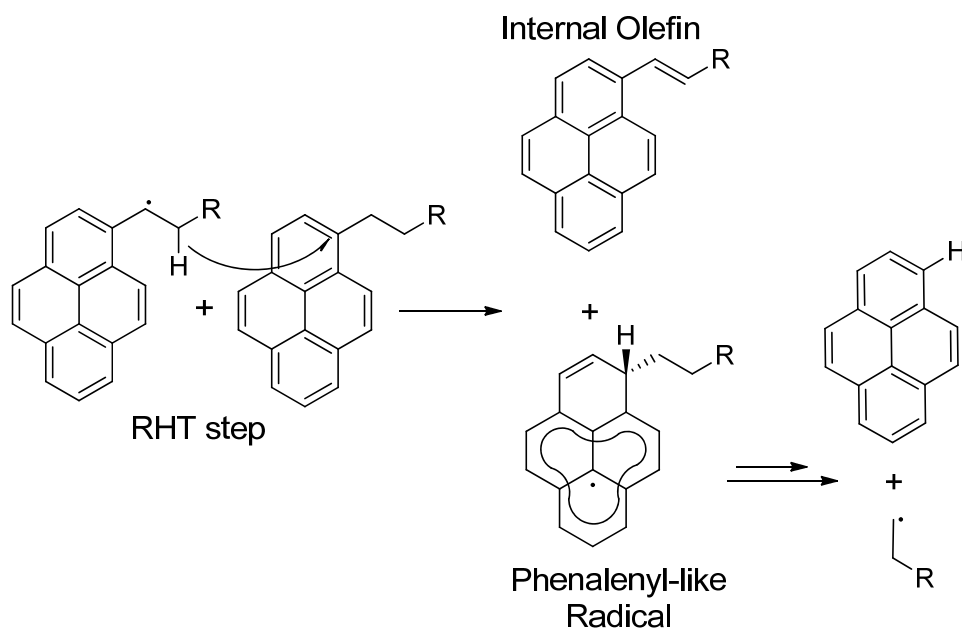


Figure 2.6: RHT and the stable radical that forms after hydrogen transfer, after Freund et al.¹⁰¹

The most important implication of the above studies, by Savage and co-workers and Freund and co-workers, is that cracking of side chains on large aromatic groups is more facile than previously believed. Therefore, similar

structures in the VR and asphaltenes may undergo similar reaction pathways and cracking kinetics during thermal upgrading processes. Unfortunately, all of these studies on the polycyclic compounds focused mainly on the cracked products. The interpretation of the mechanisms and kinetics lacked consideration of the nature and yields of addition products. Such products are expected to form since these model compounds are heavy enough that the thermal reactions are likely conducted in the liquid phase. The formation of char and insoluble materials is the most obvious evidence for the formation of these addition products.

2.3.4 Reactions of Biomarkers

Biological markers, or biomarkers, are complex molecules derived from biological organisms and are ubiquitous in crude oils.¹⁰³ Biomarkers are important because of their high stability and resistance to biodegradation, distillation, or secondary processes which make them suitable to act as natural tracers through upgrading processes such as in refinery streams.¹⁰³ Biomarkers are released during the thermal cracking of both kerogen and asphaltenes.^{15, 35} Thermal degradation and selective oxidation of kerogen and the asphaltenes suggest that naphthenic biomarkers are linked to the kerogen or asphaltenes macromolecule via labile bridges, such as alkyl, ether, ester, or sulfur bridges.^{37, 104} Pyrolysis studies with heavy water (D₂O) by Larter and co-workers¹⁰⁵ confirmed that biomarkers are attached by alkyl chains of acyclic compounds or hopanoids and by the A-ring of steroids to kerogen via labile linkages, such as ether or sulfur. Recent work by Oldenburg et al.¹⁰⁶ showed also the existence of nitrogen-containing hopanoids with the nitrogen being in aromatic rings fused with the

hopanoids at the pentacyclic ring (where the side chain is attached in the normal hopanoids). The origin of these structures, which were found at low concentrations, especially those having more than two fused aromatic rings, is not known. Oldenburg et al.¹⁰⁶ suggested possible cyclization of the alkyl chain that contains an amino group to be the source of such structures. Since biomarkers are present in the asphaltenes and are released during thermolysis, studying the thermal behavior of biomarker-like model compounds is very important in understanding the behavior of similar sub-components in the asphaltenes during thermal upgrading processes.

Among the many biomarkers, geochemists most commonly utilize terpanes, steranes, and aromatic steroids for petroleum-related studies.¹⁰³ Cholestane, shown in **Figure 2.7** with ring designation and carbon numbering, is a typical compound from the steranes family that has been used extensively in thermal cracking studies as a biomarker representative. For example, the hypothesis of formation of light cycloalkanes by decomposition of heavy polycyclic natural products, such as terpanes or steranes, was studied by thermally cracking 5 α -cholestane at conditions sufficient to induce C–C bond cleavage, which resulted in significant side chain fragmentation and only minimal ring opening.^{107, 108} The D-ring is the ring that is usually ruptured to give dimethyl-perhydrophenanthrenes, which can subsequently dehydrogenate to give a number of saturated and unsaturated products.^{107, 109} Abbott et al.¹¹⁰ identified approximately 75% of the reaction products, after 34% conversion of 5 α -cholestane, to be saturated products that mainly differ in the attached side chain

with both methyl groups (C18 and C19) still in place. But when the same reaction was conducted in the presence of water, 90% of the products were unsaturated.

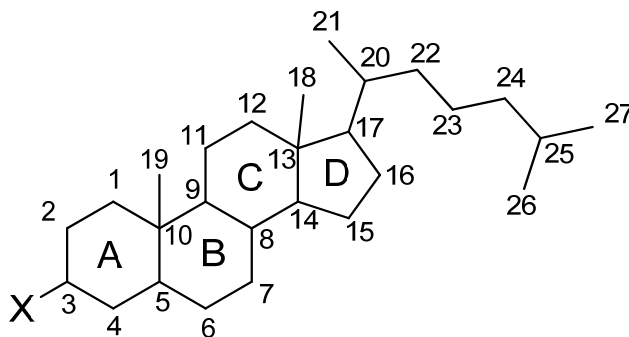


Figure 2.7: Cholestane with ring designation and carbon numbering. The (X) mark shows the most likely linkage point of similar steroids to the macromolecule of kerogen or the asphaltenes.¹⁰⁴

In addition to the D-ring opening in the thermal cracking of cholestane, the A-ring was also observed to rupture to give *n*-butyl substituted products in the presence of 10% Pd on carbon catalyst at 300 °C, which were detected by Carlson et al.¹¹¹ as attached to tricyclic diaromatic species. In addition to side-chain cleavage, dehydrogenation was a significant and an important reaction in cholestane degradation.¹¹⁰ Carlson et al.¹¹¹ suggested, based on NMR analysis of the reaction products, that C18 methyl migration and the C-ring aromatization takes place prior to decomposition to other products. The methyl migration and C-ring aromatization was observed to take place simultaneously; unlike the loss of C19 methyl and the subsequent dehydrogenation of A or B-rings, which seemed to occur independently. These observations by Carlson et al.¹¹¹ were for

the reaction under catalytic conditions, unlike the work by Abbott et al.¹¹⁰ in which most of the products from the anhydrous reaction were saturated with the methyl groups still in place.

The above observations on the reactions of cholestane give a basis for understanding the reactions of model compounds containing such moieties. The reaction pathways will be altered, when significant structural changes are made to these compounds. For example, attaching or fusing cycloalkyl groups to an aromatic species will give a new route to ring contraction of the radicals that form on the cycloalkyl group. This is a well-documented phenomenon in tetralin, where methylindane forms as a major product.⁸² Polycyclic hydroaromatics, such as 1,2,3,4,5,6,7,8-octahydroanthracene and -octahydrophenanthrene, and 1,2,3,4,5,6,7,8,9,10,11,12-dodecahydrotriphenylene, were also observed to undergo significant ring contraction at temperatures that are much lower than in tetralin reactions.^{112, 113} Therefore, fusing cycloalkyl rings, such as a cholestane molecule, with an aromatic group, similar to the identified hopanoids by Oldenburg et al.¹⁰⁶, may show similar reactions or enhance the decomposition of the whole molecule. Similarly the A-ring would be more prone to dehydrogenate first if it was fused with an aromatic ring since the C1 and C4 will become benzylic protons, which are easily abstractable by free-radicals during thermal reactions.

2.4 REFERENCES

1. Girdler, R. B., Constitution of Asphaltenes and Related Studies. *Proc. Assoc. Asphalt Paving Technol.* **1965**, 34, 45-80.
2. Speight, J. G., *The Chemistry and Technology of Petroleum*. Fourth ed.; CRC Press: Boca Raton, FL, 2007.
3. Alboudwarej, H.; Beck, J.; Svrcek, W. Y.; Yarranton, H. W.; Akbarzadeh, K., Sensitivity of asphaltene properties to separation techniques. *Energy Fuels* **2002**, 16, 462-469.
4. Mitchell, D. L.; Speight, J. G., Solubility of Asphaltenes in Hydrocarbon Solvents. *Fuel* **1973**, 52, 149-152.
5. Hildebrand, J. H., Solubility. III. Relative Values of Internal Pressures and their Practical Application. *J Am Chem Soc* **1919**, 41, 1067-1080.
6. Hildebrand, J. H.; Prausnitz, J. M.; Scott, R. L., *Regular and related solutions: the solubility of gases, liquids, and solids*. Van Nostrand Reinhold Co.: New York, 1970.
7. Gawrys, K. L.; Blankenship, G. A.; Kilpatrick, P. K., On the distribution of chemical properties and aggregation of solubility fractions in asphaltenes. *Energy Fuels* **2006**, 20, 705-714.
8. Speight, J. G.; Long, R. B.; Trowbridge, T. D., Factors influencing the separation of asphaltenes from heavy petroleum feedstocks. *Fuel* **1984**, 63, 616-620.
9. Andersen, S. I., Effect of Precipitation Temperature on the Composition of n-Heptane Asphaltenes *Fuel Sci. Technol. Int.* **1994**, 12, 51-74.

10. Freund, H.; Walters, C. C.; Kelemen, S. R.; Siskin, M.; Gorbaty, M. L.; Curry, D. J.; Bence, A. E., Predicting oil and gas compositional yields via chemical structure-chemical yield modeling (CS-CYM): Part 1 - Concepts and implementation. *Org. Geochem.* **2007**, 38, 288-305.
11. Vandenbroucke, M., Kerogen: from types to models of chemical structure. *Oil & Gas Science and Technology-Revue De L Institut Francais Du Petrole* **2003**, 58, 243-269.
12. Freund, H., Application of a Detailed Chemical Kinetic-Model to Kerogen Maturation. *Energy Fuels* **1992**, 6, 318-326.
13. Siskin, M.; Scouten, C. G.; Rose, K. D.; Aczel, T.; Colgrove, S. G.; Pabst, R. E., Detailed Structural Characterization of the Organic Material in Rundle Ramsay Crossing Oil-Shale. In *Composition, Geochemistry, and Conversion of Oil Shales*, Snape, C. E., Ed. Kluwer Academic: Dordrecht 1995; pp 143-158.
14. Saxby, J. D.; Bennett, A. J. R.; Corcoran, J. F.; Lambert, D. E.; Riley, K. W., Petroleum Generation - Simulation over 6-Years of Hydrocarbon Formation from Torbanite and Brown Coal in a Subsiding Basin. *Org. Geochem.* **1986**, 9, 69-81.
15. Pelet, R.; Behar, F.; Monin, J. C., Resins and asphaltenes in the generation and migration of petroleum. *Org. Geochem.* **1986**, 10, 481-498.
16. Siskin, M.; Kelemen, S. R.; Eppig, C. P.; Brown, L. D.; Afeworki, M., Asphaltene molecular structure and chemical influences on the

- morphology of coke produced in delayed coking. *Energy Fuels* **2006**, 20, 1227-1234.
17. Speight, J. G., *The Chemistry and Technology of Petroleum*. Second ed.; Marcel Dekker, Inc.: New York, NY, 1991.
 18. Filby, R. H.; Strong, D., Nickel (II) and Vanadium (IV) Complexes in Alberta Oil-Sands Bitumens. In *Tar Sand and Oil Upgrading Technology*, Shih, S. S.; Oballa, M. C., Eds. AIChE: New York, 1991; Vol. 87, pp 1-9.
 19. Strausz, O. P.; Lown, E. M., *The Chemistry of Alberta Oil Sands, Bitumens, and Heavy Oils*. AERI: Calgary, AB, 2003.
 20. Asprino, O. J.; Elliott, J. A. W.; McCaffrey, W. C.; Gray, M. R., Fluid Properties of asphaltenes at 310-530 degrees C. *Energy Fuels* **2005**, 19, 2026-2033.
 21. Akbarzadeh, K.; Dhillon, A.; Svrcek, W. Y.; Yarranton, H. W., Methodology for the characterization and modeling of asphaltene precipitation from heavy oils diluted with n-alkanes. *Energy Fuels* **2004**, 18, 1434-1441.
 22. Gray, M. R.; Assenheimer, G.; Boddez, L.; McCaffrey, W. C., Melting and fluid behavior of asphaltene films at 200-500 degrees C. *Energy Fuels* **2004**, 18, 1419-1423.
 23. Boduszynski, M. M., Composition of heavy petroleums. 1. Molecular weight, hydrogen deficiency, and heteroatom concentration as a function of atmospheric equivalent boiling point up to 1400.degree.F (760.degree.C). *Energy Fuels* **1987**, 1, 2-11.

24. Strausz, O. P.; Peng, P.; Murgich, J., About the colloidal nature of asphaltenes and the MW of covalent monomeric units. *Energy Fuels* **2002**, 16, 809-822.
25. Groenzin, H.; Mullins, O. C., Asphaltene molecular size and structure. *J. Phys. Chem. A* **1999**, 103, 11237-11245.
26. Groenzin, H.; Mullins, O. C., Molecular size and structure of asphaltenes from various sources. *Energy Fuels* **2000**, 14, 677-684.
27. Groenzin, H.; Mullins, O. C.; Eser, S.; Mathews, J.; Yang, M. G.; Jones, D., Molecular size of asphaltene solubility fractions. *Energy Fuels* **2003**, 17, 498-503.
28. Mullins, O. C.; Martinez-Haya, B.; Marshall, A. G., Contrasting perspective on asphaltene molecular weight. This comment vs the overview of A. A. Herod, K. D. Bartle, and R. Kandiyoti. *Energy Fuels* **2008**, 22, 1765-1773.
29. Mullins, O. C., The Modified Yen Model. *Energy Fuels* **2010**, 24, 2179-2207.
30. Strausz, O. P.; Safarik, I.; Lown, E. M.; Morales-Izquierdo, A., A critique of asphaltene fluorescence decay and depolarization-based claims about molecular weight and molecular architecture. *Energy Fuels* **2008**, 22, 1156-1166.
31. Miller, J. T.; Fisher, R. B.; Thiagarajan, P.; Winans, R. E.; Hunt, J. E., Subfractionation and characterization of Mayan asphaltene. *Energy Fuels* **1998**, 12, 1290-1298.

32. Qian, K. N.; Edwards, K. E.; Siskin, M.; Olmstead, W. N.; Mennito, A. S.; Dechert, G. J.; Hoosain, N. E., Desorption and ionization of heavy petroleum molecules and measurement of molecular weight distributions. *Energy Fuels* **2007**, 21, 1042-1047.
33. di Primio, R.; Horsfield, B.; Guzman-Vega, M. A., Determining the temperature of petroleum formation from the kinetic properties of petroleum asphaltenes. *Nature* **2000**, 406, 173-176.
34. Ignasiak, T.; Kempjones, A. V.; Strausz, O. P., Molecular-Structure of Athabasca Asphaltene - Cleavage of Carbon-Sulfur Bonds by Radical Ion Electron-Transfer Reactions. *J. Org. Chem.* **1977**, 42, 312-320.
35. Rubinstein, I.; Spyckerelle, C.; Strausz, O. P., Pyrolysis of Asphaltenes - Source of Geochemical Information. *Geochim. Cosmochim. Acta* **1979**, 43, 1-6.
36. Rubinstein, I.; Strausz, O. P., Thermal-Treatment of the Athabasca Oil Sand Bitumen and Its Component Parts. *Geochim. Cosmochim. Acta* **1979**, 43, 1887-1893.
37. Strausz, O. P.; Mojelsky, T. W.; Lown, E. M., The Molecular-Structure of Asphaltene - an Unfolding Story. *Fuel* **1992**, 71, 1355-1363.
38. Artok, L.; Su, Y.; Hirose, Y.; Hosokawa, M.; Murata, S.; Nomura, M., Structure and reactivity of petroleum-derived asphaltene. *Energy Fuels* **1999**, 13, 287-296.

39. Karimi, A.; Qian, K.; Olmstead, W. N.; Freund, H.; Yung, C.; Gray, M. R., Quantitative Evidence for Bridged Structures in Asphaltenes by Thin Film Pyrolysis. *Energy Fuels* **2011**, 25, 3581-3589.
40. Wiehe, I. A., The Pendant Core Building-Block Model of Petroleum Residue. *Energy Fuels* **1994**, 8, 536-544.
41. Jaffe, S. B.; Freund, H.; Olmstead, W. N., Extension of structure-oriented lumping to vacuum residua. *Ind. Eng. Chem. Res.* **2005**, 44, 9840-9852.
42. Peng, P.; Morales-Izquierdo, A.; Hogg, A.; Strausz, O. P., Molecular structure of athabasca asphaltene: Sulfide, ether, and ester linkages. *Energy Fuels* **1997**, 11, 1171-1187.
43. Sheremata, J. M.; Gray, M. R.; Dettman, H. D.; McCaffrey, W. C., Quantitative molecular representation and sequential optimization of athabasca asphaltenes. *Energy Fuels* **2004**, 18, 1377-1384.
44. Pfeiffer, J. P.; Saal, R. N. J., Asphaltic bitumen as colloid system. *J. Phys. Chem.* **1940**, 44, 139-165.
45. Dickie, J. P.; Yen, T. F., Macrostructures of Asphaltic Fractions by Various Instrumental Methods. *Anal. Chem.* **1967**, 39, 1847-&.
46. Andreatta, G.; Goncalves, C. C.; Buffin, G.; Bostrom, N.; Quintella, C. M.; Arteaga-Larios, F.; Perez, E.; Mullins, O. C., Nanoaggregates and structure-function relations in asphaltenes. *Energy Fuels* **2005**, 19, 1282-1289.
47. Gray, M. R., Consistency of asphaltene chemical structures with pyrolysis and coking behavior. *Energy Fuels* **2003**, 17, 1566-1569.

48. Akbarzadeh, K.; Bressler, D. C.; Wang, J. N.; Gawrys, K. L.; Gray, M. R.; Kilpatrick, P. K.; Yarranton, H. W., Association behavior of pyrene compounds as models for asphaltenes. *Energy Fuels* **2005**, 19, 1268-1271.
49. Agrawala, M.; Yarranton, H. W., An asphaltene association model analogous to linear polymerization. *Ind. Eng. Chem. Res.* **2001**, 40, 4664-4672.
50. Tanaka, R.; Hunt, J. E.; Winans, R. E.; Thiyagarajan, P.; Sato, S.; Takanohashi, T., Aggregates structure analysis of petroleum asphaltenes with small-angle neutron scattering. *Energy Fuels* **2003**, 17, 127-134.
51. Gray, M. R.; Tykwinski, R. R.; Stryker, J. M.; Tan, X., Supramolecular Assembly Model for Aggregation of Petroleum Asphaltenes. *Energy Fuels* **2011**, 25, 3125-3134.
52. Tan, X. L.; Fenniri, H.; Gray, M. R., Pyrene derivatives of 2,2'-bipyridine as models for asphaltenes: Synthesis, characterization, and supramolecular organizations. *Energy Fuels* **2008**, 22, 715-720.
53. Tan, X.; Fenniri, H.; Gray, M. R., Water Enhances the Aggregation of Model Asphaltenes in Solution via Hydrogen Bonding. *Energy Fuels* **2009**, 23, 3687-3693.
54. Dechaine, G. P.; Maham, Y.; Tan, X. L.; Gray, M. R., Regular Solution Theories Are Not Appropriate for Model Compounds for Petroleum Asphaltenes. *Energy Fuels* **2011**, 25, 737-746.

55. Cartlidge, C. R.; Dukhedin-Lalla, L.; Rahimi, P.; Shaw, J. M., Preliminary phase diagrams for ABVB + n-dodecane + hydrogen. *Fluid Phase Equilib.* **1996**, 117, 257-264.
56. Moschopedis, S. E.; Parkash, S.; Speight, J. G., Thermal Decomposition of Asphaltenes. *Fuel* **1978**, 57, 431-434.
57. Gray, M. R.; McCaffrey, W. C., Role of chain reactions and olefin formation in cracking, hydroconversion, and coking of petroleum and bitumen fractions. *Energy Fuels* **2002**, 16, 756-766.
58. Sanford, E. C., Molecular Approach to Understanding Residuum Conversion. *Ind. Eng. Chem. Res.* **1994**, 33, 109-117.
59. Olmstead, W. N.; Freund, H., Thermal Conversion Kinetics of Petroleum Residua. *AIChE 1998 Spring National Meeting, New Orleans, LA* **1998**.
60. McMillen, D. F.; Golden, D. M., Hydrocarbon Bond-Dissociation Energies. *Annu. Rev. Phys. Chem.* **1982**, 33, 493-532.
61. Rice, F. O.; Herzfeld, K. F., The thermal decomposition of organic compounds from the standpoint of free radicals VI The mechanism of some chain reactions. *J Am Chem Soc* **1934**, 56, 284-289.
62. Radmanesh, R.; Chan, E.; Gray, M. R., Modeling of mass transfer and thermal cracking during the coking of Athabasca residues. *Chem. Eng. Sci.* **2008**, 63, 1683-1691.
63. Khorasheh, F.; Gray, M. R., High-Pressure Thermal-Cracking of N-Hexadecane. *Ind. Eng. Chem. Res.* **1993**, 32, 1853-1863.

64. Wu, G. Z.; Katsumura, Y.; Matsuura, C.; Ishigure, K.; Kubo, J., Comparison of liquid-phase and gas-phase pure thermal cracking of n-hexadecane. *Ind. Eng. Chem. Res.* **1996**, 35, 4747-4754.
65. Alshareef, A. H.; Scherer, A.; Tan, X.; Azyat, K.; Stryker, J. M.; Tykwinski, R. R.; Gray, M. R., Formation of archipelago structures during thermal cracking implicates a chemical mechanism for the formation of petroleum asphaltenes. *Energy Fuels* **2011**, 25, 2130-2136.
66. Raseev, S., *Thermal and Catalytic Processes in Petroleum Refining*. Marcel Dekker: New York, 2003.
67. Wiehe, I. A., A Phase-Separation Kinetic-Model for Coke Formation. *Ind. Eng. Chem. Res.* **1993**, 32, 2447-2454.
68. Wiehe, I. A., *Process chemistry of petroleum macromolecules*. CRC: Boca Raton, FL, 2008.
69. Wiehe, I. A., A Solvent Resid Phase- Diagram for Tracking Resid Conversion. *Ind. Eng. Chem. Res.* **1992**, 31, 530-536.
70. Rice, F. O., Reactions of Organic Molecules in the Gaseous State. *Chem. Rev.* **1932**, 10, 135-159.
71. Rice, F. O.; Dooley, M. D., The Thermal Decomposition of Organic Compounds from the Standpoint of Free Radicals. XII. The Decomposition of Methane. *J Am Chem Soc* **1934**, 56, 2747-2749.
72. Rice, F. O.; Rodowskas, E. L.; Lewis, W. R., The Thermal Decomposition of Acetone. *J Am Chem Soc* **1934**, 56, 2497-2498.

73. Rice, F. O.; Reiff, O. M., The Thermal Decomposition of Hydrogen Peroxide. *J. Phys. Chem.* **1927**, 31, 1352-1356.
74. Rice, F. O., The Thermal Decomposition of Organic Compounds from the Standpoint of Free Radicals. I. Saturated Hydrocarbons. *J Am Chem Soc* **1931**, 53, 1959-1972.
75. Rice, F. O.; Herzfeld, K. F., The Mechanism of Some Chain Reactions. *J. Phys. Chem.* **1951**, 55, 975-987.
76. Moschopedis, S. E.; Speight, J. G., Influence of Metal-Salts on Bitumen Oxidation. *Fuel* **1978**, 57, 235-240.
77. Cronauer, D. C.; Jewell, D. M.; Shah, Y. T.; Kueser, K. A., Hydrogen Transfer Cracking of Dibenzyl in Tetralin and Related Solvents. *Ind. Eng. Chem. Fund.* **1978**, 17, 291-297.
78. Depeyre, D.; Urhan, M.; Flicoteaux, C., Pyrolysis of Hydrocarbon Mixtures Characteristic of Coal - Application to Dibenzyl Mixture. *Fuel* **1985**, 64, 1655-1661.
79. Benjamin, B. M.; Raaen, V. F.; Maupin, P. H.; Brown, L. L.; Collins, C. J., Thermal Cleavage of Chemical Bonds in Selected Coal-Related Structures. *Fuel* **1978**, 57, 269-272.
80. Neavel, R. C., Liquefaction of Coal in Hydrogen-Donor and Non-Donor Vehicles. *Fuel* **1976**, 55, 237-242.
81. Sekiguchi, Y.; Klabunde, K. J., Catalytic and Non-Catalytic Flow-Pyrolysis of Bibenzyl - Possible Homolytic and Heterolytic Processes on Basic Cao. *Fuel Process. Technol.* **1981**, 4, 73-84.

82. Poutsma, M. L., Free-Radical Thermolysis and Hydrogenolysis of Model Hydrocarbons Relevant to Processing of Coal. *Energy Fuels* **1990**, 4, 113-131.
83. Miller, R. E.; Stein, S. E., Liquid-Phase Pyrolysis of 1,2-Diphenylethane. *J. Phys. Chem.* **1981**, 85, 580-589.
84. Sweeting, J. W.; Wilshire, J. F., Pyrolysis of Omegaomega'-Diphenylalkanes. *Aust. J. Chem.* **1962**, 15, 89-105.
85. Vernon, L. W., Free-Radical Chemistry of Coal-Liquefaction - Role of Molecular-Hydrogen. *Fuel* **1980**, 59, 102-106.
86. McMillen, D. F.; Malhotra, R.; Chang, S. J.; Ogier, W. C.; Nigenda, S. E.; Fleming, R. H., Mechanisms of Hydrogen Transfer and Bond Scission of Strongly Bonded Coal Structures in Donor Solvent Systems. *Fuel* **1987**, 66, 1611-1620.
87. Franz, J. A.; Ferris, K. F.; Camaioni, D. M.; Autrey, S. T., Are Strong Bonds Cleaved during Coal-Liquefaction Via Radical Hydrogen-Transfer - an Ab-Initio Theoretical-Study of Thermoneutral Radical Hydrogen-Transfer. *Energy Fuels* **1994**, 8, 1016-1019.
88. Camaioni, D. M.; Autrey, S. T.; Salinas, T. B.; Franz, J. A., Calculation of the effects of branching and conjugation on intrinsic barriers for H atom transfer reactions involving hydrocarbons. *J Am Chem Soc* **1996**, 118, 2013-2022.
89. Autrey, T.; Alborn, E. A.; Franz, J. A.; Camaioni, D. M., Solvent-Induced Scission of Diarylmethanes in Dihydroarene Donor Solvents - an

Experimental and Mechanistic Modeling Study of Hydrogen-Transfer Pathways. *Energy Fuels* **1995**, 9, 420-428.

90. Safarik, I.; Strausz, O. P., The thermal decomposition of hydrocarbons .3. Polycyclic n-alkylaromatic compounds. *Res. Chem. Intermed.* **1997**, 23, 179-195.
91. Savage, P. E.; Jacobs, G. E.; Javanmardian, M., Autocatalysis and aryl-alkyl bond cleavage in 1-dodecylpyrene pyrolysis. *Ind. Eng. Chem. Res.* **1989**, 28, 645-654.
92. Savage, P. E.; Klein, M. T., Asphaltene Reaction Pathways. 2. Pyrolysis of n-Pentadecylbenzene. *Ind. Eng. Chem. Res.* **1987**, 26, 488-494.
93. Savage, P. E.; Klein, M. T., Discrimination between Molecular and Free-Radical Models of 1-Phenyldodecane Pyrolysis. *Ind. Eng. Chem. Res.* **1987**, 26, 374-376.
94. Smith, C. M.; Savage, P. E., Reactions of polycyclic alkylaromatics. 1. Pathways, kinetics, and mechanisms for 1-dodecylpyrene pyrolysis. *Ind. Eng. Chem. Res.* **1991**, 30, 331-339.
95. Smith, C. M.; Savage, P. E., Reactions of polycyclic alkylaromatics. 2. Pyrolysis of 1,3-diarylpropanes. *Energy Fuels* **1991**, 5, 146-155.
96. Smith, C. M.; Savage, P. E., Reactions of Polycyclic Alkylaromatics - Structure and Reactivity. *AIChE J* **1991**, 37, 1613-1624.
97. Smith, C. M.; Savage, P. E., Reactions of polycyclic alkylaromatics. 4. Hydrogenolysis mechanisms in 1-alkylpyrene pyrolysis. *Energy Fuels* **1992**, 6, 195-202.

98. Smith, C. M.; Savage, P. E., Reactions of Polycyclic Alkylaromatics. 7. Hydrogenolysis in Binary Mixtures. *Energy Fuels* **1994**, 8, 545-551.
99. Savage, P. E., Hydrogen-Transfer Mechanisms in 1-Dodecylpyrene Pyrolysis. *Energy Fuels* **1995**, 9, 590-598.
100. Smith, C. M.; Savage, P. E., Reactions of Polycyclic Alkylaromatics. 6. Detailed Chemical Kinetic Modeling. *Chem. Eng. Sci.* **1994**, 49, 259-270.
101. Freund, H.; Matturro, M. G.; Olmstead, W. N.; Reynolds, R. P.; Upton, T. H., Anomalous side-chain cleavage in Alkylaromatic Thermolysis. *Energy Fuels* **1991**, 5, 840-846.
102. Dewar, M. J. S., A Molecular Orbital Theory of Organic Chemistry. VI.1 Aromatic Substitution and Addition. *J Am Chem Soc* **1952**, 74, 3357-3363.
103. Peters, K. E.; Scheuerman, G. L.; Lee, C. Y.; Moldowan, J. M.; Reynolds, R. N.; Pena, M. M., Effects of Refinery Processes on Biological Markers. *Energy Fuels* **1992**, 6, 560-577.
104. Rullkötter, J.; Michaelis, W., The structure of kerogen and related materials. A review of recent progress and future trends. *Org. Geochem.* **1990**, 16, 829-852.
105. Stalker, L.; Larter, S. R.; Farrimond, P., biomarker binding into kerogens: evidence from hydrous pyrolysis using heavy water (D₂O). *Org. Geochem.* **1998**, 28, 239-253.
106. Oldenburg, T. B. P.; Huang, H.; Donohoe, P.; Willsch, H.; Larter, S. R., High molecular weight aromatic nitrogen and other novel hopanoid-related compounds in crude oils. *Org. Geochem.* **2004**, 35, 665-678.

107. Mango, F. D., The Origin of Light Cycloalkanes in Petroleum. *Geochim. Cosmochim. Acta* **1990**, 54, 23-27.
108. Kissin, Y. V., Catagenesis of Light Cycloalkanes in Petroleum. *Org. Geochem.* **1990**, 15, 575-594.
109. Sugden, M. A.; van Duin, A. C. T.; Abbott, G. D., Degradation of 5-alpha-cholestane into dimethylperhydrophenanthrenes: an experimental and theoretical study. *Org. Geochem.* **2004**, 35, 1337-1341.
110. Abbott, G. D.; Bennett, B.; Petch, G. S., The Thermal-Degradation of 5-Alpha(H)-Cholestane during Closed-System Pyrolysis. *Geochim. Cosmochim. Acta* **1995**, 59, 2259-2264.
111. Carlson, R. M. K.; Croasmun, W. R.; Chamberlain, D. E. *Transformations of Cholestane Useful for Probing Processing Chemistry*, Proceedings of the 210th National Meeting of the American Chemical Society, Chicago, IL, Aug 20-25, 1995; p 685.
112. Collin, P. J.; Gilbert, T. D.; Rottendorf, H.; Wilson, M. A., Ring Contraction and Dehydrogenation in Polycyclic Hydroaromatics at Coal-Liquefaction Temperatures. *Fuel* **1985**, 64, 1280-1285.
113. Cronauer, D. C.; Jewell, D. M.; Shah, Y. T.; Modi, R. J.; Seshadri, K. S., Isomerization and Adduction of Hydrogen Donor Solvents under Conditions of Coal Liquefaction. *Ind. Eng. Chem. Fund.* **1979**, 18, 368-376.

CHAPTER 3

*FORMATION OF ARCHIPELAGO STRUCTURES DURING THERMAL REACTIONS**

3.1 INTRODUCTION

As described in detail in Chapter 2, the two main structural motifs suggested for the heavy components of petroleum, such as the asphaltenes, are the archipelago and the island chemical structures. The objective of this study is to investigate how the heavy components may form during catagenic conditions of the petroleum or in commercial processing that thermally crack heavy fractions, such as coking, and what their main structure is. To achieve this objective, a series of well-characterized synthetic model compounds were subjected to condensed-phase thermal cracking at 365–420 °C. These compounds were designed to incorporate substructures known to be present in the asphaltenes and within the established range of molecular weights, with sufficiently high boiling points to ensure that they remain in the liquid phase during cracking reactions.

*A version of this chapter has been published: Alshareef, A. H.; Scherer, A.;[§] Tan, X.;[§] Azyat, K.;[§] Stryker, J. M.;[§] Tykwinski, R. R.;[§] and Gray, M. R. *Energy and Fuels* **2011**, 25, 2130–2136.

[§]Synthesized the model compounds.

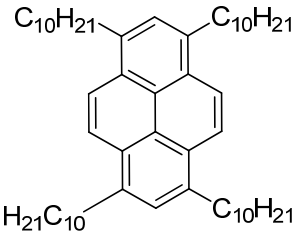
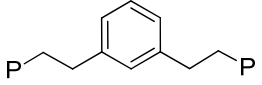
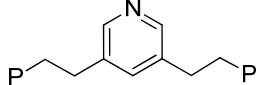
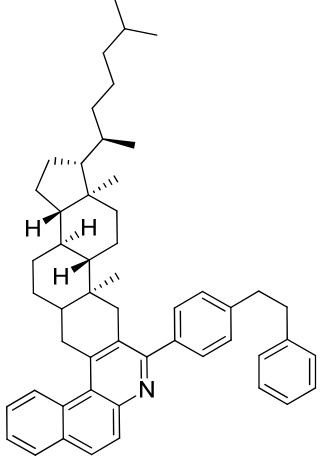
This study revealed the importance of the addition reactions in the liquid phase by quantitatively determining the yields and identifying structures of the addition products. The formation of archipelago structures during the thermal cracking of different families of model compounds is reported in this chapter.

3.2 MATERIALS AND METHODS

A series of four model compounds were selected to investigate the reactions of polyaromatic compounds under conditions relevant to thermal conversion, and to mimic catagenesis over a much shorter time scale.¹ These model compounds, shown in **Table 3.1**, were based either on pyrene as the main aromatic group (Compounds **1-3**) or a condensed cholestane-benzoquinoline structure (Compound **4**) based on aromatic biomarkers identified in crude oil.² Thermogravimetric analysis confirmed that compounds **1-4** do not evaporate prior to the onset of cracking at circa 350 °C, therefore, they were suitable for investigating cracking reactions in the liquid phase.

Thermal cracking experiments were carried out in a tubular stainless steel microreactor 5 mm in diameter and 5 cm in length attached to a high-temperature valve with a 1 mm (1/16 in.) diameter and 9 cm tube, connected and capped with Swagelok fittings. Two to three mg of each compound was loaded into a 3 × 45 mm one-end-sealed glass tube using a micro-spatula or micropipette. The loaded glass liner was placed in the microreactor with the open side up to collect easily the coke and heavy products that formed. The reactor was purged with nitrogen at least three times, closed, and then heated by immersion into a fluidized sand bath.

Table 3.1: Estimated yield of addition products from thermal cracking of model compounds

Compound	Structure	MW (g/mol)	Reaction conditions	X ^b %	Addition products, Wt% ^c
1		763.31	420 °C 20 min	77	40
2^a		534.69	400 °C 15 min	29	57
3^a		535.67	365 °C 20 min	25	62
4		702.06	420 °C 20 min	34	26

^aP in the structure represents a 1-pyrenyl group. ^bConversion: the difference between initial and final weights of the starting compound divided by the initial weight. The final weight is determined by HPLC. ^cWeight % of total products

At the end of each experiment, the reaction was terminated instantly by immersing the sealed reactor in cold water. Products were extracted with methylene chloride and concentrated using a rotary evaporator.

Thermogravimetric measurements were performed on a Thermo Cahn TherMax 400 TGA (Thermo Electron Corporation, Waltham, MA), heating 4-5 mg of sample at 10 K/min. Matrix-assisted laser desorption ionization (MALDI)-mass spectrometry (MS) and tandem MS/MS analyses (Bruker Ultraflex extreme MALDI-TOF/TOF, Bremen, Germany or Applied BioSystems Voyager Elite MALDI-TOF, Foster City, USA) were used to reveal the masses of the products and the fragmentation of selected products. In all cases, 2-[(2E)-3-(4-tert-butylphenyl)-2-methylprop-2-enylidene]malononitrile (DCTB) was used as the matrix for the MALDI experiments. Dimers of the parent compounds were not observed and only the nitrogen-containing compounds (**3** and **4**) and associated pyrolysis products gave adducts incorporating the DCTB matrix. All peaks present before the reaction or attributable to adducts with the matrix (mass 250 Da) were subtracted in the ratio calculations. ¹H-NMR spectroscopy (500 MHz Varian Inova, Santa Clara, CA USA) was conducted in CDCl₃ solution. NMR spectra of addition products were calculated using **MestReNova** software (Mestrelab Research, Santiago de Compostela, Spain).

High performance liquid chromatography (HPLC) analysis (Agilent Technologies, Santa Clara, CA USA) was performed using a Zorbax Eclipse PAH column of 4.6 × 150 mm with a C18 phase of 3.5 μm particles. The mobile phase was 70-75% methanol and 30-25% methylene chloride, with a temperature of 23 °C and maximum pressure of 400 bar. The UV detector was set at either 239 or 270 nm. The yield of cracked products such as pyrene and methylpyrene, which are too small to appear in the MALDI spectrum (*m/z* <300), were determined

from analysis by gas chromatography-flame ionization detector (GC-FID) using a Thermo Scientific Trace GC Ultra (Thermo Electron Corporation, Waltham, MA, USA). The GC column was TR5, 15 m \times 0.25 mm \times 0.1 μ m. The GC oven was set at 100 °C for 1 min, followed by continuous ramping at 10 °C/min to 350 °C. Helium was used as the carrier gas at 2 mL/min in a split mode, with a split flow of 50 mL/min.

3.3 RESULTS AND DISCUSSION

The mass spectrum of the products obtained from the pyrolysis of tetradecylpyrene (**1**) is illustrated in **Figure 3.1**, showing cracked products with masses less than the parent compound and higher molecular weight products arising from addition reactions. The mass spectrum of the initial tetradecylpyrene (**1**) does not contain these higher molecular weight peaks, except for the matrix adducts and some impurities; therefore, these heavy ions are not instrumental artifacts. The cracked products with masses below m/z 763 correspond to pyrene rings with fewer or shorter side chains than the parent compound. Assuming uniform response of the mass spectrometer for these structurally similar species, and a linear relationship between peak intensity and concentration³, the addition products comprise approximately 40% by weight of the total products of reaction. Although the intensities of the signals from the addition products are lower than the cracked products, these products each contribute greater mass.

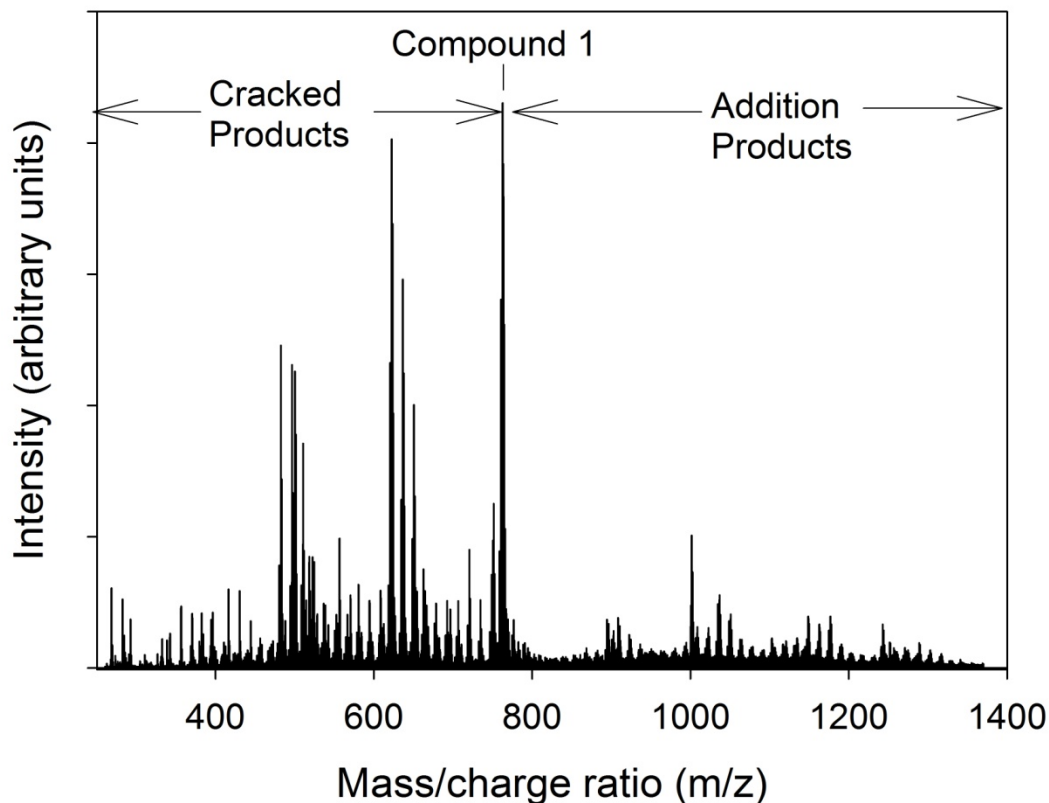


Figure 3.1: MALDI-MS of products from cracking of compound **1**. Cracked products resemble the parent compound but with fewer or shorter side chains. The addition products are bridged structures comprising the cracked fragments.

Similar mass spectra were obtained for the other compounds illustrated in **Table 3.1**, with clear and significant signals detected in each case for the formation of addition products, as well as the expected products of cracking. These mass spectra are illustrated in **Figures 3.2–3.4**. These data provide the fraction of the total product that has been converted to addition products with masses higher than that of the starting material. In all cases, the mass yields of addition products are significant in comparison to the cracked products.

Compound **4** is the most resistant of the samples to thermal cracking. While some loss of side chain is observed, the main reactions are dehydrogenation. Despite the low extent of reaction, a dimer product is clearly observed at m/z 1402 which is not present in the initial compound.

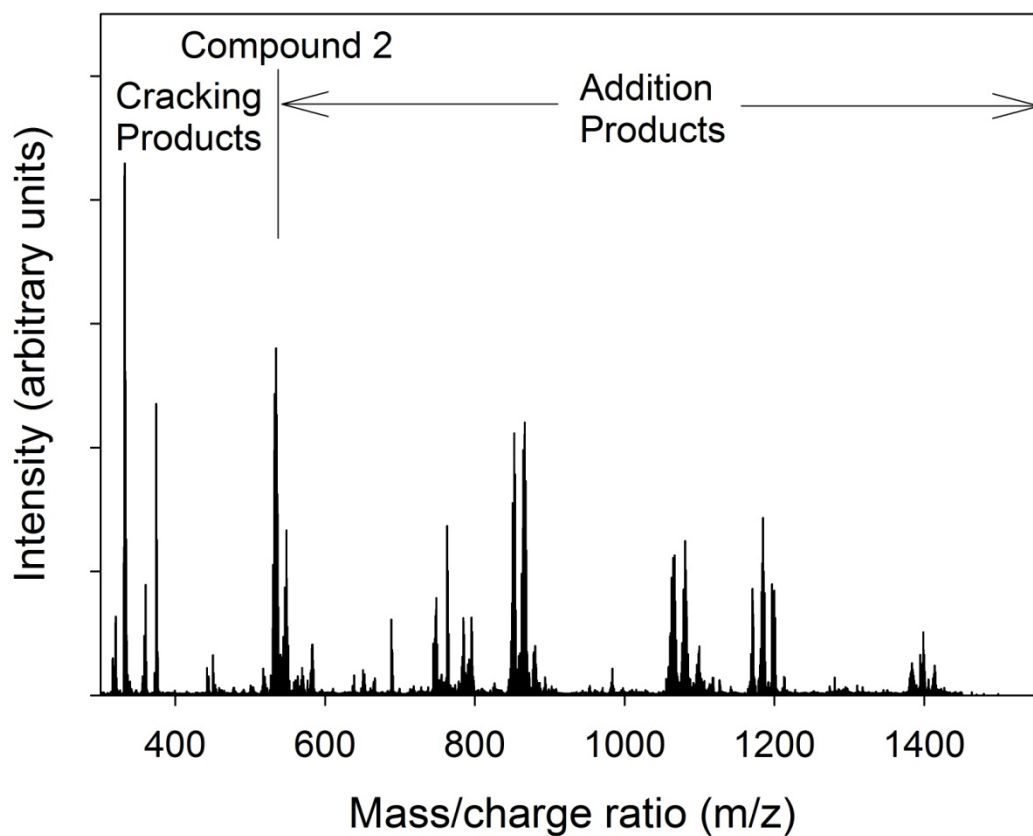


Figure 3.2: MALDI-MS of products from cracking of compound **2**. Cracked products are fragments of the parent while addition products are mainly alkyl-bridged structures composed of adducts of the cracked fragments and the original material.

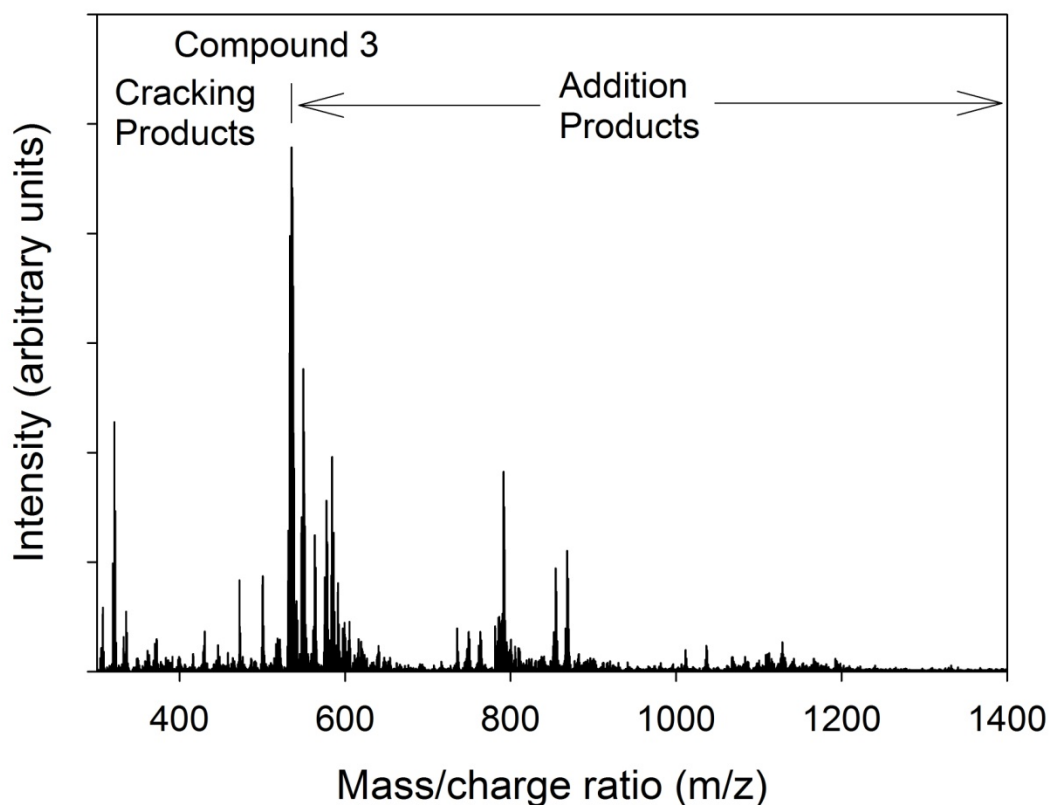


Figure 3.3: MALDI-MS of products from cracking of compound **3**. Cracked and addition products nature are similar to those obtained from cracking compound **2**.

The alkyl chains in pyrene compound **1** undergo cracking by a free-radical chain reaction mechanism, giving products containing unsaturated (olefinic) bonds.⁴ In all four compounds, unsaturated bonds can also be formed adjacent to the aromatic rings via successive hydrogen abstractions mediated by free radicals.⁵ The molecular weights of the observed addition products are fully consistent with a mechanism involving free radical addition to these unsaturated bonds.⁶ MALDI MS/MS analysis of the addition products shows significant cleavage of the parent ion to give fragments with much lower mass, consistent with scission along the bridge(s) between cyclic residues.

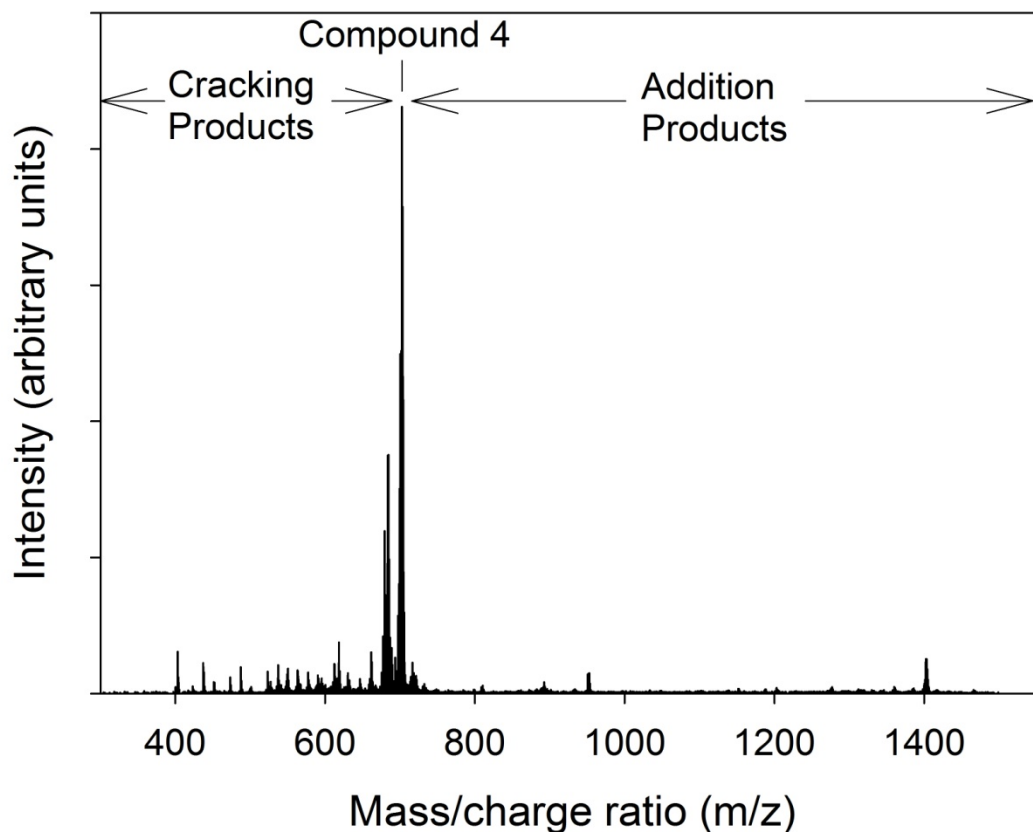


Figure 3.4: MALDI-MS of products from cracking of compound **4**. Cracked products resemble the parent with shorter side chains or methyl groups and dehydrogenated products. A dimer is clearly observed at m/z 1402.

^1H -NMR spectroscopy of the products obtained from cracking compounds **1-3** clearly show new resonances arising from both methine (CH) and methylene (CH_2) groups, characteristic of the new bridges formed between aromatic ring groups. New resonances appear at δ 3.75 and 4.69 in the ^1H -NMR spectrum of the product mixture obtained from the pyrolysis of compound **2** (**Figure 3.5**).

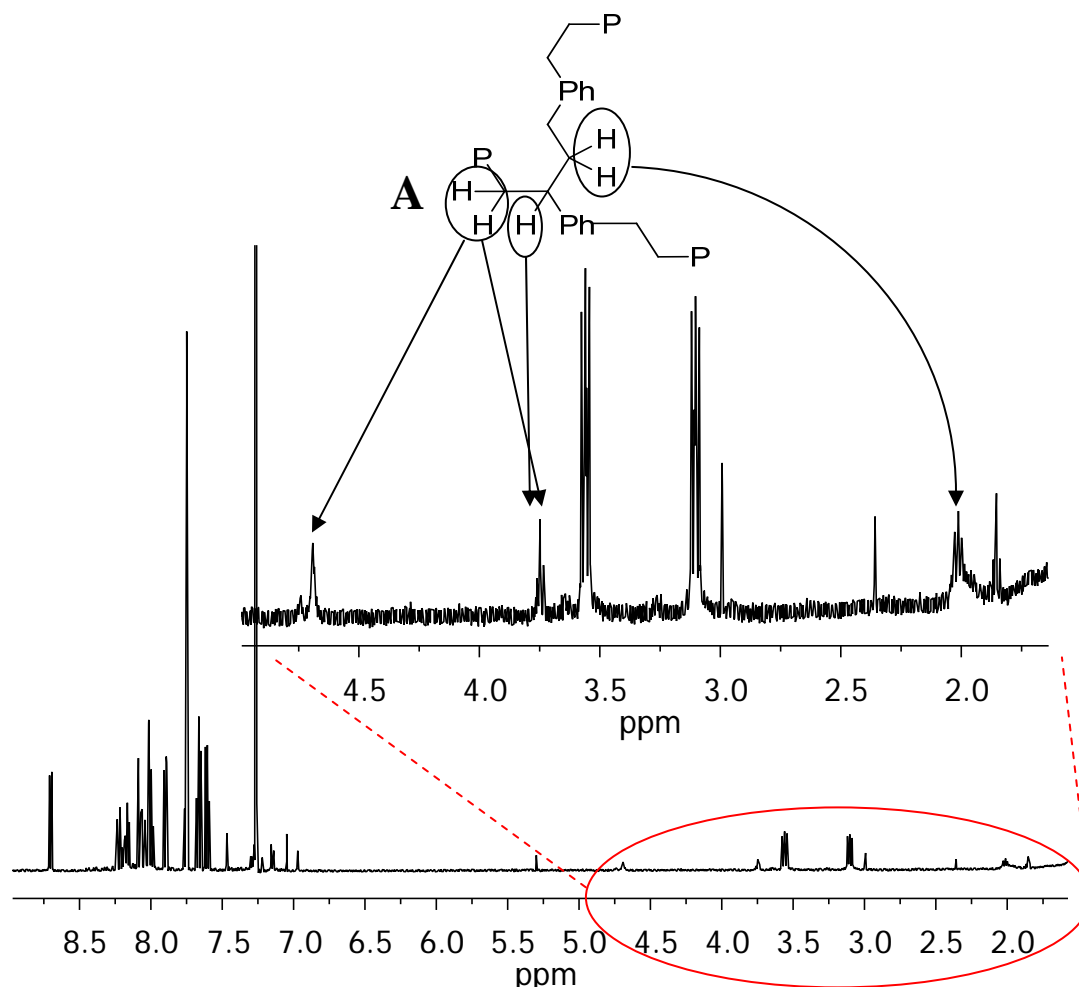


Figure 3.5: ^1H -NMR spectrum of products from compound **2** after pyrolysis at 400 °C for 15 min. The aliphatic region is enlarged, showing new resonances consistent with the product shown, where Ph is phenyl and P is pyrene. The assignments were made by simulating the ^1H -NMR spectrum of the compound in **Figure 3.7 (b)** (see **Figure 3.6**)

These signals are completely consistent with the addition of fragments of the original molecule to the ethano bridge between the aromatic groups, as illustrated in **Figure 3.6**. Resonances appearing at δ 2.97 and 3.78 for compound **1**, and at δ 3.13 and 3.64 for compound **3** are consistent with benzylic methylene groups

(CH₂) located between pyrene and methine (CH) residues, defining the formation of the new bridge in each model system (see **Figure 3.7 a, b**). In compound **4**, the new resonances in the NMR spectra do not provide a definite location for bridge formation. Combining the observations from the instrumental analyses, **Figure 3.7** shows possible structures of major addition products obtained from the model compounds, that are consistent with ¹H-NMR spectroscopy and tandem MALDI MS/MS results.

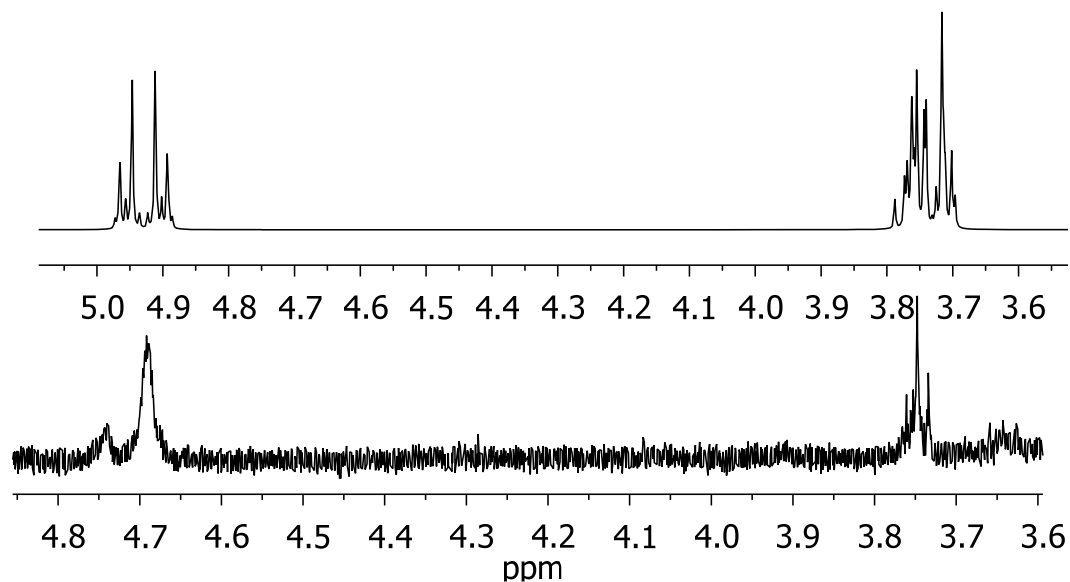


Figure 3.6: Comparison of the simulated and experimentally measured ¹H-NMR spectra of the two “benzylic” protons between the methine and pyrene groups labeled **A** in **Figure 3.5**. The top spectrum is simulated with MestReNova. The bottom spectrum was experimentally measured.

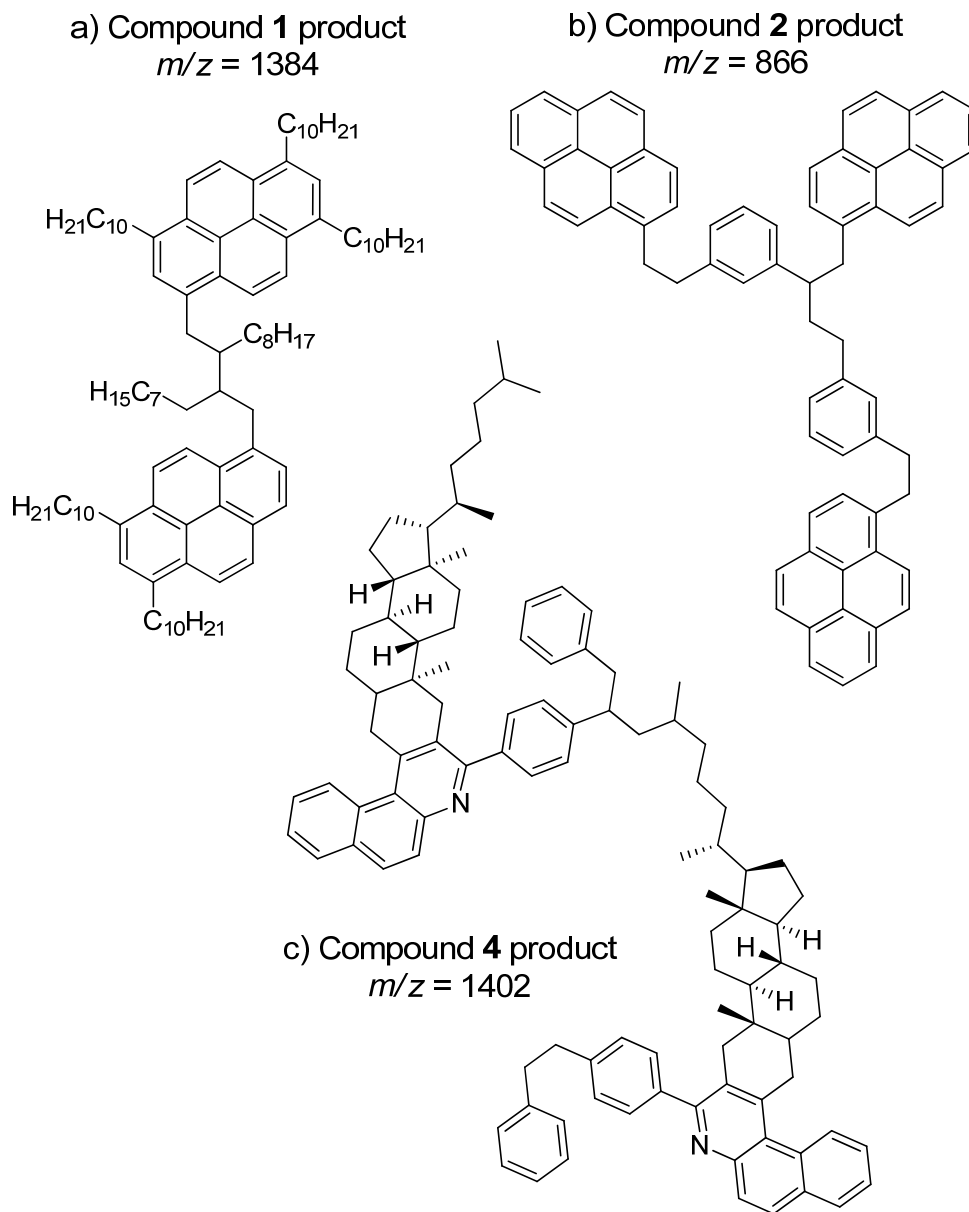


Figure 3.7: Suggested structures of major addition products

A combination of the data from mass spectrometry, HPLC, and GC were used to calculate the yield of addition products as a fraction of the total products from each compound. In the case of compounds **1** and **4**, the MALDI-MS spectra gave the yield of all products, relative to the peak from the starting compound.

Only peaks above the noise level of the spectrum were included. Contaminant peaks that were present in the MALDI-MS spectra before the reaction, or resulting from the matrix itself, were subtracted. The ratio of the addition products to the total products of reaction are reported in **Table 3.1**. These approximate values include all products except small alkyl fragments from cracking of side chains in compound **1**. In the case of compounds **2** and **3**, cracking reactions gives significant yields of products too small for analysis by MALDI-MS, so these compounds were analyzed by GC-FID. The amount of the converted reactant was first determined from HPLC, and this was assumed to equal the combined weights of all the products detected by GC-FID and MALDI; i.e., there are no undetected products. This is a reasonable approximation, since no insoluble material is formed in any of these reactions and the recovery of unreacted feed and products was high. The ratios in **Table 3.1** were then calculated from the resulting mass yields of cracked products and addition products. In all cases, the mass yield of addition products was significant, ranging from 26-62% of the total products. The balance of the products was cracked products of lower molecular weight than the starting compound.

The results of this study show two important, mechanistically consistent, trends. First, when these model compounds crack in liquid phase, the products obtained include not only fragments of the starting compound but also high molecular weight addition products incorporating the “archipelago” structural motif. Although surprisingly few studies have investigated cracking in the liquid phase, pyrolytic cracking of long-chain *n*-alkanes^{7, 8} demonstrated the formation

of branched alkanes larger than the starting compounds. Cracking of alkane in the presence of 1,2,3,4-tetrahydronaphthalene gave adducts formed from the addition of unsaturated fragments to the ring compound.⁹ In contrast to the reactivity of the bridges in model compounds **2** and **3**, which give both cracking and addition, the same ethano bridge in the monocyclic analog, 1,2-diphenylethane, gave only 6% conversion after 30 min at 400 °C¹⁰ and no significant reaction of the unsaturated products from cracking. The polycyclic aromatic groups clearly make compounds **1–3** more reactive than simple benzene analogs and lead to significantly greater formation of addition products at the levels of conversion reported in **Table 3.1**. This observation is supported by previous studies of thermal cracking of alkyl-hexabenzocoronenes¹¹, and dipyrenylalkanes,¹² which also return significant yields of addition products derived from homolytic cracking, albeit of undefined structure.

The second trend is that the addition reactions occur predominantly on the tethering alkyl chains and bridges attached to the aromatic ring systems, as illustrated in **Figure 3.7**. We cannot exclude aryl-aryl addition products, but data such as the NMR spectra (**Figure 3.5**), which showed significant concentrations of new alkyl bridges, and MS/MS analysis of the addition products indicate that such products are much less favourable. This result emphasizes that although the physical behaviour of petroleum compounds is guided by the presence of aromatic groups, the substituent alkyl groups provide the main reactive centres for thermal reactions, both cracking and addition. These data do not constitute an exhaustive study of all logical model precursors to petroleum asphaltenes, but the

results do show that addition reactions of molecular fragments in the liquid phase to form alkyl-bridged structures constitute a significant reaction pathway that must be considered in the geological generation, the physical properties, and the industrial processing of heavy petroleum fractions.

The adduct structures illustrated in **Figure 3.7** remain reactive; indeed these compounds are expected to crack even more readily than the parent compounds. As such, these compounds are intermediates in a progression of similar reaction, reacting over time to give smaller fragments (which are typically richer in hydrogen content) and higher molecular weight addition products (which are typically more aromatic) in an ever-broadening distribution of molecular size. In the limit, the terminal products would be methane and pyrobitumen (i.e. coke). The data of **Table 3.1** demonstrate, however, that initially the observed archipelago-like compounds are formed much more rapidly than they are destroyed, giving the rapid accumulation of addition products illustrated in the mass spectra of **Figures 3.1–3.3**. The implication is that such structures will be common in petroleum, where cracking and addition take place by similar mechanisms, albeit over much longer time periods¹³. In refineries, processes such as visbreaking should form even more of this material by replicating the temperature and residence time of the experiments conducted here with model compounds **1-4**. Similarly, these reactions will be extremely important in coking processes, leading to the sacrifice of lighter components and concomitant formation of higher molecular weight material.

3.4 CONCLUSIONS

1. When model compounds with three distinct molecular architectures are cracked in the liquid phase, all give significant yields of addition products larger than the starting compounds ranging from 26–62 wt%.
2. The molecular structures of the addition products are consistent with addition reactions between alkyl groups, rather than formation of aryl-aryl linkages or larger fused-ring products.
3. The yields of addition products from bridged pyrene compounds are much larger than from the corresponding phenyl analogs.

3.5 REFERENCES

1. Behar, F.; Lorant, F.; Mazeas, L., Elaboration of a new compositional kinetic schema for oil cracking. *Org. Geochem.* **2008**, 39, 764-782.
2. Oldenburg, T. B. P.; Huang, H.; Donohoe, P.; Willsch, H.; Larter, S. R., High molecular weight aromatic nitrogen and other novel hopanoid-related compounds in crude oils. *Org. Geochem.* **2004**, 35, 665-678.
3. Bucknall, B.; Fung, K. Y. C.; Duncan, M. W., Practical Quantitative Biomedical Applications of MALDI-TOF Mass Spectrometry. *J Am. Soc. Mass. Spectrom.* **2002**, 13, 1015–1027.
4. Kossiakoff, A.; Rice, F. O., Thermal decomposition of hydrocarbons, resonance stabilization and isomerization of free radicals. *J. Am. Chem. Soc.* **1943**, 65, 590-595.
5. Freund, H.; Matturro, M. G.; Olmstead, W. N.; Reynolds, R. P.; Upton, T. H., Anomalous side chain cleavage in alkylaromatic thermolysis. *Energy Fuels* **1991**, 5, 840-846.
6. Gray, M. R.; McCaffrey, W. C., Role of chain reactions and olefin formation in cracking, hydroconversion and coking of petroleum and bitumen fractions. *Energy Fuels* **2002**, 16, 756-766.
7. Khorasheh, F.; Gray, M. R., High pressure thermal cracking of n-hexadecane. *Ind. Eng. Chem. Res.* **1993**, 32, 1853-1863
8. Wu, G.; Katsumura, Y.; Matsuura, C.; Ishigure, K.; Kubo, J., Comparison of liquid-phase and gas-phase pure thermal cracking of n-hexadecane. *Ind. Eng. Chem. Res.* **1996**, 35, 4747-4754.

9. Khorasheh, F.; Gray, M. R., High pressure thermal cracking of n hexadecane in tetralin. *Energy Fuels* **1993**, 7, 960-967.
10. Miller, R. E.; Steln, S. E., Liquid-Phase Pyrolysis of 1,2-Diphenylethane. *J. Phys. Chem.* **1981**, 85, 580-589.
11. Gherghel, L.; Kubel, C.; Lieser, G.; Rader, H. J.; Mullen, K., Pyrolysis in the mesophase: A chemist's approach toward preparing carbon nano- and microparticles. *J. Am. Chem. Soc.* **2002**, 124, 13130-13138.
12. Savage, P. E.; Jacobs, G. E.; Javanmardian, M., Autocatalysis and aryl alkyl bond cleavage in 1 dodecylpyrene pyrolysis. *Ind. Eng. Chem. Res.* **1989**, 28, 645-653.
13. Pelet, R.; Behar, F.; Monin, J. C., Resins and asphaltenes in the generation and migration of petroleum. *Org. Geochem.* **1986**, 10, 481-498.

CHAPTER 4

MEASUREMENT OF CRACKING KINETICS OF PURE MODEL COMPOUNDS BY THERMOGRAVIMETRIC ANALYSIS*

4.1 INTRODUCTION

Thermal cracking reactions are typically investigated using isothermal reactors, either in batch or flow mode, with experiments at different residence times and temperatures to determine the reaction pathways and to estimate the Arrhenius kinetic parameters, namely the activation energy (E) and the pre-exponential factor (A). The isothermal method is preferred for calculating the decomposition kinetics¹, but it requires tedious work and the experiments can consume large amounts of sample. Our interest is reaction kinetics of specially synthesized model compounds to represent components of vacuum residue of petroleum and bitumen, therefore, methods based on milligram quantities of reactant are required.

*A version of this chapter has been published: Alshareef, A. H.; Azyat, K.;[§]Tykwinski, R. R.;[§] and Gray, M. R. *Energy and Fuels* **2010**, 24, 3998–4004. [§]Synthesized the model compounds.

One method to estimate the kinetics is the thermogravimetric analysis (TGA). Due to the simplicity of the instrument and calculation methods, TGA has been applied to estimate the kinetics of many processes in complex mixtures such as dehydration² or combustion³ of coal, pyrolysis of polymers⁴, conversion of petroleum residue⁵, and even testing the decomposition of drug compounds⁶. TGA has also been used to investigate reaction pathways for model compounds, for example, Freund et al.⁷ used a modified TGA instrument to look at the anomalous cleavage of side chains in a pyrene-based model compound. Unfortunately, the results from TGA experiments can be subject to factors which are not related to reaction kinetics, including mass and heat transfer limitations, evaporation, and buoyancy effects as well as the accuracy of the model or method used to calculate these parameters. In reactions of complex mixtures or solids, separating these artifacts from the intrinsic reaction kinetics is often impossible, therefore, the results from TGA measurements of kinetics are usually termed “apparent” parameters and considered unreliable for predictions.¹

The objective of the present chapter is to compare the measurement of cracking kinetics of pyrene-based model compounds in the TGA. Three different analytical methods: peak temperature, isoconversional, and differential methods are compared. The kinetics are validated by comparing results for different pyrene-derived compounds with related structural features and common decomposition pathways. In order to further verify the kinetics from the best TGA method, an isothermal batch microreactor is used to compare the predicted and actual conversion of a test compound.

4.2 KINETICS ESTIMATION METHODS IN TGA

Several methods have been proposed to estimate kinetic parameters from weight loss data in the TGA. The most commonly used have been the peak temperature method and the isoconversional method. A third approach has also been reported in the literature by estimating the kinetics differentially in non-isothermal experiments at a single heating rate.

4.2.1 The Peak Temperature Method

The peak temperature method uses the maximum rate of weight loss and the temperature at that point at multiple heating rates to calculate the kinetics. The basic equations used to determine kinetics were outlined by Redhead⁸ for kinetics of thermal desorption of gases. The mathematical solution is applicable to decomposition because the general equation form to describe rate of desorption is the same as rate of reaction:

$$\frac{-dW}{dt} = AW^n \exp\left(\frac{-E}{RT}\right) \quad (4.1)$$

where W is the weight of sample, t is time, A is the pre-exponential factor in the Arrhenius equation, n is the reaction order, E is the activation energy, R is the universal gas constant, and T is temperature.

Redhead solved this equation to find the peak temperature (T_P) at which the rate is maximal. For a first order reaction with a heating rate of β , and assuming that E is not a function of W , he found this equation:

$$\frac{\beta}{T_P^2} = \frac{AR}{E} \exp\left(\frac{-E}{RT_P}\right) \quad (4.2)$$

Plotting β/T_P^2 on a logarithmic scale versus $1/T_P$ should give a straight line with slope of $-E/R$. Redhead stated that β should be varied by at least two orders of magnitude for a reasonable accuracy.

Falconer and Schwarz⁹ surveyed many techniques for temperature programmed desorption and reactions and listed under the method of heating rate variation two independent equations that can be used to determine the kinetics. One equation is that derived by Redhead and the other is the basic rate equation applied at peak point which for $n = 1$ is

$$\left(\frac{-dW/dt}{W}\right)_P = A \exp\left(\frac{-E}{RT_P}\right) \quad (4.3)$$

The subscript P indicates that the rate and weight are at the maximum point. Plotting the normalized weight derivative at the maximum rate on a logarithmic scale versus $1/T_P$ would yield a straight line with slope of $-E/R$. The authors also stated that β must be varied by a factor of 10 and that the use of both equations can be a measure of accuracy if they yielded comparable results.

In the process of verifying the derivation by Redhead, a third form of the peak temperature was derived that could be used to calculate the kinetics and interestingly showed different results than the usually applied two forms mentioned above.

Solving the derivative of equation (4.1) at the maximum rate and temperature at a constant n gives the following equation:

$$\frac{-dW}{dT} = \frac{1}{n} W_P \frac{E}{RT_P^2} \quad (4.4)$$

Using a linear temperature profile of $dT = \beta dt$ yields the final equation:

$$\left(\frac{-dW/dt}{W}\right)_p = \frac{E}{nR} \frac{\beta}{T_p^2} \quad (4.5)$$

Plotting $-dW/dt/W$ at the peak point versus β/T_p^2 should give a slope of E/nR . Notice that equating this equation to equation (4.3) gives back Redhead equation (4.2) at $n = 1$.

Olmstead and Freund⁵ used this method to calculate the conversion kinetics of Arab Heavy and Cold Lake petroleum residue by applying linear heating rates in the range of 0.5–100 °C/min. The accuracy of their measurements was confirmed by isothermal experiments in a specially modified TGA instrument.

4.2.2 The Isoconversional Methods

The isoconversional methods assume that the reaction rate at a given level of conversion is a function of temperature only¹ and hence uses the temperature at a fixed extent of conversion at multiple heating rates to measure kinetics. Liu³ compared four model-free isoconversion methods to calculate the combustion kinetics of charcoals at various gas mixtures. Liu³ gives an excellent summary of the derivation and approximations used in these model-free isoconversional methods and thus they will not be restated here. The four methods given by Liu for determining E are: the Friedman method [plotting $\ln(dX/dt)$ vs. $1/T_f$ gives a straight line with slope $-E/R$], the Ozawa-Flyn-Wall (OFW) method [plotting $\ln(\beta)$ vs. $1/T_f$ gives a straight line of slope $-1.0518E/R$], Kissinger-Akahira-Sunose/Vyazovkin (KAS/V) [plotting $\ln(\beta/T_f^2)$ vs. $1/T_f$ gives a straight line with slope of $-E/R$], and the Starink method [plotting $\ln(\beta/T_f^{1.92})$ vs. $1/T_f$ gives a straight line with slope of $-1.0008E/R$]. In these plots, X is the conversion and T_f is the temperature at which an extent of conversion is reached for a given β .

4.2.3 The Differential Method

A number of studies in the literature reported calculating the kinetics of the data obtained in the TGA using differential analysis in non-isothermal experiments at a single heating rate. Aguado et al.¹⁰ measured almost the same value of apparent activation energy at various heating rates for pyrolysis of scrap tires but when they compared the results to microreactor and isothermal TGA, large differences were observed. Rivas et al.¹¹ used a single heating rate at 10 °C/min to measure the thermal degradation kinetics of copolymers but the basis of incorporation of heating rate into the differential equation was not clear and the number of data plotted was very little. An example of applying this differential technique on pure compounds was illustrated by Burnham et al.⁶ where a drug compound was tested at 10 °C/min but the fitting was poor and the number of points was small bringing their calculations into question.

The basis of the differential analysis lies in assuming the cracking is a first order reaction, and then calculating the reaction constant, $k = -dW/dt/W$, differentially at each measured temperature in a dynamic TGA run to give E and A by plotting $-dW/dt/W$ versus $1/T$ according to equation (4.1). The range of temperatures used is very important especially when solid residue or coke forms at higher conversion levels, indicating that the reaction is no longer a simple cracking followed by weight loss. The derivative of the weight curve with time can be obtained directly from the software of TGA instrument, which enables determining E and A accurately from a single experiment.

4.3 MATERIALS AND METHODS

The pyrene-based model compounds used in this study were synthesized at the chemistry department at the University of Alberta. Two main compounds in this investigation have the same structure of linked aromatic rings: 1,3-bis(2-pyren-1-yl-ethyl)-benzene (P-*m*Ph-P) and 2,5-bis(2-pyren-1-yl-ethyl)-thiophene (P-Th-P), which are shown in **Figure 4.1**. Seven other pyrene-based compounds with similar structure that differ only in their central group were also used. The names of the central groups, listed in increasing estimated boiling point of the compounds with the first two numbers referring to the linkage carbons, are 1,4-*n*Butyl, 1,4-benzene, 5,5'-(2,2'-bithiophene), 2,8-dibenzofuran, 1,1'-(4,4'-biphenyl), 4,4'-(2,2'-bipyridine), and 2,7-(9,9-diethyl-9H-flourene).

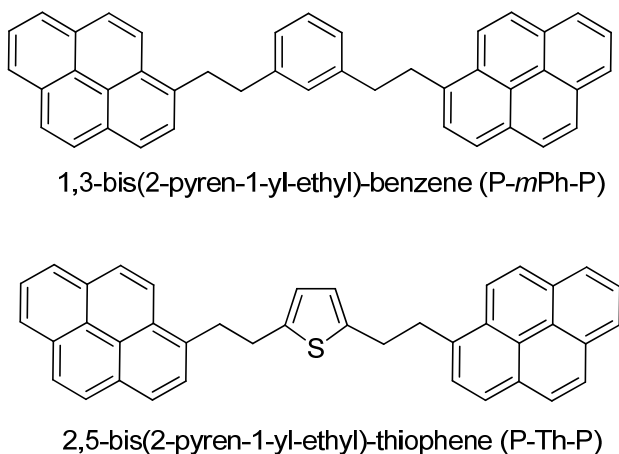


Figure 4.1: Chemical structure of P-*m*Ph-P and P-Th-P

Phenanthrene and pyrene that were used in the response factor calculation for the microreactor run were used as received. The methylene chloride (MC) and methanol used for product extraction and in HPLC analysis were HPLC and ACS grade, respectively, and were used as received from commercial suppliers.

PRAXAIR supplied all the gases needed for the TGA and GCMS with helium and argon of 5.0 grade, which is an ultra-high purity grade of 99.999% purity.

All the TGA experiments were done on a Thermo Cahn TherMax400 TGA (Thermo Electron Corporation, USA). 4–5 mg of sample was loaded on a platinum pan after taring. The variation of the quantity of sample loaded, indicating a different contact area with the pan in each run, had no impact on the observed kinetics suggesting lack of catalytic activity of the platinum pan under the inert TGA conditions. The samples, usually in a powder form, were spread evenly to minimize mass and heat transfer effects. The TGA was heated at different constant rates to 500 °C, although the final temperature was higher when higher heating rates were used. Multiple runs at 10 °C/min confirmed the repeatability of the TGA results. The 10 °C/min was selected because the range of 10–20 °C/min gave relatively fast heatup time as well as giving low fluctuation and many data points to ensure accuracy. Argon flowed continuously in the sample chamber at 80 mL/min with another excess flow at the balance chamber to prevent deposition on the hanging wire or the delicate balance. The temperature, time, weight, and derivative of weight with time were obtained directly from the instrument software (Thermal Analyst). Variable heating rates were done on P-*m*Ph-P and P-Th-P with single runs at each heating rate, except at 10 °C/min, while other model compounds were all run at 10 °C/min only with at least two runs each to confirm repeatability.

One microreactor experiment in a tubular stainless-steel microreactor was conducted on P-*m*Ph-P at 400 °C for 15 min. The reactor was ¼” diameter and 2”

long connected to a high-temperature valve via a 1/16" diameter and 3.5" long tube. Swagelok fittings were used to assemble the different parts. A sand bath was used to achieve the heating. A heat-up curve (**Figure A.5** in Appendix A) prior to the experiment showed the reactor reaches to within 5 °C of the set point in 3–4 minutes. This means that the actual bed temperature is ~395–400 °C and hence predicting the conversion in this range would be an acceptable confirmation to the differential TGA kinetics. About 2.5 mg of P-*m*Ph-P was loaded in a 3 mm × 4.5 cm long one-end-sealed glass tube that was placed inside the reactor (open end up). The glass tube provided a visual indication as well as to easily collect any solid residue if formed. The reactor and sample were purged with nitrogen at least three times before reaction. The reactor was continuously shaken by a rotary motor. The products were extracted with excess MC and then the solution was concentrated by using a rotary evaporator.

The cracked products were identified with a Thermo Scientific Trace GC Ultra connected to a DSQII mass spectrometer (both from Thermo Electron Corp., USA). The oven of the GC was set at 100 °C for 1 min followed by a ramp at 10 °C/min to 320 °C. Helium gas flow was set at 2 mL/min with a splitless mode. The column used for the separation was TR5-MS 15 m × 0.25 mm × 0.1 µm. The parent compound, P-*m*Ph-P, and any heavier addition products did not elute in the GC and hence HPLC was used. The quantification of the parent compound was achieved with an Agilent 1200 series HPLC (Agilent Technologies, USA) equipped with a Zorbax Eclipse PAH of 4.6 × 150 mm column and a non-polar C18 phase of 3.5 µm particles. Isocratic flow was used at

75% methanol – 25% MC flowing at 1 mL/min. The temperature was set at 23 °C and the UV detector wavelength was set at 270 nm.

4.4 RESULTS AND DISCUSSION

A typical curve of weight loss and the rate of weight loss versus time, dW/dt , is shown in **Figure 4.2**. As can be seen in this figure, all the model compounds in this study showed a high stability in the TGA and lost less than 3% of weight under 200 °C at a heating rate of 10 °C/min. The limit of 200 °C was chosen since cracking below this temperature is usually insignificant and therefore any weight loss at temperatures below 200 °C would be from residual solvent or due to sample evaporation and hence was ignored. The main compound in this study, P-*m*Ph-P, for which the reaction rate was verified by microreactor, showed an average of weight loss of only 1.8% under 200 °C at 10 °C/min heating rate. Increasing the heating rate generally increased the weight loss reaching up to 6.9% for this compound at 100 °C/min.

Following the recommendations of Redhead⁸ and Falconer and Schwarz⁹, the heating rates originally considered were at 1, 10, and 100 °C/min but increasing the heating rate over 50 °C/min produced fluctuations due to the rapid gas expansion, therefore, the accuracy of the results was poor. Data from heating rates of 1, 5, 10, and 50 °C/min for P-*m*Ph-P were collected instead. The rates of weight loss versus time curves of these experiments are shown in **Figure 4.3**. As expected, the peak temperature and the rate of loss increased as the heating rate increased.

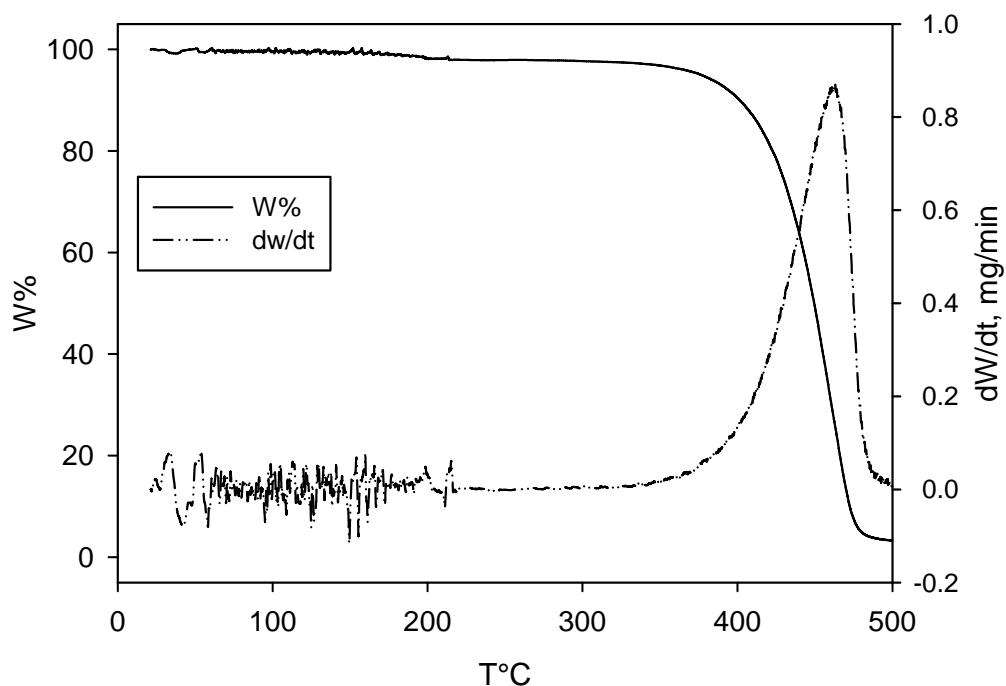


Figure 4.2: Weight loss and rate of weight loss curves for P-*m*Ph-P pyrolysis in the TGA at a heating rate of 10 °C/min.

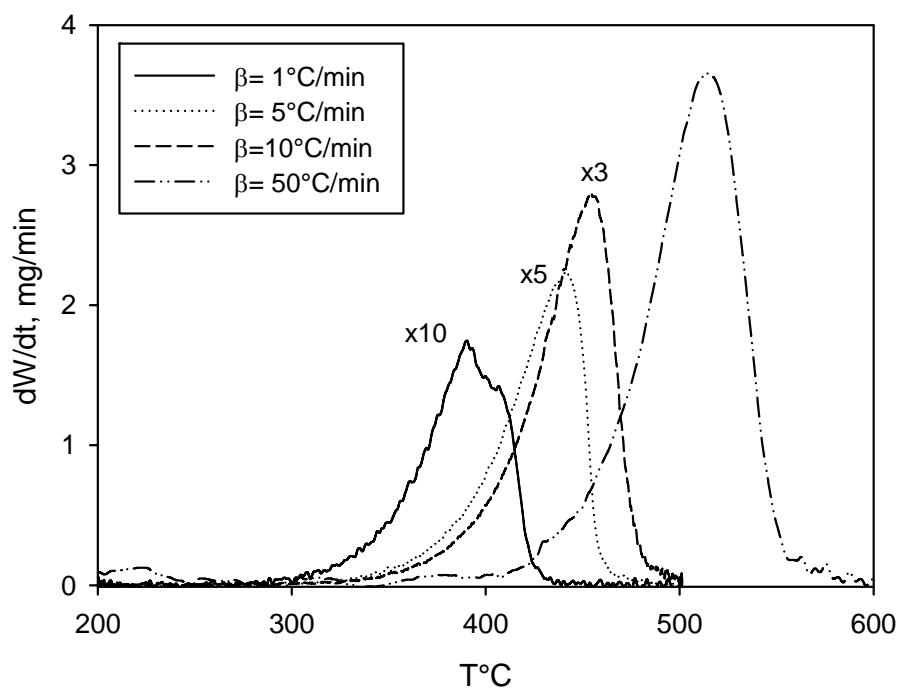


Figure 4.3: Rate of weight loss vs. T for P-*m*Ph-P at various heating rates. All the curves are enlarged by the shown value except the one at 50 °C/min.

Figure 4.4 shows the calculations by the peak temperature method using the two independent forms, equations (4.2) and (4.3). The plots are relatively comparable with a high linearity which may suggest accuracy of the calculations as suggested by Falconer and Schwarz⁹. Plotting equation (4.5) of the peak temperature method shows a completely different result with almost 100% difference as shown in **Figure 4.5**.

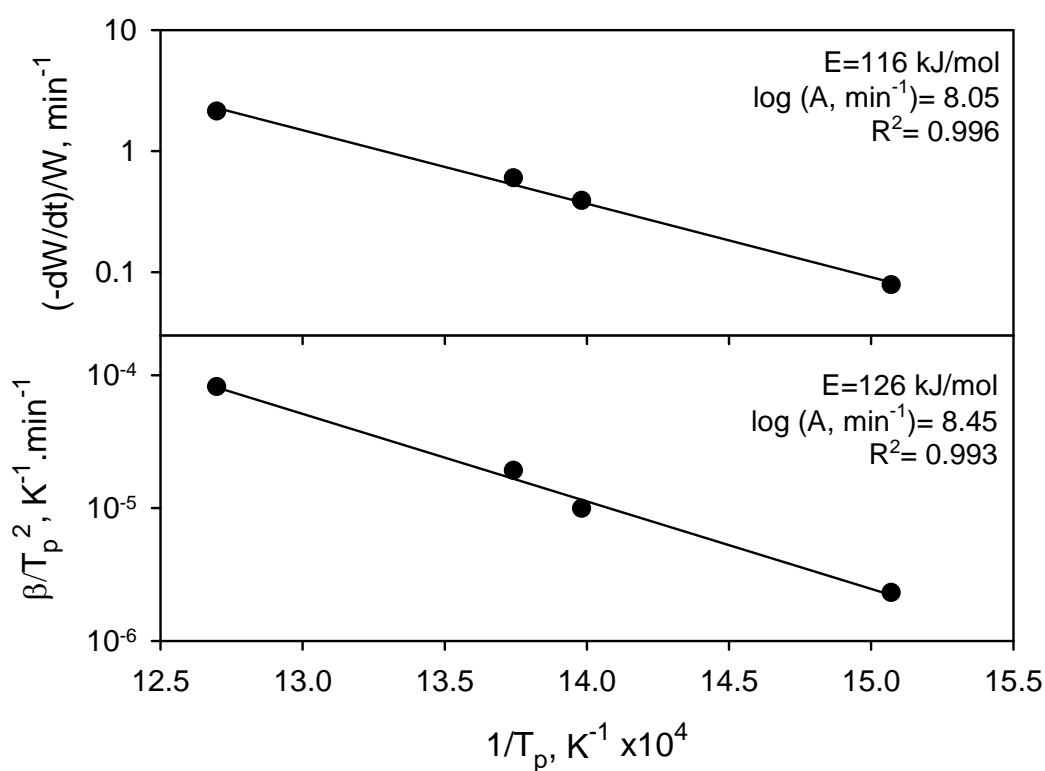


Figure 4.4: Peak temperature plots using equations (4.2) and (4.3). The shown apparent activation energies of cracking of P-*m*Ph-P are lower than expected for such a chemical structure.

The reason that equation (4.5) gives different results, which are the most accurate as will be shown below, is not clear. One possible reason is the lack of

rate of weight loss in equation (4.2) (β/T_p^2 vs. $1/T_p$) and the lack of heating rate in equation (4.3) ($-dW/dt/W$ vs. $1/T_p$) while equation (4.5) has all three parameters ($-dW/dt/W$ vs. β/T_p^2). The calculations and plots were made assuming a first order kinetics which is reasonable for cracking of bridges in the chemical structure of P-*m*Ph-P.

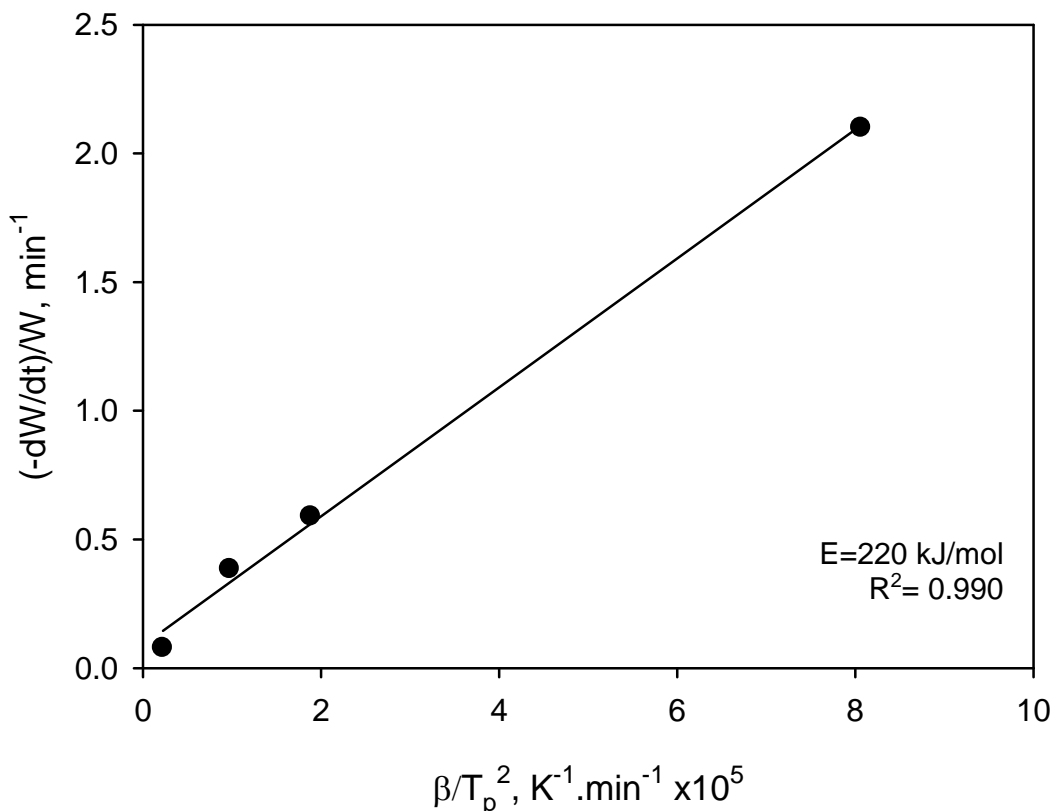


Figure 4.5: Peak temperature plot using equation (4.5).

To compare the observed results from the peak temperature method with the isoconversion method, the temperature (T_f) at a conversion of 0.3 was taken at the same runs of 1, 5, 10, and 50 °C/min. The OFW and Friedman results are shown in **Figure 4.6**, and the KAS/V and Starink results are shown in **Figure 4.7**.

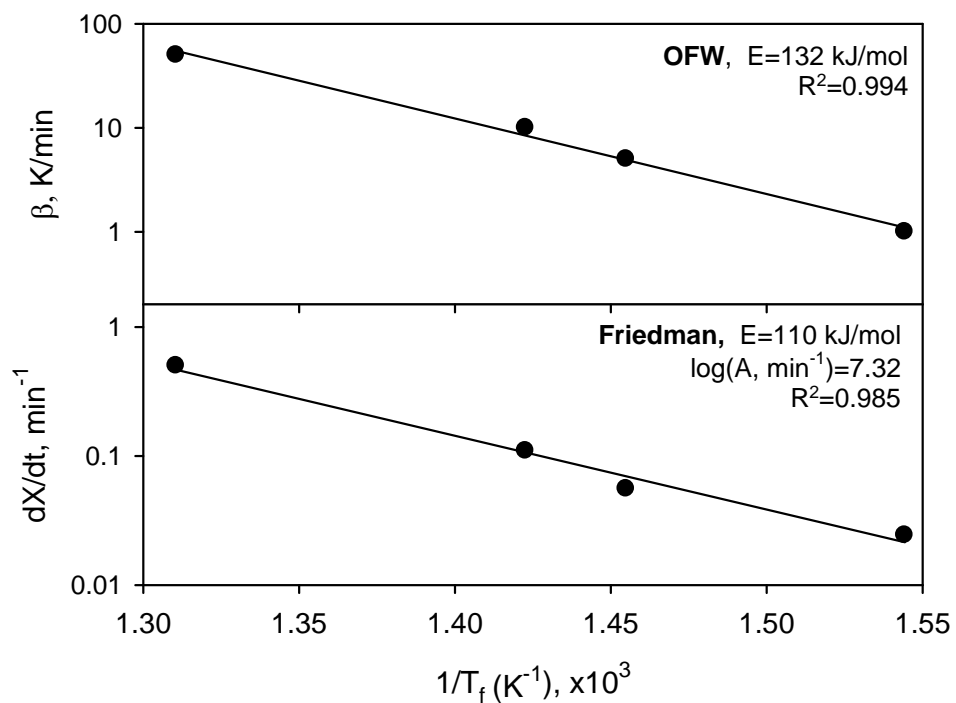


Figure 4.6: Isoconversional method at 0.3 conversion using OFW and Friedman correlations for P-*m*Ph-P runs at 1, 5, 10, and 50 °C/min.

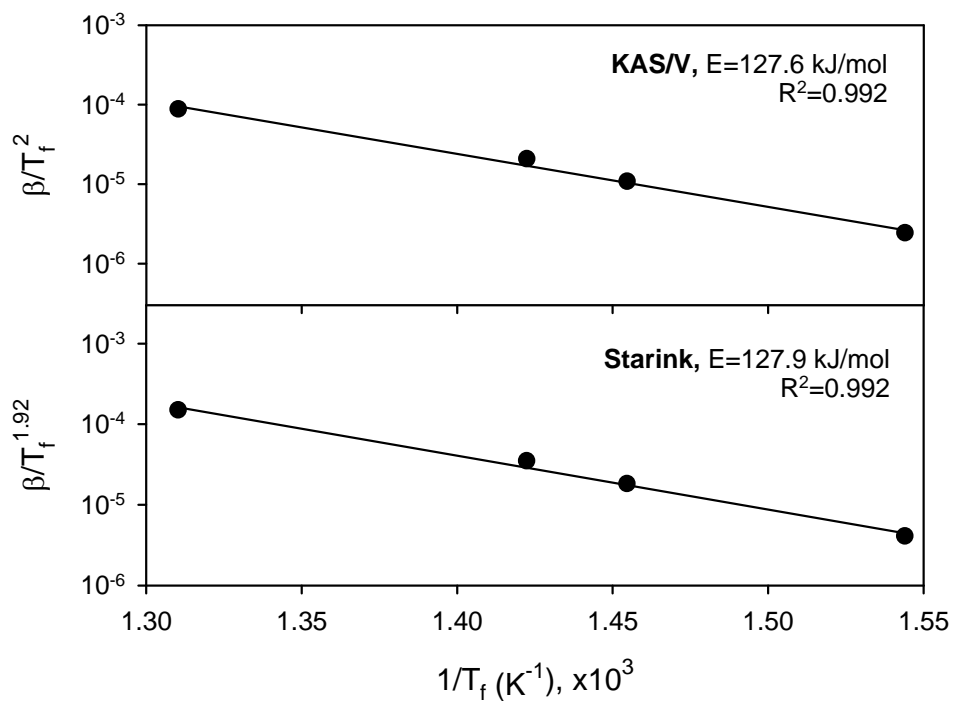


Figure 4.7: Isoconversional methods at 0.3 conversion using KAS/V and Starink correlations for P-*m*Ph-P runs at 1, 5, 10, and 50 °C/min.

All four methods showed high linearity and very close results except for the Friedman method. The results also match those calculated with the first two forms of the peak temperature method which further strengthens the possibility for their accuracy.

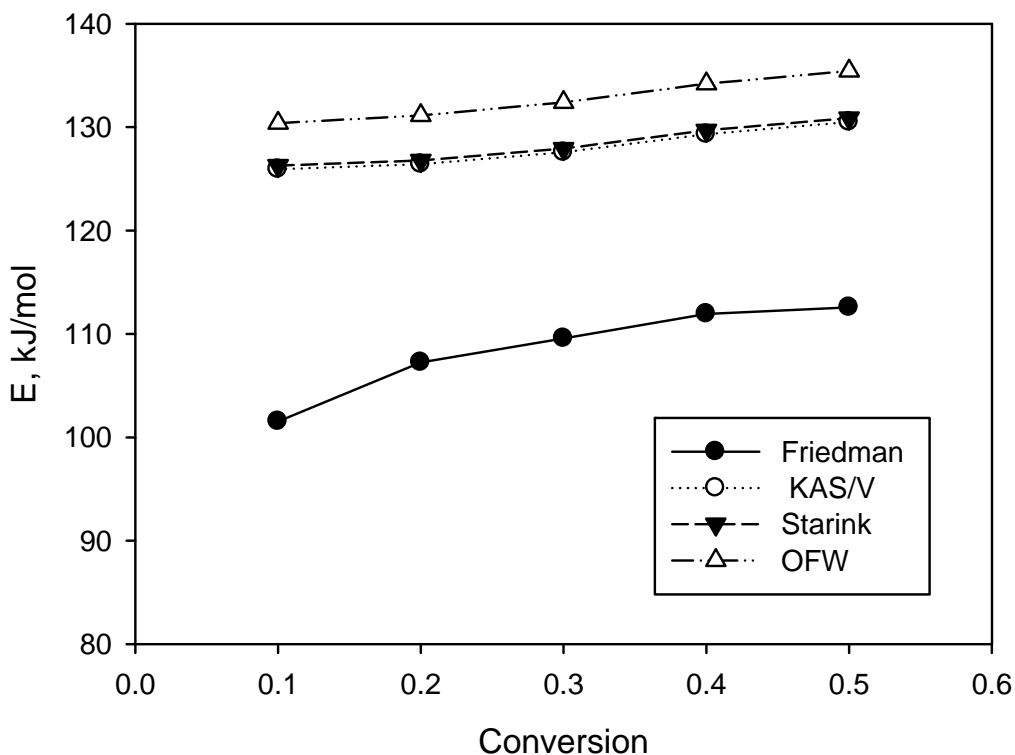


Figure 4.8: The change of activation energy with conversion for the four isoconversional methods.

The isoconversion results with the four model-free methods were calculated at different conversion levels from 0.1–0.5, which showed an increasing trend in E with conversion (**Figure 4.8**). The Friedman method showed the largest difference and gave the lowest values, similar to Liu's³ observation except that E decreased with increasing conversion, due to the different nature of reaction. The change of E with conversion was attributed by Liu to the change in control

mechanism which, in our experiments, is a valid explanation to the increase in E as conversion increases, or also because of the increasing importance of secondary reactions at higher conversion levels.

Figure 4.9 shows an interesting observation when the results from the Friedman method at various conversion levels were plotted on the same figure. The data points show a linear plot which is the basis for the differential method used in this study. Instead of obtaining data at selective conversion points, all the measured data points from TGA could be used to calculate the conversion differentially. E can be calculated then by plotting the differential rate constant versus $1/T$ following the Arrhenius equation.

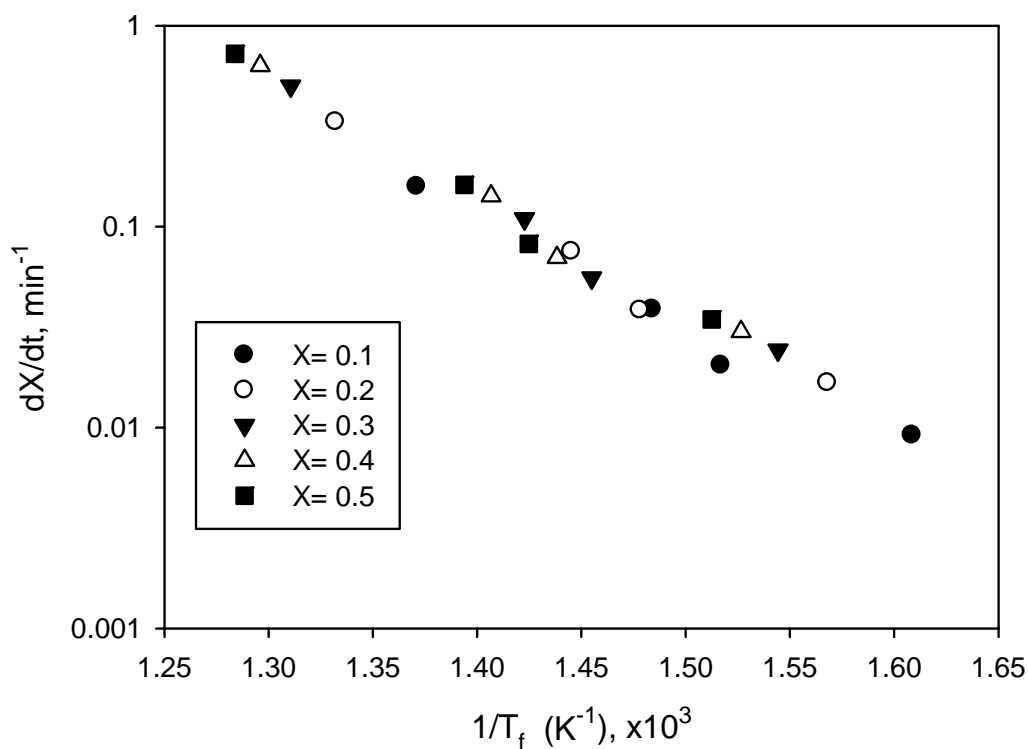


Figure 4.9: Friedman method at various conversion levels for P-*m*Ph-P experiments at 1, 5, 10, and 50 °C/min

Figure 4.10 shows a plot of the normalized rate of weight loss ($-dW/dt/W$) versus $1/T$ over the temperature range of 418–444 °C for P-*m*Ph-P at a ramping of 10 °C/min. The plot gave an activation energy of 201 kJ/mol, which is very different from the values predicted by both peak temperature (eq 4.2 and 4.3) and the isoconversional methods.

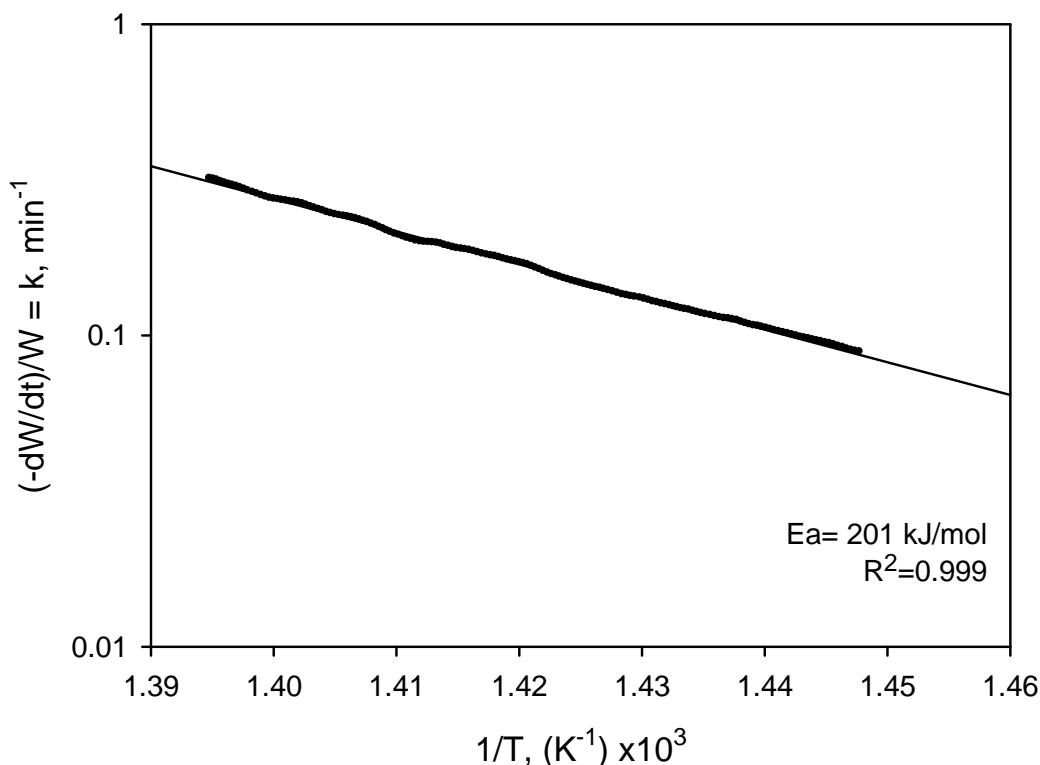


Figure 4.10: Plotting the differential calculations of k ($-dW/dt/W$) vs $1/T$ (K^{-1}) for the 10 °C/min run of P-*m*Ph-P. The regression line is not visible due to the high linearity and the many points used and hence was extended to the axes.

Table 4.1 summarizes the differential analysis at each heating rate which gave apparent activation energies that are relatively insensitive to heating rate and higher than the other methods. The range of conversion and temperatures is shown since beyond these ranges, the curves start to deviate from linearity

possibly due to interferences of secondary reactions at higher conversions, as confirmed by the formation of ~3% solid residue by P-*m*Ph-P, and due to evaporation and fluctuations without significant weight loss at lower temperatures. The apparent activation energy values show a slight increase as the heating rate increases. The error bands shown are from the regression analysis of each fit which showed a very good linearity. An interesting observation is that the average of E from these heating rates (from 1–100 °C/min) gives an apparent E of 202 kJ/mol which is almost the same as the one predicted at 10 °C/min (201 kJ/mol), further supporting the accuracy of the 10 °C/min measurements.

Table 4.1 Summary of the differential calculation of kinetics of P-*m*Ph-P at various heating rates

β (°C/min)	X% Range	T range (°C)	E (kJ/mol)	Log (A(min ⁻¹))	R ²
1	18.0–50.0	362–388	179 ± 0.5	13.0 ± 0.04	0.998
5	21.0–55.0	405–432	193 ± 1	13.6 ± 0.05	0.999
10	19.1–49.2	418–444	201 ± 1	14.1 ± 0.09	0.998
50	20.1–65.7	478–516	219 ± 1	14.9 ± 0.05	1
100	17.2–53.9	468–506	220 ± 3	15.0 ± 0.2	0.999

The average kinetics at 10 °C/min from two repeated runs for cracking of P-*m*Ph-P gave an E of 202 kJ/mol and $\log(A, \text{min}^{-1})$ of 14.15. These values predict a conversion level of 28.9% at 395 °C isothermal reaction for 15 min. The microreactor experiment at an operating temperature of 395 °C for 15 min showed a conversion level of 28.8% as measured by HPLC, consistent with the reaction

rate observed in the TGA. Since many combinations of A and E can give the same reaction rate, comparing the conversion predicted by other methods to the experimental value further supports their inaccuracy. The kinetics calculated by the differential method at 1, 5, 50, and 100 °C/min, and by peak temperature of equation 4.2 and 4.3, and by Friedman isoconversional method at $X = 0.3$ predict P-*m*Ph-P conversion at 395 °C for 15 min to be 76.3, 36.5, 7.7, 8.5, 44.6, 76.2, and 57.7%, respectively. All these predictions are totally different than the experimental value of 28.8% and hence the most accurate kinetics is the one calculated at 10 °C/min, with the kinetics at 5 °C/min still giving close –within experimental errors– results.

To ensure the accuracy of calculations of the differential approach and to compare it with the peak temperature and isoconversional methods, variable heating rates were done for another model compound, which is P-Th-P at a β of 1, 10, 20, and 50 °C/min. The results are shown in **Table 4.2**. The same observations made for P-*m*Ph-P appeared with P-Th-P. The differential E was much higher than those predicted with the isoconversional or peak temperature methods. Equation (4.5) of the peak temperature also shows comparable results to the differential values. From these two model compounds, the differential approach shows much better linearity and more accurate results compared to the very low values measured by the isoconversional and peak temperature methods.

Since similar bonds from different molecules usually break similarly giving comparable kinetics, a further check to the accuracy of the differential approach is to react series of model compounds that have similar chemical structures.

Table 4.2: Kinetic parameters from the three methods for P-Th-P

Method	E (kJ/mol)	$\text{Log}(A(\text{min}^{-1}))$	R^2
Differential Method			
Heating rate, β (°C/min)			
1	258 ± 1^a	19.3 ± 0.05	0.999
10	247 ± 1^a	18.1 ± 0.06	1
20	268 ± 1^a	19.4 ± 0.06	1
50	258 ± 3^a	18.0 ± 0.2	0.998
Peak Temperature^b			
k vs. $1/T_p$	137	9.85	0.952
β/T_p^2 vs. $1/T_p$	149	10.5	0.971
k vs. β/T_p^2	241		0.968
Isoconversional^c			
Friedman	135– 145	9.24– 10.4	0.955– 0.964
KAS/V	137– 144		0.967– 0.965
OFW	140–148		0.972–0.970
Starink	137– 144		0.967– 0.965

^a E estimation over temperature ranges of 367–381, 398–425, 413–448, and 456–490°C for β of 1, 10, 20, and 50 °C/min, respectively. ^bUnits for $k(-dW/dt/W)$, T_p , and β are min^{-1} , K, and K/min, respectively. ^cThe values of E , $\log(A)$, and R^2 correspond to a conversion level of 0.1 – 0.5, respectively.

The only difference between these compounds used in the study is the middle function group between the two ethyl-pyrenyl groups. The first bond that is likely to crack in such structures is the weak C–C bond in the ethano bridges between the pyrene group and the central aromatic group. Large amounts of 1-methylpyrene were formed supporting this hypothesis as evident in the GCMS results of P-*m*Ph-P microreactor experiment analysis. Although the GCMS analysis showed also the formation of pyrene, this compound cannot form from primary reactions at such low temperatures and was likely formed by secondary

reactions such as the radical hydrogen transfer mechanisms as explained by Freund et al.⁷ (the mechanism of pyrene formation will be addressed in details in Chapter 5). **Figure 4.11** shows the measured E for the 9 pyrene-based model compounds at 10 °C/min that are expected to crack similarly. The boiling points on the x-axis were estimated from the Marrero and Gani¹² group additivity method. The results are within a narrow band of 200–250 kJ/mol, which suggests that the low E values measured by the conventional peak temperature and isoconversional methods are inaccurate.

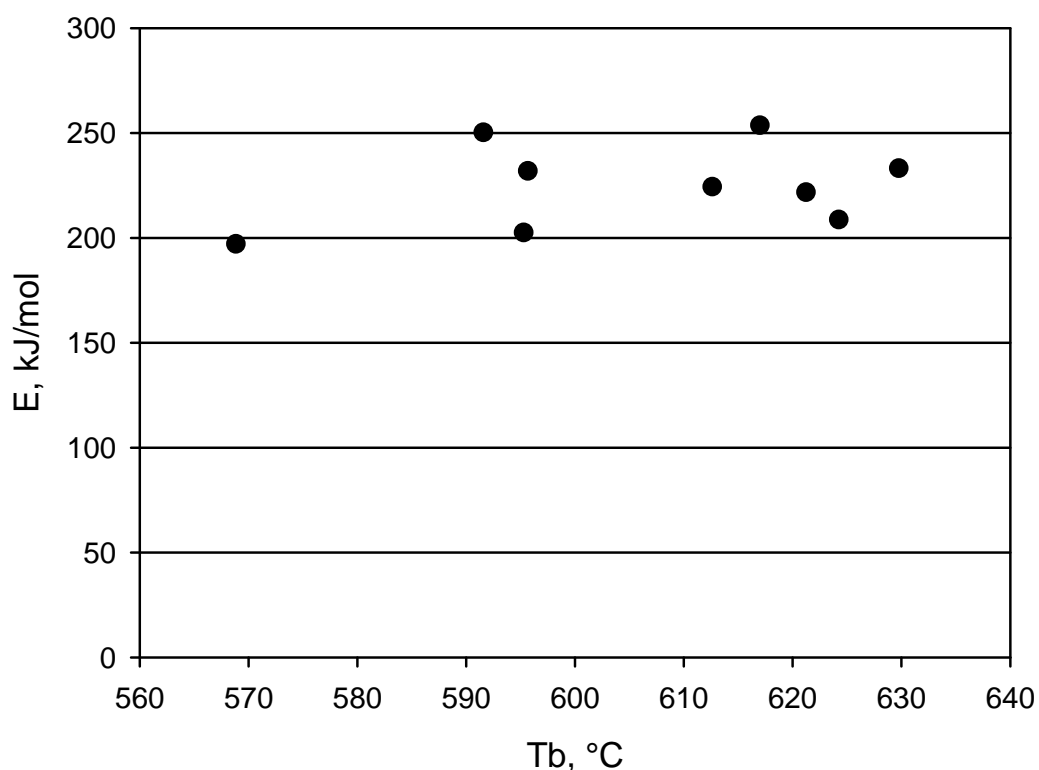


Figure 4.11: Average E for a series of pyrene-based model compounds. The central groups in these compounds in terms of increasing estimated boiling points are: 1,4-*n*Butyl, 2,5-thiophene, 1,3-benzene, 1,4-benzene, 5,5'-(2,2'-bithiophene), 2,8-dibenzofuran, 1,1'-(4,4'-biphenyl), 4,4'-(2,2'-bipyridine), and 2,7-(9,9-diethyl-9H-flourene).

A final check on the measured activation kinetics was from the literature on 1,2-diphenylethane (or bibenzyl) pyrolysis. This compound has an ethano bridge between aromatic groups and should show similar kinetics of cracking. Poutsma¹³ reviewed many literature sources for bibenzyl pyrolysis under both gas and liquid phase reactions. He reported for the liquid phase pyrolysis with tetralin carrier, which was used to capture benzyl radicals and prevent them from recombining or inducing decomposition of bibenzyl, a range of E from 201.3 – 279.6 kJ/mol and $\log(A, \text{min}^{-1})$ of 12.7–18.4. The excellent agreement between the measured kinetics of the differential approach and the literature on bibenzyl kinetics further support their accuracy.

4.5 CONCLUSIONS

Pyrene-based model compounds were thermally cracked in a thermal gravimetric analyzer (TGA) in order to measure their cracking kinetics. The kinetic parameters were calculated using two forms of the peak temperature method and four model-free isoconversional methods. The calculated values showed very low apparent activation energy compared to the values measured by the differential approach, which utilizes the Arrhenius equation to plot the normalized weight derivative with time versus $1/T$ over a specific range of temperatures. The differential kinetics successfully predicted the conversion of a microreactor experiment and were comparable to both the kinetics of a series of pyrene-based model compounds and to the values reported in the literature for bibenzyl pyrolysis, which has structural similarities to the pyrene-based model

compounds. A third form of the peak temperature method was shown to give more accurate results compared to the conventionally used two forms. Based on these experimental observations, it was concluded that the peak temperature and isoconversional methods are very sensitive to experimental errors and calibrations as suggested by many authors¹⁴ and may not be appropriate for kinetic measurements. On the other hand, successful kinetic measurements can be achieved via TGA with high-boiling model compounds using the differential method at 10 °C/min heating rate.

4.6 REFERENCES

1. Fox, D. M.; Gilman, J. W.; De Long, H. C.; Trulove, P. C., TGA decomposition kinetics of 1-butyl-2,3-dimethylimidazolium tetrafluoroborate and the thermal effects of contaminants. *J. Chem. Thermodyn.* **2005**, 37, 900-905.
2. Wang, H., kinetic analysis of dehydration of a bituminous coal using the TGA technique. *Energy Fuels* **2007**, 21, 3070-3075.
3. Liu, H., Combustion of Coal Chars in O₂/CO₂ and O₂/N₂ mixtures: A comparative study with non-isothermal thermogravimetric analyzer (TGA) tests. *Energy Fuels* **2009**, 23, 4278-4285.
4. Miranda, R.; Yang, J.; Roy, C.; Vasile, C., Vacuum pyrolysis of PVC I. Kinetic study. *Polym. Degrad. Stab.* **1999**, 64, 127-144.
5. Olmstead, W. N.; Freund, H., Thermal Conversion Kinetics of Petroleum Residua. *AIChE 1998 Spring National Meeting, New Orleans, LA* **1998**.
6. Burnham, L.; Dollimore, D.; Alexander, K. S., Kinetic study of the drug acetazolamide using thermogravimetry. *Thermochim. Acta* **2002**, 392-393, 127-133.
7. Freund, H.; Matturro, M. G.; Olmstead, W. N.; Reynolds, R. P.; Upton, T. H., Anomalous side-chain cleavage in Alkylaromatic Thermolysis. *Energy Fuels* **1991**, 5, 840-846.
8. Redhead, P. A., Thermal Desorption of Gases. *Vacuum* **1962**, 12, 203-211.
9. Falconer, J. L.; Schwarz, J. A., Temperature -Programmed Desorption and Reaction. *Catal. Rev. - Sci. Eng.* **1983**, 25, 141-227.

10. Aguado, R.; Olazar, M.; Velez, D.; Arabiourrutia, M.; Bilbao, J., Kinetics of scrap tyre pyrolysis under fast heating conditions. *J. Anal. Appl. Pyrolysis* **2005**, 73, 290-298.
11. Rivas, B. L.; Pizarro, G. d. C.; Catalan, R. E.; Tagle, L. H., Thermal degradation and determination of kinetic parameters by dynamic thermogravimetry of copolymers synthesized without initiator. *Thermochim. Acta* **1991**, 188, 163-172.
12. Marrero, J.; Gani, R., Group-contribution based estimation of pure component properties. *Fluid Phase Equilib.* **2001**, 183, 183-208.
13. Poutsma, M. L., Free-Radical Thermolysis and Hydrogenolysis of Model Hydrocarbons Relevant to Processing of Coal. *Energy Fuels* **1990**, 4, 113-131.
14. Brenner, A.; Hucul, D. A., Experimental errors in the application of temperature-programmed desorption to practical catalysts. *J. Catal.* **1979**, 56, 134-138.

CHAPTER 5

EFFECTS OF CHEMICAL STRUCTURE ON CRACKING AND COKING OF ARCHIPELAGO MODEL COMPOUNDS OF ASPHALTENES

5.1 INTRODUCTION

As summarized in detail in Chapter 2, aromaticity was suggested by Wiehe^{1, 2} to drive components to undergo liquid–liquid phase separation followed by rapid cross–linking reactions that eventually lead to coke formation. While Wiehe focused only on aromaticity as a driving force for phase separation, oligomerization, as shown in Chapter 3 for the formation of alkyl–bridged structures, is a second driving force, and any combination of these two motifs may also drive components across the phase boundary suggested by Wiehe.³

In Chapter 3, the chemical structures and yields of addition products formed during the thermal cracking of four model compounds that serve as models of asphaltenes were described by employing a number of analytical techniques. In this chapter, the reactions of a wide range of pyrene–based model compounds are

examined in more depth, in order to understand the pathways and kinetics of both cracking and coking reactions. The set of available compounds allows examining the impact of the aromatic and heteroaromatic groups on the kinetics of cracking, the pathways for the cracking reactions, and the formation of coke residue. The quantities of these compounds, and the number of compounds of interest, precluded the development of detailed kinetic models. Rather, the objective is to compare these model compounds against each other in order to understand the role of hydrocarbon versus heterocyclic aromatic rings in the cracking and coke formation processes. Reported here are the studies on a homologous series of compounds with three aromatic systems joined by ethano bridges, with a general structural motif represented as *pyrene-(C₂H₄)-A-(C₂H₄)-pyrene*, or *P-A-P* for short, where *A* is an aromatic group that may contain sulfur, nitrogen or oxygen.

5.2 MATERIALS AND METHODS

The model compounds used in this study were synthesized to incorporate sub-structures known to be present in asphaltenes.⁴ The synthetic procedures for three compounds in this series (P-*m*Ph-P, P-3,5-pyr-P, P-Th-P) were reported previously,^{5, 6} and the remaining compounds were synthesized in an analogous fashion from the corresponding dibromo- or diiodohaloarene. **Figure 5.1** shows the general structure of the model compounds, as well as the structure of one specific example; the structures of all other model compounds are shown in **Table 5.1**.

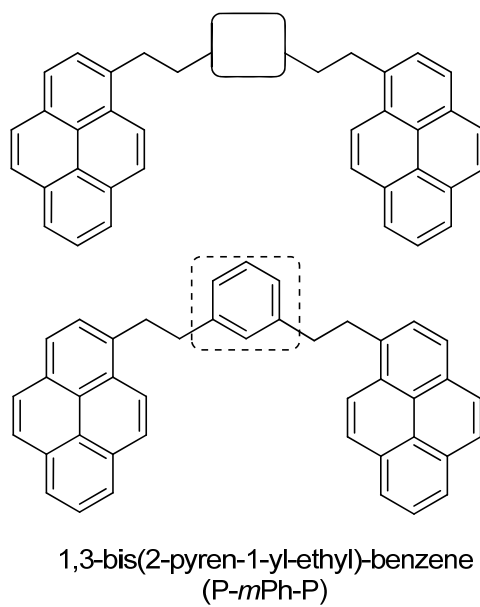
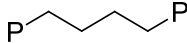
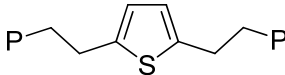
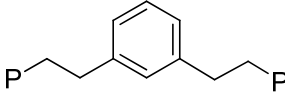
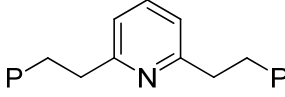
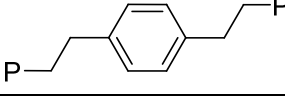
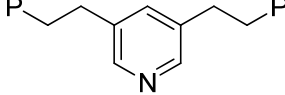
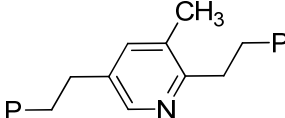
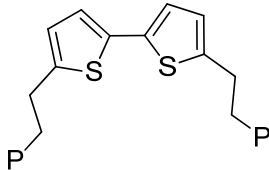
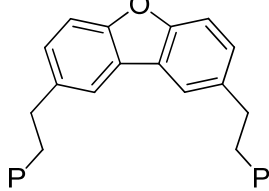
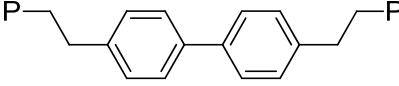


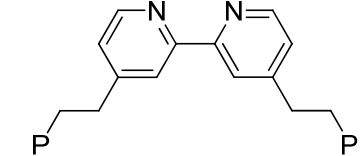
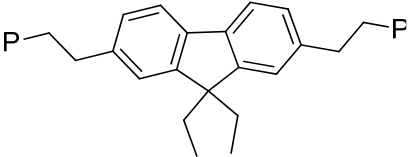
Figure 5.1: The general structure of the pyrene-based model compounds (top) with one specific example (bottom). The complete list of the archipelago model compounds is shown in **Table 5.1**.

Phenanthrene, pyrene, and benzo[a]pyrene (BP), used either in the response factor calculation or in the binary experiments, were obtained from commercial suppliers and used as received. Methylene chloride and methanol used in product extraction and in HPLC analysis were HPLC and ACS grade, respectively and were used as received from commercial suppliers. Gases in TGA, GC-FID, and GCMS were from PRAXAIR and were of a high purity grade.

Since these compounds were synthesized in limited quantities, experiments that require minimal amounts were desired. Hence, thermogravimetric analysis (TGA) was chosen to compare the coke yield and cracking kinetics of the model compounds, followed by microreactor experiments of selective samples.

Table 5.1: The archipelago model compounds, molecular weights, and estimated boiling points

Model Compounds ¹	Name	Molecular weight (g/mol)	Estimated boiling point ² (°C)
	1,4-dipyren-1-yl-butane (P- <i>n</i> But-P)	458.59	569
	2,5-Bis(2-pyren-1-yl-ethyl)-thiophene (P-Th-P)	540.71	592
	1,3-Bis(2-pyren-1-yl-ethyl)-benzene (P- <i>m</i> Ph-P)	534.69	595
	2,6-Bis(2-pyren-1-yl-ethyl)-pyridine (P-2,6-Pyr-P)	535.67	595
	1,4-Bis(2-pyren-1-yl-ethyl)-benzene (P- <i>p</i> Ph-P)	534.69	596
	3,5-Bis(2-pyren-1-yl-ethyl)-pyridine (P-3,5-Pyr-P)	535.67	599
	2,5-Bis(2-pyren-1-yl-ethyl)-3-methylpyridine (P-2,5-Pyr-3-Me-P)	549.7	601
	5,5'-Bis(2-pyren-1-yl-ethyl)-2,2'-bithiophene (P-BiTh-P)	622.84	613
	2,8-Bis(2-pyren-1-yl-ethyl)-dibenzofurane (P-DBF-P)	624.77	617
	1,1'-Bis(2-pyren-1-yl-ethyl)-4,4'-biphenyl (P-BiPh-P)	610.78	621

	4,4'-Bis(2-pyren-1-yl-ethyl)-2,2'-bipyridine (P-B-P)	612.76	624
	2,7-Bis(2-pyren-1-yl-ethyl)-9,9-diethyl-9H-fluorene (P-F-P)	678.9	630

1: P represents a 1-pyrenyl group

2: Estimated by group additivity method of Marrero and Gani⁷

The experiments were done on a Thermo Cahn TherMax400 TGA (Thermo Electron Corporation, Waltham, MA). In a typical procedure, 4–5 mg of the sample was loaded on a platinum pan and was heated at 10 °C/min to 500 °C, and the temperature was then held at 500 °C for 15 min to obtain an approximate value of the micro-carbon residue (MCR) content. Inert conditions were maintained throughout the experiment by using Argon gas flowing at 80 mL/min with a separate purging flow through the balance chamber at high flow rate to prevent condensation of products on the hanging wire or the delicate balance.

The microreactor experiments were carried out in a stainless steel tubular reactor, 5 mm in diameter and 5 cm in length, attached to a high temperature valve with a 1 mm inner diameter and 9 cm tube, connected and capped with Swagelok fittings. In a typical experiment, 2–3 mg of the sample was loaded inside a 3 × 45mm one-end-sealed glass tube. The reactor was purged with nitrogen, closed, and heated in a fluidized sand bath for the duration of the experiment with continuous shaking by a rotary motor. At the end of the experiment, the reaction was stopped by immersion in cool water and the products

were extracted with methylene chloride and concentrated using a rotary evaporator. Binary experiments with BP were performed with P-*p*Ph-P and P-*m*Ph-P using the same reactor and procedures; except that no glass liner was used in the case of P-*m*Ph-P, which appeared to have no effect on the results in this particular case.

Products of the cracking reactions were quantified using a Thermo Scientific Trace GC Ultra gas chromatography–flame ionization detector (GC–FID), with identification of the corresponding peaks achieved by using a DSQII mass spectrometer (both from Thermo Electron Corporation, Waltham, MA). The GC oven is typically set at 100 °C for 1 min followed by a continuous ramping at 10 °C/min to a final temperature up to 350 °C. Helium was used as the carrier at 2 mL/min in a split mode in the GC–FID and splitless in GC-MS. The columns were either TR5 or TR5–MS of 15 m × 0.25 mm × 0.1 µm or 7 m × 0.32 mm × 0.25 µm.

High performance liquid chromatography (HPLC) analysis (Agilent Technologies, Santa Clara, CA) was performed using a Zorbax Eclipse PAH column of 4.6 × 150 mm with a C18 phase of 3.5 µm particles. The mobile phase for HPLC was optimized for each model compound and typically the flow was isocratic at 1 mL/min with 70–80% methanol and 30–20% methylene chloride (MC). Gradient flow rates were used in the separation of the pyrolysis products of P-3,5-pyr-P and P-BiTh-P only. In P-3,5-pyr-P, the flow was 70% methanol / 30% MC at 0.5 mL/min for 5 min followed by ramping to 1 mL/min from 5–6 min. For P-BiTh-P, the flow was 65% methanol / 35% MC at 0.5 mL/min for 4

min followed by ramping to 3 mL/min from 4–5 min. The ultraviolet (UV) detector was set at either 239 or 270 nm.

Matrix assisted laser desorption/ionization–mass spectroscopy (MALDI–MS) and tandem MS/MS were performed using either Bruker Ultraflex extreme MALDI–TOF/TOF (Bremen, Germany) or Applied BioSystems Voyager Elite MALDI–TOF (Foster City, CA). DCTB, (mass = 250 Da), was used as the matrix for the MALDI analyses.

^1H nuclear magnetic resonance (NMR) spectroscopy (500 MHz Varian Inova, Santa Clara, CA) was done in CDCl_3 solution. NMR spectral analysis and simulation were performed using MestReNova software (Mestrelab Research, Santiago de Compostela, Spain).

The boiling points and the heats of formation at 298 K (ΔH_f°) for the model compounds were estimated using courtesy software provided by Gani that employs a number of group additivity methods such as the Marrero and Gani⁷ and Constantinou and Gani⁸ methods.

The cross–polarized light microscopy on a hot stage was performed using a Zeiss Axio-Observer inverted reflective microscope. The sample was observed through a window and photos were captured while the sample was being heated from ambient temperature up to 450 °C at 5–10 °C/min under inert atmosphere of nitrogen. Further details on the cross–polarized light experiments can be found elsewhere.⁹

5.3 RESULTS

5.3.1 TGA Results

All the model compounds showed little weight loss due to evaporation of solvents or impurities, with an average weight loss before 200 °C of 2.9%, and only pyridyl compounds P-3,5-pyr-P, P-2,5-pyr-3-Me-P, and P-2,6-pyr-P lose greater than 2% (losses of 4.7, 7.1, and 8.7%, respectively). The yield of coke was adjusted for mass losses before 200 °C, since no appreciable cracking is expected at such low temperatures. The onset of cracking, defined as the temperature at which 5% of corrected weight was lost (i.e. 5% weight loss after 200 °C), was high in all the cases with a minimum of 325 °C and an average of 380 °C, which confirms that these compounds did not evaporate prior to reaching the onset of cracking.

A typical curve of weight loss and temperature versus time is shown in **Figure 5.2**. The apparent activation energy of cracking (E) by first-order kinetics, calculated using a differential approach of normalized weight loss versus temperature as shown in Chapter 4, fell within a narrow range of ~190–250 kJ/mol (45–60 kcal/mol) for all the model compounds except P-3,5-pyr-P which gave 140 kJ/mol. The low value for this compound was not due to the presence of contaminants from the synthesis, because extensive purification and the examination of alternative samples of P-3,5-pyr-P gave no change in the coke yield or the cracking kinetics. Although the observed kinetics were consistent with cleavage of the ethano bridge, no trend was observed between the chemical structure and reaction kinetics based on the initial weight loss.

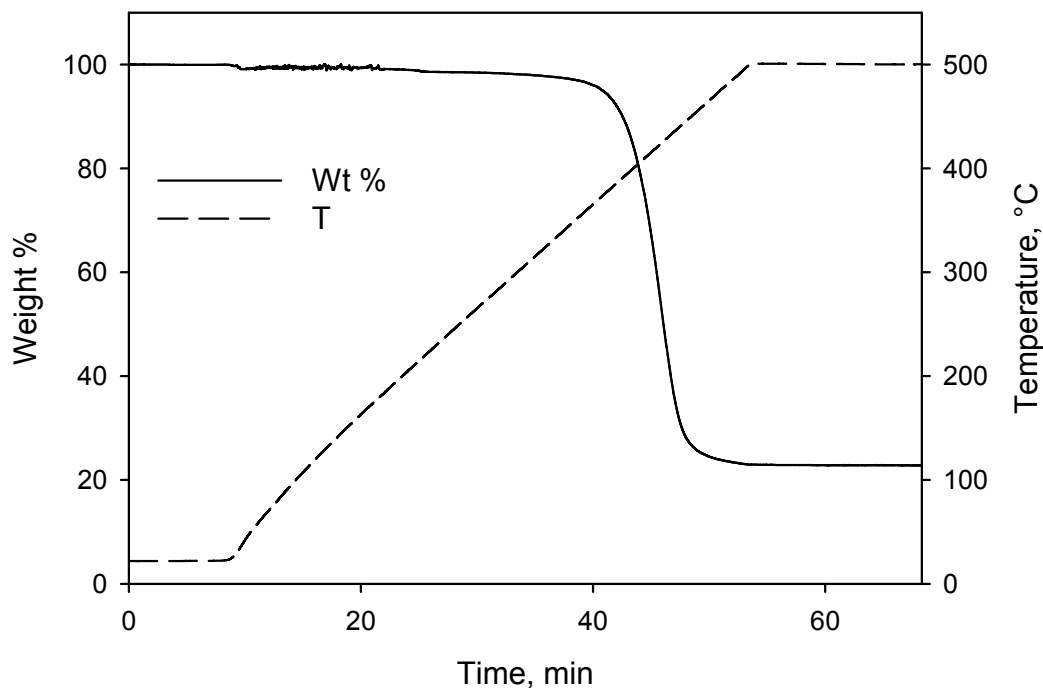


Figure 5.2: Typical curves of weight loss and temperature versus time in the TGA experiments showing the high stability of these model compounds before the onset of cracking. This curve is for P-BiTh-P after 5 min hold up at ambient temperature followed by a 10 °C/min ramp to 500 °C and a final isothermal hold up for 15 min.

Solid residue was observed for all model compounds at the end of TGA experiments at 500 °C. This solid residue was insoluble in organic solvents, and it was thus termed coke. At least two experiments were done for each compound to confirm repeatability. The coke yields from the duplicate runs were similar, with a typical deviation from the mean less than 1 wt%. To get a better statistical estimate, four replicates were performed on P-2,5-pyr-3Me-P, which gave a standard deviation from the mean of only 0.2 wt%. These replicate experiments were done using a different synthesis batch than the purer sample plotted in **Figure 5.3**, and hence no error bars are given for this sample.

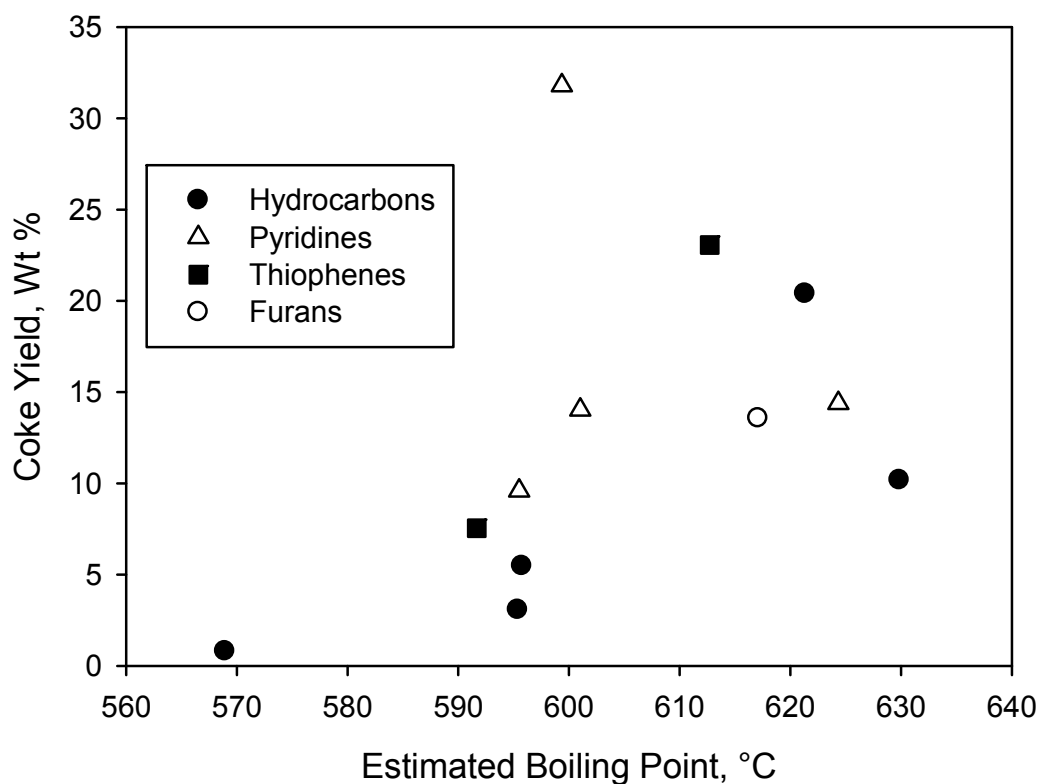


Figure 5.3: Coke yield for all the model compounds versus the estimated boiling points.

The data of **Figure 5.3** show a plot of coke yield versus estimated boiling point, and the lack of any systematic relationship indicates that evaporation of the sample was not likely significant. Thus, chemical behavior of the samples likely provides the key to understanding coke formation, and the chemistry of the central aromatic group and the location of the bridge groups are clearly important in coke formation. For example, replacing the phenyl ring of P-*m*Ph-P with a pyridyl to give P-3,5-pyr-P, increases the coke yield by 10 fold (from nearly 3% to over 30%). Shifting the attachment point of the ethano bridge on the pyridine ring, from P-3,5-pyr-P to P-2,6-pyr-P, decreased the coke yield from over 30% to only 10 wt%. Unfortunately, the solid coke residue from the TGA measurements

could not be analyzed for information on molecular structure, and the cracked products could not be recovered. Microreactor experiments were therefore used to define the main reaction pathways and explore the roles played by the central group in altering the coke yield.

5.3.2 Microreactor Experiments

The objective of the microreactor experiments was to identify the cracking products and to examine the addition products that served as precursors to the coke residue. Six representative model compounds were selected for these experiments, including hydrocarbons (P-*m*Ph-P, P-*p*Ph-P), pyridyl (P-2,6-pyr-P, P-3,5-pyr-P) and thienyl (P-Th-P, and P-BiTh-P) derivatives. This set of compounds was chosen to examine the effect of heteroatom versus hydrocarbons substitution, as well as the effect of minor structural changes in which the difference was only in the linkage points (e.g. P-2,6-pyr-P versus P-3,5-pyr-P or P-*p*Ph-P versus P-*m*Ph-P). In addition, two of these compounds (P-3,5-pyr-P and P-BiTh-P) were reacted for different times and temperatures to track the changes in the yield of cracked and addition products as the conversion was increased. Experimental conditions, percent conversion (X), and the HPLC recovery weight % are shown in **Table 5.2**. The percent conversion (X) is defined as the difference between the initial and final weights of the parent, divided by the initial weight. The HPLC recovery is not the total weight balance, but rather the amount of products detectable by HPLC analysis; the remainder of the materials would be cracked or addition products outside the range of elution and detection (i.e., compounds which may not elute, have weak absorbance in the UV region, or are

present at low concentrations), the existence of which was verified by GC–MS and MALDI–MS, respectively. Hence, as the conversion increases, the HPLC recovery decreases; consistent with formation of more addition products.

Table 5.2: List of microreactor experiments, with conversion, and HPLC recovery.

Model Compound	Reaction Conditions	Conversion %	HPLC Recovery ¹ , Wt%
P- <i>m</i> Ph-P	400 °C – 15 min	28.8	79
	R2-400 °C – 15 min	29.6	84
P- <i>p</i> Ph-P	400 °C – 15 min	26	81
P-2,6-pyr-P	390 °C – 20 min	53	63
P-3,5-pyr-P	350 °C – 20 min	16	92
	365 °C – 20 min	25	86
	390 °C – 20 min	69	62
P-Th-P	385 °C – 25 min	90	58
P-BiTh-P	365 °C – 20 min	61	85
	378 °C – 20 min	84	52
	400 °C – 20 min	98	35 ²

1: This does not represent the overall mass balance but rather the amount recovered from HPLC analysis only. The reminder would be higher molecular weight addition products with poor elution and detection by the HPLC instrument

2: Solid insoluble materials formed

Due to limits of material available, the microreactor experiments were performed only once and hence no statistical error estimates are given. The repeatability of the experiments was, however, verified by a second experiment of P-*m*Ph-P, where the conversion was within 1% for the two experiments (**Table 5.2**). In addition, the agreement between the predicted conversion of P-*m*Ph-P, from the TGA cracking kinetics as reported in Chapter 4, and the experimental results at low conversion levels in the microreactor establishes the consistency of the measurements. The reaction conditions were selected to achieve different

conversion levels, or to compare two compounds to each other at the same conditions; a full kinetic analysis on each model compound was not possible, again due to the limited availability of purified model compounds.

5.3.2.1 Cracked Products

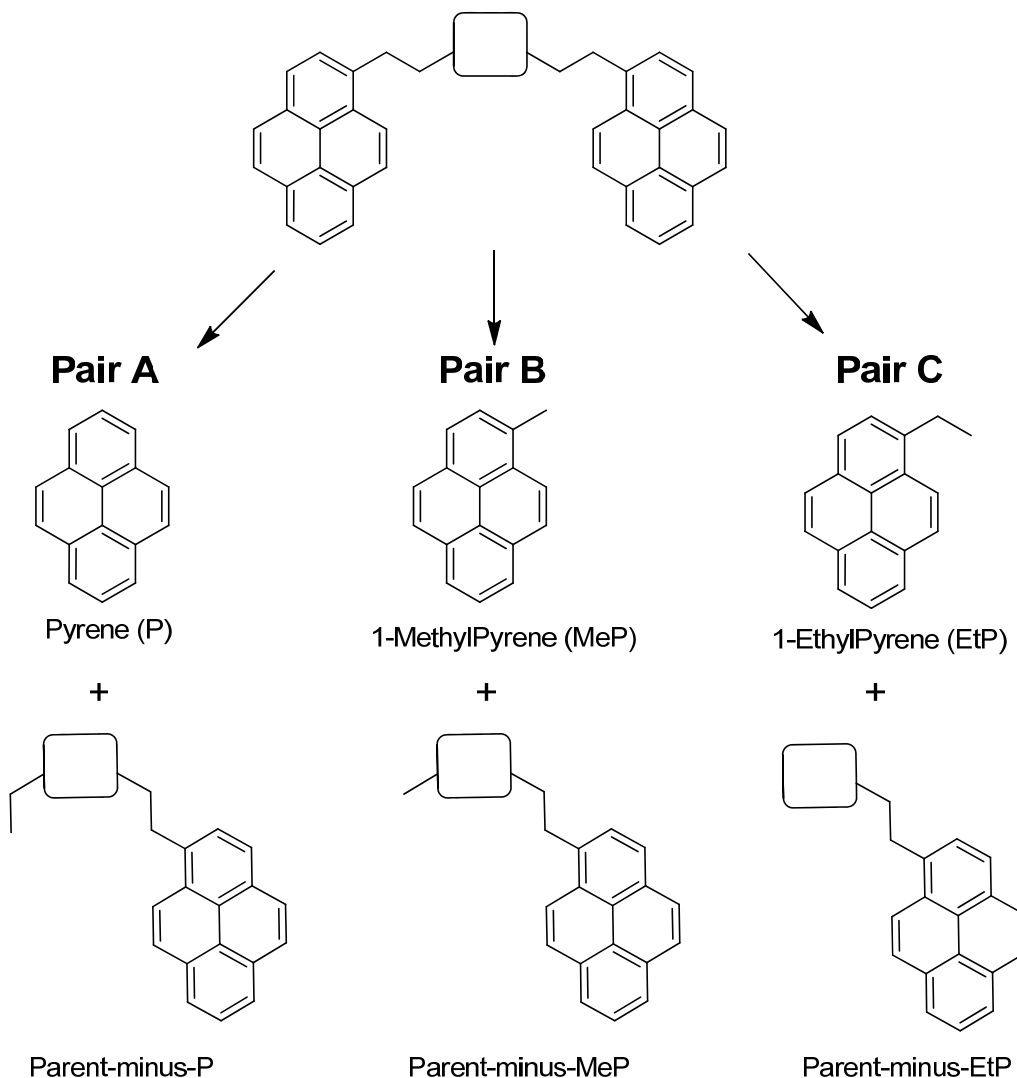


Figure 5.4: The three major pairs, A, B, and C, of cracked products formed by the tested archipelago compounds in the microreactor experiments.

The cracked products, defined as the products with molecular weights smaller than the starting compound, were formed in three major pairs of products

that differed in the position of the cleavage of the ethano bridge, as illustrated in **Figure 5.4 (Pairs A–C)**. Other minor cracked products include dimethylpyrene, methylethylpyrene, propylpyrene, and dehydrogenated (olefinic) fragments of the cracked products shown in **Figure 5.4**. In the case of the most reactive compound, P-BiTh-P, additional minor products were observed, including 1) bithiophene, from cleavage of the ethano bridge at the 5- and 5' positions, 2) products resulting from cleavage of the central bond connecting the two thienyl groups, as well as 3) small amounts of dimethyl-, methylethyl-, and diethylbithiophenes.

The molar selectivity for the major cracked products, defined as the moles of product formed from decomposition of 100 moles of model compound in the microreactor experiments, are shown in **Table 5.3**. The most abundant cracked product in all cases was 1-methylpyrene (MeP). **Figures 5.5 and 5.6** show the continuous increase in yield of MeP as the conversion for P-3,5-pyr-P and P-BiTh-P is increased, respectively. This product would result from the homolysis of the weak C–C bond of the ethano bridge followed by hydrogen abstraction. In addition to the primary route for the formation of MeP, secondary reactions, such as β -scission of radicals formed by addition reactions, could lead to its formation.

The hydrocarbon compounds, P-*m*Ph-P and P-*p*Ph-P, formed pyrene (P) and Parent-minus-MeP as the second and third most abundant cracked products, respectively. This trend was reversed for all the heteroatom island compounds, where the Parent-minus-MeP and P are the second and third major cracked products, respectively. The exception to this trend was the reaction of P-BiTh-P that was carried on to nearly complete conversion (98.2%), and in this case

Parent-minus-MeP dropped to be the third most abundant cracked product, behind MeP and P.

Table 5.3: Moles of major cracked products per 100 moles of converted model compound

Compound X% ^a	Pyrene (P)	Methylpyrene (MeP)	EthylPyrene (EtP)	Parent minus EtP	Parent minus MeP	Parent minus P
P- <i>m</i> Ph-P ^b 29.2	25.2	26.3	0.6	0.3	13.0	5.5
P- <i>p</i> Ph-P 26	14.1	22.4	nd ^c	0.4	14.0	3.9
P-2,6-pyr-P 53	6.6	36.0	0.6	0.1	15.4	0.8
P-3,5-pyr-P 16	4.1	24.3	1.1	1.9	5.3	0.2
P-3,5-pyr-P 25	4.2	28.2	0.9	1.2	7.8	0.4
P-3,5-pyr-P 69	5.7	31.0	0.8	0.6	6.1	0.6
P-Th-P 90	7.4	76.8	1.0	1.7	13.1	0.5
P-BiTh-P 61	2.4	41.2	0.4	1.7	8.8	nd ^c
P-BiTh-P 84	3.2	61.2	0.6	1.7	7.8	nd ^c
P-BiTh-P 98	4.5	62.8	0.6	0.7	2.0	nd ^c

^aConversion of parent compound from the corresponding reaction conditions listed in **Table 5.2**. ^bConversion and moles of cracked products are average of the two experiments performed at same conditions shown in **Table 5.2**. ^cNot detected

The decrease in molar yield of Parent-minus-MeP at high conversion of P-BiTh-P is consistent with the participation of this compound in secondary reactions, as evident from **Figures 5.5** and **5.6** where the molar yield reaches a maximum before declining again as a function of conversion. Formation of Parent-minus-P (indicative of the cleavage at the pyrene ring) thus prevails for the hydrocarbons, while the formation of Parent-minus-EtP (indicative of the cleavage at the central aromatic ring) is typically favored in heteroatomic species. Such striking results indicate the strong role played by central aromatic groups in affecting the cracking selectivity.

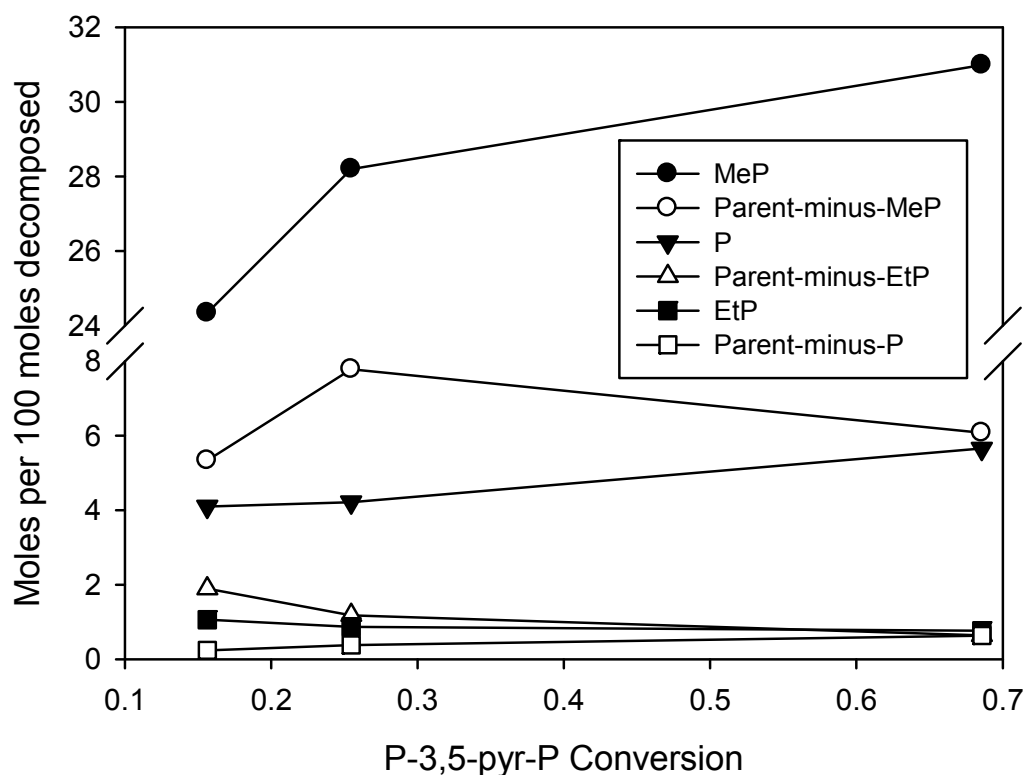


Figure 5.5: The molar yields for P-3,5-pyr-P experiments at different conversion levels.

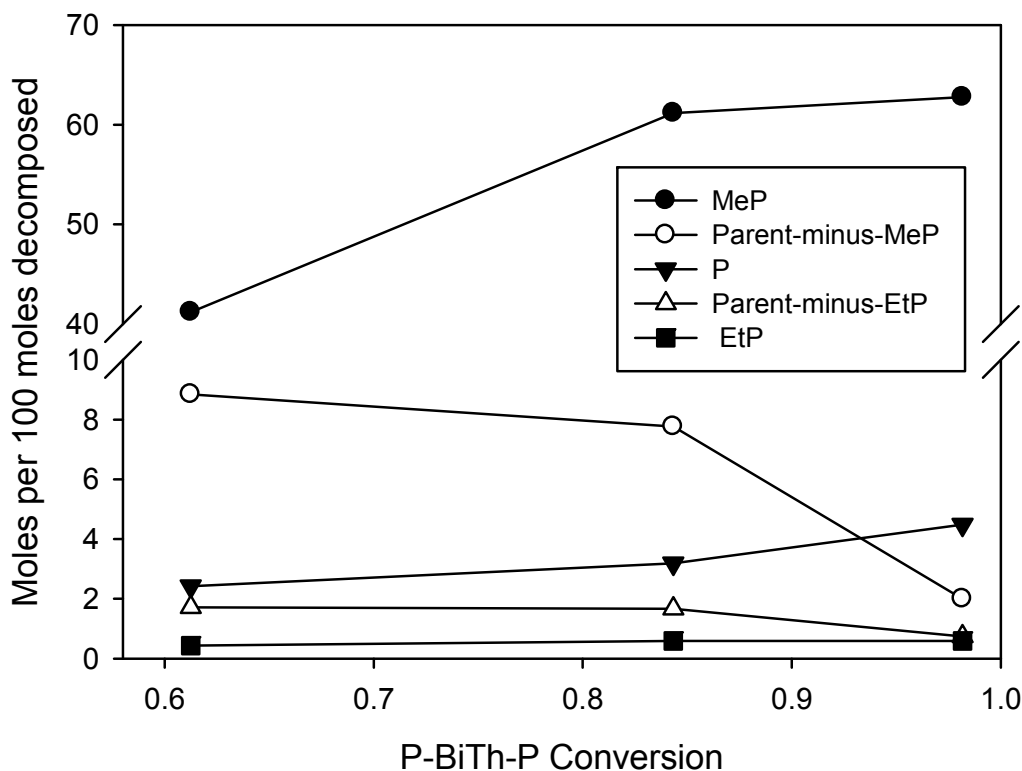


Figure 5.6: Molar yields for P-BiTh-P experiments at different conversion levels. Parent-minus-P was not detected and hence is not shown in the figure.

5.3.2.2 Addition Products

All of the model compounds showed significant yield of addition products based on MALDI-MS analysis. The structure of these addition products was dominated by an archipelago motif, resulting from mainly alkyl-alkyl addition reactions. More details of the quantitative yield and nature of the addition products formed by two of the compounds were reported in Chapter 3, using MS/MS and NMR to verify the location of bridging and, thus, addition within the products. Chapter 3 did not address the pathway to coking, but rather the nature and yield of addition products. It was hypothesized that addition products formed

at the early stages of a reaction are still reactive and would thus continue to undergo cracking and addition reactions toward larger structures. This hypothesis was verified by reacting P-3,5-pyr-P and P-BiTh-P at three conversion levels, and **Figures 5.7** and **5.8** show the MALDI mass spectra as a function of increased percent conversion of P-3,5-pyr-P and P-BiTh-P, respectively.

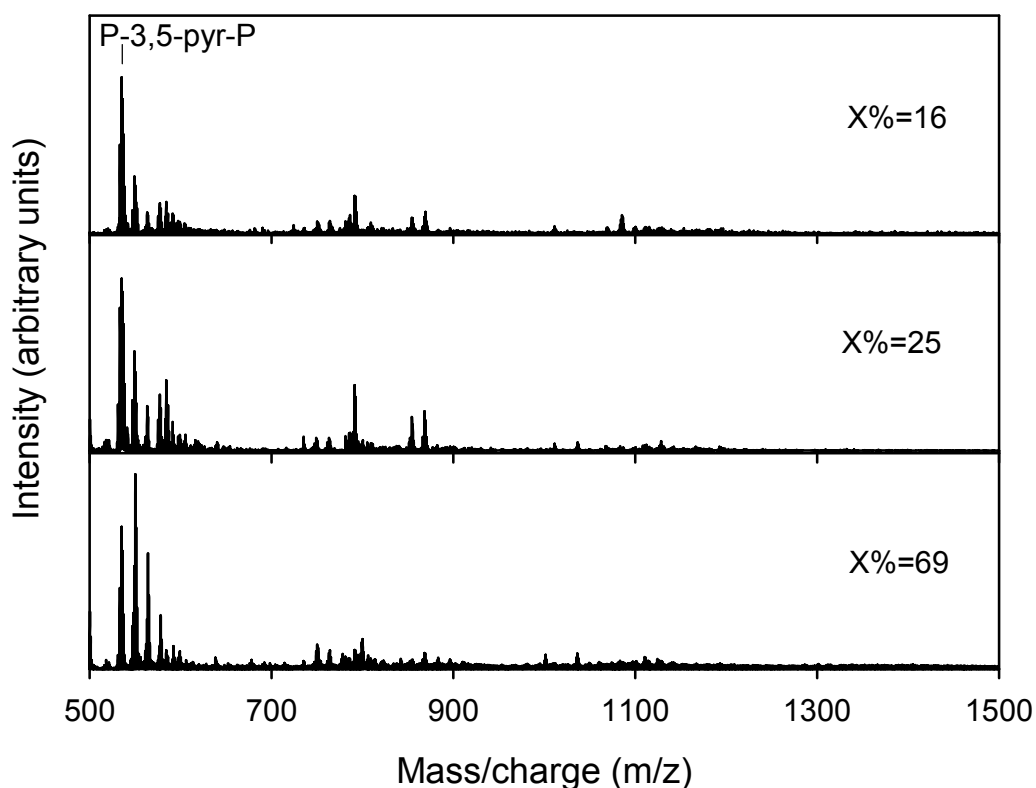


Figure 5.7: MALDI-MS spectra for P-3,5-pyr-P showing the addition product region as the conversion increases.

In **Figure 5.7**, the masses in the region of addition products (i.e., masses greater than the parent P-3,5-pyr-P) are shown at 16, 25, and 69% conversion. The addition products of low molecular weight (e.g., m/z 549) are formed early on at 16% conversion and the intensity continues to increase relative to P-3,5-pyr-P peak. The products at higher molecular weights (e.g., m/z 854 and 868), on the

other hand, increased at 25% conversion before declining again at 69% conversion. Similar trends are more visible in **Figure 5.8**, where the complete mass range measured by MALDI-MS is shown, including both the cracked products at $m/z > 300$ and the addition products.

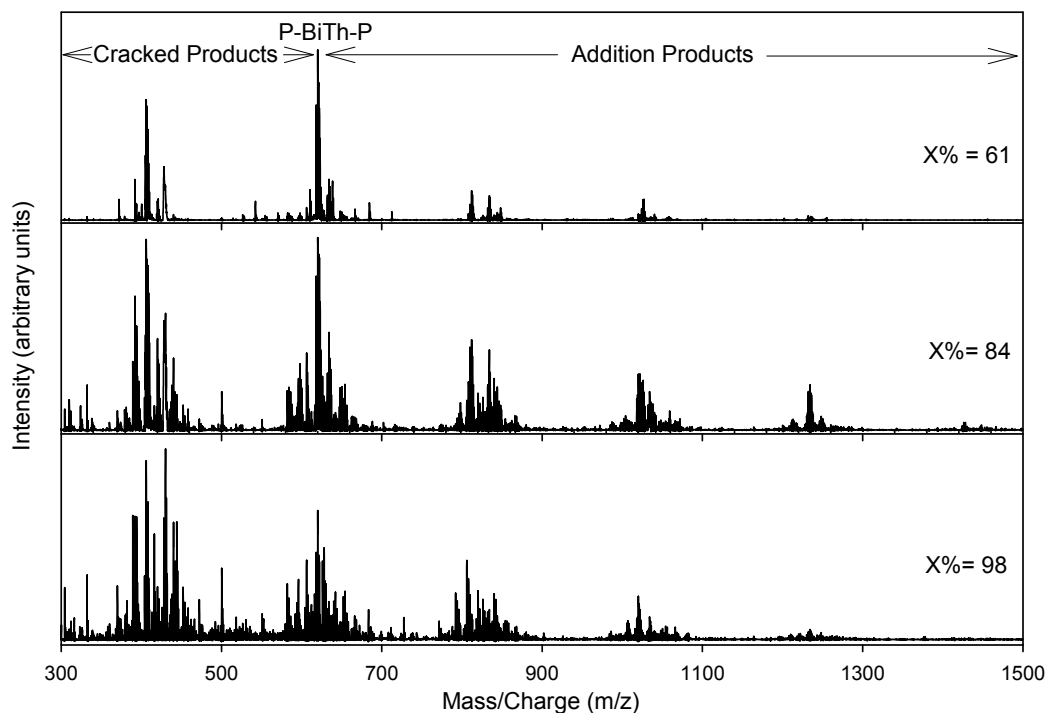


Figure 5.8: MALDI-MS spectra for P-BiTh-P at various conversion levels. New peaks appear as the conversion increases, consistent with the hypothesis that products formed at low conversion continue to crack and add to give lower and higher products, respectively.

MALDI-MS analysis of all but one of the model compounds before reaction showed no significant fragmentation of the parent compounds during analysis. The exception to this trend was P-BiTh-P, which showed the parent peak as the base peak of the spectrum (m/z 622), in addition to a fragment for the product of dehydrogenation of the parent at m/z 620 and a signal at m/z 407 for Parent-

minus-MeP fragment. Supporting the identity of the peak at m/z 407 was the signal of the dehydrogenated Parent-minus-MeP product at m/z 406, found in analysis of reaction products.

Several additional points relative to the MALDI-MS experiments are worth noting. 1) Adducts with the matrix, 250 Da, were insignificant in most of the model compounds, aside from the pyridyl derivatives. Matrix adducts with P-2,6-pyr-P and P-3,5-pyr-P were clearly distinguishable from the reaction products by comparing the parent spectra before reaction with the product mixtures, as well as by conducting tandem MS/MS analysis of suspicious peaks. Therefore, these instrumental artifacts are not significant and do not influence the conclusions drawn from this study. 2) The data of **Figures 5.7** and **5.8** confirm that the addition products that form at low conversion are not stable under the reaction conditions, and thus go on to participate in further cracking and addition reactions as conversion percentage increases. 3) Rearrangement and cyclization reactions are also possible under the reaction conditions, but such products cannot be clearly distinguished in the complex product spectra. 4) At 98% conversion of P-BiTh-P, the intensities of the signals above m/z 1300 are very low, which could be misinterpreted as lower yield of addition products, but the fact that methylene chloride-insoluble material, i.e. coke, formed suggests that there must be a significant yield of addition products of much higher molecular weights.

5.3.2.3 Binary Experiments with Benzo[a]pyrene (BP)

Experiments with addition of BP to two hydrocarbon model compounds (P-*p*Ph-P and P-*m*Ph-P) were used to probe the mechanism of decomposition, and to

investigate aryl–aryl and alkyl–aryl addition reactions. The hypothesis was that if the rate–limiting step for the formation of pyrene is a bimolecular process, e.g., a multistep or radical hydrogen transfer reaction, then diluting the reactant should decrease the rate of pyrene formation. For comparison, an experiment with pure BP was carried out at 400 °C for 15 min. The conversion of BP was only 3%, as measured with HPLC, with the major product detected being dihydrobenzopyrene and a trace of methylbenzopyrene, which probably arise from the trace impurities of the starting sample. MALDI–MS of BP (m/z 252) showed, among many other minor peaks, the formation of a BP dimer (bi-BP, m/z 502) and a smaller signal for a BP trimer (m/z 752). Unfortunately, the matrix used for the MALDI experiments has a molecular weight of 250 Da, which complicates verification of the observed peaks as genuine products, rather than adducts with the matrix, even with the use of tandem MS/MS. Nevertheless, the most important observation from the reaction of BP was that aryl–aryl addition reactions are not facile, even in the liquid phase at cracking conditions, giving only 3% conversion.

The results from microreactor reactions of the binary mixtures are listed in **Table 5.4**. Noticeably, the conversion of P-*m*Ph-P did not drop significantly, in spite of using a molar ratio of BP to P-*m*Ph-P as high as 5.6, suggesting that the rate–limiting step for the disappearance of P-*m*Ph-P is mainly unimolecular. Introducing a high concentration of a radical carrier, in this case BP, would be expected to give some reduction in the rate of any free radical chain reaction in proportion to the concentration of BP radicals as a fraction of the total number of radicals. In this case the small reduction in conversion of P-*m*Ph-P is consistent

with the relative ease of forming radical from P-*m*Ph-P by hydrogen abstraction in comparison to abstracting a hydrogen atom from BP. The conversion of BP was enhanced by the presence of the more reactive model compounds, increasing from 3% in the case of neat BP to 16% at the ratio of 0.57 moles BP per mol P-*m*Ph-P. The lack of conversion of BP at the ratio of 5.6 is likely due to the large amount of BP employed. Since the enhanced conversion of BP by the addition of P-*m*Ph-P at 0.57 ratio (from 3 to 16% conversion) indicates that BP molecules must be activated by coupling with the cracked products of the model compounds, then BP conversion at the high concentration of 5.6 ratio is expected to be very low because the fragments from the compounds are now much more diluted. Incomplete resolution of BP at this high concentration from other BP-like products in the HPLC analysis is also a contributing factor to the low estimate of the extent of conversion.

The normalized molar yields, defined as the moles of product formed divided by the moles formed without the presence of BP, are also given in **Table 5.4** and were plotted in **Figure 5.9** for the case of P-*m*Ph-P. When a small amount of BP was added to P-*m*Ph-P, the yield of all the cracked products increased. The greatest gain was in Parent-minus-EtP and pyrene, while the corresponding fragmentation products EtP and Parent-minus-P, respectively, did not increase at the same ratio. This observation suggests that the intermediates that retained the two-carbon chain (after cleavage of an aryl group) participated in secondary reactions. In contrast, both MeP and Parent-minus-MeP product yields were enhanced at the same ratio, which suggests that intermediates derived from

cleavage of the central ethylene bond ($\text{CH}_2\text{--CH}_2$) were equally likely to participate in secondary reactions. When the amount of BP was greatly increased from 0.57 to 5.6 mol / mol P-*m*Ph-P, the Parent-minus-EtP and pyrene were still the products with the largest enhancement, while the yield of products arising from other fragmentation patterns decreased. EtP was not detected at all. Under these conditions, the cleavage at pyrene as well as at the benzene ring appears more favored than in the absence of BP.

Table 5.4: Binary experiments of Benzo[a]Pyrene (BP) plus P-*m*Ph-P and P-*p*Ph-P model compounds at 400 °C – 15 min Reactions

Mixture		BP+ P- <i>m</i> Ph-P		BP+ P- <i>p</i> Ph-P
Ratio ¹		0.57	5.6	0.42
Compound X%		27	24	19
BP X%		16 ⁴	-0.2	5.2 ⁴
Recovery ² , Wt%		90	97	90
Normalized Molar Yield (moles formed / moles formed without BP ³)	P	2.3	1.8	1.2
	MeP	1.6	0.8	1.5
	EtP	1.2	nd ⁵	– ⁶
	Parent-minus-EtP	2.6	2.4	0.7
	Parent-minus-MeP	1.6	1.0	1.5
	Parent-minus-P	1.3	0.6	1.0

- 1: The ratio of moles BP added per mol of model compound
- 2: Based on total weight of model compound plus BP. Similar to **Table 5.2**, the recovery is the mass balance from HPLC only not the overall mass balance.
- 3: Molar yields of major cracked products without BP are shown in **Table 5.3**. To calculate the non-normalized molar yields of each compound, multiply the normalized yields with yields without BP shown in **Table 5.3**.
- 4: Average values of conversion measured from HPLC and from GC–FID.
- 5: Not detected
- 6: The molar yield of EtP was 0.4 mol/100 moles P-*p*Ph-P converted but the normalized ratio cannot be calculated since EtP was not detected from the reaction of P-*p*Ph-P without BP (**Table 5.3**)

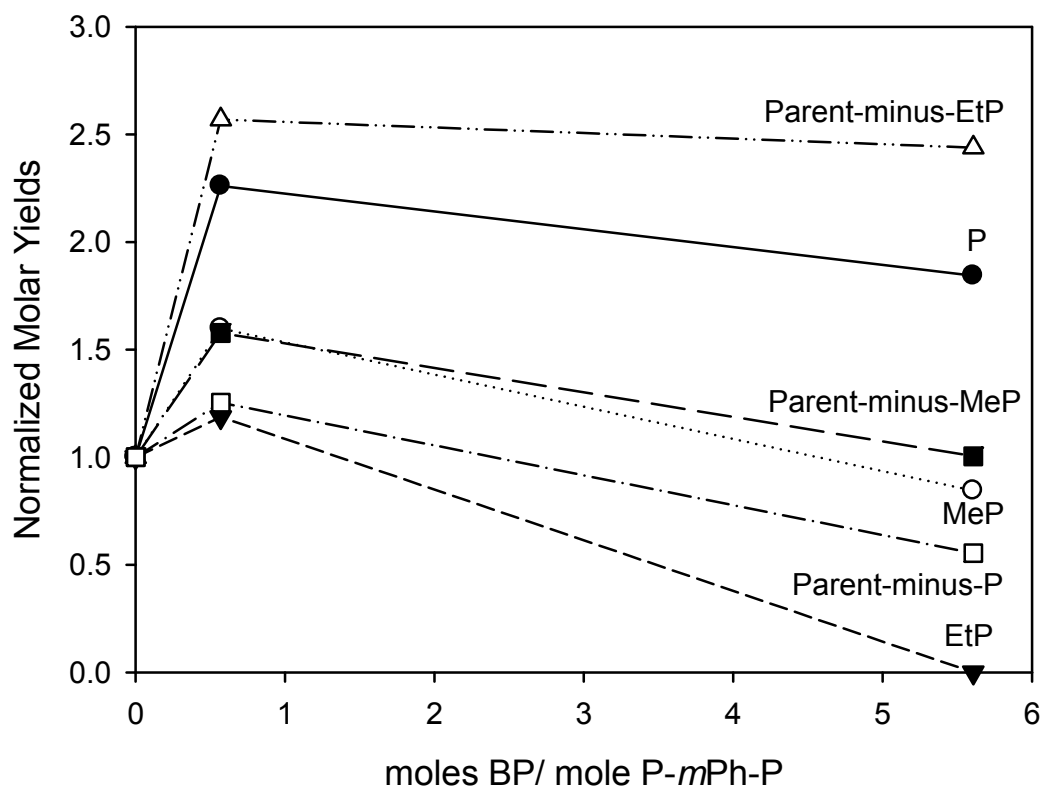


Figure 5.9: The normalized molar yields (moles formed with BP/ moles formed without BP) of major cracking products by P-*m*Ph-P with BP as a diluent.

Figure 5.10 shows the MALDI mass spectra for microreactor reaction of P-*m*Ph-P with and without BP added. To obtain good peak intensity of all the products, the bottom spectrum was measured at a higher laser power due to the high concentration of BP. Hence, adduct peaks due to the matrix appear much larger than the top two spectra (for example the m/z of 500, 750, 1001...etc). Nevertheless, the presence of BP during cracking clearly did not prevent the formation of the addition products that were observed without BP. New addition products were also formed by addition of BP to fragments of the model compounds, which after forming continued to participate in addition reactions

giving even higher molecular weight products. For example, the products at m/z 570 and 584 were consistent with addition reactions between BP and the Parent-minus-MeP and Parent-minus-P, respectively. Two more groups of either Parent-minus-MeP or Parent-minus-P adding to the m/z 584 product yielded the products at m/z 902 and 916, respectively. The m/z 902 product could also result from the m/z 570 compound plus Parent-minus-P.

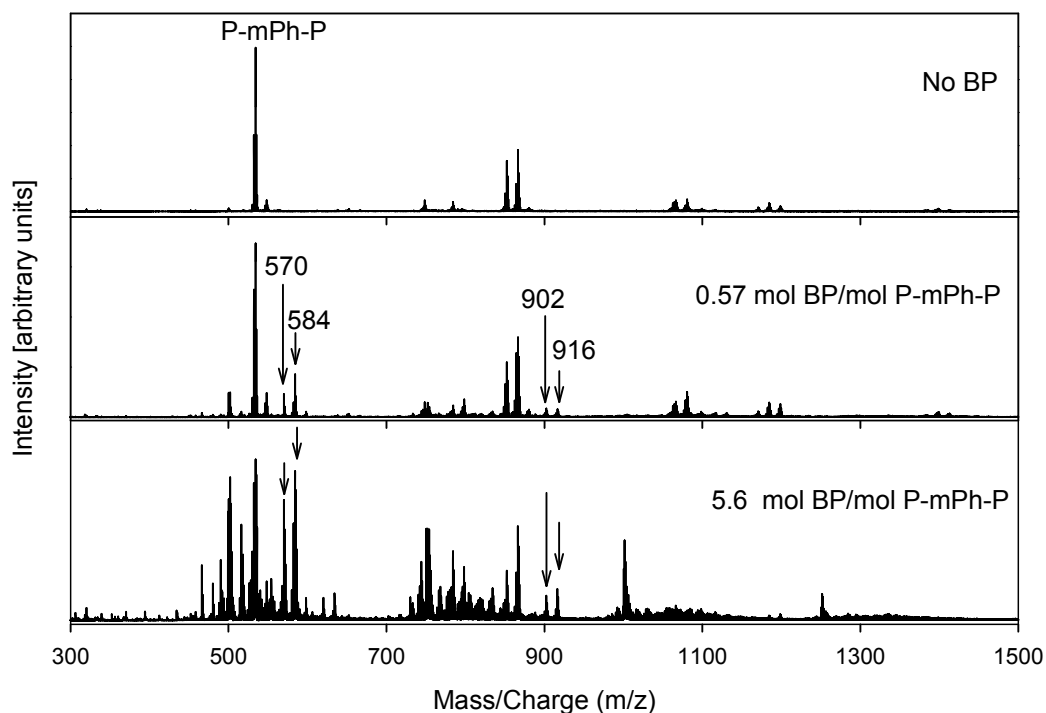


Figure 5.10: MALDI-MS of P-*m*Ph-P with and without BP at two different molar ratios. New peaks, such as the one at m/z 584, result from addition reactions between major cracked products of P-*m*Ph-P and BP.

MALDI-MS/MS analysis revealed how the BP added to the fragments of P-*m*Ph-P. **Figure 5.11**, shows the MS/MS of the product at m/z 584, which was the major addition product in the bottom spectra of **Figure 5.10**. The cleavage of the

m/z 584 product to give m/z 265 (methylbenzopyrene ion) and m/z 215 (methylpyrene ion) strongly supports an alkyl-aryl addition reaction, consistent with the structure drawn on **Figure 5.11**. Aryl-aryl addition would not give easy fragmentation of BP from the ion, nor would a methylBP fragment be detected. These observations are consistent with the previously reported structure of addition products of P-*m*Ph-P and P-3,5-pyr-P, shown in Chapter 3 (**Figure 3.7**).

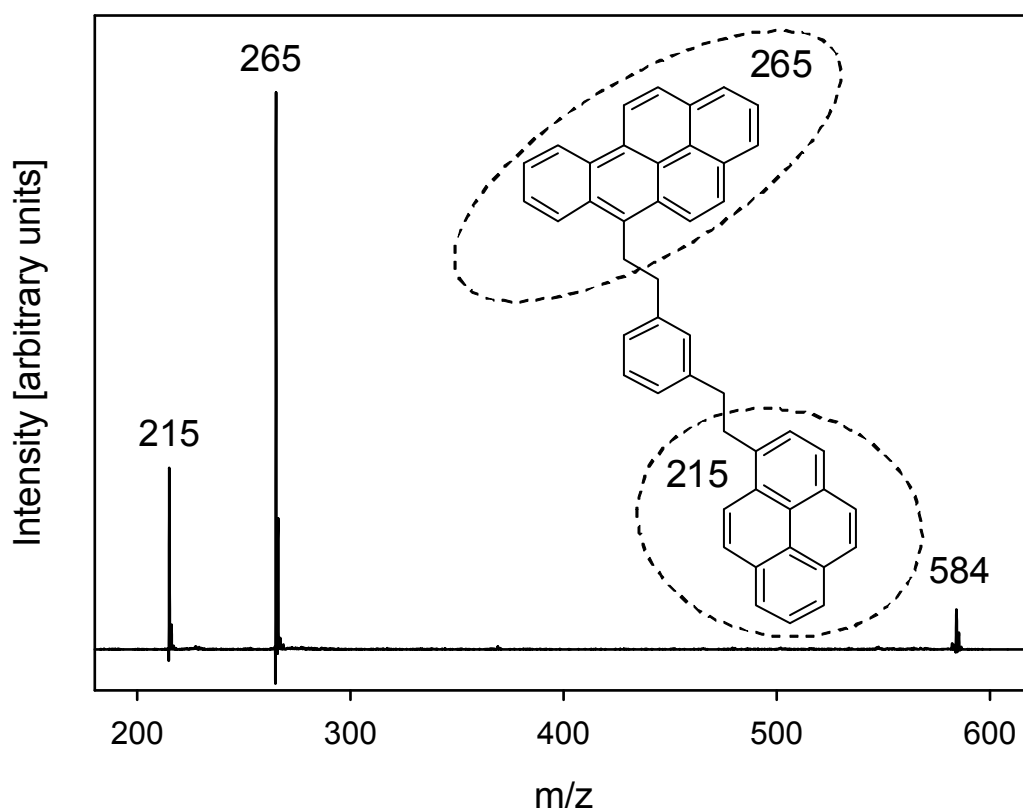


Figure 5.11: MALDI-MS/MS of the m/z 584 signal shown in **Figure 5.10**. The splitting patterns indicate methylbenzopyrene and methylpyrene ions as the major fragments, consistent with an alkyl-aryl addition between BP and m/z 333 fragment (Parent-minus-P), consistent with the drawn structure.

5.3.3 Cross-Polarized Light Microscopy

Six archipelago compounds (P-*m*Ph-P, P-*p*Ph-P, P-F-P, P-2,5-pyr-3-Me-P, P-BiTh-P, and P-3,5-pyr-P) were examined on a hot stage microscope at temperatures ranging from ambient to 450 °C. The hypothesis was that liquid crystalline behavior during cracking could enhance coke formation by aligning molecules for addition reactions. The six compounds all formed liquid crystal (LC) phase(s) that persisted as the sample was heated before disappearing to give an isotropic liquid.

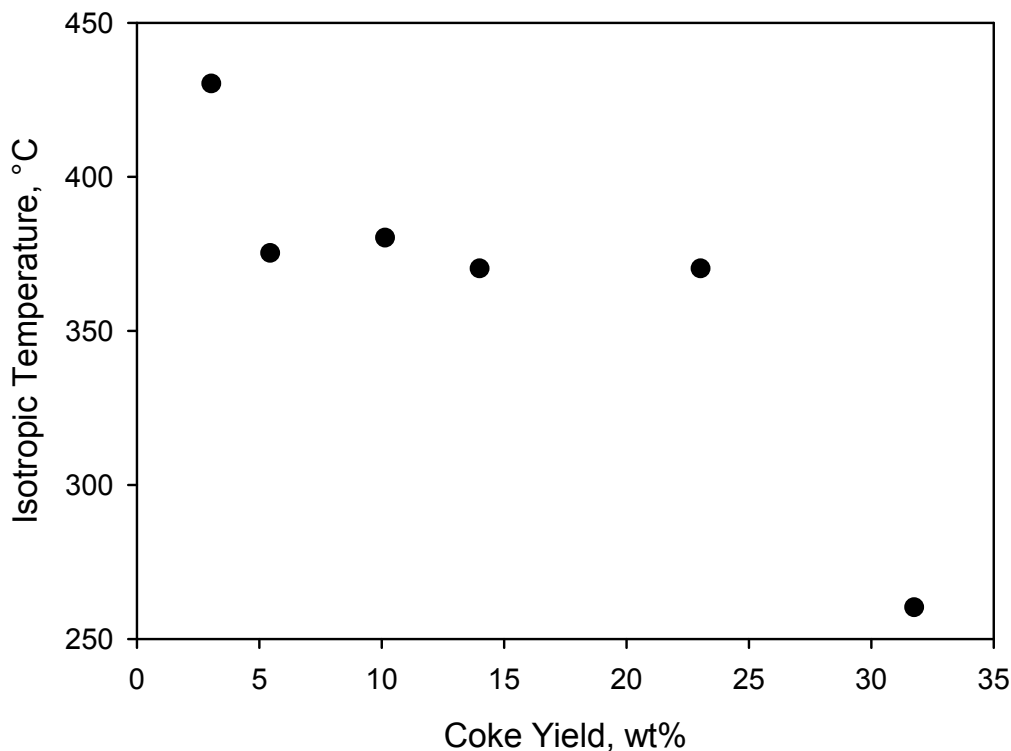


Figure 5.12: A negative correlation is apparent between the isotropic temperature (the temperature of liquid crystals disappearance) and the coke yield of the archipelago model compounds.

Figure 5.12 shows a negative correlation between the approximate temperature at which the LC phase disappears (isotropic temperature) and the

coke yield of these model compounds as measure by TGA. Clearly, the compound forming the lowest coke yield, P-*m*Ph-P, has the highest isotropic temperature, while P-3,5-pyr-P gave the largest coke yield with lowest isotropic temperature. The correlation across all compounds is not ideal (R^2 of only 0.76), but a trend is nonetheless established.

The pyridyl derivatives, P-3,5-pyr-P and P-2,5-pyr-3-Me-P, showed striking similarity in terms of LC shape to those formed in Athabasca asphaltenes at 85 °C as reported by Bagheri et al.⁹ The LC formed by P-3,5-pyr-P, shown in **Figure 5.13**, appeared at 70–80 °C and disappear at approximately 260 °C.

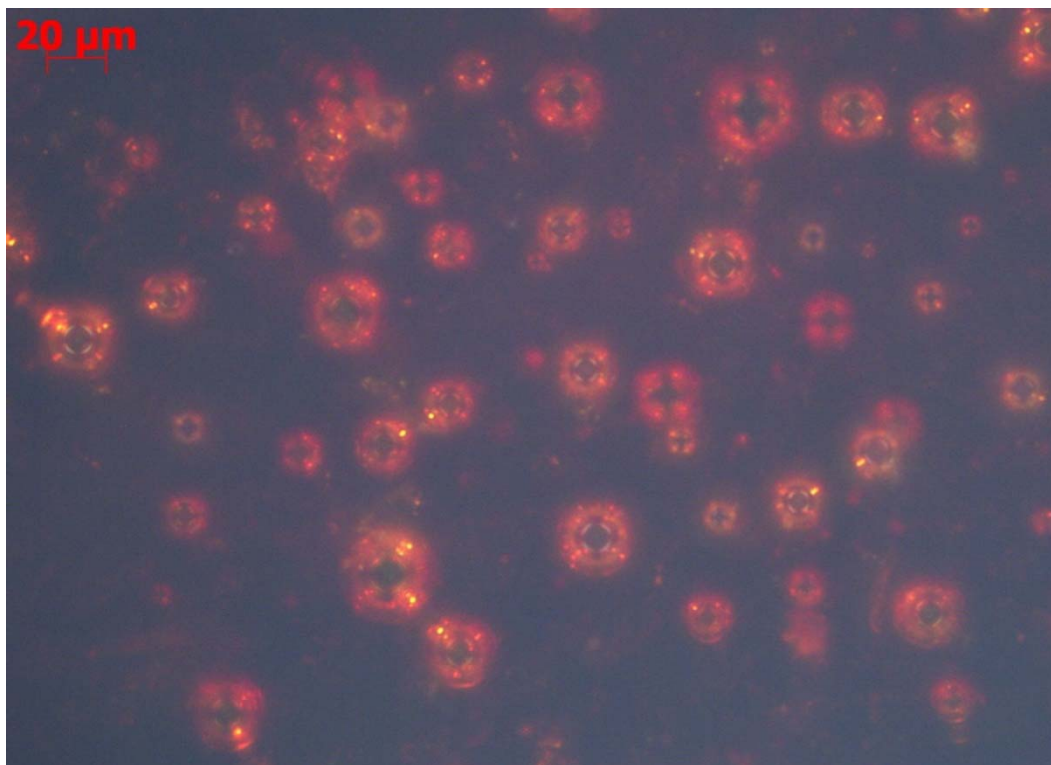


Figure 5.13: The liquid crystals formed by P-3,5-pyr-P during the hot stage microscopy under cross-polarized light. These LC started to form at ~70–80 °C and disappeared at ~260 °C.

5.4 DISCUSSION

Both TGA and microreactor experiments and the subsequent analyses were repeatable within a synthesis batch suggesting no instrumental artifacts. Mass spectroscopy and NMR analysis of the reactants did not show major contaminants, indicating that the starting model compounds were >95% pure. The typical contaminants expected from the synthesis procedures would be residual alkenes, alkynes, and halides. Halides could initiate radical reactions at low temperatures, while the alkenes and alkynes could participate in addition reactions. In several cases, the coke yields by TGA differed between synthesis batches of the same compound. These differences were likely due to contaminants or residual solvents from the synthesis steps. In these cases, the samples were repurified and the analysis was repeated. The cracking kinetics of these model compounds, as measured from TGA following the differential method (Chapter 4), show high apparent activation energy of cracking in the range of ~190–250 kJ/mol without major differences among the various structures. If the contaminants had a major impact and were significant in some samples, then the cracking kinetics would be significantly affected and the results would not be within the range of the rest of the samples. Therefore, we conclude that the results reported here are due to the reported model compounds, and are not caused by contaminants or instrumental artifacts.

5.4.1 Cracking Reactions

5.4.1.1 Initiation

The $\text{H}_2\text{C}-\text{CH}_2$ bond of the ethano bridge is expected to be the weakest, and therefore cleavage of this bond should initiate chain reactions. A similar initiation reaction was reported for 1,2-diphenylethane (bibenzyl), which is structurally quite similar to the archipelago compounds.¹⁰ The estimated bond dissociation energy (BDE) for bibenzyl at 298 K is 66.6 kcal/mol, based on a correlation between C–C bond length and BDE.¹¹ A more accurate value can be estimated by using group additivity⁷ to predict the heat of formation at 298 K (ΔH_f°) of bibenzyl as 35.4 kcal/mol, and by taking ΔH_f° of benzylic radicals to be 47.8 kcal/mol¹², giving a BDE of 60.2 kcal/mol for the C–C bond in bibenzyl. This BDE for the bridge C–C bond is expected to be even less for the pyrene-based compounds, since the generated radicals from homolysis can be efficiently delocalized by resonance over many carbon atoms in pyrene. Taking the difference in resonance stabilization energy between the benzylic radical and methylpyrene radical to be 5.1 kcal/mol¹⁰, gives an estimate of 55.1 kcal/mol for the BDE of P-*m*Ph-P. This value is in close agreement with the estimate of 54.7 kcal/mol using the ΔH_f° of the P-*m*Ph-P fragments, as shown in **Figure 5.14**. All other bonds would be much stronger and unlikely to initiate the reaction. For the compounds with heteroatomic central rings, we consider the C–H BDE at the methylene position as an indication of the stability of the radical adjacent to the central ring. By this argument, the thiophenic groups would make the ethano bridge cleavage more facile, while the pyridines will have similar activity as the hydrocarbons. For

example, the C–H BDE in 2-methylthiophene is 3.3 kcal/mol weaker than in methylbenzene.¹³

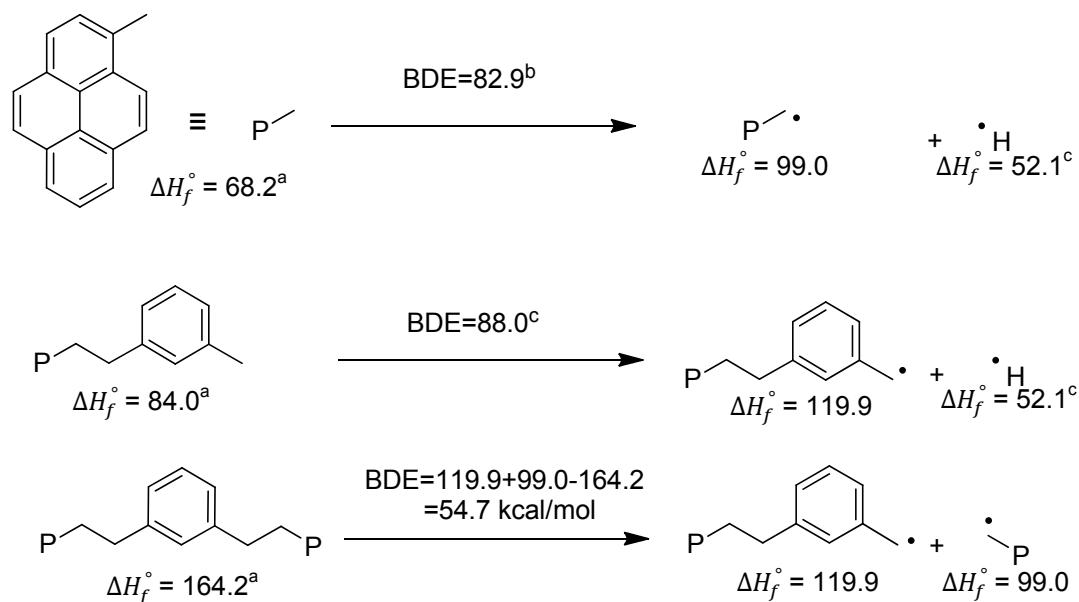


Figure 5.14: Estimated bond dissociation energies (BDE) of C–C and C–H bonds in P-*m*Ph-P, as well as standard heat of formation values (ΔH_f°) at 298 K. ^a Estimated by Marrero and Gani group additivity method⁷. ^b From Smith and Savage¹⁴. ^c From McMillen and Golden¹². All values are given in kcal/mol.

Following the initiation step, MeP and Parent-minus-MeP radicals will abstract hydrogen from the parent compound to form the major cracked products, **Pair B** in **Figure 5.4**. MeP is stable and continues to increase in concentration as the reaction progresses. Secondary reactions can produce MeP by β -scission of higher molecular weight radicals, i.e. larger than the parent radicals, which would be resulting from alkyl–alkyl addition reactions⁶ (Chapter 3). Parent-minus-MeP, on the other hand, is more prone to being consumed in secondary reactions, likely

addition reactions because MALDI-MS/MS revealed this product fragment as a constituent of some addition products.

5.4.1.2 Aryl-Alkyl Bond Cleavage

5.4.1.2.1 Uni- vs. Bi-Molecular Cracking Mechanism

Hydrogenolysis reactions are expected to induce cleavage at either the pyrene or the central aromatic ring. Alkylpyrene compounds have been observed to cleave at the pyrene ring much more easily than their benzene-based counterparts.¹⁵⁻¹⁹ These studies suggest that the cleavage of the stronger alkyl-aryl bond is caused by hydrogenolysis reactions, where a hydrogen is transferred to the *ipso* (substituted) position in the aromatic ring followed by rapid cleavage of the alkyl side chain, although the mechanism by which hydrogen is transferred remains controversial. Three mechanisms have been reported to be responsible for the alkyl-aryl cleavage: H-atom transfer²⁰, reverse radical disproportionation (RRD), and radical hydrogen transfer (RHT)²¹. The H-atom transfer was found to be more significant in smaller ring systems, such as alkylbenzenes or bibenzyl, in which RRD could also play an important role depending on the solvent and conditions employed.²² In alkylpyrenes, however, H-atom transfer was not a major pathway because the alkyl cleavage decreased with increasing temperature, opposite to the observed trend for alkylbenzenes.¹⁵ RHT, on the other hand, was reported to play a major role in the cleavage of alkylpyrenes with side chains longer than one carbon.^{15, 23} In the case of MeP, RHT cannot take place and hence RRD was reported as the major cleavage pathway¹⁴ where pyrene formed as a primary reaction product. The continuous increase in production of pyrene is

attributed to secondary reactions leading to the dealkylation of primary products, such as MeP.¹⁸ In our experiments, MeP formation increased as a function of conversion, as shown in **Table 5.3** for P-3,5-pyr-P and P-BiTh-P, but the increase in MeP was contrasted by very little increase in pyrene formation, suggesting that the dealkylation of MeP had a minor impact on the production of pyrene. Taking these previous studies into consideration, and accepting RHT or a combination of H-atom transfer and RRD mechanisms to be responsible for the hydrogenolysis, these reaction steps still do not explain the differences observed by changing the central ring in these model compounds. If, for example, RHT was operative in P-*m*Ph-P or P-*p*Ph-P leading to the significant formation of pyrene, why is not this mechanism operative in the case of P-3,5-pyr-P or P-BiTh-P where the pyrene formation is much less, although they have the same ethano bridge connected to pyrene? Clearly, the proximity of a nearby aromatic ring affects the cleavage pathway.

The binary experiments with benzo[a]pyrene (BP) were performed to examine if a bimolecular mechanism, such as RHT, is operative in the model compounds of this study. The hypothesis is that the rate of bimolecular processes leading to formation of pyrene, such as RHT, would decrease if the system was diluted significantly. Dilution of P-*m*Ph-P resulted in almost doubling the pyrene formation as well as the Parent-minus-EtP, but the rate of disappearance of P-*m*Ph-P dropped only very slightly even after nearly 10-fold dilution (from 0.57 to 5.6 moles BP / moles P-*m*Ph-P), as shown in **Table 5.4**. This result suggests that RHT between two parent molecules is not a major pathway to pyrene formation

as reported by previous studies. The enhancement of the aryl–alkyl cleavage was attributed by Smith and Savage²⁴ to the hydrogen shuttling capability of polycyclic aromatics. They reported that the alkyl–aryl cleavage in the case of 1-undecylnaphthalene with 1-methylpyrene as an additive was enhanced following a trend similar to **Figure 5.9**, where the formation of naphthalene increased significantly at low molar ratio of the additive, which then decreased somewhat as the additive concentration increased. A variety of large PAH compounds like BP are effective agents for hydrogen transfer.²⁵ Consequently, the small decrease in pyrene formation as the molar ratio of the additive increases from 0.57 to 5.6 (**Table 5.4**) may be due to the balance between two competing processes: the enhanced hydrogen transfer by the addition of a large PAH, and the dilution effect after the additive is introduced to the mixture. If the role of BP in the increased cleavage to form pyrene was only due to the enhanced hydrogen transfer and shuttling ability, then the effect of enhancing the cleavage at the pyrene ring would be the same for both P-*m*Ph-P and P-*p*Ph-P, which is not the case. Pyrene formation was more than doubled in P-*m*Ph-P (2.3 normalized molar yield at 0.57 BP / P-*m*Ph-P ratio) while it was only slightly increased in P-*p*Ph-P (1.2 at 0.42 BP/ P-*p*Ph-P). Therefore, the binary experiments suggest that in addition to bimolecular processes and hydrogen transfer enhancements by PAH groups, a unimolecular mechanism, such as a rearrangement process involving the central aromatic group may also play a role in shifting the cracking selectivity.

5.4.1.2.2 Rearrangement Reactions

The proximity of the central aromatic group to pyrene makes the molecule prone to different reactions than simple alkylarene molecules. Ring closure via cyclodehydrogenation in diphenylalkanes²⁶, such as the formation of phenanthrene by bibenzyl, is one example of these reactions. Another reaction taking place in the presence of two adjacent aromatic groups is the 1,2-aryl shift, giving 1,1-diphenylethane as one of the major products in the liquid-phase pyrolysis of bibenzyl, likely via a neophyl-like rearrangement²⁷. Leardini et al.²⁸ found that in the case of 2-(9-anthryl)ethyl, the rearrangement was rapid, taking place via spirocyclopropane radicals which have considerable thermodynamic stability to enable their detection in electron paramagnetic resonance spectroscopy. Since pyrene has a localization energy, as measured by Dewar reactivity number, between that of benzene and anthracene¹⁹, an ethylpyrene radical is expected to experience the neophyl-like rearrangements more than in benzene and somewhat less than that of anthracene.

To assess the impact of such rearrangements on the cracking of the model compounds, thermochemical estimates for the case of P-*m*Ph-P are used, in which the C-H BDE for the different fragments can be assumed to be approximately equal to those of benzene-based structures (see **Table 5.5**). The rearrangement of the parent radical, in which the radical is adjacent to the benzene ring, with ΔH_f° of 197.5 kcal/mol, to the 1-pyrenyl-1-phenylethane radical, which has an estimated ΔH_f° of 193.4 kcal/mol, gives a change of enthalpy of -4.1 kcal/mol! Moreover, once this exothermic rearrangement takes place, β -scission to give

pyrene radical and Parent-minus-P olefin ($\text{PCC}\Phi\text{C}=\text{C}$) is only 18.8 kcal/mol endothermic. On the other hand, the cleavage on the other side to give vinylpyrene ($\text{PC}=\text{C}$) and Parent-minus-EtP ($\text{PCC}\Phi^*$) radical requires 48.8 kcal/mol. These cracking pathways for P-*m*Ph-P are shown in **Figure 5.15**.

Table 5.5: Thermochemical estimates for P-*m*Ph-P fragments. All values are given in kcal/mol.

Compound ¹	ΔH_f° , 298 K	Radical ³	C–H BDE to yield radical ⁴	Radical ΔH_f° , 298 K ⁵
P- <i>m</i> Ph-P or $\text{PCC}\Phi\text{CCP}$	164.2 ²	$\text{PCC}\Phi\text{C}^*\text{CP}$	85.4 (for benzylic hydrogen in ethyl benzene)	197.5
$\text{PCC}\Phi\text{-C-P}$ C	145.5 ⁶	$\text{PCC}\Phi\text{-C-P}$ C*	100 (for primary CH)	193.4
$\text{PCC}\Phi$	91.9 ²	$\text{PCC}\Phi^*$	110.9 (for CH in benzene)	150.7
P	49.9 ⁷	P*	107.1 ⁸ (for CH in pyrene at the 1 position)	104.9
$\text{PCC}\Phi\text{C}=\text{C}$	107.3 ²			
$\text{PC}=\text{C}$	91.5 ²		–	

1: P is pyrene, CC represents the carbon atoms in the ethano bridge, Φ is the benzene ring

2: Estimated using Marrero and Gani⁷ method.

3: Bearing atom marked with an asterisk (*)

4: From McMillen and Golden¹².

5: ΔH_f° of radical = ΔH_f° of compound + BDE – ΔH_f° of hydrogen atom. $\Delta H_{f,298K}^\circ(\cdot H) = 52.1$ kcal/mol.

6: Estimated using Constantinou and Gani⁸ method.

7: From Freund et al.¹⁵

8: Aihara, J.-i.; Fujiwara, K.; Harada, A.; Ichikawa, H.; Fukushima, K.; Hirota, F.; Ishida, T. *J. Mol. Struct.: THEOCHEM* **1996**, 366, 219-226.

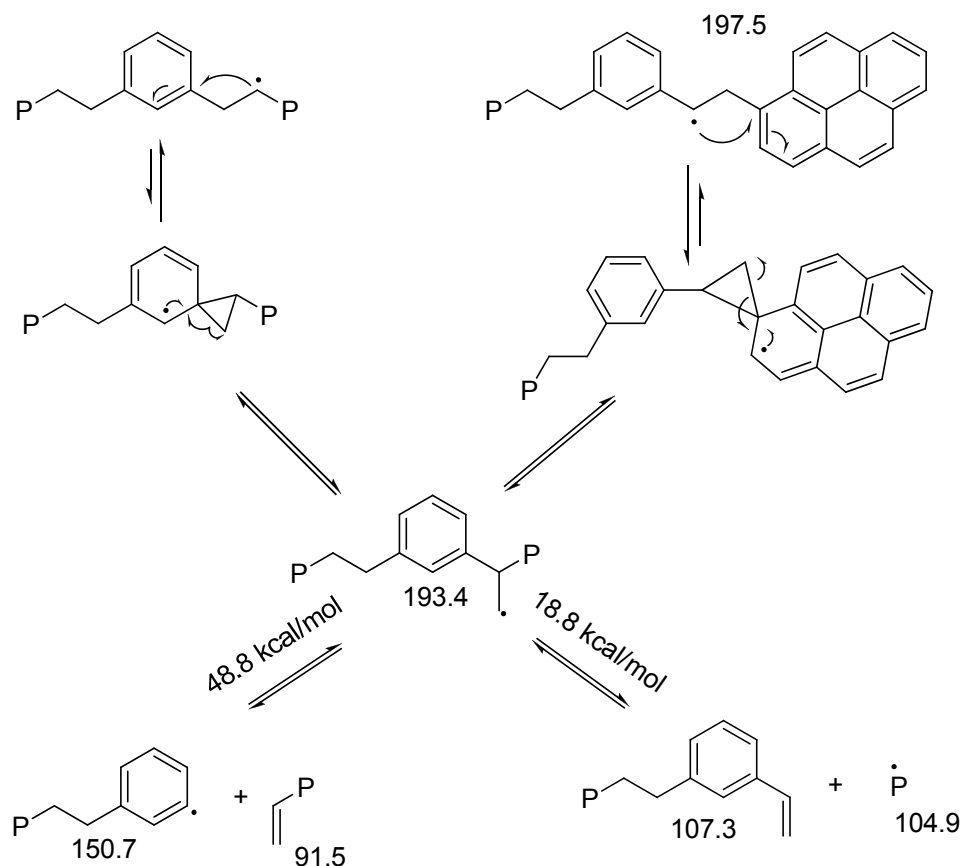


Figure 5.15: Cracking pathways via β -scission of the rearranged radical in P-*m*Ph-P. The addition through pyrene is expected to be the major pathway as the resultant radical can be delocalized over many atoms in pyrene. Numbers on arrows are enthalpy changes while those next to the structures are the standard heats of formation at 298 K in kcal/mol, as estimated and summarized in **Table 5.5**.

Alternatively, rather than the direct cleavage via β -scission, the transition state for the rearrangement of the parent radical in P-*m*Ph-P could undergo benzene-pyrene ring addition, generating a highly stable radical, **Figure 5.16 (a)**, that is efficiently delocalized over the entire structure. Such ring-ring addition is not expected to be a major pathway at employed conditions, and is expected to be much slower than cracking. Nevertheless, when this ring-closure takes place, the

resulting radical in the aromatic rings could abstract hydrogen to form a hydroaromatic compound, which can subsequently transfer hydrogen to the ipso position in another molecule via RHT or RRD. This radical, through resonance, would also have a presence at the ipso position of both pyrene and benzene (depending on in which ring the rearrangement is taking place) that can abstract a hydrogen directly followed by the alkyl loss and the rapid rearomatization to generate pyrene and the Parent-minus-EtP olefin (**Figure 5.16 (b)**).

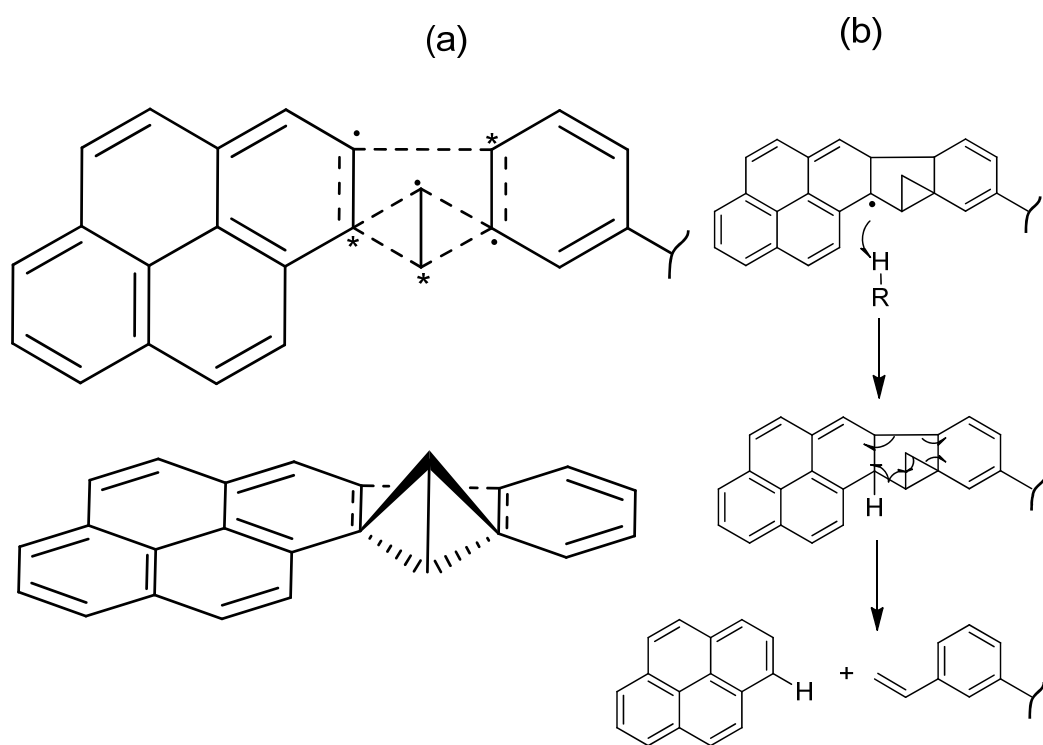


Figure 5.16: (a) The transition state resulting from the benzene–pyrene ring addition after the initial alkyl–pyrene or alkyl–benzene ring closure. The resulting radicals are marked differently to easily follow their resonance steps (not both in the same molecule). (b) If the radical in (a) formed by 1,2–aryl shift through benzene followed by benzene–pyrene closure, the resulting radical at the ipso position in pyrene could abstract hydrogen then rapidly rearomatize to pyrene and Parent-minus-EtP olefin.

Based on the yield of cracking products, shown in **Table 5.3**, the presence of heteroatoms may give additional stabilization for the radical at the central aromatic ring, and hence the β -scission to give a radical on the central ring will be more favorable than in hydrocarbons, though still less favorable than the cleavage towards pyrene radical. The low yield of pyrene in the model compounds with heteroatoms likely indicates that participation of rearranged radicals in secondary reactions is more favorable than cleavage to release a second pyrene group. The fact that the heteroatomic model compounds are much more reactive, and hence start building the concentration of cracked radicals and olefins that participate in addition reactions at an earlier stage, compared to hydrocarbon compounds, supports this hypothesis. For example, the radical next to the bithiophenic rings, resulting from homolysis or hydrogen-abstraction, will rapidly crack at the other side of the molecule by resonance to give a diolefin and another methylpyrene radical (**Figure 5.17**). This pathway explains the high cracking and addition activity of bithiophene and thiophene groups as well as the much higher yield of MeP compared to other compounds in which such cleavage does not take place. A similar diolefin could also form in P-*p*Ph-P but not in P-*m*Ph-P, which may explain its slightly higher yield of solid residue, however in these compounds no appreciable products resulting from cracking at both sides of the molecule were detected. Therefore, in heteroatomic model compounds, pyrene likely forms mainly from secondary reactions, while in hydrocarbons, pyrene likely forms as both primary and secondary product.

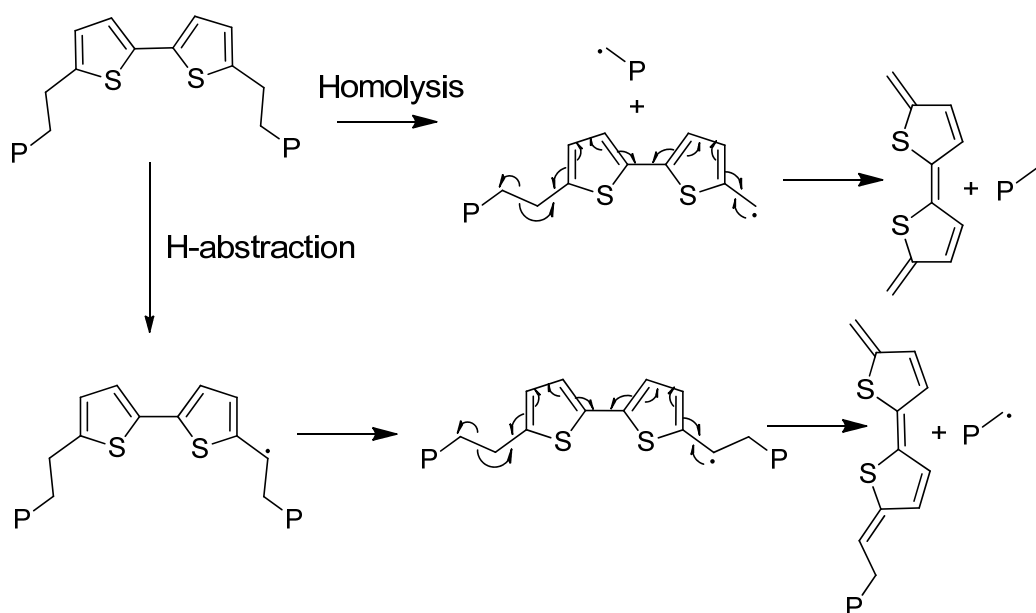


Figure 5.17: The rapid cleavage of P-BiTh-P to a diolefin and two radicals build the radicals and olefins pool quickly and engage in addition reactions at a higher rate and more effectively than in hydrocarbons

Although the proposed reaction steps seem plausible based on the estimates of heats of formation, the lack of activation energies for each step presents a source of uncertainty. Nevertheless, the proposed pathways give an explanation for the observed results of hydrocarbon versus heteroaromatic model compounds, in addition to the already published studies for the different reaction pathways of hydrogen transfer mechanisms.

5.4.2 Coking Reactions

As the various cracked and rearranged products form and build up in the reacting liquid, secondary reactions will soon follow. Olefins forming in the ethano bridge due to any mechanism, such as radical disproportionation (RD) or RHT will be the most reactive species for the addition reactions with radicals. The

radicals will also add to the aromatic rings, as seen from the binary experiments with BP. The resulting radical from the radical–olefin addition reaction will likely stabilize by abstracting hydrogen from another molecule. The combination of radical–olefin addition followed by stabilization apparently has a higher rate than cracking, as supported by detecting significant alkylated products from MALDI and NMR results. Alternatively, the generated radical from the addition step could participate in other reactions such as cracking via β -scission, rearranging into a more stable radical, undergoing RD to create another olefin, terminating the reaction chain temporarily by radical combination, or adding to another olefin. All these steps would take place simultaneously during the reaction, where both new cracked and addition products will be generated simultaneously. These sequential steps will eventually build larger archipelago compounds with different islands, causing the molecule to be less and less soluble, with subsequent reactions leading eventually to coke formation.

Within the series of model compounds, two factors seem to be at play that will affect their coke yield: the rate of addition reactions and the stability of the addition products. Theoretically, the higher the rate of addition reactions, the higher the expected coke yield. But if the initial addition products are very stable, they will not participate in further addition reactions to build larger structures and would instead stabilize by hydrogen abstraction or radical combination. The addition products from all the model compounds form at a rate higher than they are consumed, and hence they are detected in MALDI-MS. But the model compounds that are much more reactive, such as P-BiTh-P which undergoes 61%

conversion after only 20 min at 365 °C, will generate more radicals and olefins and will start secondary reactions at a much earlier stage than a less reactive compound at the same reaction conditions. Moreover, due to the higher reactivity of the fragments, the initially formed addition products are consumed very rapidly into further cracking and addition reactions leading to faster building of large structures. The effect of the central ring is likely due to its enhancement of the cracking of the compound at much lower temperatures, leading to higher yields of addition products and eventually to more coke.

Another factor that may affect coke yield is the association or aggregation of molecules in the liquid phase before reaction begins. Hydrocarbon compounds are not expected to form strong associations or aggregations without the presence of polar groups.²⁹ The pyridines, on the other hand, are known to self aggregate even at temperatures higher than room temperature, such as P-B-P which existed as a mixture of dimers and monomers in toluene at 75 °C³⁰, and the presence of a small amount of water made the aggregation of this compound even stronger.³¹ Therefore, compounds with heteroatoms are expected to have an enhanced association in the liquid melt before reaction. The cross-polarized light microscopy showed liquid crystals (LC) formation by all the archipelago compounds that were examined. LC by P-3,5-pyr-P formed as low as 70–80 °C and remained until ~260 °C when the liquid became isotropic, in striking similarity to the liquid crystals formed by asphaltenes. The asphaltenes, which typically give MCR content or coke yield of approximately 50 wt %³², have low isotropic temperatures (disappearance temperature of LC) in the range of 150-160

°C⁹, consistent with the observed trend of the model compounds where the highest coke producer (P-3,5-pyr-P) had the lowest isotropic temperature (**Figure 5.12**).

A fundamental difference between the model compounds and the asphaltenes is the amount of liquid crystalline phase. The pure model compounds are entirely LC over the reported range of temperature, whereas the LC phase in asphaltenes and maltenes coexists with amorphous or isotropic material. A pure compound can become isotropic due to disorder or by cracking to form complex products, whereas in the asphaltenes the LC phase can dissolve in a second phase. Nevertheless, the correlation between the isotropic transition temperature and coke yield in **Figure 5.12** is intriguing, and suggests that LC phases may be less prone to addition reactions. In the model compounds, the combination of an early onset of isotropic phase with a low apparent activation energy of cracking, ~140 kJ/mol (~33.7 kcal/mol), seem to be responsible for the exceptionally high coke yield by P-3,5-pyr-P.

To summarize the above discussion, the coke yield is likely influenced from the beginning of the reaction by the reactivity of the parent compound as well as by the nature of the cracked products and their ability to give stable addition products. In addition to such kinetic factors, the possible enhancement of intermolecular association in the liquid melt could combine to give the highest coke yields.

Figure 5.18 summarizes the reaction steps leading to coke formation starting from cracking and addition reactions before the phase separation takes places. The

model compounds undergo C–C homolysis to initiate the reaction chain, which then abstract hydrogen from the parent to yield species that can subsequently offer abstractable hydrogen atoms or cleave to give more radicals. The parent radical can undergo rearrangement followed by β -scission to yield an olefin and another radical. The rearranged radical, and also the unrearranged one, can lose a hydrogen via radical disproportionation (RD) or radical hydrogen transfer (RHT) to form more olefins. The generated radicals would add then to the olefins to make larger (with more aromatic groups) radicals, which can start this reaction cycle multiple times before it becomes largely immobile with insignificant solubility leading to phase separation. For this family of compounds, the MALDI–MS data suggest that the solubility of a molecule is insignificant when the present aromatic groups are ≥ 10 , i.e. when the mass exceeds 1600 Da. Once the liquid–liquid phase separation takes place, coke formation is rapid as suggested by Wiehe¹. **Figure 5.18** emphasizes and summarizes the above points that the activity of the parent, the instability of the cracked and addition products leading to their rapid consumption in secondary reactions in sequential manner, as well as association and alignment of the molecules, are driving factors to higher addition rates and subsequently higher coke yields.

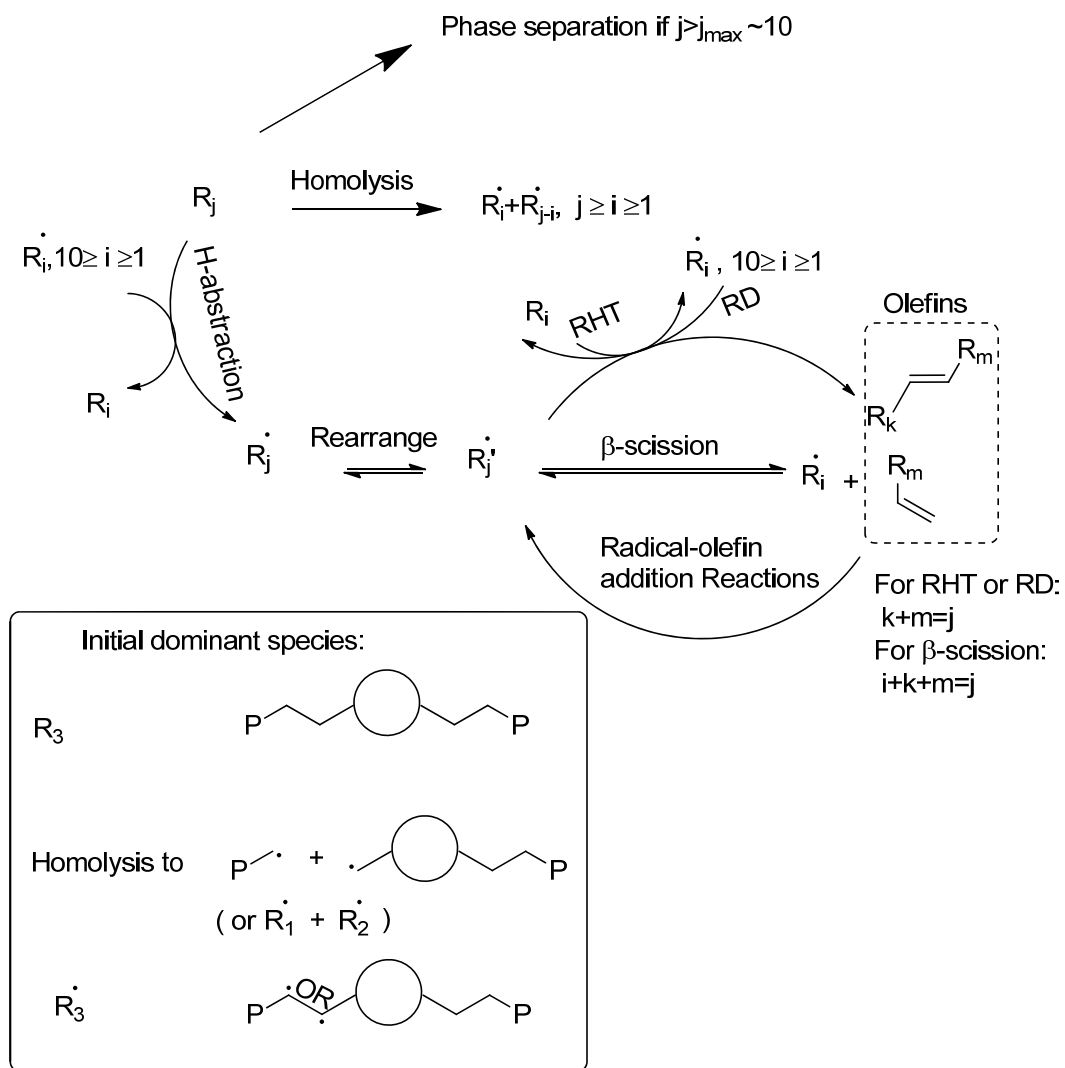


Figure 5.18: A simplified reaction network for coke formation. The indices i , j , k , and m represent the number of ring groups. Experimental results for the largest detected products from MALDI-MS suggest that for $j > 10$ in this family of pyrene compounds, the solubility is insignificant. Termination reactions by radical combinations can take place at any point of the reaction.

5.5 CONCLUSIONS

1. In addition to the reported bimolecular mechanisms for the formation of pyrene, the decompositions of the pyrene-based model compounds could involve a unimolecular rearrangement mechanism, such as the neophyl-like rearrangement.
2. The central ring in the model compounds has major impact on both the cracking and coking of the whole compound. One example is the 10-fold increase in coke yield by replacing benzyl with a pyridyl group.
3. The coke yield from a series of pyrene model compounds is controlled by the activity of the parent compound, the rate of addition reactions and the nature and activity of cracked and addition products.
4. The possible enhancement of intermolecular association in the liquid melt combined with kinetic factors could give the highest coke yields.
5. Aryl-aryl addition is not a favorable reaction and is much slower than cracking at the employed conditions. Alkyl-alkyl and alkyl-aryl (as observed from binary experiments with benzopyrene) additions are much faster, despite cracking reactions, and are dominant in building larger product molecules.

5.6 REFERENCES

1. Wiehe, I. A., A Phase-Separation Kinetic-Model for Coke Formation. *Ind. Eng. Chem. Res.* **1993**, 32, 2447-2454.
2. Wiehe, I. A., *Process chemistry of petroleum macromolecules*. CRC: Boca Raton, FL, 2008.
3. Wiehe, I. A., A Solvent Resid Phase- Diagram for Tracking Resid Conversion. *Ind. Eng. Chem. Res.* **1992**, 31, 530-536.
4. Strausz, O. P.; Lown, E. M., *The Chemistry of Alberta Oil Sands, Bitumens, and Heavy Oils*. AERI: Calgary, AB, 2003.
5. Alshareef, A. H.; Azyat, K.; Tykwinski, R. R.; Gray, M. R., Measurement of Cracking Kinetics of Pure Model Compounds by Thermogravimetric Analysis. *Energy Fuels* **2010**, 24, 3998-4004.
6. Alshareef, A. H.; Scherer, A.; Tan, X.; Azyat, K.; Stryker, J. M.; Tykwinski, R. R.; Gray, M. R., Formation of archipelago structures during thermal cracking implicates a chemical mechanism for the formation of petroleum asphaltenes. *Energy Fuels* **2011**, 25, 2130-2136.
7. Marrero, J.; Gani, R., Group-contribution based estimation of pure component properties. *Fluid Phase Equilib.* **2001**, 183, 183-208.
8. Constantinou, L.; Gani, R., New Group-Contribution Method for Estimating Properties of Pure Compounds. *AIChE J* **1994**, 40, 1697-1710.
9. Bagheri, S. R.; Bazyleva, A.; Gray, M. R.; McCaffrey, W. C.; Shaw, J. M., Observation of Liquid Crystals in Heavy Petroleum Fractions. *Energy Fuels* **2010**, 24, 4327-4332.

10. Poutsma, M. L., Free-Radical Thermolysis and Hydrogenolysis of Model Hydrocarbons Relevant to Processing of Coal. *Energy Fuels* **1990**, 4, 113-131.
11. Zavitsas, A. A., The relation between bond lengths and dissociation energies of carbon-carbon bonds. *J. Phys. Chem. A* **2003**, 107, 897-898.
12. McMillen, D. F.; Golden, D. M., Hydrocarbon Bond-Dissociation Energies. *Annu. Rev. Phys. Chem.* **1982**, 33, 493-532.
13. Zhao, S. W.; Liu, L.; Fu, Y.; Guo, Q. X., Assessment of the metabolic stability of the methyl groups in heterocyclic compounds using C-H bond dissociation energies: effects of diverse aromatic groups on the stability of methyl radicals. *J. Phys. Org. Chem.* **2005**, 18, 353-367.
14. Smith, C. M.; Savage, P. E., Reactions of polycyclic alkylaromatics. 4. Hydrogenolysis mechanisms in 1-alkylpyrene pyrolysis. *Energy Fuels* **1992**, 6, 195-202.
15. Freund, H.; Matturro, M. G.; Olmstead, W. N.; Reynolds, R. P.; Upton, T. H., Anomalous side-chain cleavage in Alkylaromatic Thermolysis. *Energy Fuels* **1991**, 5, 840-846.
16. Savage, P. E.; Jacobs, G. E.; Javanmardian, M., Autocatalysis and aryl-alkyl bond cleavage in 1-dodecylpyrene pyrolysis. *Ind. Eng. Chem. Res.* **1989**, 28, 645-654.
17. Smith, C. M.; Savage, P. E., Reactions of polycyclic alkylaromatics. 1. Pathways, kinetics, and mechanisms for 1-dodecylpyrene pyrolysis. *Ind. Eng. Chem. Res.* **1991**, 30, 331-339.

18. Smith, C. M.; Savage, P. E., Reactions of polycyclic alkylaromatics. 2. Pyrolysis of 1,3-diarylpropanes. *Energy Fuels* **1991**, 5, 146-155.
19. Smith, C. M.; Savage, P. E., Reactions of Polycyclic Alkylaromatics - Structure and Reactivity. *AIChE J* **1991**, 37, 1613-1624.
20. Vernon, L. W., Free-Radical Chemistry of Coal-Liquefaction - Role of Molecular-Hydrogen. *Fuel* **1980**, 59, 102-106.
21. McMillen, D. F.; Malhotra, R.; Chang, S. J.; Ogier, W. C.; Nigenda, S. E.; Fleming, R. H., Mechanisms of Hydrogen Transfer and Bond Scission of Strongly Bonded Coal Structures in Donor Solvent Systems. *Fuel* **1987**, 66, 1611-1620.
22. Autrey, T.; Alborn, E. A.; Franz, J. A.; Camaioni, D. M., Solvent-Induced Scission of Diarylmethanes in Dihydroarene Donor Solvents - an Experimental and Mechanistic Modeling Study of Hydrogen-Transfer Pathways. *Energy Fuels* **1995**, 9, 420-428.
23. Savage, P. E., Hydrogen-Transfer Mechanisms in 1-Dodecylpyrene Pyrolysis. *Energy Fuels* **1995**, 9, 590-598.
24. Smith, C. M.; Savage, P. E., Reactions of Polycyclic Alkylaromatics. 7. Hydrogenolysis in Binary Mixtures. *Energy Fuels* **1994**, 8, 545-551.
25. Morgenthaler, J.; Ruchardt, C., Bimolecular formation of radical by hydrogen transfer, 15 - New hydrogen transfer catalysts. *Eur. J. Org. Chem.* **1999**, 2219-2230.
26. Sweeting, J. W.; Wilshire, J. F., Pyrolysis of Omegaomega'-Diphenylalkanes. *Aust. J. Chem.* **1962**, 15, 89-105.

27. Miller, R. E.; Stein, S. E., Liquid-Phase Pyrolysis of 1,2-Diphenylethane. *J. Phys. Chem.* **1981**, 85, 580-589.
28. Leardini, R.; Nanni, D.; Pedulli, G. F.; Tundo, A.; Zanardi, G.; Foresti, E.; Palmieri, P., On the Neophyl-Like Rearrangement of 2-(9-Anthryl)Ethyl Radicals. *J Am Chem Soc* **1989**, 111, 7723-7732.
29. Akbarzadeh, K.; Bressler, D. C.; Wang, J. N.; Gawrys, K. L.; Gray, M. R.; Kilpatrick, P. K.; Yarranton, H. W., Association behavior of pyrene compounds as models for asphaltenes. *Energy Fuels* **2005**, 19, 1268-1271.
30. Tan, X. L.; Fenniri, H.; Gray, M. R., Pyrene derivatives of 2,2'-bipyridine as models for asphaltenes: Synthesis, characterization, and supramolecular organizations. *Energy Fuels* **2008**, 22, 715-720.
31. Tan, X.; Fenniri, H.; Gray, M. R., Water Enhances the Aggregation of Model Asphaltenes in Solution via Hydrogen Bonding. *Energy Fuels* **2009**, 23, 3687-3693.
32. Siskin, M.; Kelemen, S. R.; Eppig, C. P.; Brown, L. D.; Afeworki, M., Asphaltene molecular structure and chemical influences on the morphology of coke produced in delayed coking. *Energy Fuels* **2006**, 20, 1227-1234.

CHAPTER 6

THERMAL CRACKING OF SUBSTITUTED CHOLESTANE– BEZOQUINOLINE MODEL COMPOUNDS

6.1 INTRODUCTION

Biomarkers, or biological markers, are important components of the asphaltenes that are released upon thermal cracking, as presented in details in Chapter 2. Model compounds that resemble some biomarkers are studied here. The chemical structure of these compounds is that of biomarkers, represented by 5 α -cholestane (shown in **Figure 6.1** with ring designation and carbon numbering), fused with a benzoquinoline aromatic moiety, which is substituted with a different aromatic group in each compound. Similar hopanoids that are fused with aromatic groups have been recently identified by Larter and co-workers in highly biodegraded oils.¹

The results from subjecting a series of six biomarker-like model compounds to thermal cracking conditions are presented in this chapter. The objective of these experiments was to examine the thermal behavior of these compounds given

the small amounts of samples that were available. In particular, understanding the thermal reactions of the fused naphthenic rings with aromatic groups, as in these model compounds, may help in elucidating the behavior of heavy naphthenoaromatic moieties in petroleum under thermal cracking conditions.

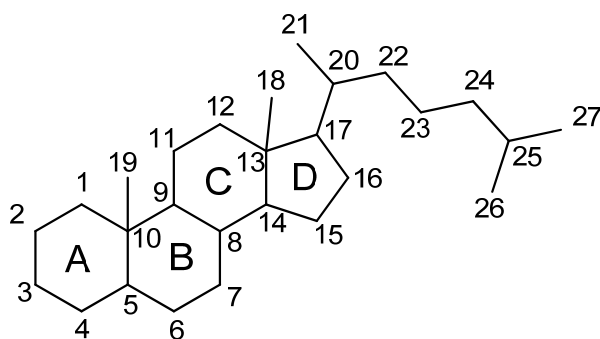


Figure 6.1: Structure of cholestane with ring designation and carbon numbering.

6.2 MATERIALS AND METHODS

Six model compounds with molecular weights of 598–722 g/mol were synthesized to incorporate the cholestane structure fused in substituted benzoquinoline moiety, as shown in **Figure 6.2**. The only difference between these six compounds is the nature of the pendant aryl group. The synthesis of one of these compounds, chol-BB, was reported in detail elsewhere.² The quantities of these model compounds were very limited and hence extensive microreactor experiments at constant temperature and variable times, to follow the successive steps of reaction or to measure the cracking kinetics, were not possible. Instead, minimal samples were used to obtain thermal kinetics behavior from thermogravimetric analysis (TGA) followed by microreactor experiment, at different reaction conditions, for selective compounds only.

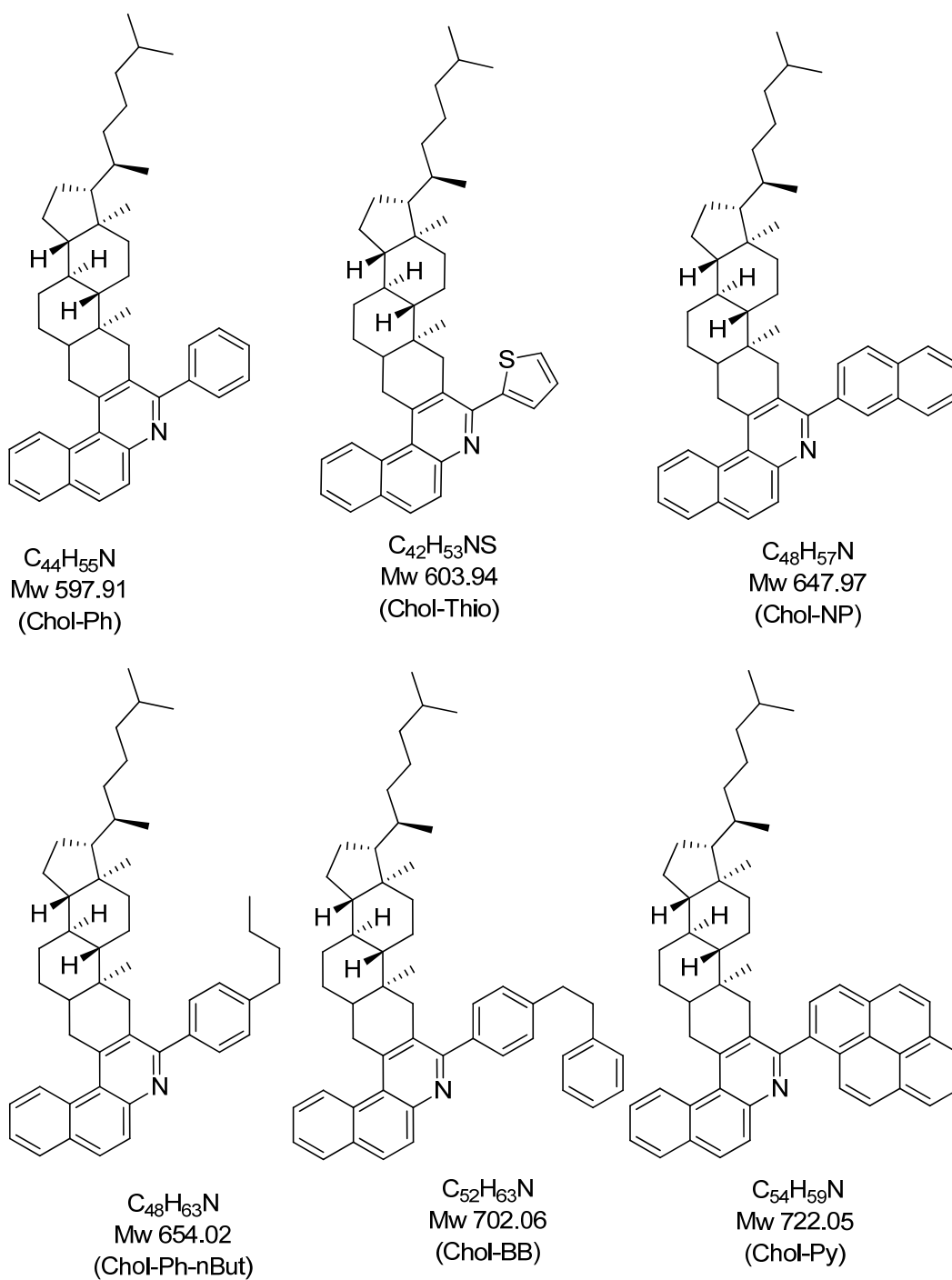


Figure 6.2: Structure, molecular weight, and short name notation (in parentheses) of the six model compounds.

Phenanthrene and pyrene, used as internal standards, were obtained from commercial suppliers and were used as received. Methylene chloride (MC) and methanol (MeOH) used in product extraction and in HPLC analysis were HPLC and ACS grade, respectively. Gases used in TGA and gas chromatography/spectroscopy were from PRAXAIR and were of a high purity grade.

Two TGA experiments were conducted for the majority of compounds to ensure repeatability. Two compounds, Chol-Py and Chol-NP, were reacted only once due to the limited amounts available. The TGA experiments were carried out on a Thermo Cahn TherMax400 (Thermo Electron Corporation, Waltham, MA). Approximately 4–5 mg of each sample was loaded on a platinum pan and was heated in the TGA at 10 °C/min to 500 °C followed by a 15 min holdup at 500 °C. Argon gas was used to provide the inert atmosphere during the experiments with a flow through the furnace chamber at 80 mL/min and a separate excess flow at the balance chamber, to prevent condensation of products on the balance or the hanging wire. The solid residue at the end of the heating profile is the reported coke yield while the initial cracking kinetics, the Arrhenius apparent activation energy (E) and pre-exponential factor (A), were calculated following the differential method reported in Chapter 4.

The microreactor experiments were performed to identify the major reaction products, from both cracking and addition reactions. Three of the six model compounds (Chol-Ph, Chol-BB, Chol-Py) were reacted in tubular stainless steel microreactors, 5 mm in diameter and 5 cm in length. The reactor was attached to a high temperature valve with 1 mm (1/16") internal diameter and 9 cm long tube,

connected and capped with Swagelok fittings. Approximately 2–3 mg of each compound was loaded in a one-end-sealed glass tube, 3 mm in diameter and 45 mm in length. After loading the sample, the reactor was leak-tested and purged with nitrogen, closed and immersed in a heated fluidized sand bath at the desired temperature. The reactor was continuously shaken during the reaction by a rotary motor. After the desired time elapsed, the reaction was stopped instantaneously by immersing the closed reactor in cool water. The reaction products were extracted using MC and the resulting solution was concentrated with a rotary evaporator. The standards, used to measure the conversion of the parents, were added after the reaction but before concentrating the products with the rotary evaporator. Phenanthrene was used as the internal standard in the experiments of Chol-Ph and Chol-Py while pyrene was used in Chol-BB since the bibenzyl fragment in this compound could, if cleaved, form phenanthrene.³

Thermo Scientific Trace GC Ultra gas chromatography–flame ionization detector (GC–FID), coupled with a DSQII mass spectrometer (GCMS) (both from Thermo Electron Corporation, Waltham, MA) were used to identify and quantify and cracked products of masses < 300 m/z . Any products higher than m/z 300 would be identified with matrix assisted laser desorption/ionization (MALDI)–mass spectroscopy (MS) and tandem MS/MS using either Bruker Ultraflex extreme MALDI–TOF/TOF (Bremen, Germany) or Applied BioSystems Voyager Elite MALDI–TOF (Foster City, CA). The matrix used in the MALDI experiments was DCTB, which has a molecular weight of 250 Da. The observed species in MALDI spectra of these nitrogen-containing compounds were usually the protonated ions

(parent+H). Adducts of the matrix by itself (m/z 500, 750, 1000...etc) formed as well as few adducts with the starting compounds (parent + 250). No adducts of the compound molecules were observed before the reaction.

The conversion, defined as the difference between initial and final weights divided by the initial weight of the parent model compounds, was measured by high performance liquid chromatography (HPLC) analysis (Agilent Technologies, Santa Clara, Ca). A Zorbax Eclipse PAH column of 4.6×150 mm with a C18 phase of 3.5 μ m particles was employed in the separation with the mobile phase flowing isocratically at 1 mL/min with 72% MeOH–28% MC (80% MeOH–20% MC for Chol-Py only). The column was maintained at 23 °C and the ultraviolet (UV) detector was set at 239 nm.

The reaction products were analyzed by ^1H nuclear magnetic resonance (NMR) spectroscopy at 500 MHz using Varian Inova (Santa Clara, CA) in CDCl_3 . NMR spectra are referenced to CDCl_3 resonance at δ 7.26. All the analysis and simulations for various compounds were performed using MestReNova software (Mestrelab Research, Santiago de Compostela, Spain).

6.3 RESULTS AND DISCUSSION

6.3.1 Thermogravimetric Analysis (TGA)

The results of the TGA experiments for the six model compounds are shown in **Table 6.1**. The TGA results were reasonably repeatable, as seen from the results of the replicates on Chol-Ph, Chol-Thio, Chol-Ph-*n*But, and Chol-BB. For example, the difference in the coke yield by two replicates of these four compounds was 2.4, 0.8, 0.5, and 0.3 wt%, respectively. **Figure 6.3** shows the

excellent repeatability of the two runs of Chol-Thio in the TGA following the same heating profile. The weight loss below 200 °C was very small in all experiments, indicating that no significant residual solvents were present, and since any cracking would be insignificant at such low temperatures, this weight loss below 200 °C was ignored. The temperatures of the onset of decomposition, defined as the temperature at which 5 wt% of the sample was lost after 200 °C, were high for all model compounds, which confirms the stability of these compounds prior to cracking, and that the evaporation of the samples before cracking begins is minimal. The weight loss after the onset of decomposition corresponds to cracking of the molecules in the liquid phase followed by evaporation of the cleaved fragments. The evaporation of these fragments in the TGA typically takes place at temperatures below their actual boiling points due to the continuous stripping by the flowing inert gas. The solid remaining on the TGA pan at the end of the heating profile is the solid residue reported in **Table 6.1**. This value is corrected for weight loss below 200 °C, as mentioned above. The yield of solid residue was surprisingly similar among all the compounds, except Chol-Py which gave a much higher yield, suggesting no systematic effect of the substituent groups on the coke yield.

In **Figure 6.3**, the curves of rate of weight loss (dW/dt) versus time were used to calculate the kinetics of cracking, where the increasing portion of the curve (increasing rate of weight loss with time) was used to calculate the apparent Arrhenius activation energy (E) and the pre-exponential factor (A) following differential analysis, presented in Chapter 4. The results of these kinetic

calculations are given in **Table 6.1**. The cracking kinetics were similar for the six compounds, within experimental variation, with activation energies in a narrow range of 195–225 kJ/mol. These values are high enough to confirm that the weight loss was mainly due to cracking and not to evaporation, but also, and more importantly, they suggest that similar bonds cleave in all of these compounds leading to the observed kinetics. Since the compounds with direct aryl–aryl linkages, such as Chol-Ph or Chol-Py, have similar cracking kinetics to the compounds with substituted groups that have more labile benzylic bonds (Chol-BB and Chol-Ph-*n*But), these results suggest that the main cleavages in the model compounds are likely to occur in the cholestane part of the molecules.

Table 6.1: TGA results for the six model compounds

Compound	Weight loss <200 °C, Wt%	Onset of Decomposition, °C	Coke Yield, Wt %	<i>E</i> , kJ/mol	Log (<i>A</i> , min ⁻¹)
Chol-Ph	0.92	354	1.1	222	16.4
	0.98	354	3.5	219	16.2
Chol-Thio	1.4	370	2.7	206	14.8
	1.7	371	3.5	217	15.6
Chol-NP	2.9	300	2.4	195	13.8
Chol-Ph- <i>n</i> But	1.2	353	1.7	206	15.0
	1.4	358	2.2	199	14.3
Chol-BB	1.5	372	1.5	200	14.3
	1.3	373	1.8	198	14.1
Chol-Py	4.1	351	9.9	225	15.6

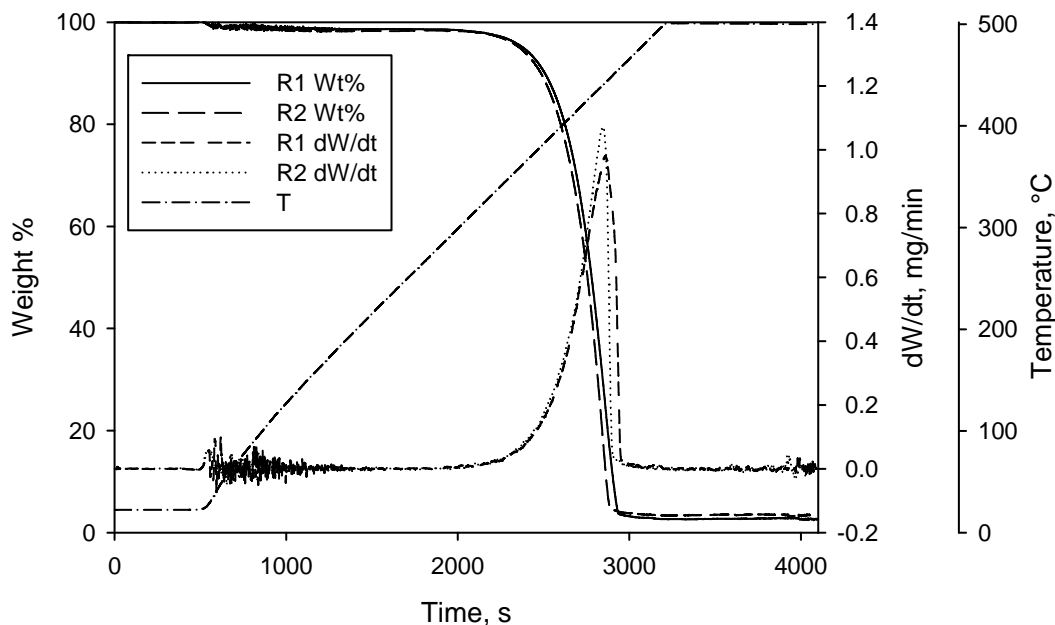


Figure 6.3: Two TGA runs of Chol-Thio show very good repeatability. The derivative curves are used to calculate the kinetics shown in **Table 6.1**. The temperature profile curve is also shown.

Figure 6.4 shows the rate of weight loss versus temperature for all the model compounds. The data show a systematic progression in maximum temperature through the series of compounds, which generally correlates with the molecular weight of the series. For example, Chol-Ph, which has the lowest molecular weight, has the lowest peak temperature while Chol-Py has both the highest molecular weight and the highest peak temperature of 464 °C. This trend is consistent with the mass of the largest fragment of the molecules after cracking of a group on the cholestane rings. As the mass of the parent compound increases due to the substituted group on the benzoquinoline, so does the mass of the remaining fragment.

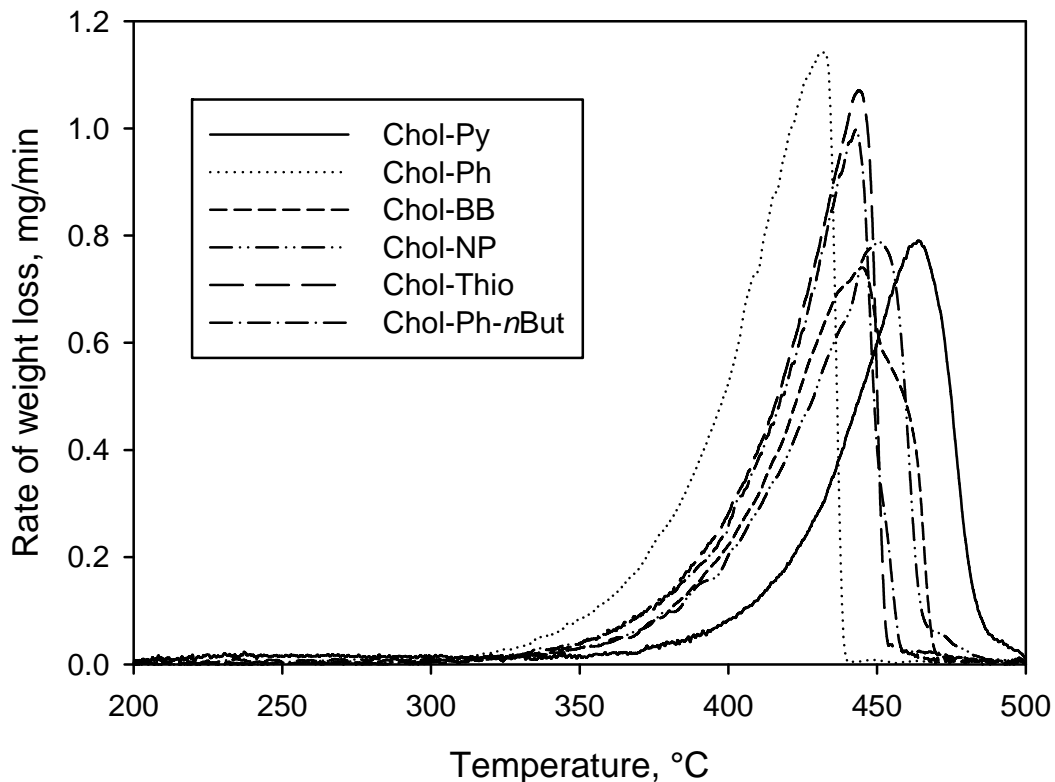


Figure 6.4: Rate of weight loss versus temperature for the six cholestane-based model compounds as measured in the TGA. Chol-Py has the highest temperature at the maximum rate of weight loss in this family of compounds.

6.3.2 Decomposition in Batch Reactions

Chol-Ph, Chol-BB, and Chol-Py were thermally cracked in microreactor at the conditions shown in **Table 6.2**. The conversion (X) is defined as the difference between initial and final weights of the parent model compound divided by its initial weight. The mass of remaining parent compound was measured using HPLC. The high conversion of the parent compounds is in contrast to the very low conversion reported for the pyrolysis of 5α -cholestane (cholestane). Abbott et al.⁴ measured a conversion of only 34% in the anhydrous

pyrolysis of cholestane in a stainless-steel reactor at 350 °C for 48 h. Kissin⁵ cracked cholestane for longer durations to examine the catagenesis of light cycloalkanes from biomarkers, and obtained conversion of only 50% after a 240 h reaction at 300 °C. Experimental evidence suggests that the isomerization and aromatization of sterane hydrocarbons follow pseudo-first order kinetics⁶, therefore, we assume that the overall degradation of cholestane also follows first-order kinetics. The results of Abbott and Kissin give an estimate of E as 65.2 kJ/mol and A as 2524 h⁻¹. Extrapolating to the conditions of **Table 6.2**, these parameters give a cholestane conversion of only 1% for the reaction at 420 °C for 20 min. This conversion is much lower than the experimental results of conversion of 25, 34, and 72% by Chol-Ph, Chol-BB, and Chol-Py, respectively, at 420 °C for 20 min.

Table 6.2: Microreactor experiments and conversion of the parent compounds

Compound	Reaction Conditions	Conversion (X) %
Chol-Ph	375 °C–20 min	18
	420 °C–20 min	25
Chol-BB	420 °C–20 min	34
	420 °C–40 min	84
Chol-Py	420 °C–20 min	72

The enhanced conversion by incorporating an aromatic moiety suggests a strong effect of the substituted benzoquinoline part of the model compounds. Moreover, the wide range of conversion among the model compounds at the same conditions, 25–72% at 420°C – 20 min reaction, indicates the significant role of

the substituent group on the disappearance of the parent compound. Although the TGA results indicate minimal effect of the substituent groups on the cracking kinetics, the microreactor experiments suggest an important role in the conversion of the parent compound is played by the substituent group. This apparent discrepancy is due to the different types of reaction between the TGA and the microreactor experiments. In the TGA the effects of cracking and addition reactions (the later by the formation of coke) are obtained. On the other hand, the conversion in the microreactor experiments includes additional reactions, such as aromatization and dealkylations, which are discussed in detail later in this discussion.

The small cracked products in the microreactor experiments, with masses typically less than 300 Da, were identified by gas chromatography (GC) coupled with mass spectrometry (MS) and quantified by GCFID. The GC results show insignificant low-boiling fragments from all three compounds. For example, for Chol-Ph no appreciable products were observed. In the reactions of Chol-Py and Chol-BB, the GC-eluting products were not significant either, but loss of the substituent groups was observed, in addition to many minor peaks which could be trace fragments or contaminants. For example, in the pyrolysis of Chol-Py, pyrene, methylpyrene, and dimethylpyrene were formed at low concentrations. Among these products, pyrene was the major fragment detected in GC at a yield of only 6.8 moles for each 100 moles decomposed of Chol-Py. Similarly, Chol-BB yielded low amounts of both bibenzyl and methylbibenzyl at 1.7 and 4.4 moles per 100 moles converted of Chol-BB, respectively. These selectivities

apparently were maintained during the course of the reaction such that at 84% conversion, the yield was still at 1.2 and 2.6 moles for bibenzyl and methylbibenzyl, respectively, per 100 moles converted of Chol-BB. The loss of the substituent groups is likely via hydrogenolysis reactions. No evidence was observed in the GC analysis for products resulting from opening of the cholestane rings.

Since all the model compounds in this study have high boiling points, most of the products did not elute in GC. MALDI-MS was used instead to identify both the cracked products, with masses from 300 Da up to the mass of the parent compound, and addition products with masses higher than the parent compound. **Figure 6.5** shows the MALDI mass spectrum of the reaction products of Chol-Ph at 18% conversion. Only two major products are present, both 16 m/z units apart from Chol-Ph. The major cracked product ($m/z = 581$) is consistent with loss of a methyl group and a hydrogen to form a double bond, while the addition product indicates addition of a methyl group and a hydrogen to the parent. Subsequent reactions of these products gave mainly dealkylation and dehydrogenation or aromatization, giving rise to many new peaks as the reaction progresses, as shown in **Figure 6.6** for Chol-Ph at 25% conversion. The major cracked product in **Figure 6.6** has m/z of 579 which is likely the dehydrogenation product from the peak at m/z 581 observed at 18% conversion. The addition product of m/z 613 at 18% conversion also undergoes dehydrogenation to form m/z 611 product. A dimer is clearly observed as the major addition product with m/z of 1193.

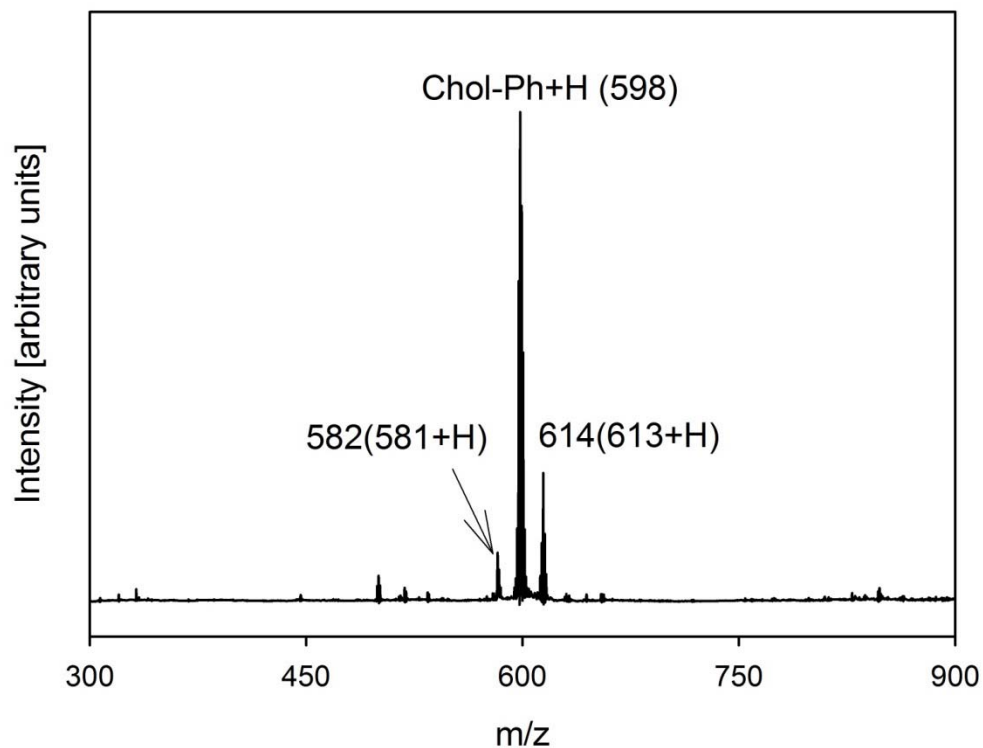


Figure 6.5: MALDI-MS of Chol-Ph reaction products at 375 °C–20 min. Only two major products are observed that are 16 m/z from the parent.

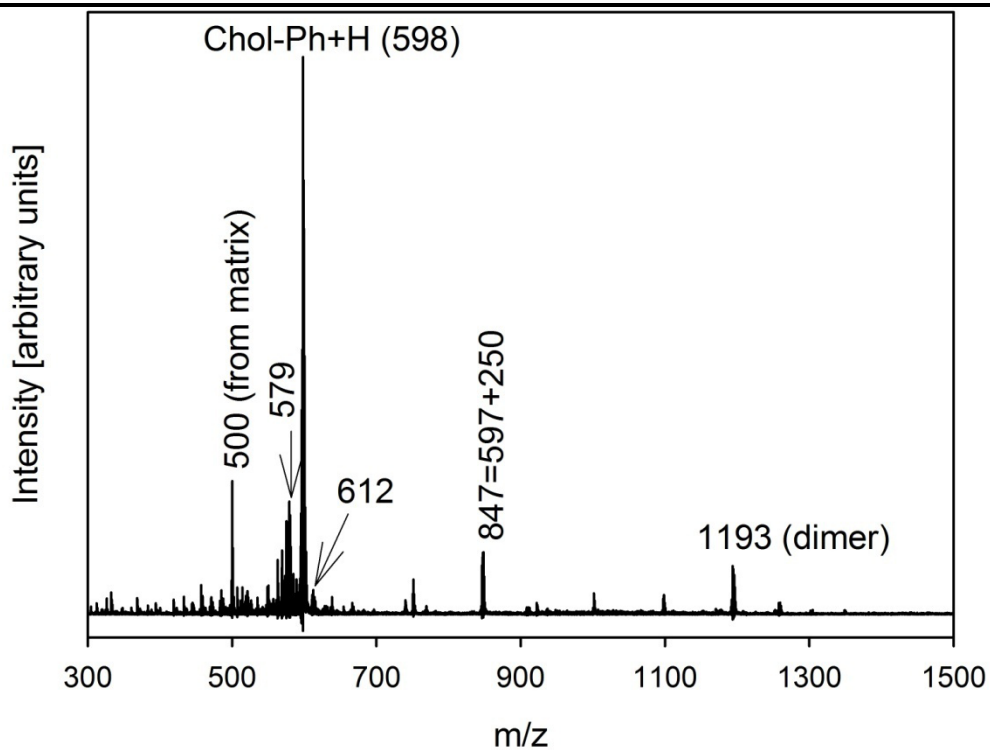


Figure 6.6: MALDI-MS of Chol-Ph reaction products at 420 °C–20 min.

Peaks due to adducts with the matrix are identified in **Figure 6.6** too. For example, the m/z 847 signal is made up of the parent and a molecule of the matrix. Also, the m/z 500 signal could be due to a product or adduct of two molecules of the matrix.

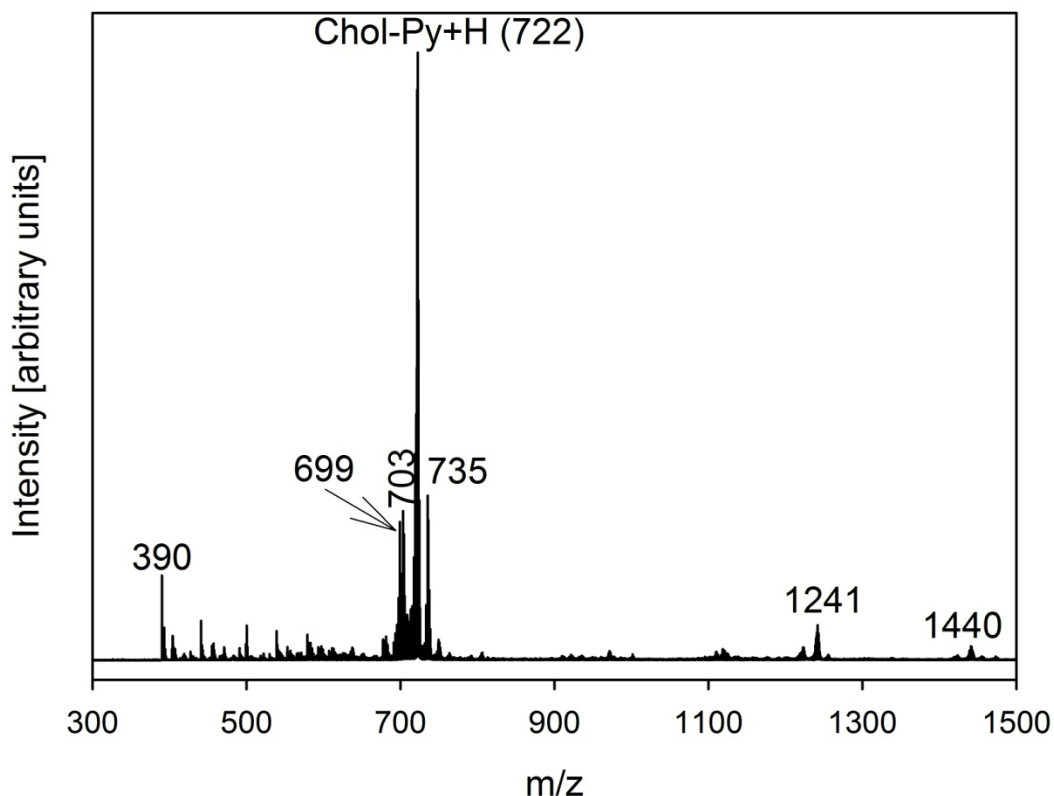


Figure 6.7: MALDI-MS of Chol-Py reaction products at 420 °C–20 min. More addition products are visible, consistent with the higher level of coke formation from this compound in TGA. Cracked products are mainly dealkylated and dehydrogenated structures of the parent with the product at m/z 390 likely due to loss of the pyrene substituent.

Similar trends were observed for Chol-Py, as illustrated in **Figure 6.7**. The major addition product has an m/z of 735, likely resulting from the dehydrogenation of the m/z 737 intermediate that would result from addition of a

methyl group and hydrogen, thus likely forming by the same pathway as the product at m/z 611 in Chol-Ph pyrolysis. The cracked products experience loss of a methyl group coupled with formation of a double bond as a major cracking pathway followed by further dehydrogenation and dealkylation, following the same trends as Chol-Ph. The lowest mass product at m/z 390 is consistent with the loss of the substituent group, pyrene, as well as loss of the side chain and partial dehydrogenation and demethylation in the cholestane rings.

Figure 6.8 shows the MALDI-MS of the reaction products of Chol-BB, which compares the products at relatively low (34%) and high (84%) conversions. Clearly, the cracked products that form at low conversion, such as the product at m/z 683, continue to dehydrogenate resulting in the product at m/z 679 instead of 683 as the major product. In addition to aromatization of the naphthenic rings, fragmentation of the side chain and/or loss of the methyl groups are the main types of reactions taking place. The low molecular weight addition products increase as the conversion increases, such as the product at m/z 716, but the high molecular weight products appear less stable, such as the dimer at m/z 1402, and they further crack or add to form new cracked or addition products. This pattern of addition of cracked fragments to the parent compound and its fragments is very similar to bridged pyrene and alkyl pyrene compounds under thermal cracking conditions (Chapter 5), which suggests similar pathways to coke formation from these compounds. No evidence of significant ring opening or loss of naphthenic rings, releasing mono-, di-, or tricyclic products, was observed from either MALDI or GC analyses in the three pyrolyzed model compounds.

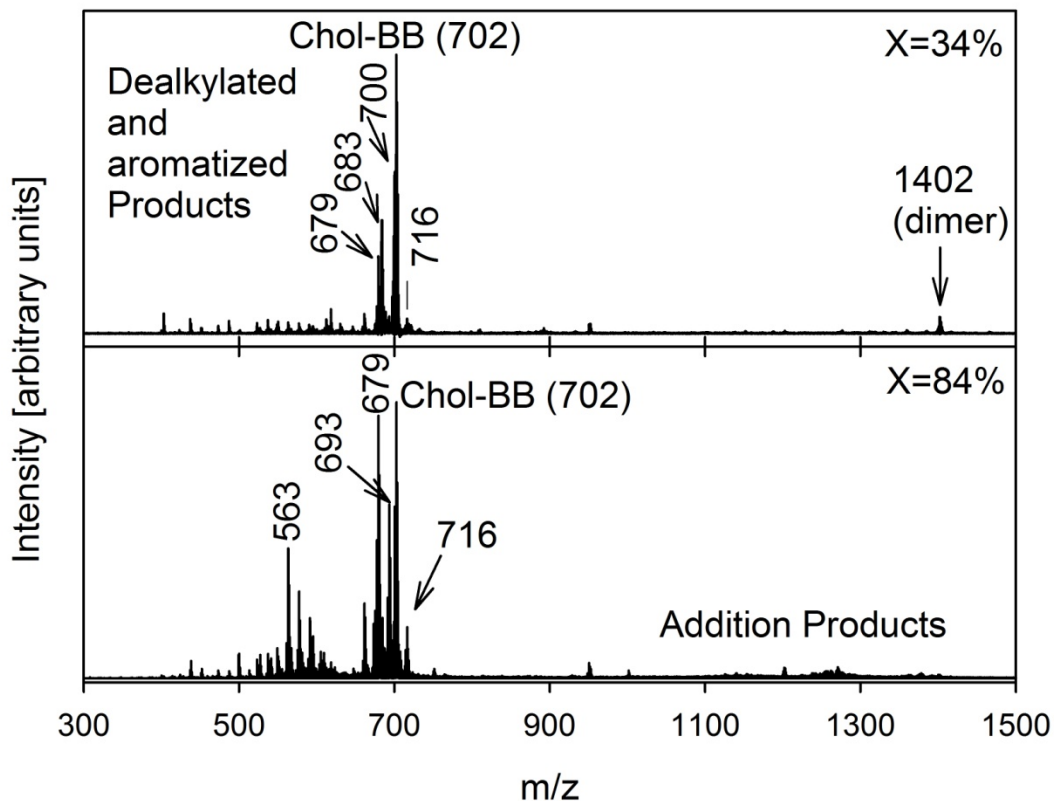


Figure 6.8: MALDI-MS of Chol-BB products of reactions at 34 and 84% conversion. Cracked products on the top spectra dehydrogenate and dealkylate to give the observed peaks in the bottom.

6.3.3 Addition Reactions and Coking.

All the model compounds formed solid residue, or coke, in the TGA experiments with Chol-Py forming the highest yield of coke. Analysis of Chol-Py before reaction by GCMS showed the presence of trace impurities. In the TGA experiment of Chol-Py, the weight loss below 200 °C was only 4 wt%, which is likely due to residual solvents or the detected trace impurities. The high coke yield, though, is not due to these impurities because they are present in low concentrations and evaporate prior to onset of decomposition. In addition, the high activation energy of Chol-Py cracking (225 kJ/mol), which is also within the

range observed for the rest of the compounds, suggests no significant effects of such impurities on the cracking kinetics or the coke yield. Therefore, the high coke yield of Chol-Py is not an artifact.

Chol-Py has the highest molar mass of the series of compounds, and loss of the side chain, for example, would give a higher boiling fragment than from the other compounds in the series. After loss of the side chain, the fragment resulting from Chol-Py would have a boiling point of 590 °C, as estimated using the Marrero and Gani⁷ group additivity method. The remaining fragments in the other model compounds, after cleaving the side-chain, will be lighter with estimated boiling points of 512, 515, 534, 546, and 553 °C for the fragments from Chol-Thio, Chol-Ph, Chol-Ph-*n*But, Chol-NP, and Chol-BB, respectively. The benzylic bonds in the substituent of Chol-BB and Chol-Ph-*n*But could suffer additional fragmentation making them even lighter and more susceptible to evaporation, with an estimated boiling point of only 521 °C for the resulting fragments. The fact that Chol-Py has the highest temperature for the maximum rate of weight loss (**Figure 6.4**) is consistent with the above arguments. However, the same progressive increase in maximum temperature and molar mass in **Figure 6.4** is not reflected in the yield of the solid residue shown in **Table 6.2**. Instead, the yield of residue was a minimum for Chol-BB and Chol-Ph-*n*But, and higher for the lighter and heavier compounds in the series. Therefore, volatility of the parent compounds and their fragments is not the only controlling factor in determining the coke yield.

All three model compounds examined in the microreactor formed addition products, as described above in the MALDI spectra. Chol-Py, in particular, showed qualitatively more addition products in the MALDI spectrum (**Figure 6.7**) compared to Chol-Ph or Chol-BB. These products are formed by addition reactions in the liquid phase, which contribute to formation of larger and cross-linked structures in model compounds² (Chapter 3) and bitumen fractions⁸ that could subsequently lead to coke formation. In addition to the direct observation in MALDI of formation of more addition products by Chol-Py, this compound is also the most reactive (i.e., having the highest conversion) among the three compounds examined at the same reaction conditions of 420 °C for 20 min in the microreactor. Moreover, the rate constant from TGA is the lowest of the series of compounds, therefore, the rate of weight loss is significantly lower than the rate of conversion of the parent compound. This discrepancy is consistent with more rapid formation of addition products which consume the parent compound and slow mass loss under the TGA conditions. Similar observations on formation of coke by highly reactive species were reported for different types of model compounds that are of an archipelago structure made by three aromatic cores and connected by ethano bridges (Chapter 5). Therefore, the higher tendency for Chol-Py to engage in addition reactions is consistent with its higher reactivity and degree of conversion in the microreactor as well as the formation of the largest amount of coke in the TGA experiments. The pyrene group must participate in the addition reactions more than the smaller aromatic groups in Chol-Ph, Chol-Thio, and Chol-NP, possibly due to the weaker aromatic character of the pyrene ring.

6.3.4 Dealkylation and Aromatization Reactions.

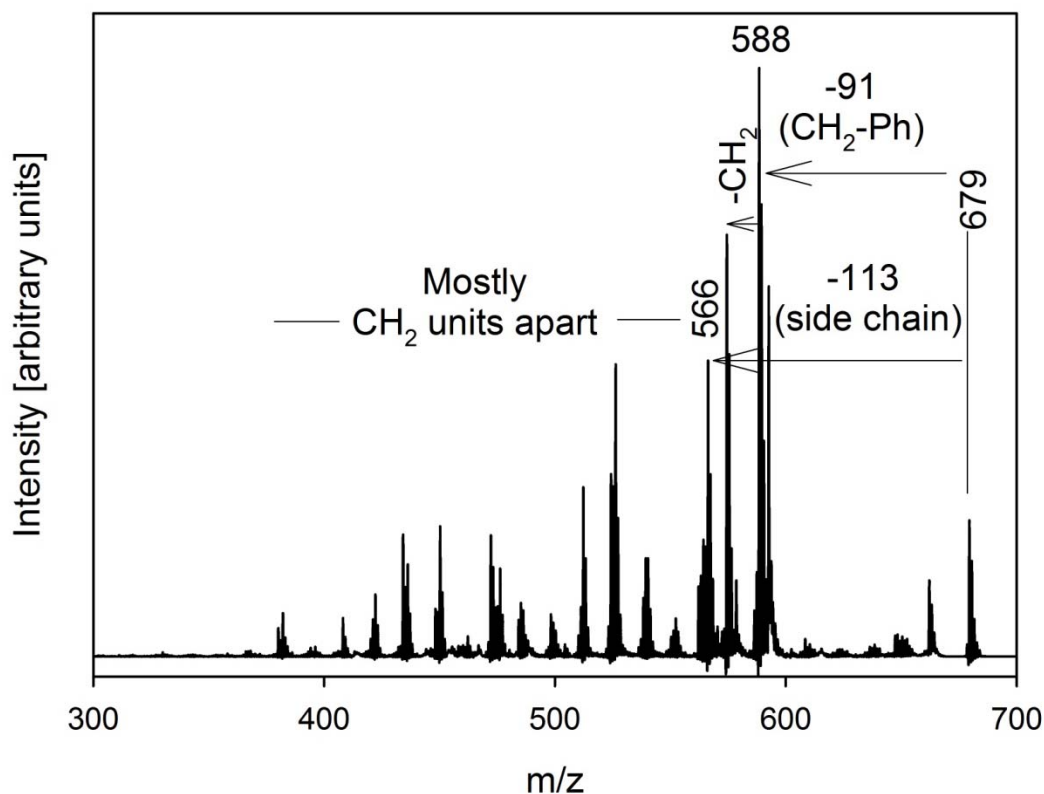


Figure 6.9: MALDI-MS/MS of the major product of m/z 679 from Chol-BB reaction at 420 °C–40 min. The cleavage pattern indicates that this product still has the alkyl chain and the bibenzyl group attached.

The MALDI spectra in **Figures 6.5–6.8** indicate initial formation of major products, both cracked and addition, by either methyl loss or addition. The presence of a labile bibenzyl bond in Chol-BB did not seem to give a significant alternative to this major decomposition pathway. **Figure 6.9** shows the tandem MALDI-MS/MS fragmentation pattern of the major cracked product of m/z 679 that formed in the pyrolysis of Chol-BB at 84% conversion (**Figure 6.8**). The fragmentation of the m/z 679 ion is consistent with a compound that still bears both the side chain and the bibenzyl group. This result is surprising because the

C–C bond in bibenzyl was expected to be the easiest bond to break to give two stable benzylic radicals. Since the major products in a free-radical chain mechanism typically form in the propagation steps, the MALDI results clearly suggest that cleavage of the bibenzyl C–C bond is not a major propagation step.

The side chain on the D-ring of the cholestane was expected to undergo significant fragmentation without necessarily altering the naphthenic ring structure, as observed in cholestane pyrolysis.^{4, 5} For example, Abbott et al.⁴ identified approximately 75% of the reaction products, after 34% conversion of 5 α -cholestane, as saturated products that mainly differ in the fragmentation degree of the attached side chain with both methyl groups (C18 and C19 in **Figure 6.1**) still in place. Exact structures of the unsaturated products were not proposed, although monounsaturated products of most of the saturated products were identified. Full aromatization of the C-ring was observed after cracking the D-ring and leaving the C18 methyl in place.^{4, 9} On the other hand, Carlson et al.¹⁰ suggested, based on NMR analysis of the reaction products of cholestane pyrolysis with palladium catalyst, that C18 methyl migration and the C-ring aromatization takes place prior to decomposition to other products. The methyl migration and C-ring aromatization were observed to take place simultaneously; unlike the loss of C19 methyl and the subsequent dehydrogenation of A- or B-rings, which seemed to occur independently. In this study, however, the initial reaction products at low conversion do not indicate that complete dehydrogenation takes place with the observed demethylation, such as in Chol-Ph at 18% conversion. Using the arguments of Carlson et al., the observed

demethylation is likely from the loss of the C19 methyl group rather than the C18 methyl. Moreover, forming the major products observed in the MALDI spectra with only methyl loss and methyl addition suggests that the demethylation is an important reaction step. The transformations in the work of Carlson et al. may have been catalytically-induced and would not necessarily take place in purely thermal reactions, but their insight on the demethylation mechanisms are valuable to compare to the extensive demethylation observed in the model compounds of this study without the use of catalyst.

To examine the energetics of the loss of the methyl group, an estimate of the bond dissociation energy (BDE) of the C10–C19 bond is given in **Figure 6.10 (A)**, using *trans*-decalin and 9-methyldecalin as an approximate structure. The estimated BDE of 71.9 kcal/mol (301 kJ/mol) is expected to be less in cholestane due to the additional substitution, by the C-ring, on the carbons adjacent to the radical. In the model compounds of this study, the presence of the aromatic group γ to the radical centre provides a possible stabilization by resonance with the aromatic rings that can subsequently lead to ring contraction, similar to that experienced by a radical at the 2-position in tetralin or hydroaromatics^{11, 12}, although no conclusive evidence that ring contraction takes place in these model compounds was obtained. Such stabilization offered by the nearby aromatic rings would likely make the BDE of the C19 methyl lower than all the C–C in the side chain and comparable, or even lower, than that in bibenzyl, which is estimated to range from 251³ to 279¹³ kJ/mol, making the demethylation of C19 an important reaction step.

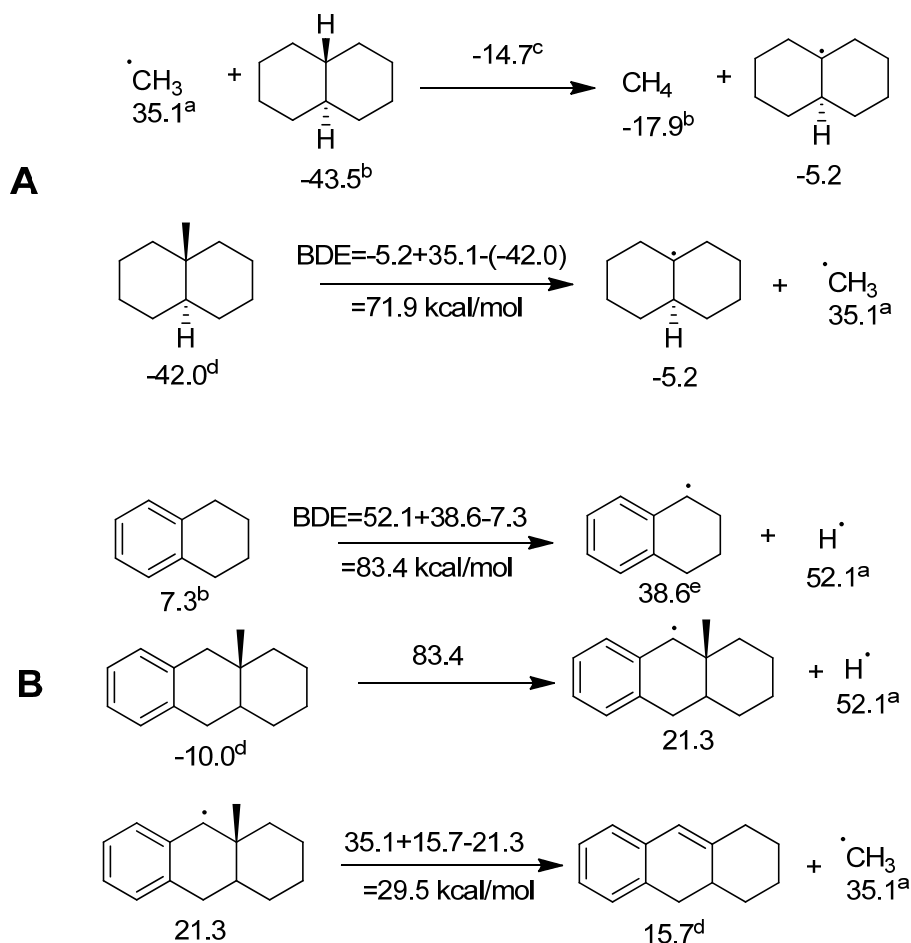


Figure 6.10: (A) Estimation of the BDE of the C10–C19 bond in cholestane using 9-methyldecalin as an approximation. (B) Estimation of the heat of reaction for the β -scission to expel a methyl group and form a double bond at the C1–C10 position in the cholestane part of the molecules. Values under the structures are the enthalpy of formation at 298 K, while those on the arrows are BDE or the enthalpy. All values are given in kcal/mol. ^a McMillen, D. F.; Golden, D. M., *Annu. Rev. Phys. Chem.* **1982**, 33, 493-532. ^b Cox, J. D; Pilcher, G. *Thermochemistry of Organic and Organometallic Compounds*. Academic Press: New York, 1970. ^c Chae, K.; Violi, A. *J. Org. Chem.* **2007**, 72, 3179-3185. ^d Marrero, J.; Gani, R. *Fluid Phase Equilib.* **2001**, 183, 183-208. (using a courtesy software that employs the method). ^e Franz, J. A.; Barrows, R. D.; Camaioni, D. M. *J. Am. Chem. Soc.* **1984**, 106, 3964-3967.

For comparison, the BDEs for the C–C bonds in the side chain are 316, 330, 335, 336, and 339 kJ/mol for C17–C20, C24–C25 and C20–C22, C25–C26(C27), C23–C22(C24), and C20–C21, respectively. These values were extrapolated from McMillen and Golden¹⁴ for *i*C₃H₇–*i*C₃H₇, *i*C₃H₇–*n*C₃H₇, CH₃–*s*C₄H₉, C₂H₅–*n*C₃H₇, and CH₃–*i*C₃H₇, respectively, to resemble the corresponding bonds in the side chain of cholestane. These estimates suggest that the C19 methyl group is more likely to cleave and initiate the decomposition of the compound compared to the bonds in the side chain.

The high energy required to crack the C19 methyl group suggests propagation step that is more energetically–favorable is responsible for the extensive demethylation rather than simple homolysis. If a radical is formed at the C1 position after abstracting a benzylic proton, which also benefits the radical stabilization offered by the neighboring aromatic rings, loss of the C19 methyl via β -scission to form a double bond between the C1 and C10 carbons can occur. **Figure 6.10 (B)** shows the estimation of the energy required for the β -scission using the C–H BDE to form 1-tetralyl radical and a hydroaromatic structure to resemble the part of the model compounds that experience the β -scission, with replacing the pyridyl with a benzyl ring. The enthalpy for the expulsion of C19 methyl via β -scission is then estimated to be only 29.5 kcal/mol (123 kJ/mol). Moreover, the activation energy for the β -scission in 1-tetralyl radical to form 1,2-dihydronaphthalene and hydrogen atom is estimated to be 172 kJ/mol.¹⁵ Due to the additional substitution in the hydroaromatic structure shown in **Figure 6.10 (B)**, and that the expelled radical is methyl rather than hydrogen, the activation

energy for the β -scission is then expected to be less than 172 kJ/mol but higher than 123 kJ/mol (the enthalpy change). Estimates of both the activation energy and the change in enthalpy thus suggest that the β -scission is far more energetically favorable than simple homolysis and thus is a feasible propagation step.

Once demethylation and hydrogen loss between C1 and C10 take place, dehydrogenation of the rings, loss or migration of C18 methyl group, and fragmentation of the side chain likely follow. **Figure 6.11** shows the ^1H -NMR spectra of the aliphatic region of Chol-BB, before and after the reaction at two conversion levels. The resonances at δ 0.68 and 0.93 arise from C18 and C19 methyl groups, respectively, where both signals clearly decrease relative to other methyl groups as the conversion increases. At 84% conversion, the intensity of the C19 signal is even lower than that arising from C18 indicating preferential loss of the C19 methyl group. The strong resonance at δ 1.26 is observed in the reaction products of all the compounds, as well as in some of the reactants; therefore, it is likely due to a contaminant such as *n*-hexadecane. The resonance at δ ~1.4, marked with an asterisk in **Figure 6.11**, is also from a known contaminant (diethylphthalate) that was probably introduced during concentration in the rotary evaporator.

The resonance of bibenzyl protons is clearly still present after 84% conversion of Chol-BB as shown in **Figure 6.11**, although new resonances appeared close to it suggesting the formation of new benzylic protons. An example would be methylbibenzyl, which was detected in GC and can give

different coupling pattern of the benzylic protons. Another contribution would be the partial dehydrogenation of one ring that is adjacent to an aromatic ring. Such products are expected to be responsible for most of these new resonances based on the results from the MALDI experiments.

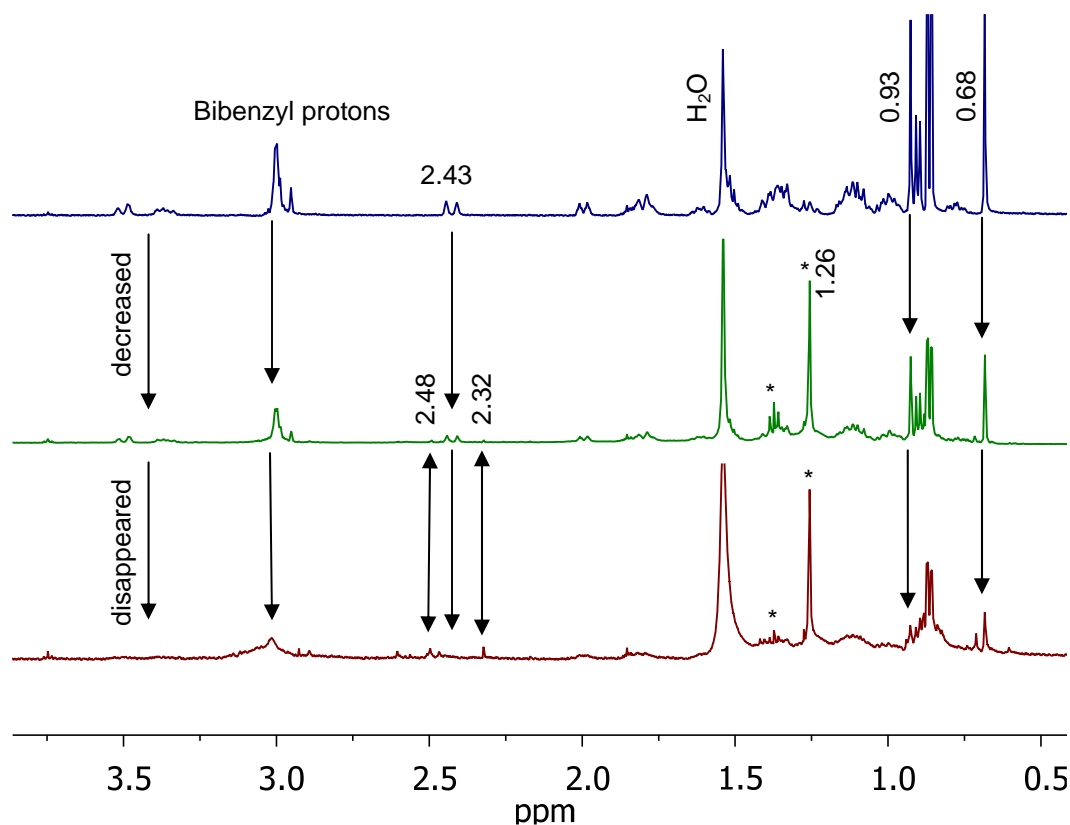


Figure 6.11: The aliphatic region in the ¹H-NMR of Chol-BB before reaction (top), at 34% conversion (middle), and at 84% conversion (bottom). Resonances with an asterisk are contaminants.

Figure 6.12 shows the experimental and simulated spectra for Chol-BB. Protons that give clear resonances and are expected to experience changes during the course of the reaction are marked **a–f**. For example, the **a** and **b** resonances which arise from C18 and C19 methyl groups, respectively, were observed to

decrease in **Figure 6.11**. Similarly, tracking the changes to the **c** and **d** resonances, which arise from the protons at C1 and C4, respectively, could give evidence for dehydrogenation of the A–ring.

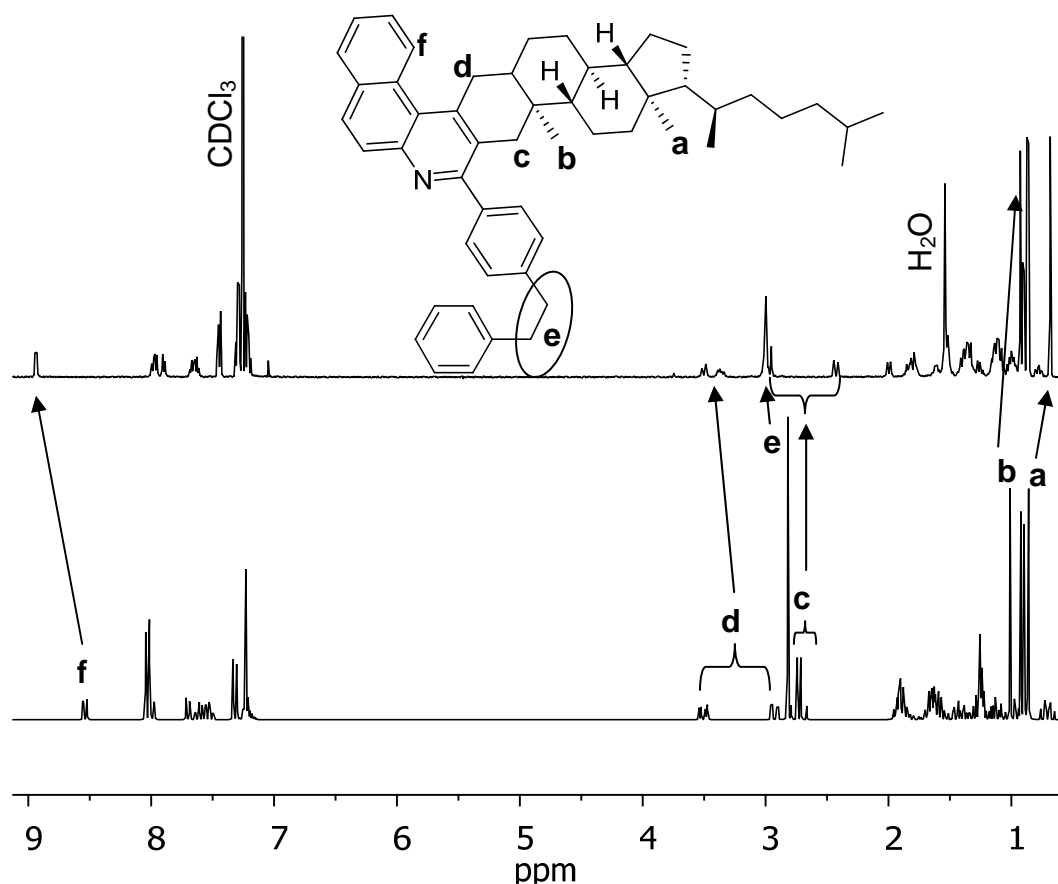


Figure 6.12: Comparison of the experimentally measured ^1H -NMR spectrum for Chol-BB (top) and the calculated or simulated spectrum using MestReNova (bottom). The arrows show the position of corresponding resonances in the experimental spectrum for some protons.

The simulation software reasonably predicts the chemical shift and the coupling pattern, although the shifts differ slightly from the experimental values by up to 0.2 ppm. For example, the benzylic protons are experimentally measured at δ 3.00

(with reference to CDCl₃ at 7.26 ppm) while the simulated value was at δ 2.82. Nevertheless, the ability of the software to predict the resonances of such complex structures is a powerful tool in examining possible products that could give rise to the observed resonances in the experimental spectra

Figure 6.13 shows expansions of the ¹H-NMR spectra of the benzylic region in **Figure 6.11**. The bottom two simulated spectra in **Figure 6.13** are for the structures **(a)** and **(b)** shown in **Figure 6.14**, which are suggested structures for the major cracked product at *m/z* 679 observed in the reaction products of Chol-BB (**Figure 6.8**). Since the simulated spectra were not at the correct shift, as shown in **Figure 6.12**, the simulated spectra in **Figure 6.13** were shifted with reference to the bibenzyl protons at δ 3.00 to align them with experimental values. The suggested structures give rise to new resonances that are consistent with the experimental resonances that appeared after the reaction. For example, the resonances at δ 2.35 and 2.48, which appeared after the reaction and increased in intensity with conversion, could arise from the C12 and C11 protons, respectively, in a partially hydrogenated C-ring in a structure similar to that shown in **Figure 6.14 (b)**. Similarly in such a structure, the protons of the partially hydrogenated B-ring and those at C15 are also calculated to give rise to resonances similar to those observed experimentally as shown in **Figure 6.13**.

The structure in **Figure 6.14 (a)**, which has the same mass as **(b)**, would also give rise to new benzylic resonances such as the δ 2.91 and 3.30 which could arise from the protons at the C14 and C11, respectively. The appearance of these aliphatic protons was coupled with the decrease or disappearance of other

resonances, such as those at δ 2.43, 2.95 and δ 3.33–3.51, which arise from C1 and C4 protons, respectively (**c** and **d** protons in **Figure 6.12**, respectively). The disappearance of signals for these protons, especially at higher conversion, indicates complete aromatization of the A–ring.

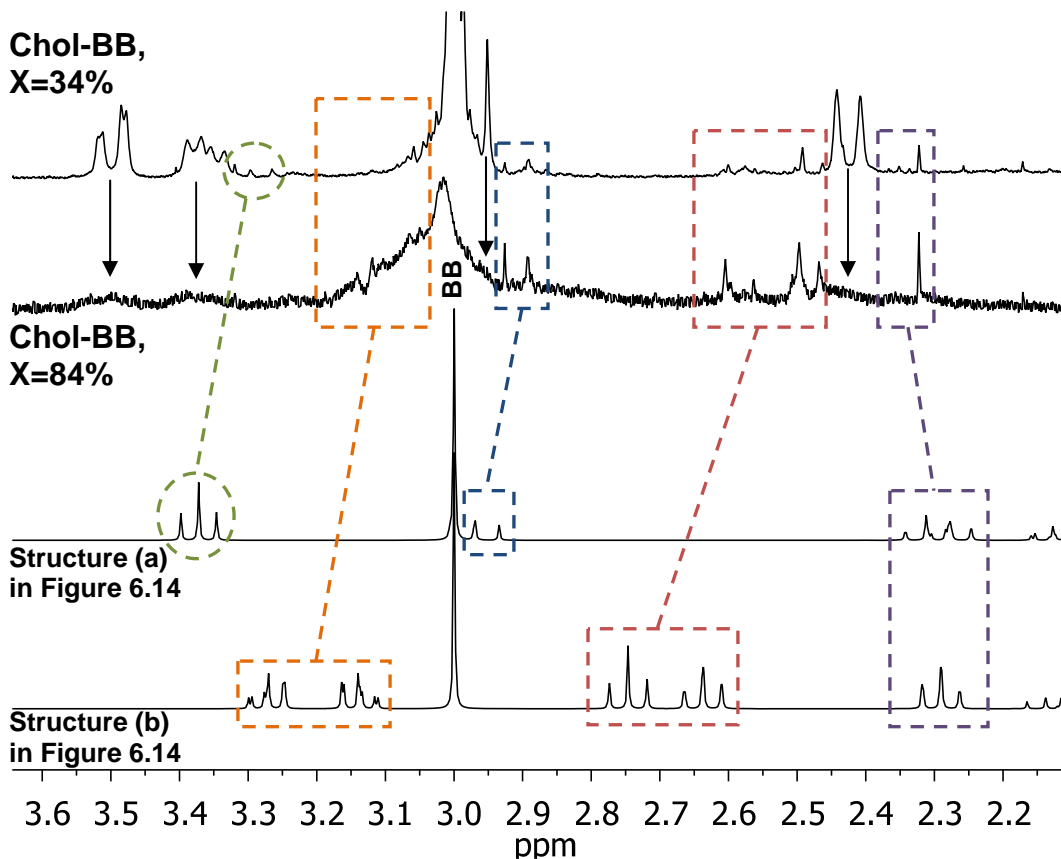


Figure 6.13: Enlarged region around the benzylic position of the NMR spectra of Chol-BB at 34% and 84% conversion along with the simulation of the two possible structures of the major cracked product of 679 m/z shown in **Figure 6.14**. BB denotes the resonance arising from the benzylic protons in bibenzyl (protons **e** in **Figure 6.12**).

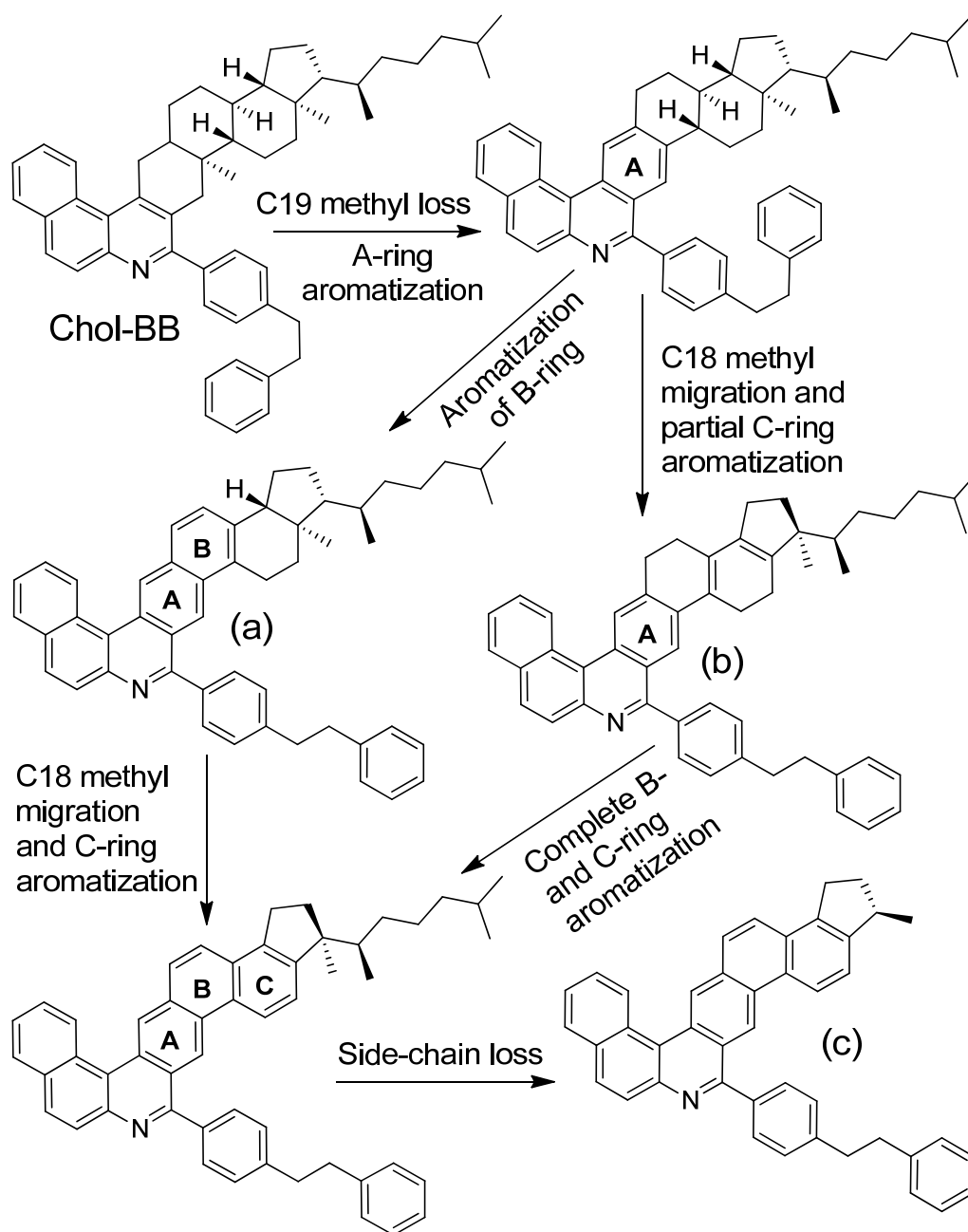


Figure 6.14: Suggested decomposition pathway for Chol-BB to form the major cracked products of m/z 679 (**(a)**) and (**(b)**). Subsequent aromatization of A, B, and C rings with loss of the 8-carbon side chain (after methyl migration in (**(a)**)) would give the (**(c)**) product of m/z 563 from both (**(a)**) and (**(b)**).

In addition to the appearance and disappearance of signals in the aliphatic regions, the aromatization of the rings is also supported by the appearance of

many new signals in the region expected for aromatic protons as shown in **Figure 6.15**. For example, the resonances of the deshielded proton appearing after δ 9.2 are consistent with protons at C1 and C4 in compounds where the A, B, and C-rings are completely aromatized. The NMR analysis of Chol-Ph and Chol-Py showed similar results to the observations made for Chol-BB. The resonances marked with an asterisk in **Figure 6.15** are also from the diethylphthalate contaminant that gave resonances in **Figure 6.11** (experiment closely matches simulated resonances of diethylphthalate at δ 8.03, 7.72, 4.31, and 1.30 ppm).

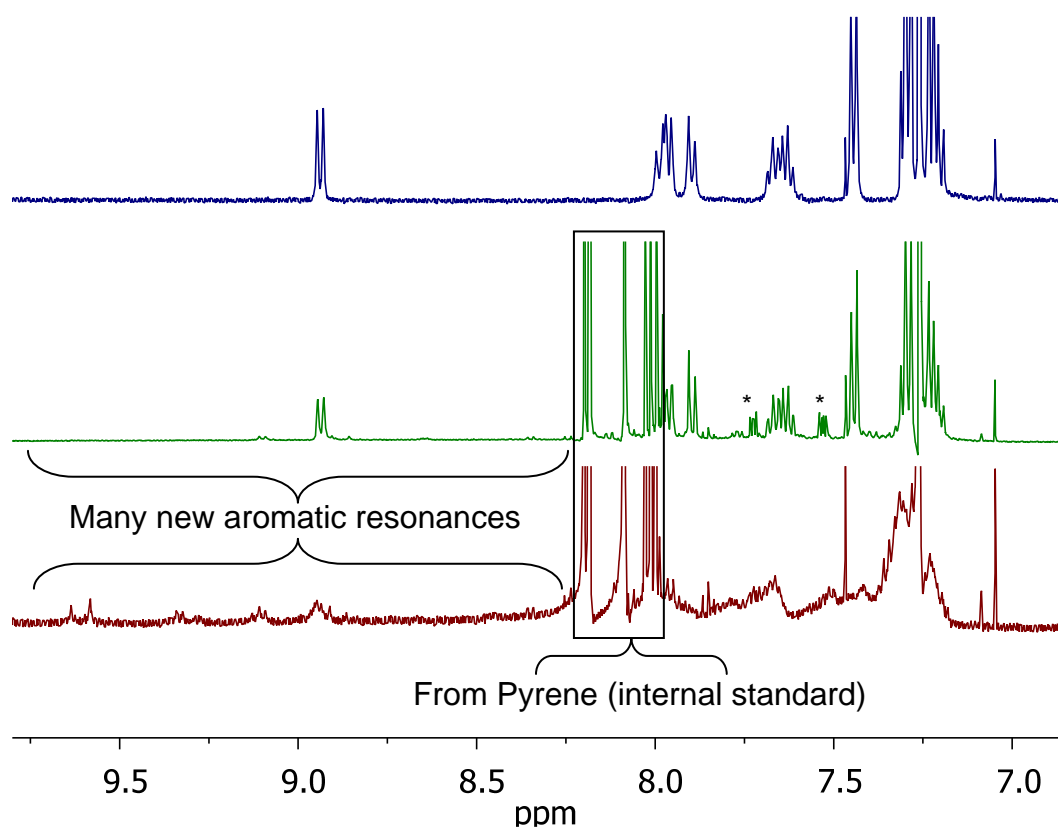


Figure 6.15: The aromatic region in the ^1H -NMR of Chol-BB before reaction (top), at 34% conversion (middle), and at 84% conversion (bottom). The resonances marked with an asterisk are from a known contaminant (diethylphthalate, also the ones at $\delta \sim 1.4$ in **Figure 6.11**).

6.3.5 Summary of Decomposition Pathways

The proposed decomposition pathways for Chol-BB to give the major cracked product of m/z 679 at 84% conversion are represented in **Figure 6.14** based on the arguments on the loss of methyl groups, the ^1H -NMR results, the MALDI-MS of Chol-BB (**Figure 6.8**) and tandem MS/MS of this product (**Figure 6.9**). These products would result by either loss of the C19 methyl at the 10 position, followed by losing one hydrogen atom at C1 to form a double bond, or by the more energetically-favorable path of hydrogen abstraction at the benzylic position, C1, followed by demethylation via β -scission. Complete aromatization of the A-ring, the ring adjacent to benzoquinoline, then takes place rapidly. These first steps in the reaction mechanism can also be inferred more clearly from the MALDI-MS results of Chol-Ph (**Figures 6.5 and 6.6**) as well as Chol-Py (**Figure 6.7**) as discussed above. Although Carlson et al.¹⁰ suggested that the C-ring aromatization occurs first after C18 methyl migration in the pyrolysis of cholestane, this reaction does not seem to be the first step in the model compounds because an initial loss of only two hydrogens (**Figure 6.5**) and then four hydrogens (**Figures 6.6, 6.7, top spectrum of 6.8**) was coupled with the methyl loss rather than six hydrogens that are required to aromatize the C-ring. After the A-ring aromatization, a conjugated double bond forms at the C8-C9 position followed by either complete B-ring aromatization to give structure **(a)** or dehydrogenation at the C13-C14 position, which is coupled with C18 methyl migration to C17, giving structure **(b)**. Aromatizing the C-ring in **(a)** will require the C18 methyl to cleave or migrate which will give the same product as **(b)** after

complete aromatization of B- and C-rings. Subsequent dealkylation and dehydrogenation of these structures is consistent with the observed masses in the MALDI spectrum in **Figure 6.8**. For example, complete aromatization of A-, B-, and C-rings with dealkylation of the side chain, leaving the migrated methyl in place, would give a cracked product of m/z of 563 (structure (c) in **Figure 6.14**), which is observed at the higher conversion level in **Figure 6.8**. Suggesting two possible structures to explain the new resonances in NMR is important since the reaction products are expected to be a mixture of many different structures during the course of the reaction.

The above results suggest that when an aromatic moiety is fused with naphthenic rings, the reaction of the saturated rings is accelerated, likely, by facilitating dehydrogenation and dealkylation of methyl groups or side chains attached to the naphthenic rings. In addition to dealkylation and dehydrogenation reactions, the naphthenic rings in such structures may experience ring contraction and rupturing to give alkylated aromatics but *not* crack into mono-, di-, or tri-cyclic products. No significant cracking of the backbone of these model compounds was observed, so that neither the cholestane moiety nor smaller naphthenic ring groups were released, even at high conversion levels. Since biomarkers are released during the thermolysis of kerogen and asphaltenes, the results suggest that these “free” biomarkers are predominantly linked to larger structures via labile bonds such as alkyl, ester, ether, or sulfide tethers rather than being fused in aromatic structures, as suggested by a number of studies.^{16, 17}

Fused combinations of biomarkers and aromatics, analogous to the series of compounds examined here, were detected in crude oils by Oldenburg et al.¹ These fused aromatic-cycloalkyl species are more reactive than cholestane, likely by providing easily-abstractable benzylic protons to give free-radical intermediates, which subsequently leads to the rapid conversion of the whole molecule through dealkylation and dehydrogenation reactions. The thermal cracking of heavy petroleum fractions is accompanied by both significant yields of methane^{18, 19} and an increase in aromatic carbon²⁰. The results of this study suggest that composite aromatic-cycloalkyl compounds can react to contribute selectively to these observations, with much less loss of attached side groups than expected. In the present series of compounds, the alkyl side chains and aromatics on two-carbon bridges were much more resistant to cleavage or cracking than expected.

6.4 CONCLUSIONS

1. Fusing cholestane with aromatic rings enhances the conversion of the whole molecule compared to cholestane alone.
2. The most important reactions of these model compounds were demethylation, dehydrogenation, and side-chain fragmentation.
3. The demethylation is an important reaction step. Extensive dehydrogenation and side-chain fragmentation likely commences only after demethylation and/or methyl migration takes place.
4. Mono-, di-, or tri-cyclic products were not detected from the pyrolysis of model compounds having naphthenic groups (cholestane) fused with substituted benzoquinoline aromatic group.

6.5 REFERENCES

1. Oldenburg, T. B. P.; Huang, H.; Donohoe, P.; Willsch, H.; Larter, S. R., High molecular weight aromatic nitrogen and other novel hopanoid-related compounds in crude oils. *Org. Geochem.* **2004**, 35, 665-678.
2. Alshareef, A. H.; Scherer, A.; Tan, X.; Azyat, K.; Stryker, J. M.; Tykwinski, R. R.; Gray, M. R., Formation of archipelago structures during thermal cracking implicates a chemical mechanism for the formation of petroleum asphaltenes. *Energy Fuels* **2011**, 25, 2130-2136.
3. Miller, R. E.; Stein, S. E., Liquid-Phase Pyrolysis of 1,2-Diphenylethane. *J. Phys. Chem.* **1981**, 85, 580-589.
4. Abbott, G. D.; Bennett, B.; Petch, G. S., The Thermal-Degradation of 5-Alpha(H)-Cholestane during Closed-System Pyrolysis. *Geochim. Cosmochim. Acta* **1995**, 59, 2259-2264.
5. Kissin, Y. V., Catagenesis of Light Cycloalkanes in Petroleum. *Org. Geochem.* **1990**, 15, 575-594.
6. Abbott, G. D.; Lewis, C. A.; Maxwell, J. R., Laboratory simulation studies of steroid aromatisation and alkane isomerisation. *Org. Geochem.* **1984**, 6, 31-38.
7. Marrero, J.; Gani, R., Group-contribution based estimation of pure component properties. *Fluid Phase Equilib.* **2001**, 183, 183-208.
8. Gray, M. R.; McCaffrey, W. C., Role of chain reactions and olefin formation in cracking, hydroconversion, and coking of petroleum and bitumen fractions. *Energy Fuels* **2002**, 16, 756-766.

9. Mango, F. D., The Origin of Light Cycloalkanes in Petroleum. *Geochim. Cosmochim. Acta* **1990**, 54, 23-27.
10. Carlson, R. M. K.; Croasmun, W. R.; Chamberlain, D. E. *Transformations of Cholestane Useful for Probing Processing Chemistry*, Proceedings of the 210th National Meeting of the American Chemical Society, Chicago, IL, Aug 20-25, 1995; p 685.
11. Cronauer, D. C.; Jewell, D. M.; Shah, Y. T.; Modi, R. J.; Seshadri, K. S., Isomerization and Adduction of Hydrogen Donor Solvents under Conditions of Coal Liquefaction. *Ind. Eng. Chem. Fund.* **1979**, 18, 368-376.
12. Collin, P. J.; Gilbert, T. D.; Rottendorf, H.; Wilson, M. A., Ring Contraction and Dehydrogenation in Polycyclic Hydroaromatics at Coal-Liquefaction Temperatures. *Fuel* **1985**, 64, 1280-1285.
13. Zavitsas, A. A., The relation between bond lengths and dissociation energies of carbon-carbon bonds. *J. Phys. Chem. A* **2003**, 107, 897-898.
14. McMillen, D. F.; Golden, D. M., Hydrocarbon Bond-Dissociation Energies. *Annu. Rev. Phys. Chem.* **1982**, 33, 493-532.
15. Poutsma, M. L., Free-Radical Thermolysis and Hydrogenolysis of Model Hydrocarbons Relevant to Processing of Coal. *Energy Fuels* **1990**, 4, 113-131.
16. Strausz, O. P.; Lown, E. M., *The Chemistry of Alberta Oil Sands, Bitumens, and Heavy Oils*. AERI: Calgary, AB, 2003.

17. Stalker, L.; Larter, S. R.; Farrimond, P., biomarker binding into kerogens: evidence from hydrous pyrolysis using heavy water (D₂O). *Org. Geochem.* **1998**, 28, 239-253.
18. Moschopedis, S. E.; Parkash, S.; Speight, J. G., Thermal Decomposition of Asphaltenes. *Fuel* **1978**, 57, 431-434.
19. Sanford, E. C., Molecular Approach to Understanding Residuuum Conversion. *Ind. Eng. Chem. Res.* **1994**, 33, 109-117.
20. Japanwala, S.; Chung, K. H.; Dettman, H. D.; Gray, M. R., Quality of distillates from repeated recycle of residue. *Energy Fuels* **2002**, 16, 477-484.

CHAPTER 7

THERMOGRAVIMETRIC ANALYSIS OF BINARY MIXTURES OF MODEL COMPOUNDS

7.1 INTRODUCTION

Although the thermal reactions of individual model compounds revealed many insights on reaction pathways and product selectivities (Chapter 3, 5, and 6), these observations provide limited information on the possible interactions within complex, multifunctional, and multi-component systems like the asphaltenes. The free radicals generated from one molecule in the asphaltenes can interact with another molecule, which then result in reaction pathways, kinetics, and product yields that are different from the reaction of these two molecules separately.¹ Such interactions are evident from the binary experiments presented in Chapter 5, where benzo[a]pyrene added to the archipelago compounds affected both the reaction rate of the parent compound and the product yields.

Few literature studies are available on binary mixtures that highlight the effect of binary interactions on the overall reaction network. For example, Kruse et al.² examined the pyrolysis of mixtures of polypropylene and polystyrene to

develop a quantitative understating of the binary interactions present during co-processing of solid plastic wastes. Zhou and Crynes³ pyrolyzed *o*-ethylphenol with dodecane, to investigate the behavior of oxygen-containing model compounds of coals, and found that the rate of cracking of both species was affected, where dodecane cracking was inhibited while the cracking of *o*-ethylphenol was enhanced. Similarly, Savage¹ developed a reaction model to simulate the pyrolysis of mixtures of *n*-pentadecylbenzene and *n*-tridecylcyclohexane compounds and provided a methodology for assessing the acceleration or inhibition of conversion of one compound by the addition of another. Smith and Savage⁴ investigated hydrogen transfer mechanisms in thermal reactions of polycyclic alkylaromatics in binary mixtures and found that the structure of polycyclic aromatics in complex mixtures strongly affected hydrogenolysis and decomposition reactions.

In this chapter, the effect of binary interactions in model compounds on the coke yield and cracking kinetics is examined. Due to limited availability of the model compounds, full analysis of reaction pathways and product yields at controlled conversions using microreactor experiments was not feasible. Rather, six model compounds were mixed with each other at different ratios (two compounds at a time) and were thermally cracked using thermogravimetric analysis (TGA). The TGA data provided information on the coke yield and overall cracking kinetics of these binary mixtures.

7.2 MATERIALS AND METHODS

The six model compounds employed in this study, P-Th-P, P-BiTh-P, P-2,5-pyr-3-Me-P, P-3,5-pyr-P, P-*m*Ph-P, and 1,3,6,8-tetrahexylpyrene (THP), are shown in **Figure 7.1** (see **Table 5.1** for full name for the archipelago structures). Binary mixtures of these compounds were prepared with different ratios by mixing the appropriate amount of each compound in a powder form. A spatula was used to achieve thorough mixing. Addressing the possibility of inadequate mixing following this simple approach, one sample (P-BiTh-P + P-*m*Ph-P) was thoroughly mixed using solvent mixing but the results did not differ from those obtained by simple mechanical mixing (**Table 7.1**). For the solvent mixing, the prepared mixture was first mixed as usual with spatula but then dissolved completely in excess methylene chloride (MC). The sample was shaken thoroughly and then the vial was left in the fume hood to evaporate most of the MC. The mixture was then loaded on the TGA pan. A small amount of MC was used to extract all materials from the vial and the extract was loaded on the pan drop-wise with a pipette. The pan was then gently blown with air to dry MC completely before loading in the TGA.

The experiments were done on a Thermo Cahn TherMax400 TGA (Thermo Electron Corporation, Waltham, MA). In a typical procedure, 4–5 mg of the sample was loaded on a platinum pan and was heated at 10 °C/min to 500 °C, and the temperature was then held at 500 °C for 15 min to obtain an approximate value of the micro-carbon residue (MCR) content. Inert conditions were maintained throughout the experiment by using Argon gas flowing at 80 mL/min

with a separate purging flow through the balance chamber at high flow rate to prevent condensation of products on the hanging wire or the balance.

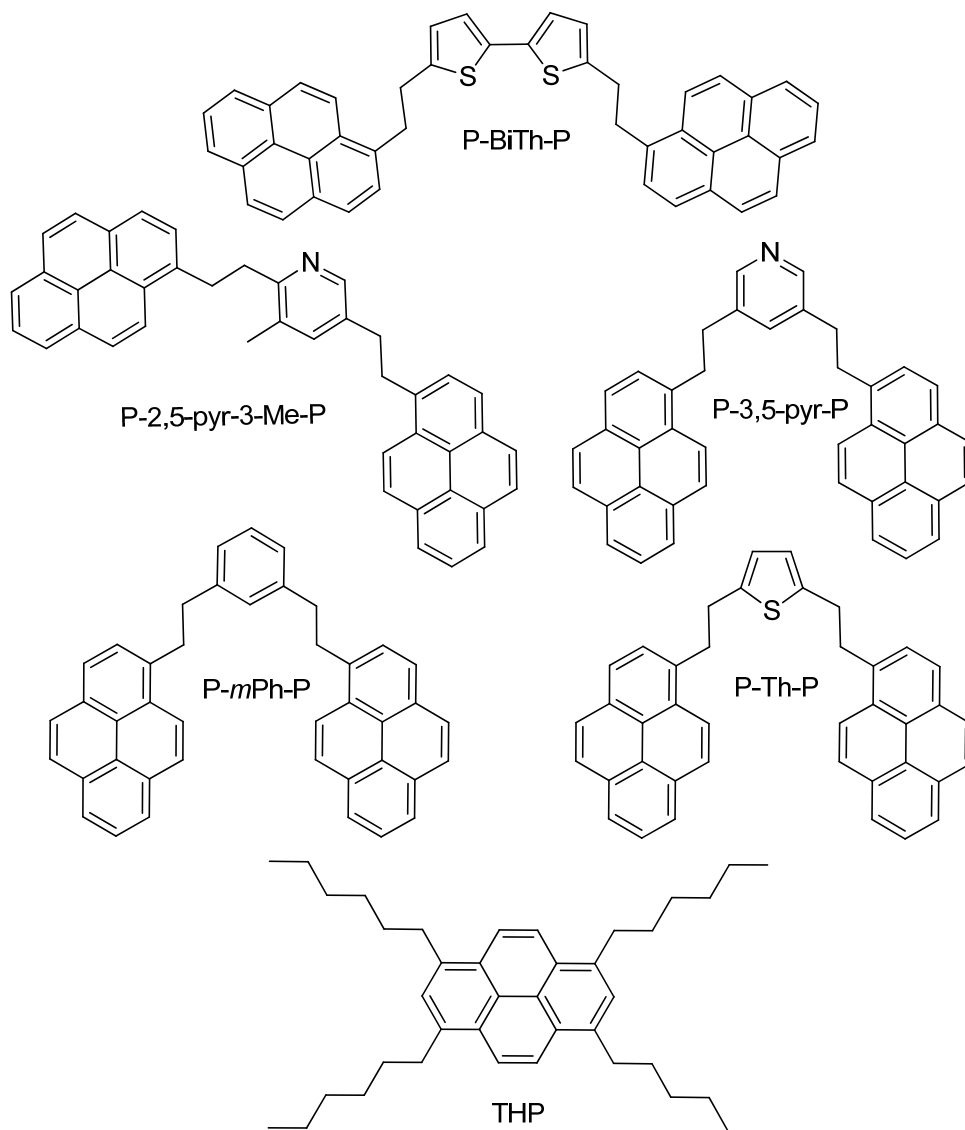


Figure 7.1: The molecular structures of the model compounds used in this study.

Initial experiments with P-3,5-pyr-P + P-mPh-P were performed twice on each mixture to confirm repeatability. After repeatability was established, most other experiments were performed only once due to the limited amounts available of each compound.

7.3 RESULTS AND DISCUSSION

A complete list of all the TGA experiments with the binary mixtures is shown in **Table 7.1**. The weight loss below 200 °C was less than 3 wt% in all experiments except the pure P-Th-P and samples containing P-2,5-pyr-3-Me-P. These low values suggest that no significant residual solvents or contaminants are present, and since the cracking is insignificant below 200 °C, this weight loss was ignored. The onset of decomposition is the temperature at which 5 wt% of the sample is lost after 200 °C. The temperatures are high in all the examined samples, except for those with THP, with a minimum of 325 °C and values in the range of 350–380 °C for most experiments, indicating that the mass losses are mainly due to cracking followed by weight loss rather than evaporation. The low temperatures in the case of THP indicate evaporation of this compound prior to reaching temperature ranges where the rate of thermal cracking is expected to be significant. Observing two distinct peaks in the TGA results of mixtures of THP and P-3,5-pyr-P, as will be shown below, along with the low apparent activation energies (E) and the pre-exponential factors (A) support the partial loss of THP due to evaporation.

The coke yield in the binary experiments showed two distinct behaviors along with the corresponding E values. In each binary mixture we compare the coke yield to the simple additive case, where the total coke yield is the mass-weighted coke yield from the two components:

$$Y_{coke,T} = w_1 Y_{coke,1} + w_2 Y_{coke,2} \quad (7.1)$$

where w is the weight fraction of each component.

Table 7.1: List of All TGA Binary Experiments

Mixture (A+B)	Fraction (A/(A+B))	Wt Loss <200 °C	T at 5% Wt Loss, °C	Coke, Wt%	E, kJ/mol	Log (A, min ⁻¹)
P-3,5-pyr-P + P-mPh-P	0	1.68	387	3.41	201.3	14.12
	0.334	1.89	368	8.93	177.4	12.45
		1.93	367	10.29	178.5	12.52
	0.501	2.39	372	14.74	171.7	11.97
		2.25	369	13.91	173.3	12.10
	0.669	2.44	359	19.94	161.1	11.19
		2.33	357	18.26	160.7	11.19
	1	2.81	354	33.37	140.4	9.62
	0	1.04	279	0.60	153.2	12.77
P-3,5-pyr-P + THP	0.251	1.61	269	7.37	123.5 ^a /101.3	10.15 ^a /7.10
	0.497	1.89	275	12.04	104.5 ^a /120.5	8.29 ^a /8.49
	0.746	2.36	278	20.31	91.0 ^a /123.8	6.92 ^a /8.67
		2.16	280	20.73	87.2 ^a /123.2	6.53 ^a /8.57
	0.252	1.33	367	8.07	173.8	12.48
P-BiTh-P + P-mPh-P	0.504	1.40	366	11.70	190.3	13.88
	0.50 ^b	2.39	366	11.94	193.6	14.11
	0.753	1.20	364	17.87	206.4	15.28
	1 ^d	0.928	360	22.06	217.0	16.23
	0	3.80	377	7.48	246.7	18.14
P-BiTh-P + P-Th-P	0.501	2.85	364	14.58	214.0 ^c	15.92 ^c
	1 ^d	0.934	377	23.07	223.9	16.34
	0	3.80	377	7.48	246.7	18.14
P-2,5-pyr-3-Me-P + P-mPh-P	0.496	4.91	342	5.63	179.3	12.83
	1	7.08	325	14.03	188.4	13.16

^aTwo peaks were present, the first is attributed to THP (first values) and the second to P-3,5-pyr-P (second values in each entry). ^b Solvent mixing. ^cStrong fluctuations, unreliable estimates. ^dTwo different runs by two operators.

Two types of behavior were observed; in one case the yield of coke was reduced below the expected value from equation (7.1). In the second case, the yield of coke followed equation (7.1) to within experimental error. No enhancement of coke yield above the additive value was observed in any of the mixtures analyzed in TGA.

7.3.1 Coke Reduction Behavior

Archipelago model compounds containing a pyridine central group typically gave higher coke yield compared to similar hydrocarbon compounds, as shown in Chapter 5. In particular, P-3,5-pyr-P generated the highest coke yield among the model compounds with over 33 wt%. The higher reactivity of this compound, low activation energy of cracking, and the associative behavior in the liquid phase, as examined with polarized light microscopy, were hypothesized to be the factors responsible for the high coke yield.

To examine the nature of coke formation in this compound, low-coke producers (P-*m*Ph-P and THP) were mixed with P-3,5-pyr-P at different ratios and analyzed by TGA. The hypothesis was that if association within the pyridyl compounds was important, anything that disrupts these associative forces will decrease the coke yield. On the other hand, fragments from the low-coke producers could also interact with fragments from P-3,5-pyr-P and participate in free radical reactions, whereas they would simply evaporate if cracked separately. Such coupling would result in affecting the total coke yield, and thus demonstrate a complex behavior that may depend on the weight fraction of each component in the mixture.

7.3.1.1 P-3,5-pyr-P / P-*m*Ph-P Experiments

Figure 7.2 shows the weight loss and rate of weight loss (dW/dt) with time and temperature for a 1:1 ratio mixture of P-3,5-pyr-P and P-*m*Ph-P, along with the pure compounds. The solid residue of the mixture is clearly lower than the midpoint between the curves of weight loss of the two compounds. Not only the 1:1 mixture gives this reduction, all examined ratios give coke yield lower than that predicted by equation (7.1). At weight fractions of P-3,5-pyr-P of 0.33, 0.5, and 0.67, eq. (7.1) predicts a coke yield of 13.3, 18.4, and 23.5 wt%, respectively. The average experimental values of two runs at each ratio shown in **Table 7.1** are 9.6, 14.3, and 19.1 wt%, respectively. These results are plotted in **Figure 7.3**.

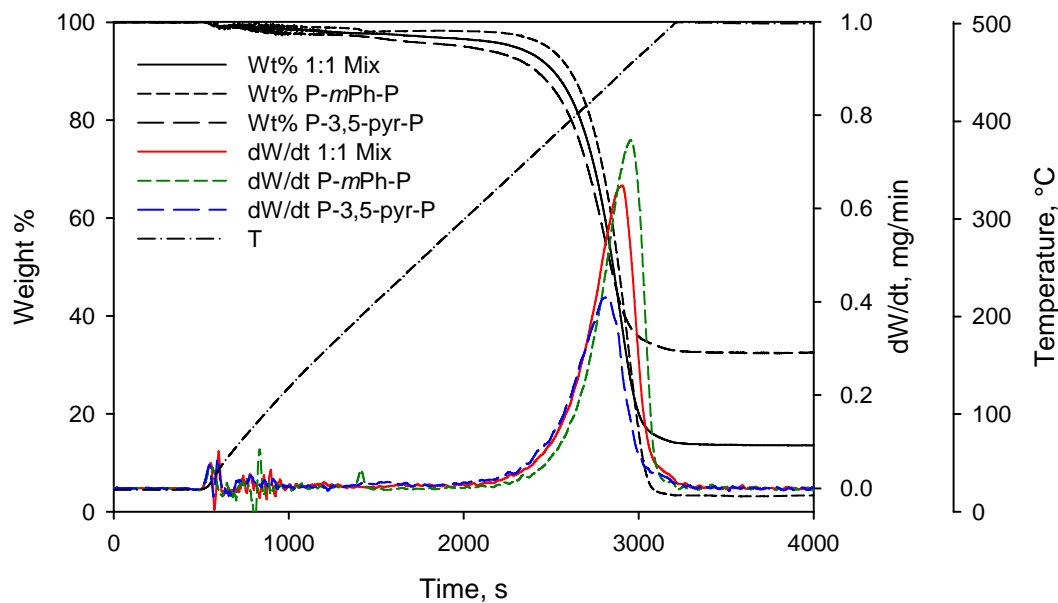


Figure 7.2: Comparison of the TGA trends for P-*m*Ph-P, P-3,5-pyr-P, and a 1:1 mixture of the two compounds, all following the same temperature profile shown on the figure.

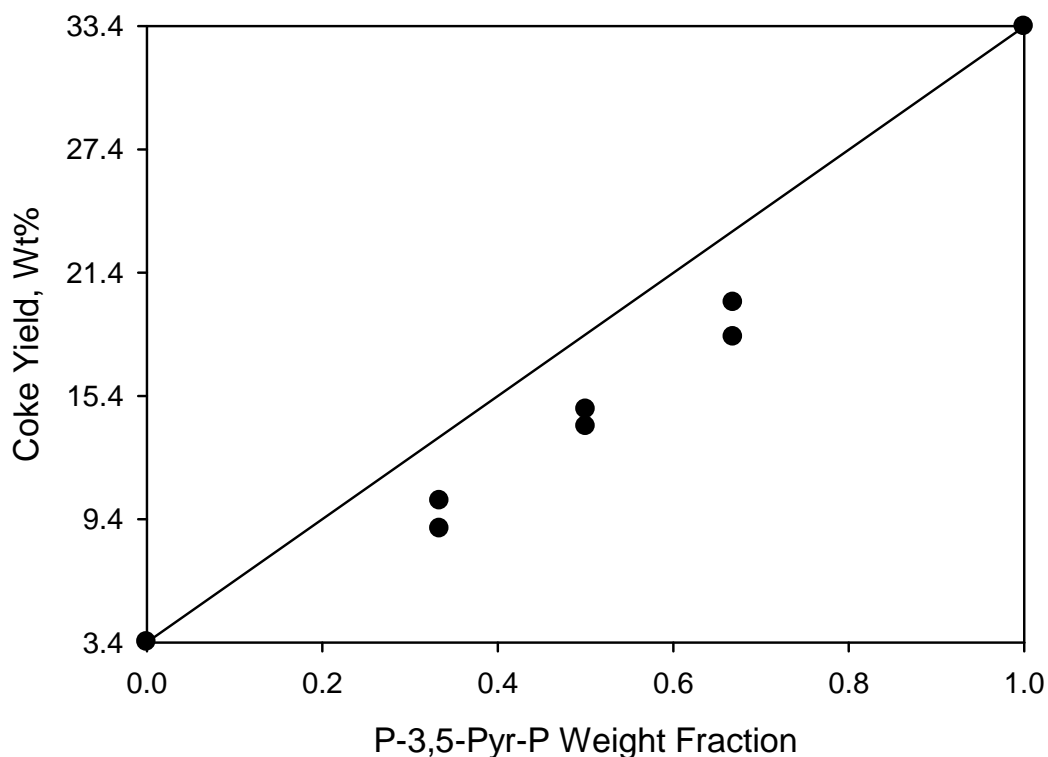


Figure 7.3: Coke yield as a function of P-3,5-pyr-P weight fraction, in mixtures with P-*m*Ph-P.

The line shown in **Figure 7.3** is the additivity line, plot of equation (7.1), on which the results should lie if the coke yield was additive. The total coke yield is systematically lower than the coke yield that would be produced by each compound separately.

Using the arguments given previously in Chapter 5 for estimating the relative stability of a radical adjacent to the central aromatic ring in archipelago compounds, the C–H bond dissociation energy in 3(or 5)-methylpyridine is only 0.8 kcal/mol higher than in methylbenzene.⁵ Therefore, radicals adjacent to the central rings from both P-*m*Ph-P and P-3,5-pyr-P are formed relatively equally (especially in the 1:1 mixture to eliminate concentration effects). But the radicals formed in P-*m*Ph-P are much less reactive than in P-3,5-pyr-P, as shown in

Chapter 5 such that the verified cracking kinetics of P-*m*Ph-P predict a conversion of 8% at 365 °C–20 min reaction whereas P-3,5-pyr-P has a conversion of 25% at the same conditions. This added radical carrier (P-*m*Ph-P) is then going to reduce the overall rate of cracking and addition resulting in lower coke yield, similar to the toluene effect in inhibition of the cracking of *n*-alkanes.⁶ In addition, the strong associations of P-3,5-pyr-P, as hypothesized in Chapter 5 to be a contributing factor in the high coke yield in this compound, may have been disrupted by the addition of P-*m*Ph-P and resulted in preventing P-3,5-pyr-P molecules from forming coke as in the pure state.

The parameters of cracking kinetics, namely the apparent activation energy of cracking (*E*) and the pre-exponential factor (*A*), were calculated from the rate of weight loss following the differential method described in Chapter 4, and are listed in **Table 7.1**. Plotting the apparent activation energy values of the mixtures against the weight fraction of the high-coke former in these experiments (P-3,5-pyr-P) gives the trend shown in **Figure 7.4**. The line connecting the data points of the pure compounds is also shown in **Figure 7.4**, where the data points from the mixture experiments should lie if the behavior is additive. In this mixture of compounds, the mixture *E* is apparently the weighted average of the separate compounds activation energies. As the weight fraction of P-3,5-pyr-P increases, the *E* value of the mixture approaches the *E* of pure P-3,5-pyr-P in a linear fashion.

The activation energy of cracking for mixtures is rather a complex property that can be affected by conversion, temperature, mixture composition, rate

constants of the reactants, as well as the range of activation energies of the single components.⁷ Golikeri and Luss⁷ showed that the activation energy for a mixture can be the weighted average in some cases while in other cases it is not, with the mixture E not even within the range of the minimum and maximum E 's of the components. The results in **Figure 7.4** thus do not imply that additive behavior should be obtained for activation energies, but rather these results are unique for this mixture. As well be shown below, other binary mixtures did not show such additivity (although some mixtures had an additive coke yield).

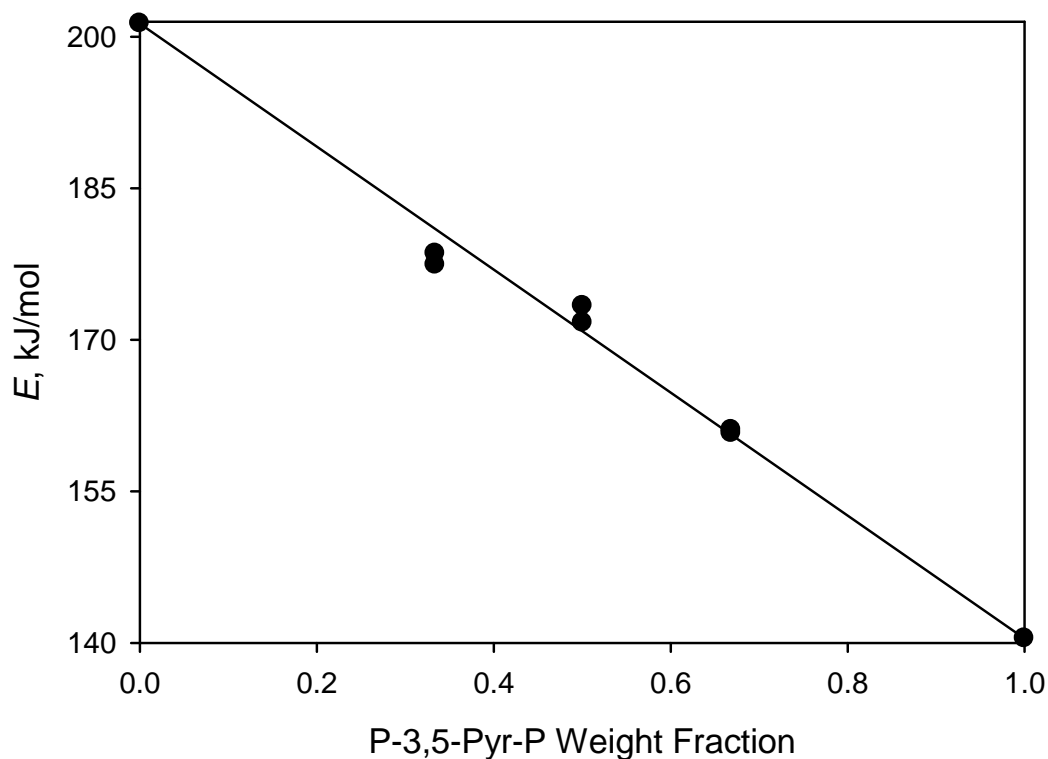


Figure 7.4: E versus the weight fraction of P-3,5-pyr-P mixed with P-*m*Ph-P.

7.3.1.2 P-3,5-pyr-P / THP Experiments

Figure 7.5 shows the weight loss and rate of weight loss curves for a 1:1 mixture of THP and P-3,5-pyr-P along with the trends from the pure compounds.

Two peaks are present for the rate of weight loss suggesting separate losses by the two compounds, as they align with the losses of the pure samples. The slopes of the curves of both compounds are slightly different than the ones from pure samples resulting in different activation energies.

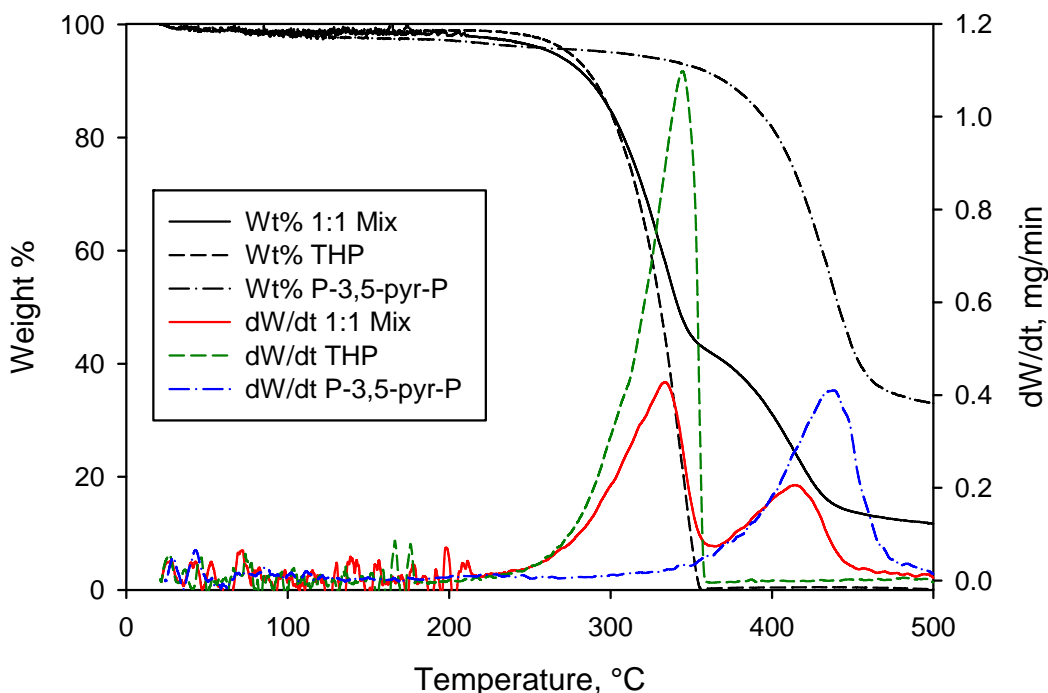


Figure 7.5: TGA results of THP, P-3,5-pyr-P, and a 1:1 mixture of the two compounds.

The weight loss curve in **Figure 7.5** indicates also that the coke yield is lower than the midpoint between the pure THP and P-3,5-pyr-P curves. **Figure 7.6** shows the total coke yield of the mixtures as a function of the weight fraction of P-3,5-pyr-P. The systematic reduction of coke yield is similar to that observed by mixing this high coke former, P-3,5-pyr-P, with P-*m*Ph-P (shown in **Figure 7.3**). Apparently, the factors affecting the coke yield in mixing THP with P-3,5-pyr-P are similar to those observed by adding P-*m*Ph-P. THP, or its fragments

after cracking, may disrupt the associative forces in the liquid phase of P-3,5-pyr-P, and if radicals are formed in THP, they will be much less reactive than those in P-3,5-pyr-P, thus causing a reduction in the observed coke yield.

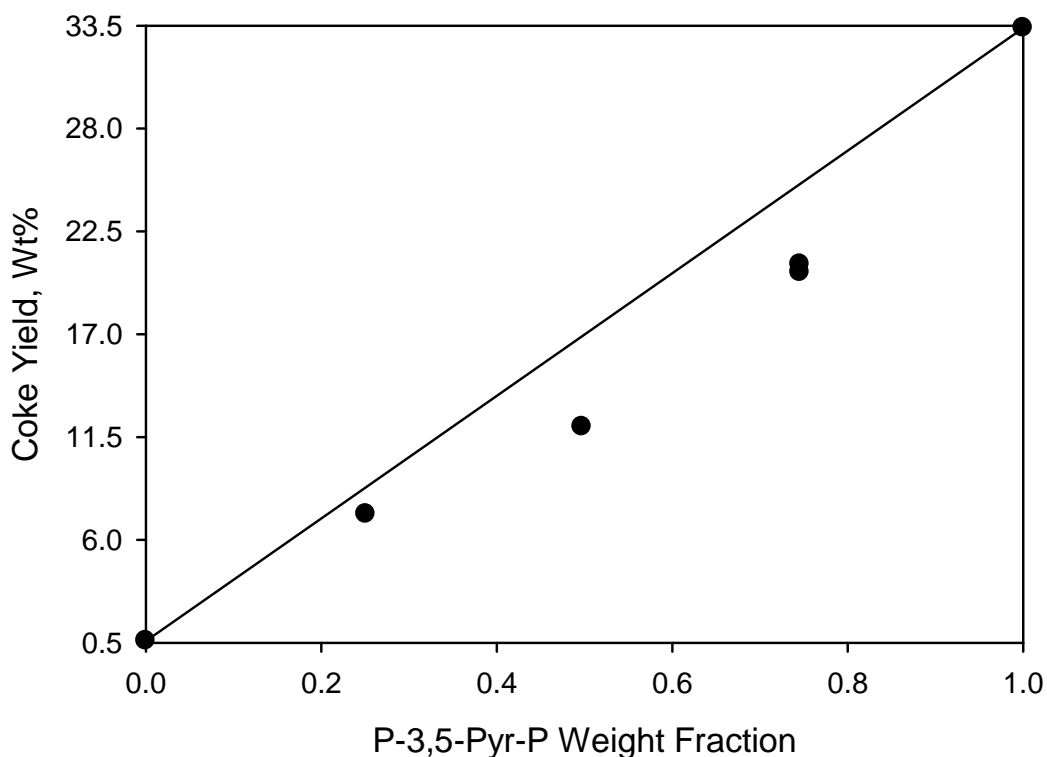


Figure 7.6: Total coke yield from THP and P-3,5-pyr-P mixtures shown against the weight fraction of P-3,5-pyr-P.

Figure 7.7 shows the E values calculated from the separate peaks observed in **Figure 7.5**. Clearly evaporation is significant in the case of THP, especially at low concentration where the E from first peak was only ~ 90 kJ/mol. As the concentration of THP increased, E approached the value of pure THP. E for the P-3,5-pyr-P dominant peak (second one in **Figure 7.5**), on the other hand, was affected by the partial evaporation of THP prior to the onset of cracking

temperatures. Unfortunately, separating the evaporation losses from those due to thermal cracking in the TGA data is not possible, which in turn precludes adequate interpretation of the cracking results.

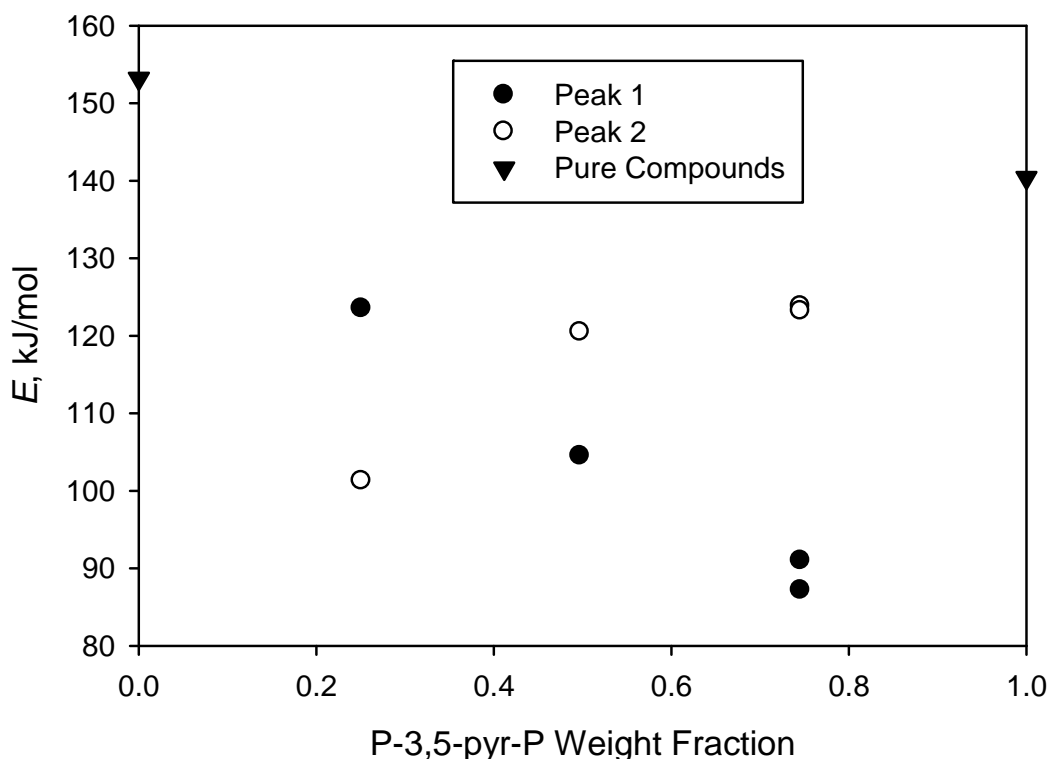


Figure 7.7: The apparent activation energy of cracking (E) values from the separate peaks observed in TGA (**Figure 7.5**) for P-3,5-pyr-P and THP mixtures. Black circles are from the first peak (mainly THP mixture) and white circles are calculated from the second peak (mainly P-3,5-pyr-P mixtures).

7.3.1.3 P-2,5-pyr-3-Me-P / P-mPh-P Experiment

To examine whether the observed reduction in coke yield was only due to the P-3,5-pyr-P sample and to rule out the possibility of contributing factors, such as contaminants, to the observed trends, TGA experiment with a single ratio of 1:1

of another pyridyl compound (P-2,5-pyr-3-Me-P) with P-*m*Ph-P was performed (shown in **Table 7.1**). Analyzing the pure compounds gave a coke yield of 3 and 14 wt% for P-*m*Ph-P and P-2,5-pyr-3-Me-P, respectively. If the coke yield was additive, a 1:1 mixture should give a coke yield of about 8.5 wt%. The experimental coke yield was only 5.6 suggesting reduction in coke yield occurred by the addition of P-*m*Ph-P, which is similar to the behavior observed with P-3,5-pyr-P mixtures with THP and P-*m*Ph-P.

7.3.2 Simple Additive Behavior

Similar to P-3,5-pyr-P, P-BiTh-P formed a large amount of coke, although the liquid crystalline behavior, in terms of the temperature at which the liquid crystals disappeared, was different from P-3,5-Pyr-P (shown in **Figure 5.12**). The high coke formed in this thiophenic compound was attributed to its higher reactivity, where early cracking at low temperatures generates large amounts of olefins which would engage in addition reactions at a higher rate for longer times (Chapter 5). Adding a low coke-former, in this case P-*m*Ph-P, is expected then to enhance the coke formation by donating fragments, that would evaporate otherwise, to add to the olefins generated by P-BiTh-P, assuming radicals from both compounds form equally and undergo cracking and addition reactions at the same temperatures.

7.3.2.1 P-BiTh-P / P-*m*Ph-P Experiments

The coke yield as a function of the weight fraction of P-BiTh-P is shown in **Figure 7.8**. The results indicate an additive behavior where each compound forms coke as it would if pyrolyzed separately. The method of mixing had no effect on

the observed coke yield, as indicated by the similar results obtained with and without solvent mixing.

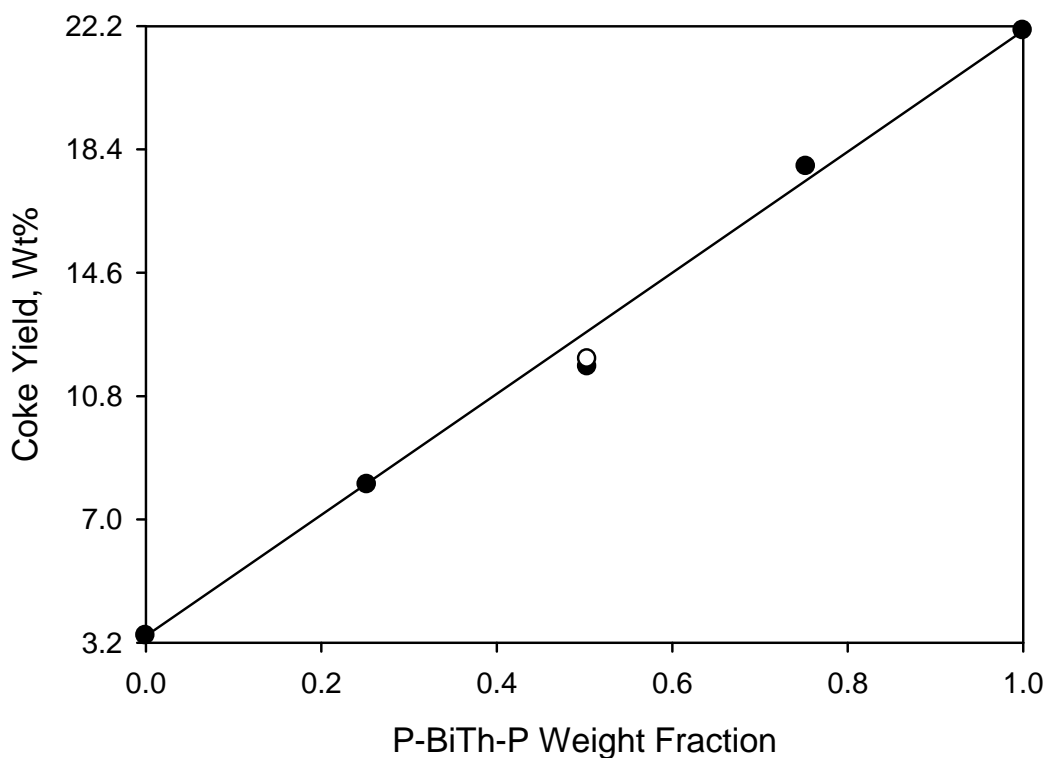


Figure 7.8: The coke yield by a mixture of P-BiTh-P and P-*m*Ph-P. The sample mixed using MC solvent is shown as a white circle.

In contrast to the P-3,5-pyr-P / P-*m*Ph-P mixture where the radicals adjacent to the central rings form equally, the bond dissociation energy for a 2-methylthiophene is 3.3 kcal/mol weaker than methylbenzene.⁵ In addition, P-BiTh-P is much more reactive giving a 61% conversion for a reaction at 365 °C for 20 min (P-*m*Ph-P estimated at only 8% at these conditions). Hence radicals are formed and carried more favorably on P-BiTh-P, as they would have before adding P-*m*Ph-P. The difference in reactivity leads to participation in cracking and

addition reactions at different rates by these two compounds, resulting in additive coke formation behavior.

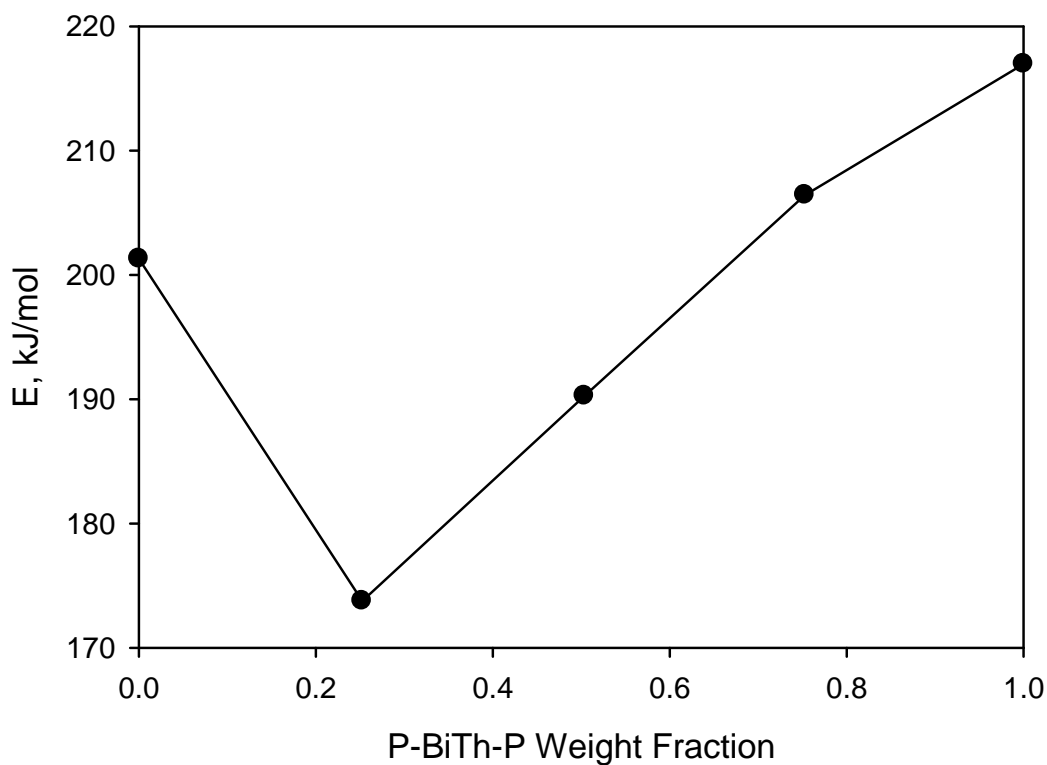


Figure 7.9: The apparent activation energy of cracking for a mixture of P-BiTh-P and P-*m*Ph-P model compounds as a function of the weight fraction of P-BiThP.

The rate of weight loss curve showed a single peak, similar to the mixtures of P-3,5-pyr-P with P-*m*Ph-P. **Figure 7.9** shows the activation energy of cracking for the mixture, calculated from this rate of weight loss curve, against the weight fraction of P-BiTh-P. In contrast to P-3,5-pyr-P / P-*m*Ph-P mixture, the *E* values were not additive. In fact, a reduction in the activation energy, without the evidence of evaporation that was observed in the case of THP, is observed in these mixtures. This confirms the previous arguments on the additivity in the

activation energy for P-3,5-pyr-P / P-*m*Ph-P mixture being specific to that mixture. In spite of the additive coke yield, the activation energies are not additive, and two values fall outside the bounds of the pure compounds, as described by Golikeri and Luss⁷. Nevertheless, the reduction in the apparent activation energy by adding small amounts of P-BiTh-P is consistent with initiating the cracking of P-*m*Ph-P at lower temperatures as P-BiTh-P was observed to crack at much lower temperatures than P-*m*Ph-P (Chapter 5). In other words, P-BiTh-P activated the decomposition of P-*m*Ph-P fragments at lower temperatures than they would if pyrolyzed separately. As the concentration of P-BiTh-P is increased, the *E* values approaches that of P-BiTh-P cracking.

7.3.2.2 P-BiTh-P / P-Th-P Experiment

To assess the possibility of liquid–liquid phase separation between P-*m*Ph-P and P-BiTh-P, which will make each compound form coke separately, another experiment with a more compatible compound (P-Th-P) was performed at a single mixture ratio.

The two thiophenic compounds, P-BiTh-P and P-Th-P, were chosen for this experiment since they are expected to have similar phase behavior and thus give a direct indication to the effect of phase separation on the coke yield. The coke yield by P-Th-P and P-BiTh-P as individual compounds was 7.5 and 23.1, respectively. If the coke yield by a 1:1 mixture were additive, the coke yield should be ca. 15.3 wt%. The experimental value was within 1 wt% of the predicted coke yield at 14.6 wt%, confirming the additivity of the coke yield in this mixture also, similar to the mixture of P-BiTh-P and P-*m*Ph-P.

Coke yield in the binary experiments varied from additive behavior to coke reduction. In actual residues, however, the fractions MCR content, which is proportional to the coke yield determined from the TGA in this study, follows rather a simple additive behavior. For example, the sum of coke yields from the saturates, aromatics, resins, and asphaltenes separated from Cold Lake vacuum residue equals that of the feed.⁸ The hundreds of thousands of compounds present in crude oils⁹, residua, and the asphaltenes thus make observing any interactions between specific functional groups impossible.

7.4 CONCLUSIONS

Although the generated data from the TGA was not enough to explain all the observed effects on the coke yield and apparent activation energy of cracking for the different binary mixtures, a few key points are worth noting from this study:

- 1) The coke yield was either reduced or remained unaffected by addition of one compound to another. In multicomponent multifunctional systems, like the asphaltenes, such interactions may not be readily observed.
- 2) The additive yield of coke from a binary mixture did not necessarily give an additive relationship in the activation energy of cracking.
- 3) Compounds that are more reactive can lower the energy required to crack other components by initiating free radicals at lower temperatures.

7.5 REFERENCES

1. Savage, P. E., Pyrolysis of a binary mixture of complex hydrocarbons: Reaction modeling. *Chem. Eng. Sci.* **1990**, 45, 859-873.
2. Kruse, T. M.; Levine, S. E.; Wong, H.-W.; Duoss, E.; Lebovitz, A. H.; Torkelson, J. M.; Broadbelt, L. J., Binary mixture pyrolysis of polypropylene and polystyrene: A modeling and experimental study. *J. Anal. Appl. Pyrolysis* **2005**, 73, 342-354.
3. Zhou, P.; Crynes, B. L., Thermolytic reactions of o-ethylphenol. *Ind. Eng. Chem. Process Des. Dev.* **1986**, 25, 898-907.
4. Smith, C. M.; Savage, P. E., Reactions of Polycyclic Alkylaromatics. 7. Hydrogenolysis in Binary Mixtures. *Energy Fuels* **1994**, 8, 545-551.
5. Zhao, S. W.; Liu, L.; Fu, Y.; Guo, Q. X., Assessment of the metabolic stability of the methyl groups in heterocyclic compounds using C-H bond dissociation energies: effects of diverse aromatic groups on the stability of methyl radicals. *J. Phys. Org. Chem.* **2005**, 18, 353-367.
6. Lannuzel, F.; Bounaceur, R.; Michels, R.; Scacchi, G.; Marquaire, P.-M., Reassessment of the Kinetic Influence of Toluene on n-Alkane Pyrolysis. *Energy Fuels* **2010**, 24, 3817-3830.
7. Golikeri, S. V.; Luss, D., Analysis of Activation Energy of Grouped Parallel Reactions. *AIChE J* **1972**, 18, 277-282.
8. Wiehe, I. A., A Solvent Resid Phase- Diagram for Tracking Resid Conversion. *Ind. Eng. Chem. Res.* **1992**, 31, 530-536.

9. Hughey, C. A.; Rodgers, R. P.; Marshall, A. G., Resolution of 11 000 compositionally distinct components in a single Electrospray ionization Fourier transform ion cyclotron resonance mass spectrum of crude oil. *Anal. Chem.* **2002**, 74, 4145-4149.

CHAPTER 8

SYNTHESIS AND CONCLUSIONS

8.1 SYNTHESIS

The previous chapters presented new insights into the reactions leading to coke formation in the liquid phase. Alkyl–alkyl and alkyl–aryl addition reactions were found to form alkyl–bridged structures (Chapter 3) that subsequently rearrange, crack further, or undergo further addition reactions to give rise to coke (Chapter 5). The cholestane–based compounds and alkyl aromatics did not participate as efficiently as the archipelago compounds in addition reactions, resulting in lower coke yields (Chapters 3 and 6). Instead, dealkylation (for alkyl aromatics) and both dealkylation and dehydrogenation reactions were dominant in these two families. Confirming the importance of intermolecular associations in controlling the coke yield, the binary experiments in the TGA suggested the possibility of coke reduction (Chapter 7). The cracking kinetics of these model compounds, which were important in all the previous chapters, were calculated by a new method (Chapter 4) that enabled comparing the kinetics of cracking of the different model compounds with minimal amounts of samples.

Industrial and practical implications for the results derived from this work along with some of the gaps and sources of errors and uncertainties are summarized below.

8.1.1 Implications to Practical Issues

The most important finding from this research is that larger structures, and presumably coke, form in upgrading processes by sequences of addition, rearrangement, and dehydrogenation reactions in the liquid phase. To enhance the liquid yield and reduce the coke formation in vacuum residue or heavy oil upgrading processes, this sequence has to be interrupted. The free-radical chain reactions are essential in fragmenting the large components in the heavy feedstocks, and thus the suppression of free-radical formation is undesirable. Rather, controlling the addition reactions and how large the added structures are allowed to grow is a more promising approach to minimizing the coke formation. Catalytic hydrogenation of the generated olefins, for example, or the rapid removal of these cracked fragments from the liquid pool, can reduce the rate of addition reactions and subsequently the rate of coke formation. Similarly, disrupting the intermolecular associative forces may reduce the total coke yield, for example, by addition of another component.

8.1.2 Sources of Uncertainties

The set of model compounds, experimental procedures, and analytical methods generated many useful insights on the molecular-level behavior under thermal cracking conditions. Nevertheless, a few gaps and sources of errors have to be addressed for future research in order to improve this approach of

investigating thermal reactions using model compounds and linking the observed results to the asphaltenes.

The first source of possible errors is from the model compounds. These compounds were especially synthesized and are not commercially available. Most of them were made in limited quantities and thus statistical analysis by replicates, full examination of hypotheses, and detailed microreactor experiments for kinetics or reaction pathways were not possible. Moreover, the small amounts of samples generated, in turn, low amounts of the newly formed products, making the determination of their nature uncertain in the different analytical methods, such as NMR and MALDI. The possible contaminants present in these compounds could also affect the results. Halogen contaminants, for example, if present in the products would initiate the free radicals at very low temperatures, thus affecting the formed products and observed cracking kinetics.

Since these model compounds are not commercially available, their physical, chemical, and thermodynamic properties are not known. Approximations to smaller structures are used, which are not always valid. The discussion on the possible initiation or decomposition steps based on the thermochemical estimates from group additivity methods may then be affected, and thus require reinterpretation of data.

Finally, the structure of most of these compounds, the archipelago family for example, was simple and symmetrical. The actual asphaltene molecules, as presented in detail in Chapter 2, are much more complex and unsymmetrical with more alkylation on the aromatic groups and variable lengths for the connecting

bridges. As the synthesis of these compounds evolve, better representation of asphaltene molecules is needed.

The second source of errors is from the limitations in the employed analytical instruments. Gas chromatography was unable to elute most of the products due to their large molecular weights and high boiling points. Therefore quantification of the addition products was estimated in some reactions from the intensity of MALDI analysis. The MALDI-MS gives only observed masses but no indication about the possible compounds of different structures that can give rise to these signals. Hence, although rearranged or cyclized products were expected, no direct detection in MALDI was feasible. To prove their formation, experiments of controlled conversion (to follow the successive steps) with more feed (to generate more products) followed by NMR (preferentially after separating products into classes to simplify the NMR spectrum) are required.

Similarly, the HPLC analysis did not resolve all peaks for products that are very similar, for example if differing only in the dehydrogenation degree. Also many addition products were below the detection limit of HPLC. The matrix used in the MALDI instrument, DCTB of a weight of 250 Da, formed adducts with nitrogen-containing compounds and its molecular weight, or its adducts, were in some cases close to the weights of expected products or the starting compounds (for example benzopyrene with a weight of 252 Da). The matrix then introduced some uncertainties in verifying that some signals were genuine products, in spite of applying MALDI-MS/MS. The MALDI-MS/MS analysis for compounds with longer side-chains, such as the cholestane-based compounds or the alkyl

aromatics, typically gave strong noise close to the m/z of the analyzed signal, likely due to the ability of these side chains to distribute the indicted energy without cracking, thus complicating identifying the fragments from the analyzed product. An example of the combined limitation of MALDI MS, MS/MS, and NMR was in determining the favoured addition location, whether to olefins or to the aromatic systems such as to pyrene in archipelago family reactions or to both pyrene and benzopyrene in the binary experiments.

A final limitation is that coke cannot be analyzed. Coke from the TGA experiments of each model compound was collected and MALDI analyses for few samples were attempted. No useful information could be obtained from these methylene chloride insolubles. Therefore, the exact steps to go from the detected products to insoluble coke are not fully proven.

8.2 CONCLUSIONS

1. Thermal cracking in the liquid phase generates both smaller and larger compounds, than the parent, simultaneously.
2. In addition to the reported bimolecular mechanisms for cleavage of strong bonds, unimolecular rearrangements, such as 1,2-aryl shift, are important in the liquid phase pyrolysis.
3. The larger, or addition, products form by sequences of addition, rearrangement, and dehydrogenation reactions.

4. Alkyl–alkyl and alkyl–aryl addition reactions are much more favourable than aryl–aryl fusions, resulting in building alkyl–bridged, or archipelago, structures as intermediates in all of the compounds studied.
5. Coke formation is controlled by reactivity of the starting compound as well as the initially formed cracked and addition products (which could be affected by minor structural changes), rate of addition reactions, and intermolecular association in the liquid melt.
6. Mixing a high coke–former with another compound can either have no effect or decrease the total coke yield from the binary mixture.
7. Aromatic groups, when fused with naphthenic rings, accelerate the decomposition of the whole molecule by providing resonance stabilization for radicals at the benzylic positions after hydrogen abstraction.
8. No release of mono–, di–, or tri–cyclic compounds from large naphthenoaromatic moieties is expected at the commercial thermal cracking conditions.

8.3 RECOMMENDATIONS

1. Synthesize more model compounds, with multiple functionalities, more alkyl substitutions on the aromatics, and variable lengths of the bridges connecting the aromatic systems, to better represent the complex structures in the asphaltenes.

2. The synthesized model compounds should be provided with sufficient quantities with the highest purity possible.
3. Determine the physical properties of each compound, such as the boiling and melting temperatures, vapor pressure, and thermochemical data.
4. Confirm and identify the structure of the reaction products by performing the microreactor experiments at larger scales and separating the products into different classes.
5. Examine important hypotheses from this work, such as confirming the kinetics and pathways of the radical rearrangements and cyclization reactions, and the radical addition reactions to both olefins and to aromatics, for example by adding synthetic olefins and quantitatively determining where addition is favourable.
6. Examine coke yield, cracking kinetics, as well as the liquid crystalline behavior using polarized light microscopy for more binary mixtures (e.g. two high-coke formers).

APPENDIX A

CALIBRATION CURVES AND OPTIMIZATION OF ANALYTICAL INSTRUMENTS

A.1 THERMOGRAVIMETRIC ANALYSIS (TGA)

The experimental procedures for the TGA method were summarized in Chapters 3–7. The temperature profile to determine the coke yield was selected following the ASTM method numbered D4530–07 titled “Standard Test Method for Determination of Carbon Residue (Micro Method)”. Following this method, the temperature was ramped to 500 °C and then was maintained at this temperature for 15 min. In most experiments, the sample was allowed to cool down to at least 200 °C while still under the inert flow of argon gas before opening the TGA.

The performance of the TGA was routinely checked with analysis of calcium oxalate (CaOx), which exists as a hydrated salt with the chemical formula $\text{CaC}_2\text{O}_4 \cdot \text{H}_2\text{O}$ (for the monohydrate salt), especially after maintenance of the instrument. Leak tests with copper powder were also performed when leakage was suspected to affect the obtained results.

A.1.1 Performance Tests with CaOx

Calcium oxalate is typically applied to test the performance of the TGA. The instrument manual also recommends analyzing CaOx for routine checks. Three distinct losses are observed when the material is analyzed in the TGA due to the initial loss of water, CO, and finally CO₂. The weight% losses, temperatures at the maximum rate of weight loss, and residue from each material loss can then be compared with previous runs, reported values in the literature, as well as with the instrument manual.

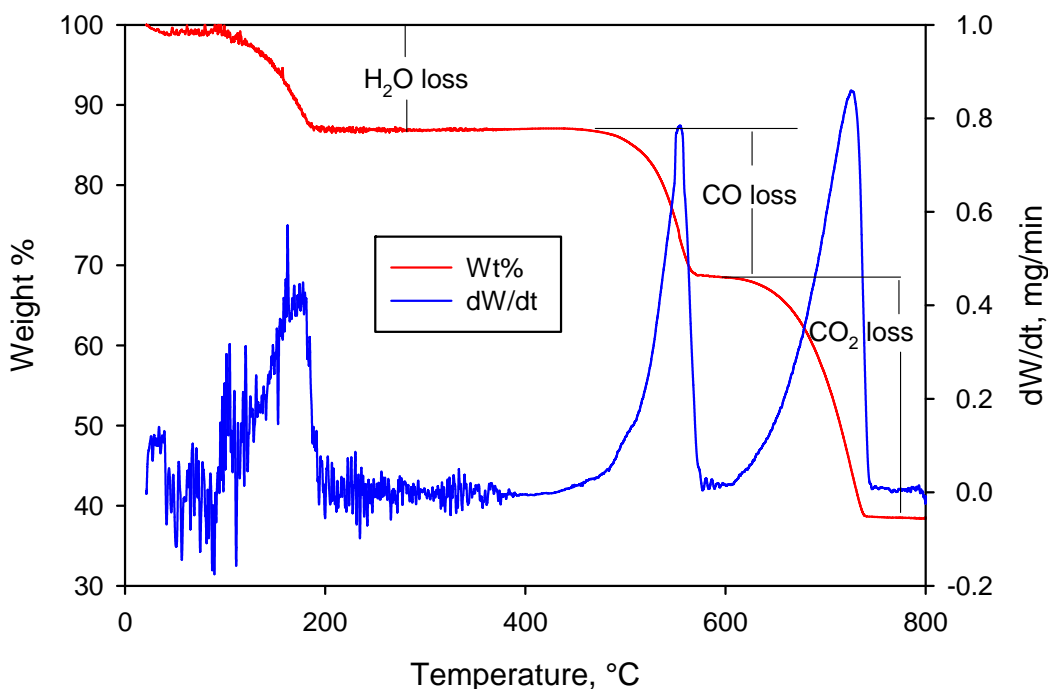


Figure A.1: TGA experiment with CaOx performed on Oct09.

Figure A.1 shows the typical results expected from analyzing CaOx in the TGA. The temperature profile for all the experiments follows a 5 min holdup at ambient temperature, then ramping to 800 °C at 20 °C/min, and a final holdup at

800 °C for 5 min. The TGA was maintained under inert conditions with a flow of argon gas at 80 mL/min throughout the experiments.

Comparison of the TGA performance with CaOx pyrolysis over two years is shown in **Figure A.2**. The runs are titled by the month and year in which the test was conducted.

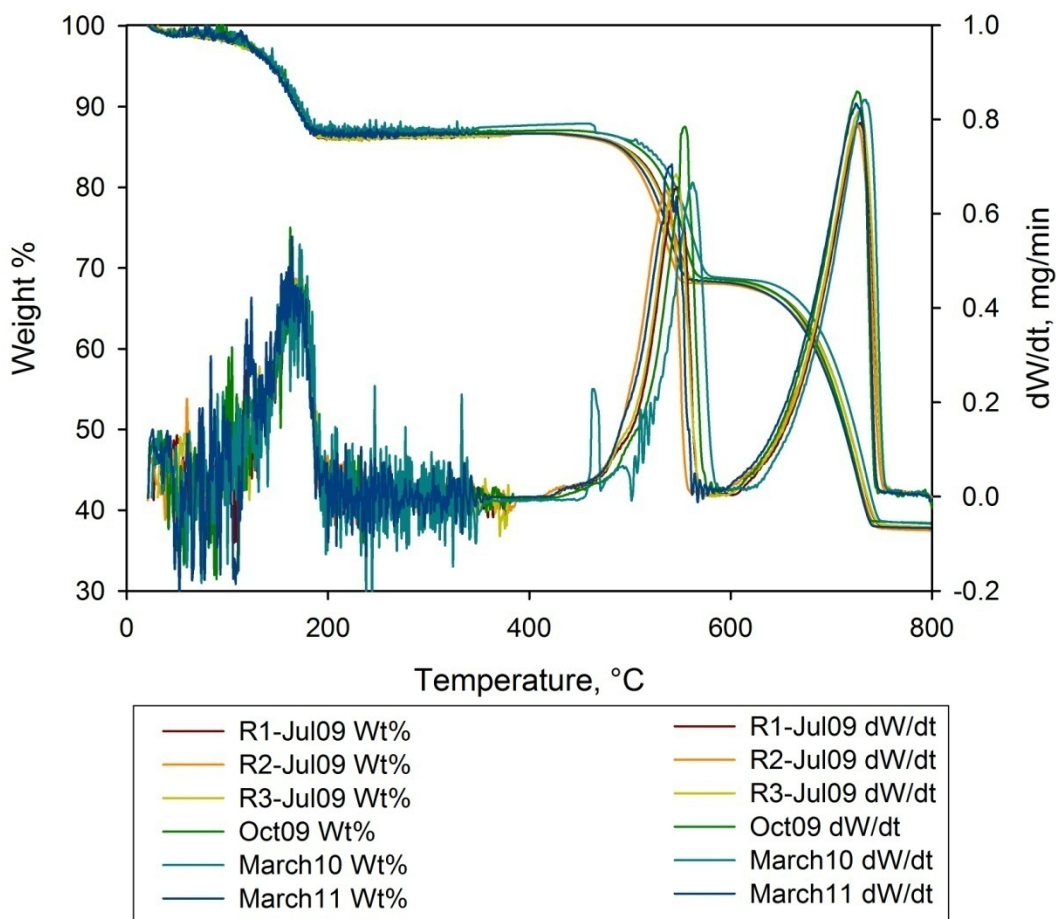


Figure A.2: Six experiments on CaOx typically performed after instrument maintenance. The repeatability of the results over two years (July 2009 – March 2011) is very good.

The parameters compared from these runs are shown in **Table A.1**. The percent weight loss, residue, and the maximum rate of weight loss (peaks of the dW/dt curves shown in **Figures A.1** and **A.2**) were all repeatable with the standard deviation from the mean being less than 0.3 wt%, 0.4 wt% and 0.04 mg/min, respectively. The greatest variation was in the peak temperature values with a standard deviation from the mean in the range of 2–10 °C. The peak temperatures are very sensitive to minor experimental variations as concluded in Chapter 4, and hence this behavior is expected.

Table A.1: Comparing the parameters of the CaOx pyrolysis in the TGA with the average (Avg) and standard deviation (StD).

		R1 ^a	R2 ^a	R3 ^a	Oct 2010	March 2010	March 2011	Avg	StD
H ₂ O loss	Wt%	13.26	13.36	13.25	13.13	12.82	13.35	13.19	0.20
	T _P ^b , °C	168	169	171	168	167	164	167.8	2.30
	(dW/dt) _P	0.419	0.458	0.452	0.389	0.379	0.443	0.423	0.033
CO loss	Wt%	18.58	18.53	18.49	18.40	18.60	18.37	18.49	0.093
	T _P , °C	546	536	546	554	562	539	547	9.90
	(dW/dt) _P	0.656	0.650	0.684	0.742	0.663	0.691	0.681	0.034
CO ₂ loss	Wt%	30.12	30.33	30.04	29.61	29.91	30.13	30.02	0.244
	T _P , °C	728	725	728	725	733	725	727	3.11
	(dW/dt) _P	0.792	0.789	0.819	0.852	0.843	0.827	0.820	0.026
	Residue	38.04	37.81	38.22	38.76	38.67	38.15	38.27	0.37

^aThese experiments were performed in July 2009. ^bThe **P** subscript indicates the peak or maximum point in the rate of weight loss curve versus temperature shown in figures **A.1** and **A.2**.

A.1.2 Leak Test

When leakage of air to the samples was suspected, check experiments with copper powder were performed. Copper reacts with oxygen at high temperatures and forms copper oxide (CuO) which will give an increase in the weight. **Figure A.3** shows one experiment of Cu in the TGA following a 10 min holdup at ambient temperature, 20 °C/min ramp to 600 °C, and finally a 30 min holdup at 600 °C. The difference between initial and final (after cooling the sample) weights was only 0.01 mg indicating no significant leakage of air during the experiment.

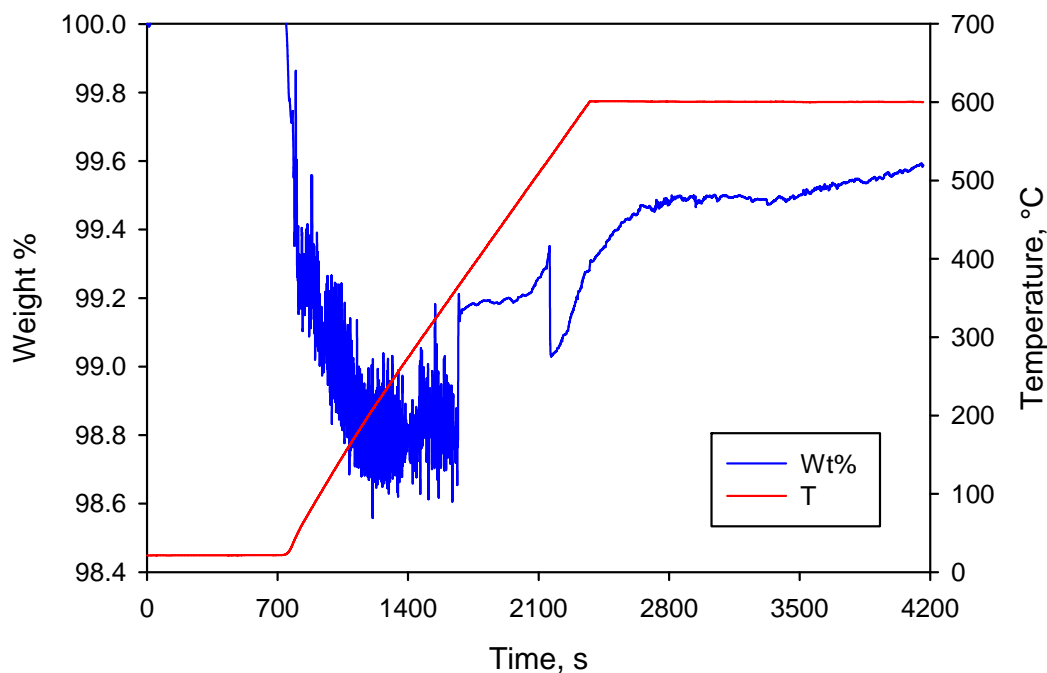


Figure A.3: Oxygen leak test with copper powder. The results suggest no oxygen leakage because the weight percent did not increase significantly.

A.2 SAND BATH PERFORMANCE

Before performing the microreactor experiments, the heating profile for the reactors were determined to assess the performance of the sand bath (SB). Two sand baths were tested [Left hand side (LHS) and right hand side (RHS)]. For these experiments, a K-type thermocouple was inserted inside the microreactor from a reducing union instead of a cap at the bottom of the reactor. All other parts were as reported in the experimental sections in Chapters 3–6. The temperature controllers for the SB were set at 430 °C in all of these experiments. The actual sand bath temperature is typically lower than this temperature as shown below.

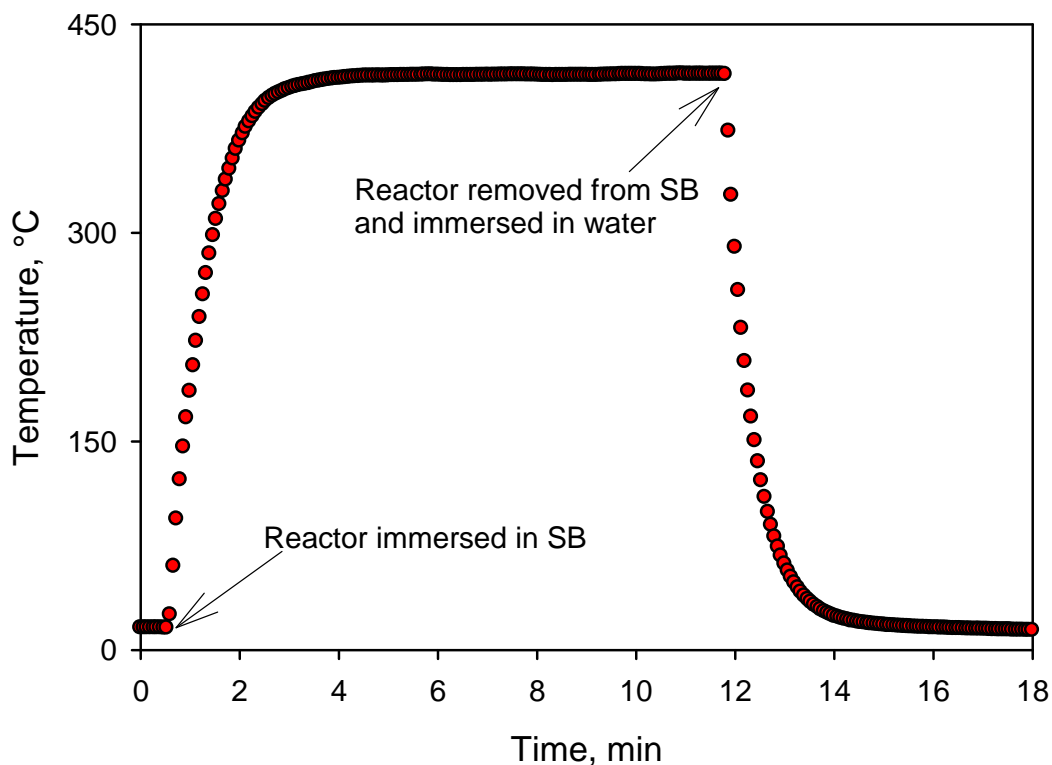


Figure A.4: Temperature curve for the LHS SB. Maximum temperature reached was 414 °C although the controller was set at 430 °C.

One of the experiments on the LHS SB is shown in **Figure A.4**. The induction period at the beginning is the time between when recording measurements began and when the reactor was dipped in the SB. The abrupt change at the end is when the reactor was removed from the SB and immersed in cool water.

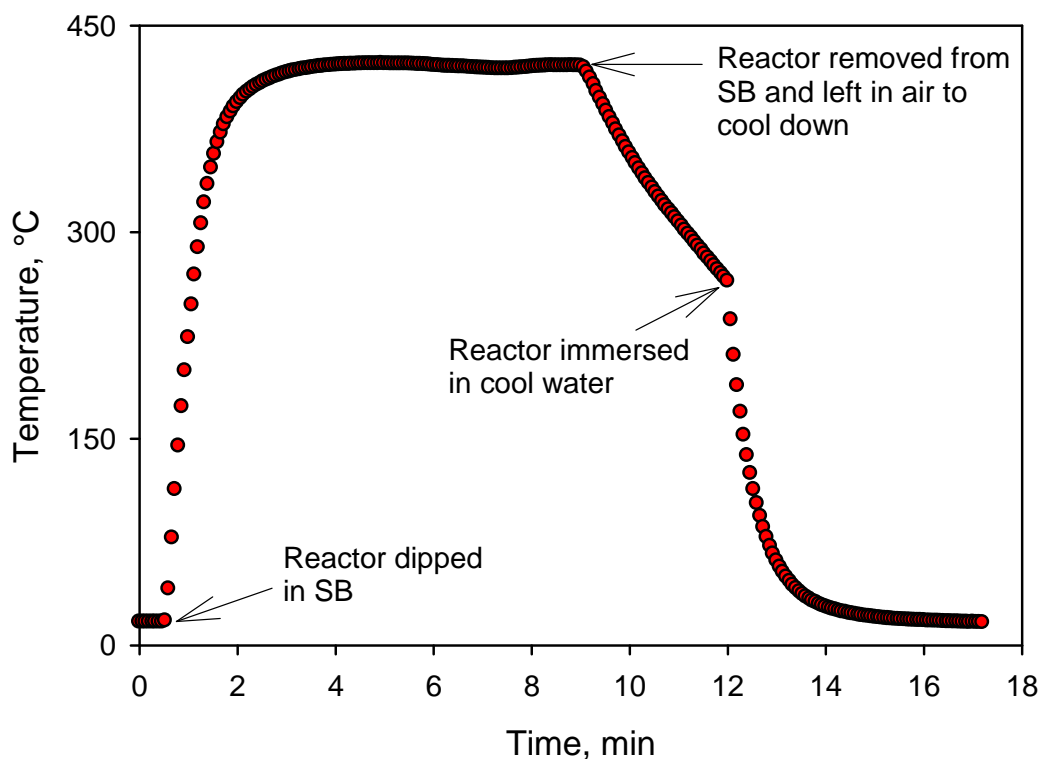


Figure A.5: The temperature profile for heating a microreactor in the RHS SB. After reaching the final temperature, the reactor was removed and was allowed to cool in air followed by immersion in cool water.

The RHS SB, on the other hand, showed a higher final temperature of 422 °C, which increased to over 425 °C when the shaking motor was ON. **Figure A.5** shows one run performed on the RHS SB. The first decline in temperature was when the reactor was removed from the SB but left in air to cool down, followed

by immersing in cool water, which is shown as the abrupt change in temperature. How the reactor cools in air was examined because glass liners were planned to be inserted in the reactors and thus may crack by the extreme change in temperatures over a very short time.

Finally, two runs were done with an empty glass liner inserted in the microreactor, and are shown in **Figure A.6**. In one experiment, the reactor was removed from the SB and dipped immediately in cool water. In the second, the reactor was allowed to cool down in air until its temperature dropped below 200 °C before immersion in cool water. In both cases, the glass liner was intact.

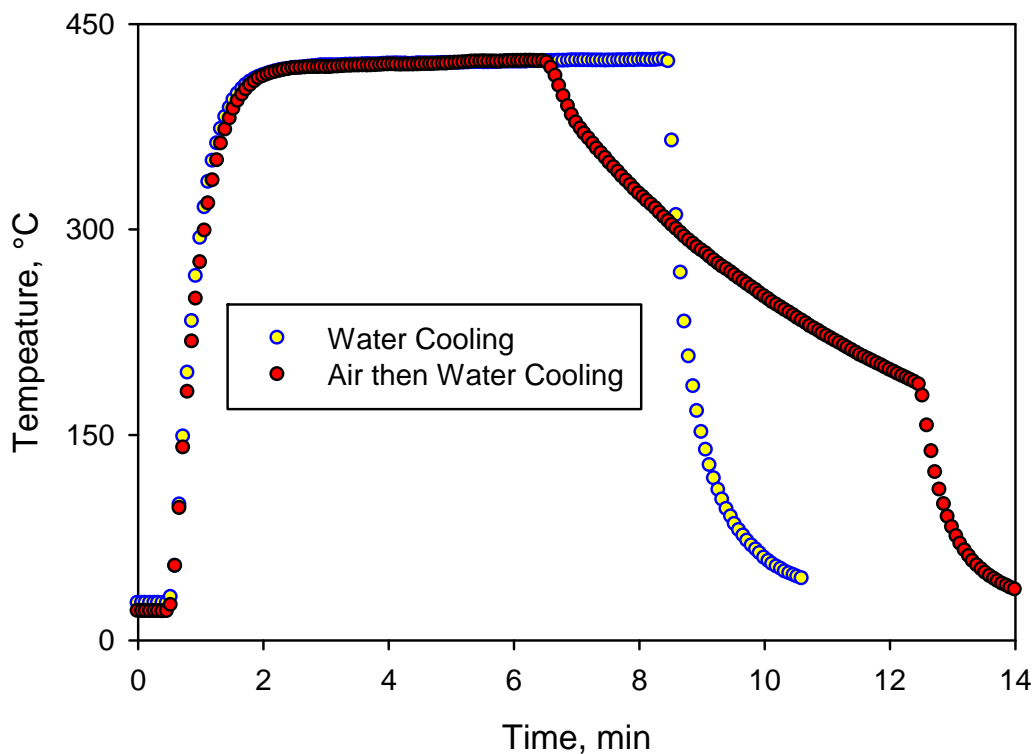


Figure A.6: Two experiments of heating the microreactor with a glass liner inside followed by two different cooling profiles.

Based on these experiments, the RHS SB was selected with the motor shaker operating, as the temperature in such case would reach within 5 °C of the set value in less than 3 min. The reaction times were thus limited to a minimum of 15 min in order to make the reaction times much longer than the heat-up time. The glass liner was intact at the end of these experiments in spite of the motor shaker being ON and the cooling being by rapid immersion in water. Therefore, reacting the model compounds in glass liners and the subsequent cooling with water was done.

A.3 GAS CHROMATOGRAPHY

Gas chromatography (GC) equipped with a flame ionization detector (FID) was used to quantify the cracked fragments from the model compounds. The preliminary experiments to test the performance of the microreactor and to optimize the GC analysis were performed with a bibenzyl (BB) with naphthalene (NP) as the standard with which the response factor of bibenzyl was calculated. At least three different concentrations with multiple runs of each concentration were performed.

Figure A.7 shows the area versus the concentration of BB in methylene chloride (MC) while **Figure A.8** shows the ratio of A_{BB}/C_{BB} versus the A_{NP}/C_{NP} , where **A** stands for the area under the detected peak in GC and **C** is the concentration in the prepared samples. The slope gives the response factor that is used to quantify BB in samples with unknown concentrations. High linearity is obtained from these experiments.

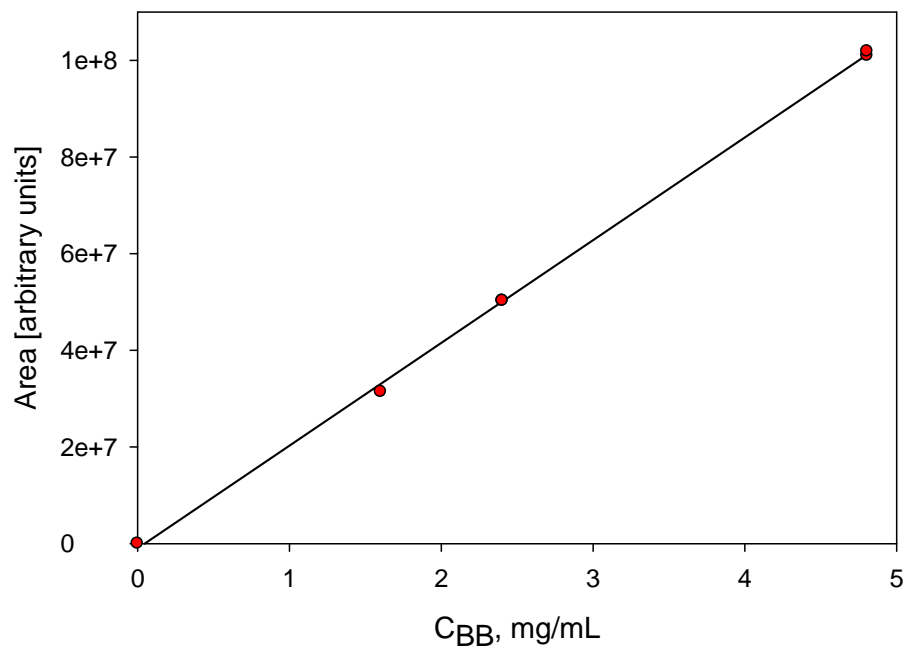


Figure A.7: The integrated area of GC peaks as a function of the concentration of BB in MC. The line shown is the regression line.

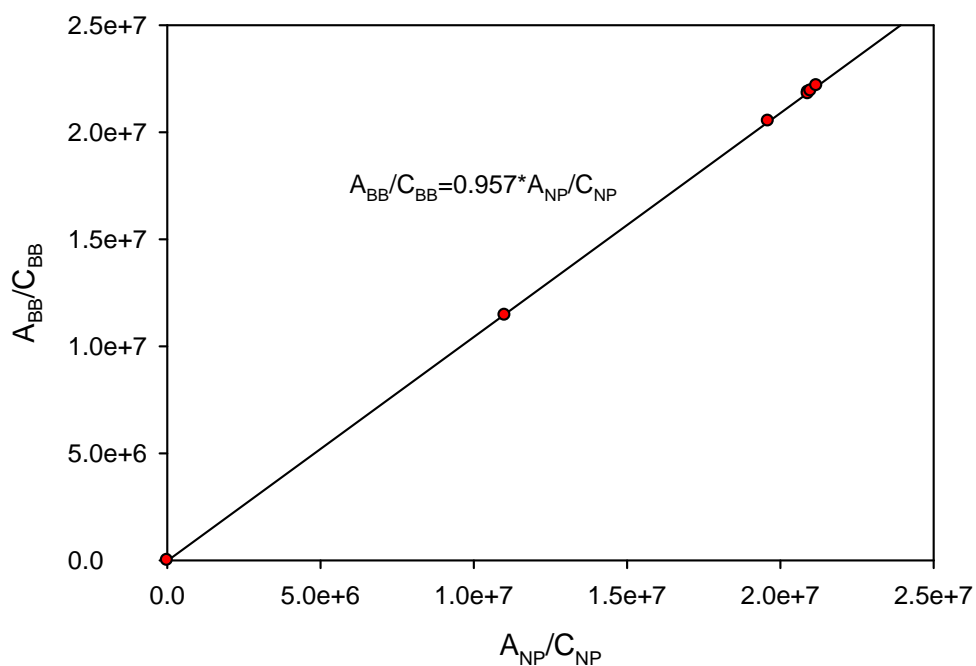


Figure A.8: Response factor of the GC experiments of BB with NP as the calibration standard (equals the slope). The line shown is the regression forced through the origin giving the shown equation.

Figure A.8 shows that even if experimental variations happened, which may be uncontrollable, the ratio of the FID response to BB to that of NP remains constant. Therefore using the response factor, rather than the area under the BB peaks only, gives the most accurate results.

A.3.1 Optimization of the Main Controlling Factors

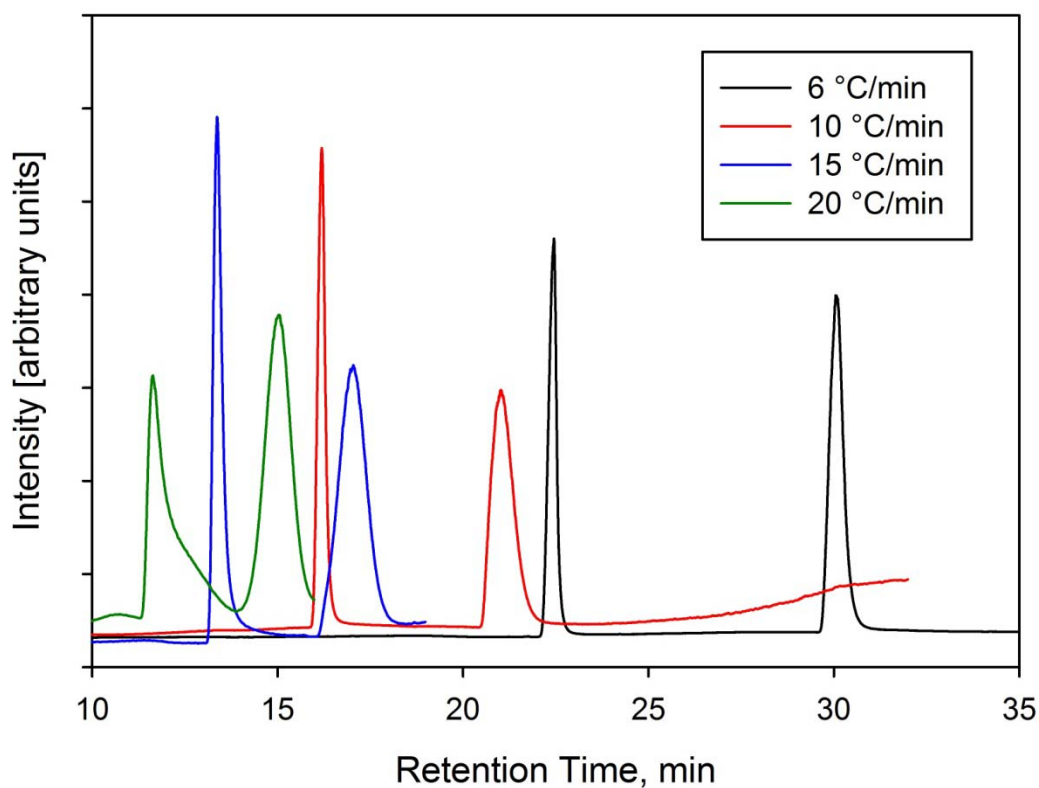


Figure A.9: Effect of ramping temperature while fixing the oven starting temperature at 40 °C and the carrier gas flow rate at 0.2 mL/min.

While performing the preliminary experiments with BB and NP, the main controlling factors were also identified in order to optimize them when reaction products of the model compounds are analyzed. The ones addressed below are the ramping temperature (RT), carrier gas flow rate (FR), and the GC oven starting

temperature (ST), the effect of which are shown in **Figures A.9–A.11**. The first peak is for NP while the second peak is for BB in all of these figures.

Figure A.9 shows the effect of RT while fixing other parameters. As the ramping temperature increases, the elution time decreases. But the short elution affects the shape of the peak and thus the measured area. The lowest RT to elute all products in reasonable times is therefore desired to obtain the best results.

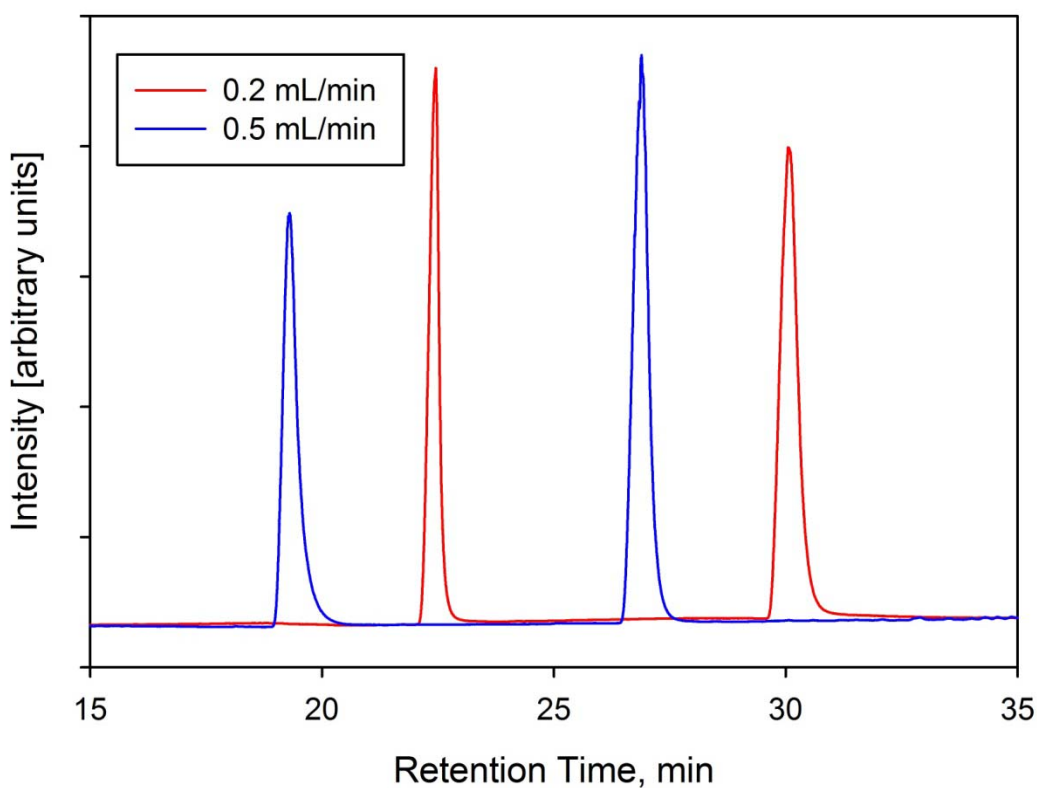


Figure A.10: Effect of helium gas flow rate on the GC results. The oven ramping and starting temperatures are fixed at 6 °C and 40 °C, respectively.

Figure A.10 shows the effect of FR while fixing the ST at 40 °C and RT at 6 °C/min of the GC oven. A higher flow rate gives shorter retention times but

sometimes larger tails. The lowest FR to give reasonable elution times is thus desired. Finally the effect of ST on the GC peaks and elution times is shown in **Figure A.11**. Higher starting temperatures of the GC generally give better peak shapes and shorter retention times. Therefore, the highest ST, as long as the peaks are resolved and with uniform shape, is desired.

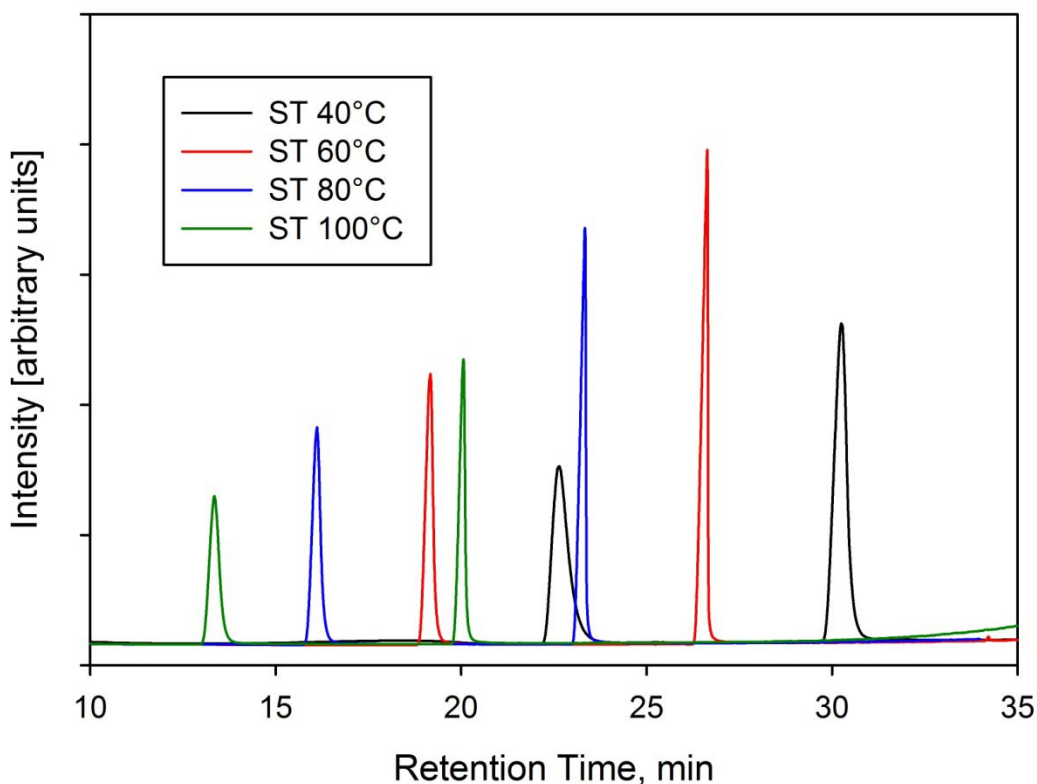


Figure A.11: Effect of oven starting temperature on the retention time and peak shapes. FR and RT fixed at 0.2 mL/min and 6 °C/min, respectively.

Although these factors affect the products separation and retention times, again the ratio of the analyzed sample to the standard remains constant. The response factor calculations and the ratio of A/C between BB and NP for the previous runs (at variable RT, FR, and ST) are shown in **Figure A.12**.

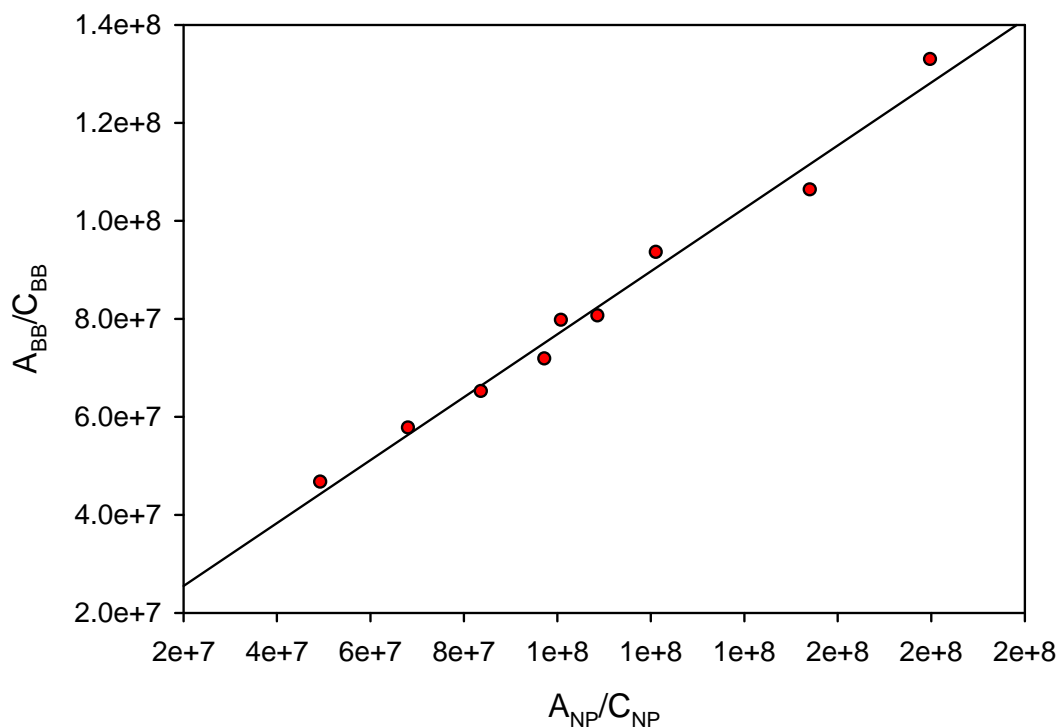


Figure A.12: A linear relationship exists between the area/concentration ratio of BB to NP in spite of the variable RT, FR, or ST used in obtaining the above data points.

In the analysis of the products from reactions of the model compounds, these parameters, among others, were kept constant to enable comparisons. Most samples were run according to the following method: ST 100 °C for 1 min holdup followed by 10 °C/min ramp to ~300–350 °C. The flow rate of the carrier gas, helium, was kept at 2 mL/min and the mode was usually split to obtain the best peak shapes. In the next section, the calibration curves for some model compounds are shown.

A.3.2 Calibration Curves for the Quantification of Cracked

Products in GC

The calibration curves and response factor calculations for P-3,5-pyr-P, P-BiTh-P, and BP are listed below. Other archipelago compounds used the average response factor from P-3,5-pyr-P and P-BiThP since the cracked fragments (typically pyrene, alkylated pyrenes, parent-minus-pyrene, and parent-minus-methylpyrene, and their dehydrogenated products) and the calibration standard (phenanthrene) were the same. Pyrene and alkylated pyrenes from Chol-Py were quantified using this value too. For Chol-BB fragments, a response factor of 1 was assumed due to lack of proper calibration standards.

A.3.2.1 Calibration for P-3,5-pyr-P

Pyrene (P), P-3,5-pyr-P, and phenanthrene (Phen) were dissolved in MC at known concentrations and the response factor (**F**) was calculated for P / Phen [**F** = $(A_P/C_P)/(A_{Phen}/C_{Phen})$]. The results are shown in **Table A.2** and **Figures A.13** and **A.14**.

Table A.2: GC calibration data for Pyrene with P-3,5-pyr-P in MC

C_P	A_P	C_{Phen}	A_{Phen}	A_P/C_P	A_{Phen}/C_{Phen}	F
0.235	21980396.8	0.447	46609170.0	93353036.4	104207493.9	0.896
0.235	22031153.8	0.447	46942885.0	93568606.7	104953604.7	0.892
0.118	11820306.8	0.224	24689929.0	100404150.0	110402121.5	0.909
0.118	11679919.5	0.224	24499654.5	99211671.4	109551300.6	0.906
0.047	4909166.0	0.089	10198727.5	104248698.8	114010165.14	0.914
0.047	4986228.500	0.089	10452903.000	105885161.2	116851557.9	0.906

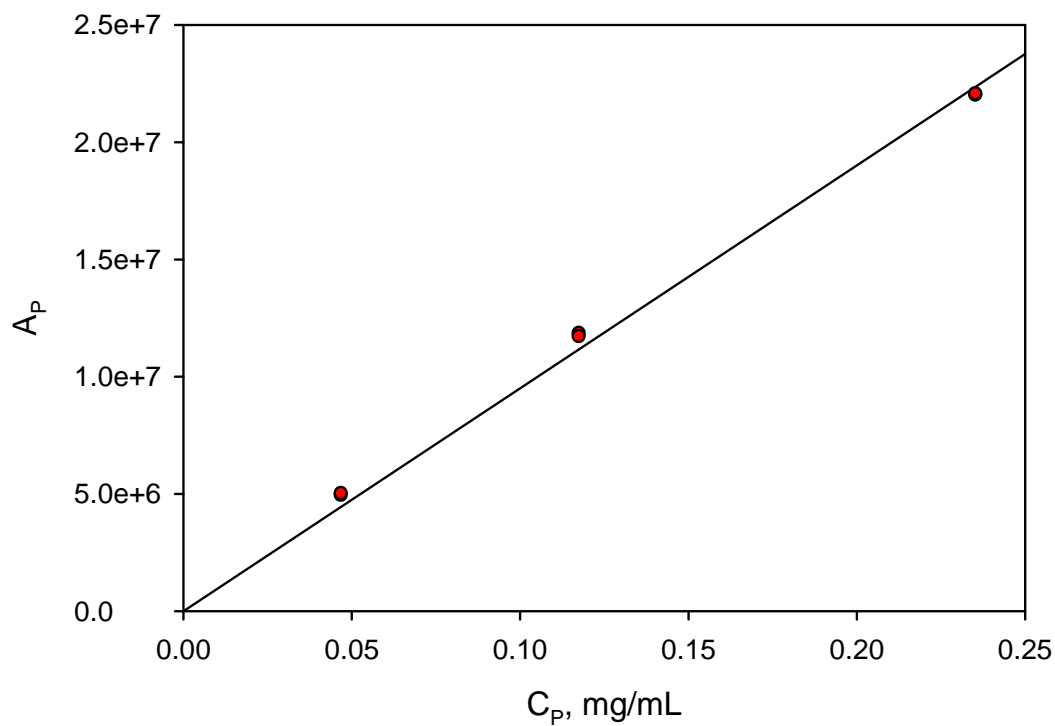


Figure A.13: Integrated area of pyrene peak in GC as a function of C .

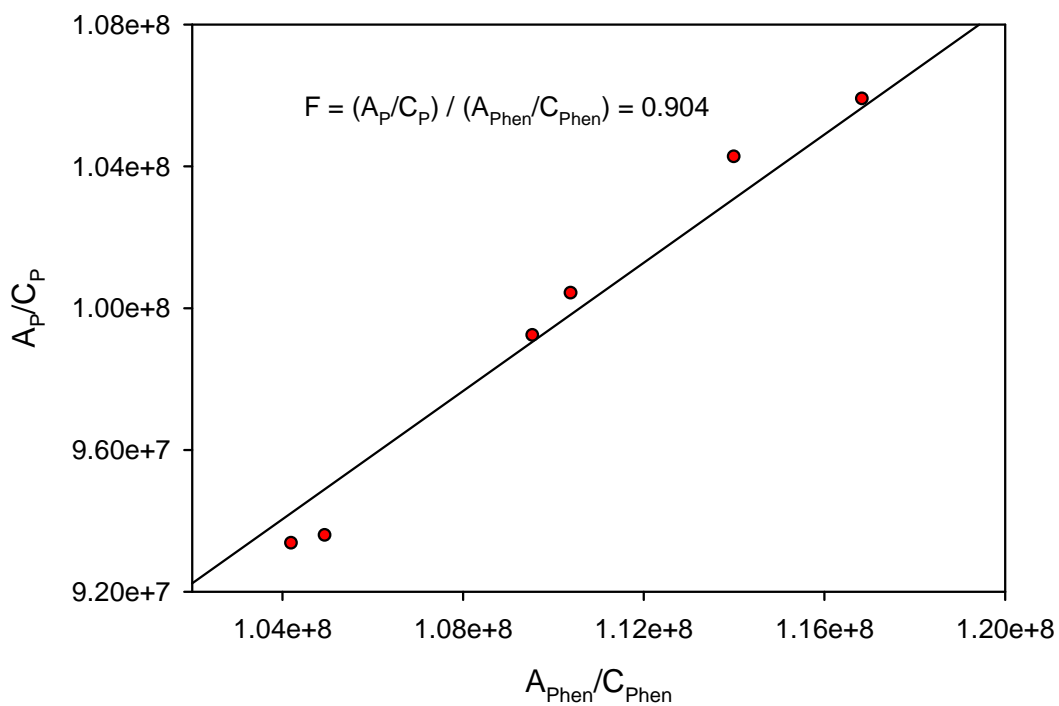


Figure A.14: Response factor calculation of P / Phen in solution with P-3,5-pyr-P

A.3.2.2 Calibration for P-BiTh-P

The P/Phen **F** values were re-calculated for solutions with P-BiTh-P to eliminate possible effects of the parent on the calibration data obtained with P-3,5-pyr-P. The results are shown in **Table A.3** and **Figures A.15** and **A.16**.

Table A.3: GC calibration data for pyrene with P-BiTh-P in MC

C_P	A_P	C_{Phen}	A_{Phen}	A_P/C_P	A_{Phen}/C_{Phen}	F
0.355	26310455.255	1.015	81493879.744	74113958.465	80289536.694	0.923
0.355	26594108.150	1.015	81375808.750	74912980.704	80173210.591	0.934
0.178	13497840.250	0.508	41124261.000	76044170.423	81033026.601	0.938
0.178	13088756.500	0.508	39534484.750	73739473.239	77900462.562	0.947
0.071	6084773.000	0.203	18274412.500	85701028.169	90021736.453	0.952
0.071	6064609.500	0.203	18108208.000	85417035.211	89202995.074	0.958

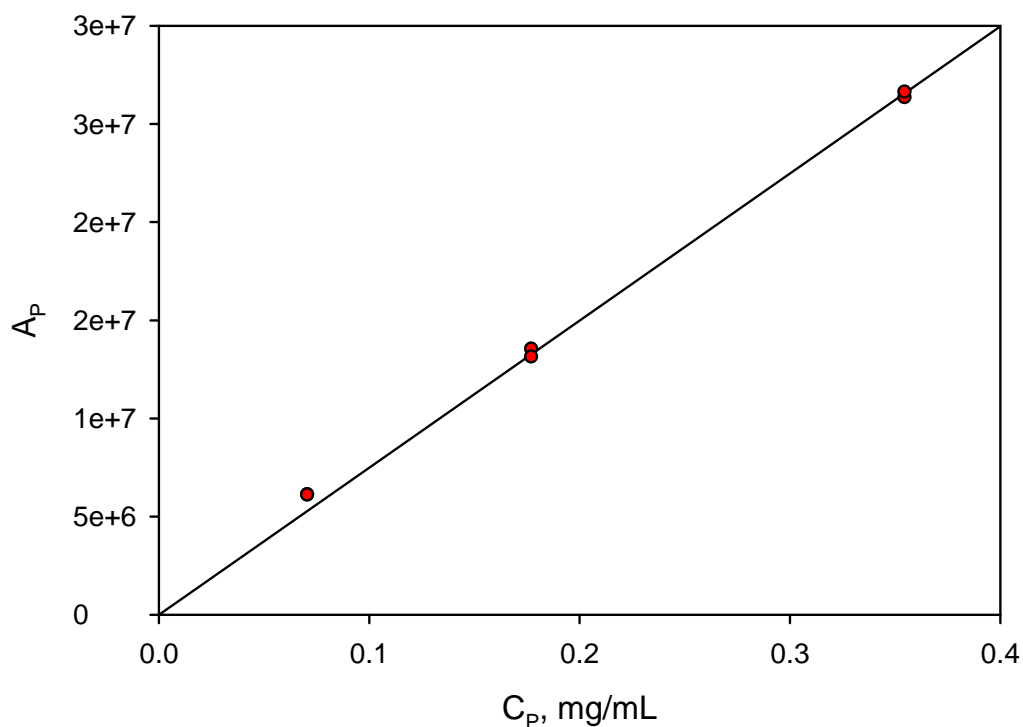


Figure A.15: Area of P in GC as a function of **C** with P-BiTh-P in MC.

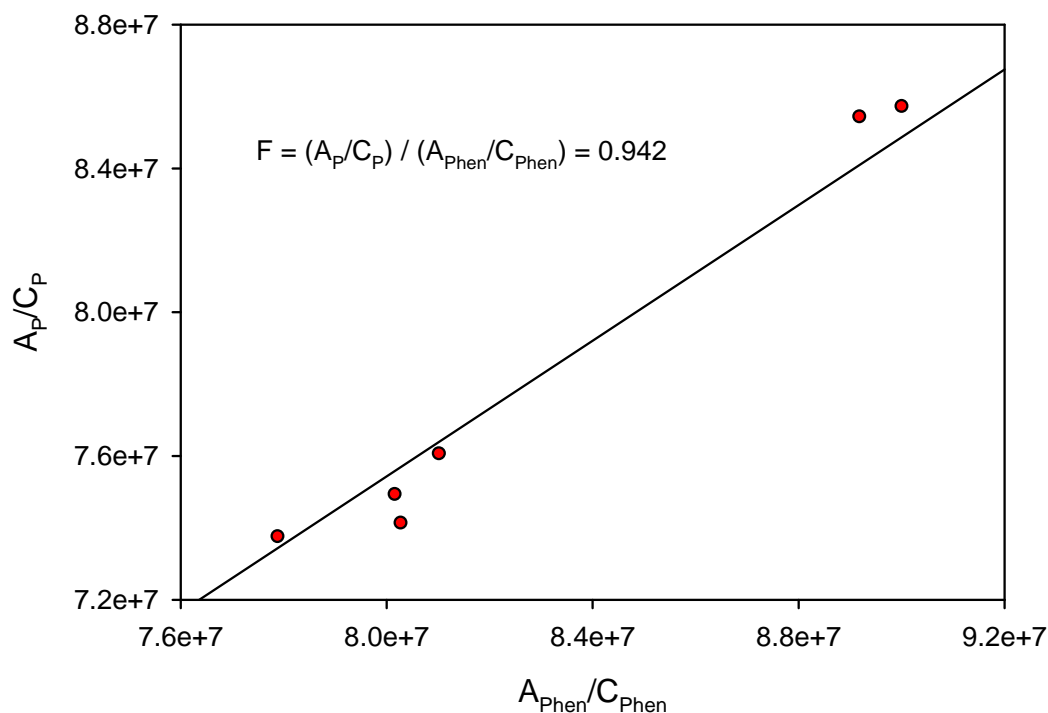


Figure A.16: Response factor calculation of pyrene to phenanthrene in solution with P-BiTh-P

A.3.2.3 Calibration for BP

Since Benzo[a]pyrene (BP) may have different response than pyrene, a solution of known concentration of BP and Phen was analyzed in the GC. The calibration results are shown in **Table A.4** and **Figures A.17** and **A.18**.

Table A.4: GC calibration data for BP with Phen in MC

C_{BP}	A_{BP}	C_{Phen}	A_{Phen}	A_{BP}/C_{BP}	A_{Phen}/C_{Phen}	F
3.270	70551210.492	0.491	13877291.595	21578593.208	28292133.731	0.763
3.270	77741283.222	0.491	15043791.420	23777728.467	30670318.899	0.775
1.635	37287927.250	0.245	6641000.000	22809559.413	27078491.335	0.842
1.635	30012556.750	0.245	5233269.500	18359111.026	21338509.684	0.860
0.654	14823278.000	0.098	2409486.000	22669028.904	24561529.052	0.923
0.654	8376041.036	0.098	1394132.325	12809360.814	14211338.685	0.901

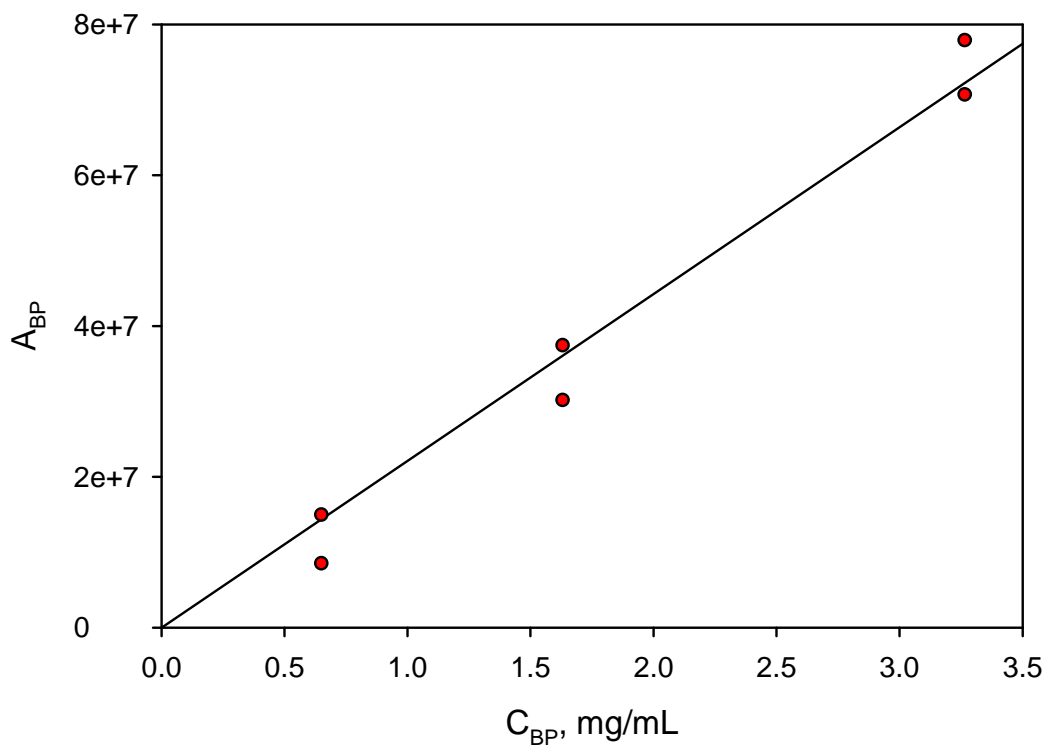


Figure A.17: Area of BP in GC as a function of concentration in MC.

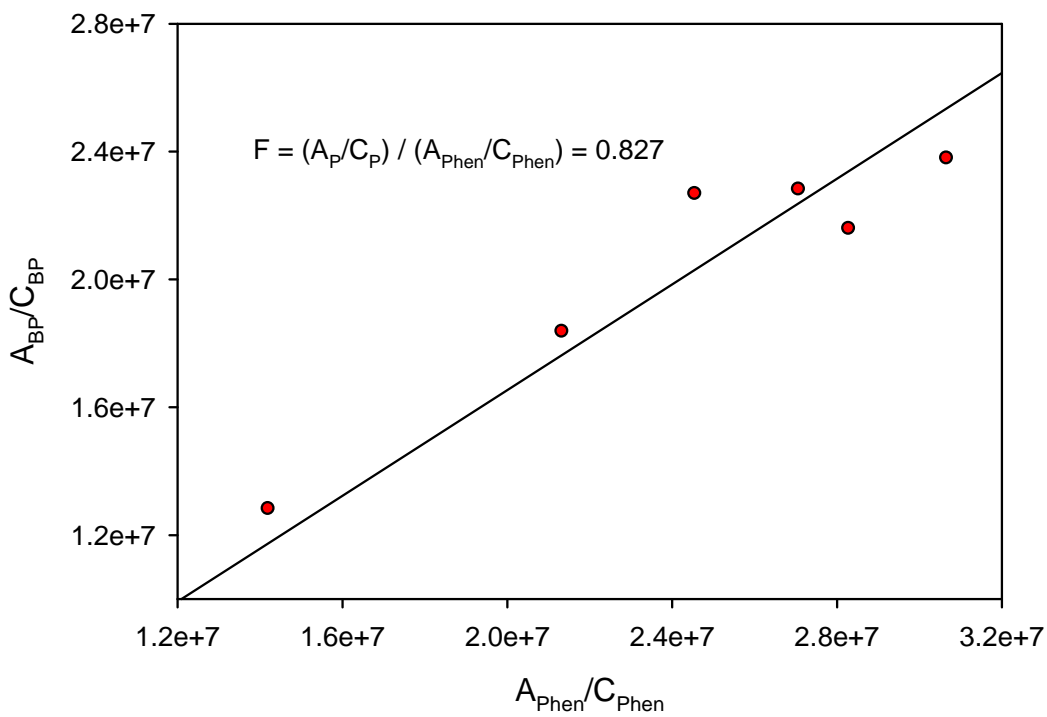


Figure A.18: Response factor calculation of BP to Phen dissolved in MC.

A.4 HIGH PERFORMANCE LIQUID CHROMATOGRAPHY

HPLC was used to quantify the parent compound in order to calculate the conversion after the reaction. The response factor (**F**) used for the quantification was used for all the addition products eluting after the parent, as well as the heavy cracked products (parent-minus-pyrene and parent-minus-methylpyrene). Pyrene and alkylpyrenes were quantified using the response factor of pyrene/phenanthrene. Hence, pyrene (P), phenanthrene (Phen) and the parent were dissolved in MC at known concentration for **F** calculation.

Listed below are the main parameters optimized in the HPLC analysis followed by the calibration curves of the model compounds reacted in microreactors.

A.4.1 Main Controlling Factors in HPLC Analysis

The separation column (Zorbax Eclipse PAH column of 4.6×150 mm with a C18 phase of $3.5 \mu\text{m}$ particles) and a column temperature of 23°C were kept constant in all the experiments. The UV lamp wavelength of the detector and the mobile phase flow profile (i.e. flow rate or flow type) were the main parameters varied and optimized for each model compound. One example of the trial runs made on each compound to optimize the HPLC analysis is given for P-BiTh-P. A series of 11 runs were performed while varying the flow profile of a mixture of methylene chloride (MC) and methanol (MeOH), and the detector settings. **Table A.5** lists these runs, and comparisons of the obtained spectra are given in **Figure A.19** and **A.20** for the effect of flow profile and detector settings, respectively.

Table A.5: HPLC optimization runs with P, Phen, and P-BiTh-P in MC.

Run #	T (°C)	Detector Wavelength / bw, in nm	Flow profile	Results & Notes
1	23	270/4	1µL injected. Flow @ 75% MeOH – 25% MC at 1 mL/min. Flow increased to 2 mL/min at 17.3 min. Conc. ramped @ 22-23min to 60%MeOH –40% MC. Ramp conc. to 100% MC from 29-30min	P and Phen are separated. Two peak appeared could be due to analyte, one at~14.5min and a larger one at~31min. The baseline deviated after 15 min.
2		270/4	Flow @ 75% MeOH – 25% MC at 1 mL/min for 3 min then ramp to 100% MC from 3-5 min.	Analyte- eluted ~6.5min but there are humps before and after the peak.
3		270/4	Flow @ 75% MeOH – 25% MC at 1 mL/min for 3 min. 3-8 min ramp flow to 2 mL/min and conc. To 35% MeOH – 65% MC	Good but there is a baseline shift (due to change in mobile phase concentration)
4		270/4	Inject 5µL sample. Flow @ 65% MeOH – 35% MC at 0.5 mL/min for 3 min. 3-4 min ramp flow to 3 mL/min	Excellent separation in 5 min. No baseline shift
5		270/4	Inject 3µL sample Flow @ 65% MeOH – 35% MC at 0.5 mL/min for 4 min 4-5 min ramp to 3 mL/min flow	Excellent separation
6		272/4 and 16 239/16 335/16	Inject 1µL sample Flow @ 65% MeOH – 35% MC at 0.5 mL/min for 4 min 4-5 min ramp to 3mL/min flow	272 nm at both bw are similar to 270 nm. 239 nm showed the greatest intensity for the three analytes. 335 nm had similar intensity for analyte as 272 nm but lower for P and much lower for Phen.
7		239/16 254/16 320/16 335/4 and 16	Same as R6	Among these detector settings, the best are 239 nm and 335 nm at 16 band width
8		239/16 320/16 335/16	Same as R6 but inject 2µL	The best performance was for 239 nm, 16 bw
9		239/16 335/16	Same as R6	239 nm is much better and excellent separation
10		239/16 335/16	Same as R6 inject 5µL	Excellent separation and 239 nm is best
11		239/16	Inject 1µL sample Flow @ 65% MeOH – 35% MC at 0.5 mL/min for 4 min 4-5 min ramp to 3mL/min flow	Final method

The two parameters varied in the detector settings in **Table A.5** are the absorbance wavelength and the bandwidth (bw), which is the range of absorbance wavelength where the set value is the midpoint. For example, if the wavelength was set at 270 nm and the bw at 4, then the absorbance is measured over the range of 268–272 nm.

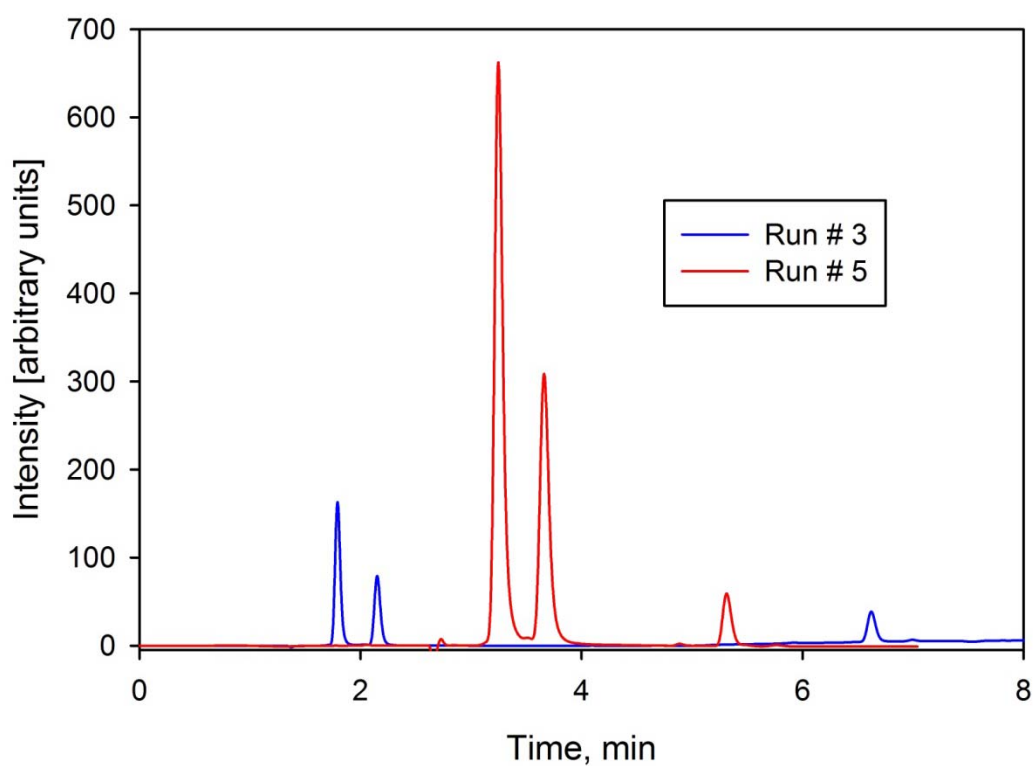


Figure A. 19: Effect of flow method. The order of eluting peaks corresponds to Phen, P, and P-BiTh-P, respectively.

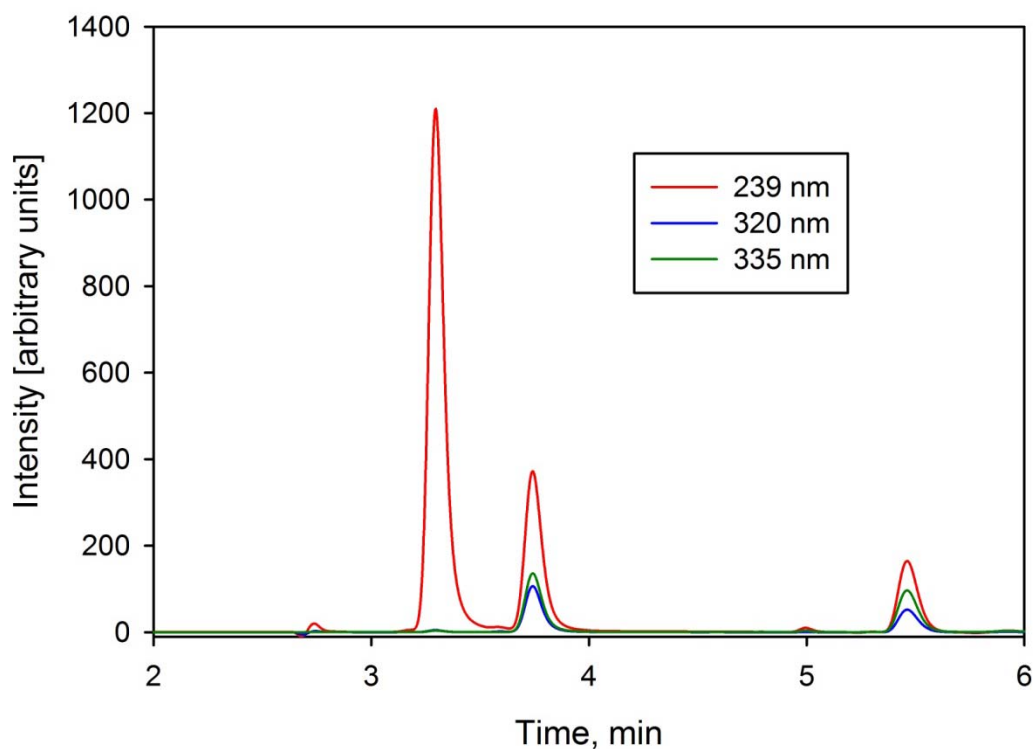


Figure A. 20: Effect of detector settings. The order of eluting peaks is similar to **Figure A.19**.

A.4.2 Calibration Curves for the Model Compounds in HPLC

After separation optimization of each compound in the HPLC, samples of at least three different concentrations are run several times to construct the calibration curves and response factors. The calibration standard is phenanthrene (Phen) in all the cases except in Chol-BB where pyrene (P) was used as the standard. Since pyrene was expected to be one of the major products in all the archipelago compounds, P/Phen **F** was also calculated. Tables of the response factor calculations and plots of the integrated area as measured in HPLC vs the analyte concentrations are given below. All given concentrations (**C**) are in mg/mL and area (**A**) in arbitrary units.

A.4.2.1 Calibration for P-BiTh-P

Table A.6: HPLC calibration data for P-BiTh-P to Phen, with P in MC

$C_{\text{P-BiTh-P}}$	$A_{\text{P-BiTh-P}}$	C_{Phen}	A_{Phen}	$A_{\text{P-BiTh-P}}/C_{\text{P-BiTh-P}}$	$A_{\text{Phen}}/C_{\text{Phen}}$	F
2.119	2069.807	1.015	12728.643	976.785	12540.535	0.0779
2.119	2030.501	1.015	12897.421	958.235	12706.819	0.0754
1.060	1174.795	0.508	6738.955	1108.820	13278.728	0.0835
1.060	1141.641	0.508	6747.258	1077.528	13295.090	0.0810
0.424	502.651	0.203	2983.423	1186.057	14696.663	0.0807
0.424	506.876	0.203	2991.152	1196.026	14734.737	0.0812
Average F =						0.0800

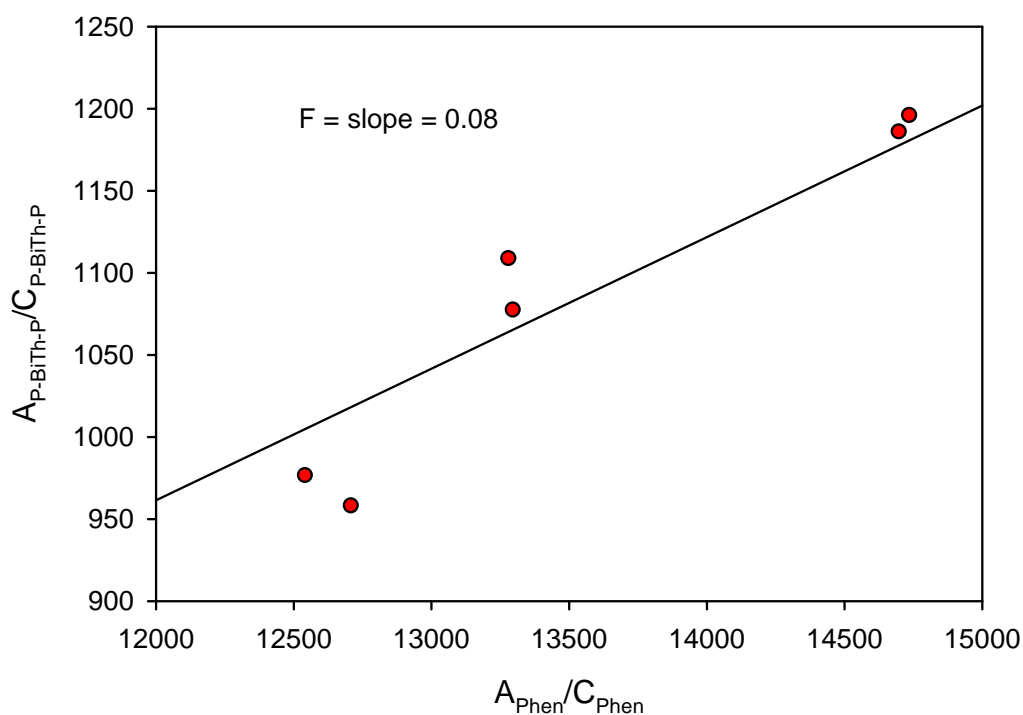


Figure A.21: Response factor calculations for P-BiTh-P to Phen dissolved in MC in HPLC.

The slope of the curve is typically the same as the average shown in the tables, therefore, the response factor calculation figures will not be given for the rest of the compounds. Instead, plots of the analyte concentration versus its

integrated area will be given. In the case of P-BiTh-P, this is shown in **Figure A.22**.

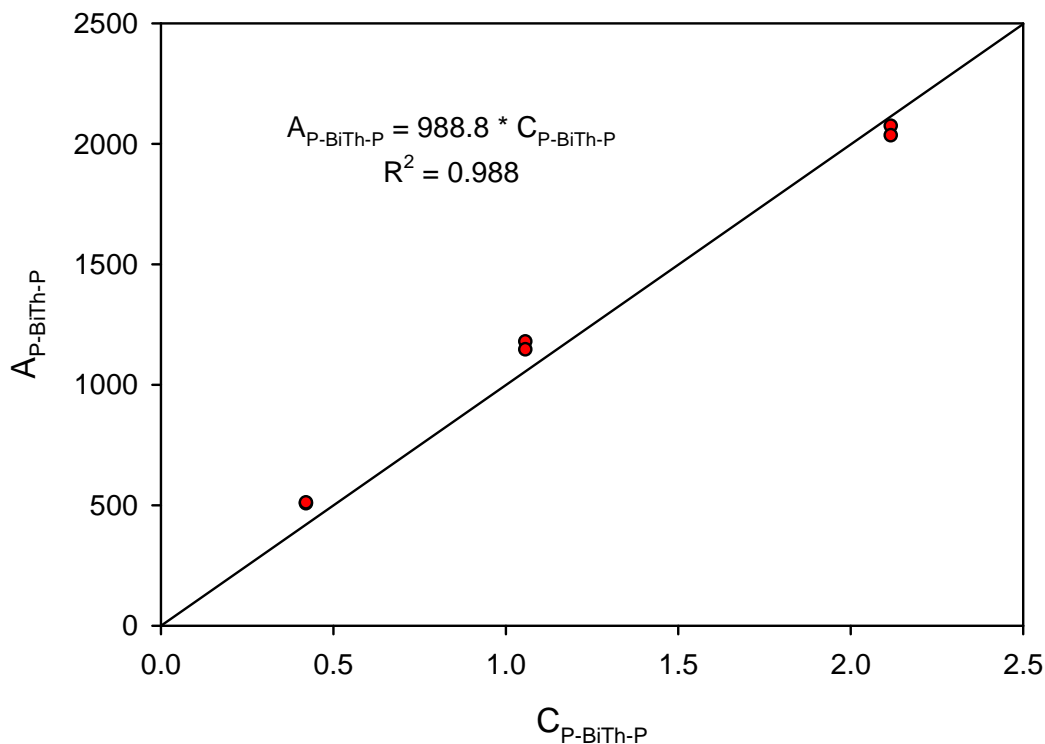


Figure A.22: Integrated area of P-BiTh-P in HPLC as a function of C.

Table A.7: HPLC calibration data for P to Phen, with P-BiTh-P in MC

C_P	A_P	C_{Phen}	A_{Phen}	A_P/C_P	A_{Phen}/C_{Phen}	F
0.355	4625.066	1.015	12728.643	13028.356	12540.535	1.039
0.355	4778.647	1.015	12897.421	13460.979	12706.819	1.059
0.178	2350.914	0.508	6738.955	13244.586	13278.728	0.997
0.178	2339.075	0.508	6747.258	13177.886	13295.090	0.991
0.071	1043.837	0.203	2983.423	14701.930	14696.663	1.000
0.071	1040.803	0.203	2991.152	14659.195	14734.737	0.995
Average F =						1.014

Table A.7 shows the **F** calculation for pyrene (P) to phenanthrene (Phen) which were dissolved along with the analyte (P-BiTh-P) with known

concentrations. This value is used to measure the pyrene and alkylated pyrenes in the reaction products of P-BiTh-P. **Figure A.23** shows the integrated area as a function of pyrene concentration (C) in MC.

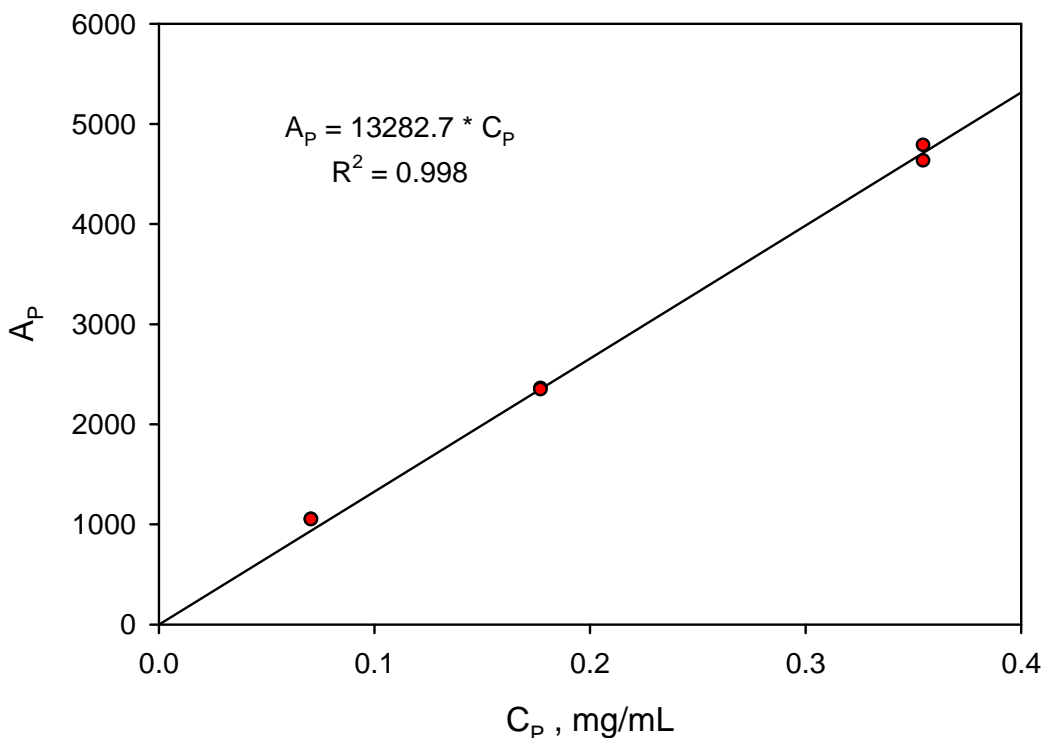


Figure A.23: Area of P in HPLC as a function of C. P is in MC solution with Phen and P-BiTh-P.

A.4.2.2 Calibration for P-3,5-pyr-P

Table A.8: HPLC calibration data for P to Phen, with P-3,5-pyr-P in MC

C_P	A_P	C_{Phen}	A_{Phen}	A_P/C_P	$A_{\text{Phen}}/C_{\text{Phen}}$	F
0.235	9257.723	0.447	17604.465	39318.513	39359.576	0.999
0.235	9286.457	0.447	17609.502	39440.551	39370.838	1.002
0.118	5112.868	0.224	10379.450	43429.764	46412.176	0.936
0.118	5123.115	0.224	10395.645	43516.805	46484.589	0.936
0.047	2257.441	0.089	4592.464	47937.935	51338.519	0.934
0.047	2246.242	0.089	4572.347	47700.129	51113.637	0.933
Average F =						0.957

Table A.8 shows the response factor calculations for pyrene to phenanthrene in the same solution with P-3,5-pyr-P. This is to check if the parent being in solution with pyrene will affect the response factor. The average **F** of 0.957 is almost the same as the one obtained with P-BiTh-P (1.014 in **Table A.7**). This value was examined with all the model compounds and it was always ~ 1. Area versus concentration of pyrene in this sample is also shown in **Figure A.24** which also gives a linear response similar to that obtained with P-BiTh-P (**Figure A.23**). The slope is different than that in **Figure A.23** because the flow profile for separation of the P-3,5-pyr-P is different than that of P-BiTh-P. Therefore, **F** calculations and area versus concentration curves for pyrene/phenanthrene will not be given for the rest of the compounds.

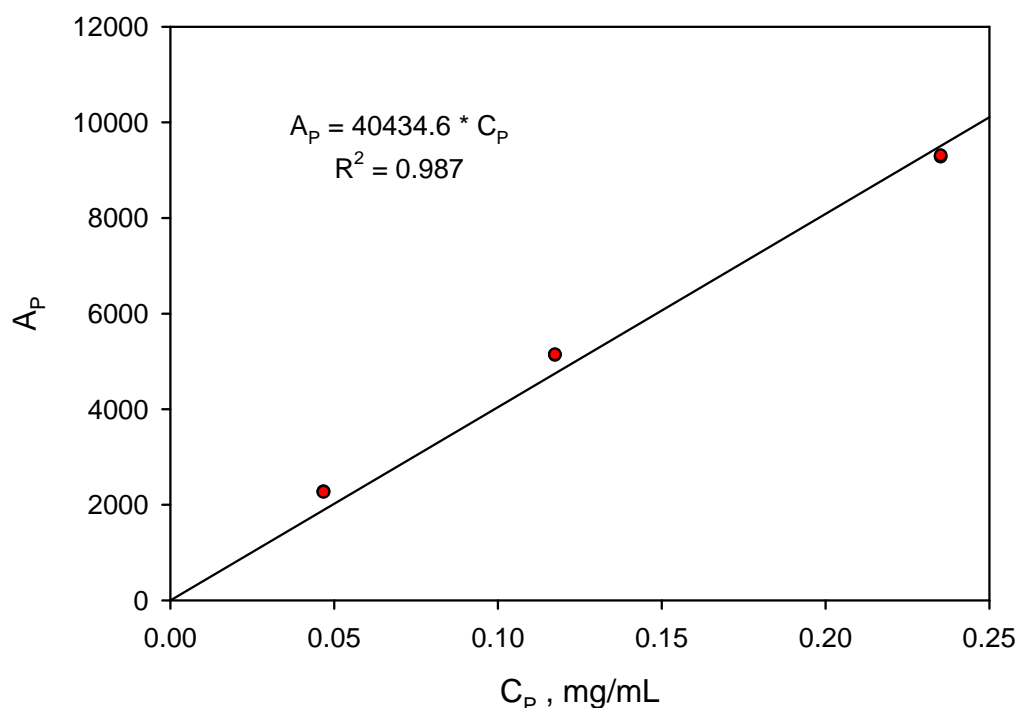
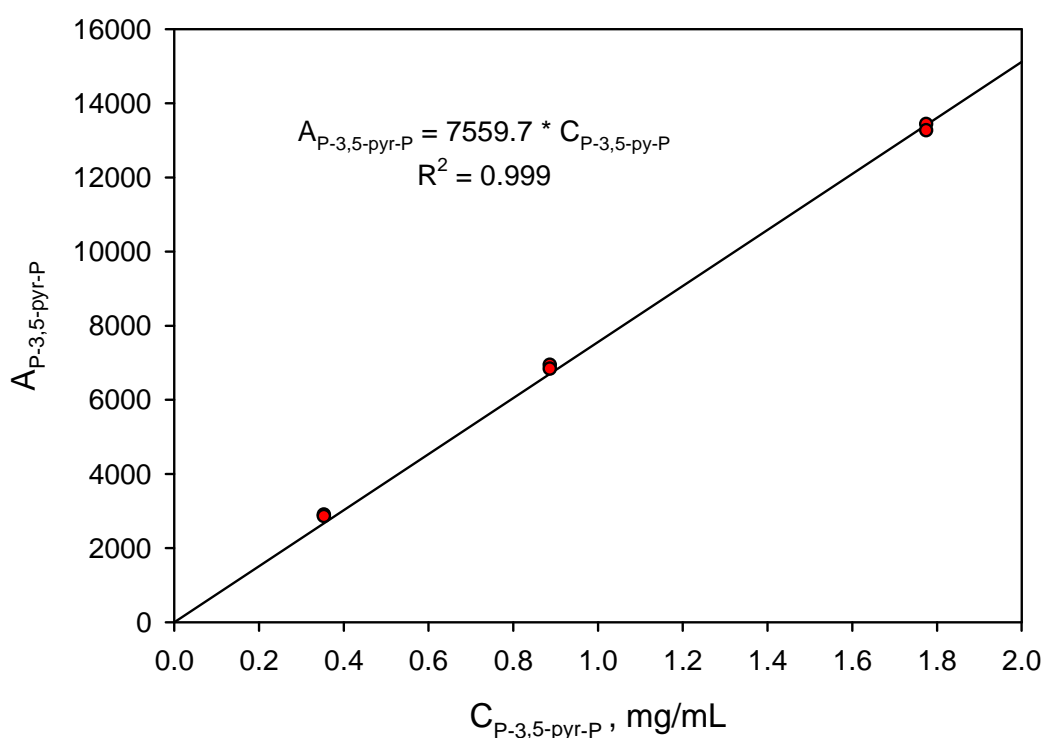


Figure A.24: Area of P in HPLC as a function of C. P is in MC solution with Phen and P-3,5-pyr-P.

Table A.9: HPLC calibration data for P-3,5pyr-P to Phen, with P in MC

$C_{P-3,5-pyr-P}$	$A_{P-3,5-pyr-P}$	C_{Phen}	A_{Phen}	$\frac{A_{P-3,5-pyr-P}}{C_{P-3,5-pyr-P}}$	$\frac{A_{Phen}}{C_{Phen}}$	F
1.777	13409.844	0.447	17604.465	7547.111	39359.576	0.192
1.777	13242.470	0.447	17609.502	7452.912	39370.838	0.189
0.888	6912.277	0.224	10379.450	7780.511	46412.176	0.168
0.888	6809.799	0.224	10395.645	7665.161	46484.589	0.165
0.355	2874.306	0.089	4592.464	8088.351	51338.519	0.158
0.355	2833.526	0.089	4572.347	7973.595	51113.637	0.156
Average F =						0.171

**Figure A.25:** Area of P-3,5-pyr-P in HPLC as a function of C.

As evident from **Table A.9**, **F** for P-3,5-pyr-P to Phen is different from P-BiTh-P to the same standard. The mobile phase method is also different from one model compound to another. For the rest of the compounds, tables for the response factor calculations and the calibration curves of the integrated area versus the concentration are given next.

A.4.2.3 Calibration for P-2,6-pyr-P

Table A.10: HPLC calibration data for P-2,6pyr-P

$C_{P-2,6-pyr-P}$	$A_{P-2,6-pyr-P}$	C_{Phen}	A_{Phen}	$\frac{A_{P-2,6-pyr-P}}{C_{P-2,6-pyr-P}}$	$\frac{A_{Phen}}{C_{Phen}}$	F
0.606	3410.384	0.367	3970.636	5627.696	10809.353	0.521
0.606	3374.306	0.367	3935.556	5568.162	10713.854	0.520
0.606	3400.284	0.367	3955.154	5611.030	10767.206	0.521
0.606	3393.918	0.367	3968.943	5600.524	10804.744	0.518
0.227	1256.702	0.138	1494.517	5530.040	10849.488	0.510
0.227	1283.081	0.138	1528.911	5646.122	11099.174	0.509
0.227	1284.103	0.138	1529.402	5650.620	11102.738	0.509
0.091	515.776	0.055	631.494	5674.104	11460.867	0.495
0.091	523.323	0.055	629.036	5757.131	11416.260	0.504
0.091	522.953	0.055	629.530	5753.062	11425.221	0.504
Average F =						0.511

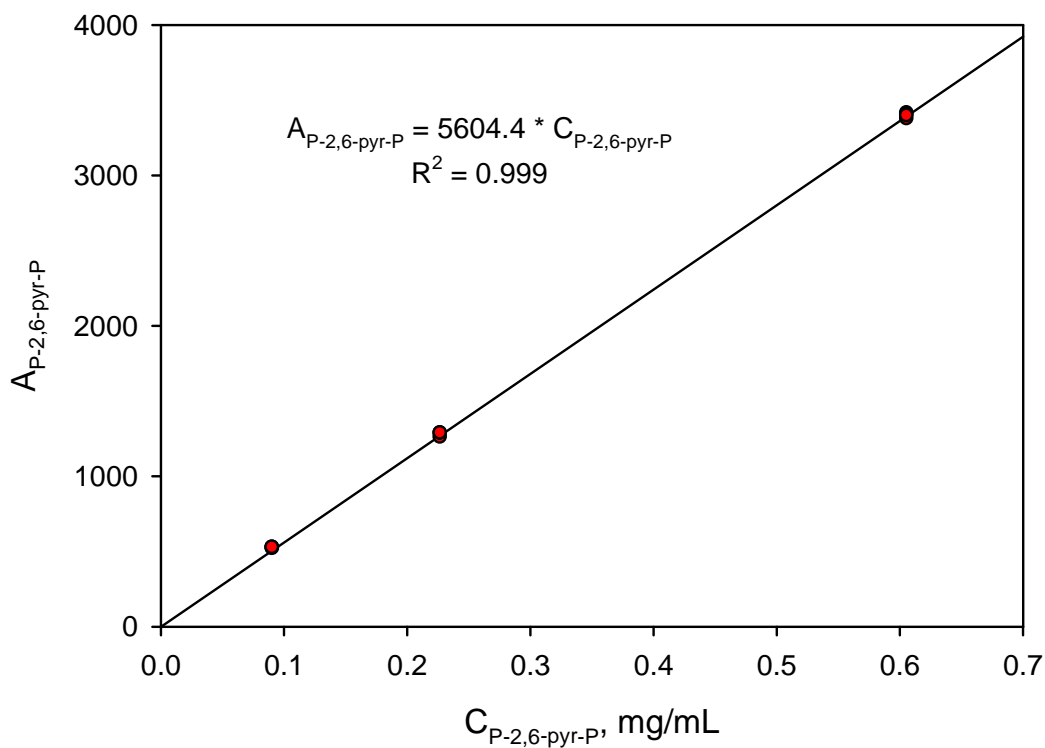


Figure A.26: Area of P-2,6-pyr-P in HPLC as a function of C.

A.4.2.4 Calibration for P-mPh-P

Table A.11: HPLC calibration data for P-mPh-P

$C_{P-mPh-P}$	$A_{P-mPh-P}$	C_{Phen}	A_{Phen}	$A_{P-mPh-P}/C_{P-mPh-P}$	A_{Phen}/C_{Phen}	F
1.941	13872.455	0.395	4361.826	7148.908	11042.597	0.647
1.941	13967.596	0.395	4355.005	7197.936	11025.330	0.653
1.941	13876.040	0.395	4400.338	7150.755	11140.096	0.642
0.970	7080.881	0.198	2331.211	7297.997	11803.598	0.618
0.970	7150.556	0.198	2297.201	7369.807	11631.397	0.634
0.970	7160.378	0.198	2294.890	7379.931	11619.697	0.635
0.388	3392.245	0.079	1006.307	8740.646	12738.063	0.686
0.388	3155.004	0.079	996.163	8129.358	12609.659	0.645
0.388	3185.214	0.079	1003.112	8207.199	12697.620	0.646
Average F=						0.645

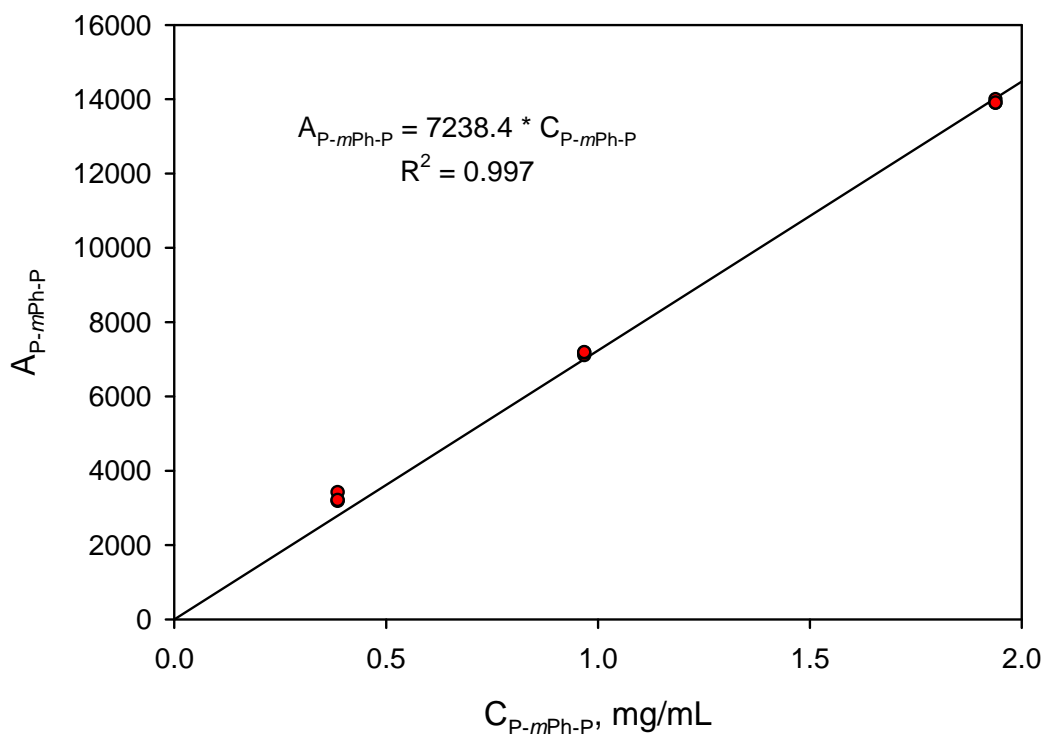


Figure A.27: Integrated area of P-mPh-P in HPLC as a function of C. In this sample, P-mPhP, P, Phen, and BP were dissolved in MC.

A.4.2.5 Calibration for P-pPh-P

Table A.12: HPLC calibration data for P-pPh-P

$C_{P-pPh-P}$	$A_{P-pPh-P}$	C_{Phen}	A_{Phen}	$A_{P-pPh-P}/C_{P-pPh-P}$	A_{Phen}/C_{Phen}	F
1.572	9772.555	0.221	2358.464	6215.320	10687.905	0.582
1.572	9762.489	0.221	2339.094	6208.918	10600.122	0.586
1.572	9849.754	0.221	2367.101	6264.418	10727.044	0.584
0.786	5917.778	0.110	1246.599	7527.383	11298.476	0.666
0.786	6033.409	0.110	1238.703	7674.465	11226.920	0.684
0.786	6080.219	0.110	1207.308	7734.007	10942.365	0.707
0.314	2445.151	0.044	574.234	7775.549	13011.356	0.598
0.314	2423.600	0.044	548.212	7707.018	12421.728	0.620
0.314	2540.527	0.044	532.575	8078.843	12067.405	0.669
Average F=						0.633

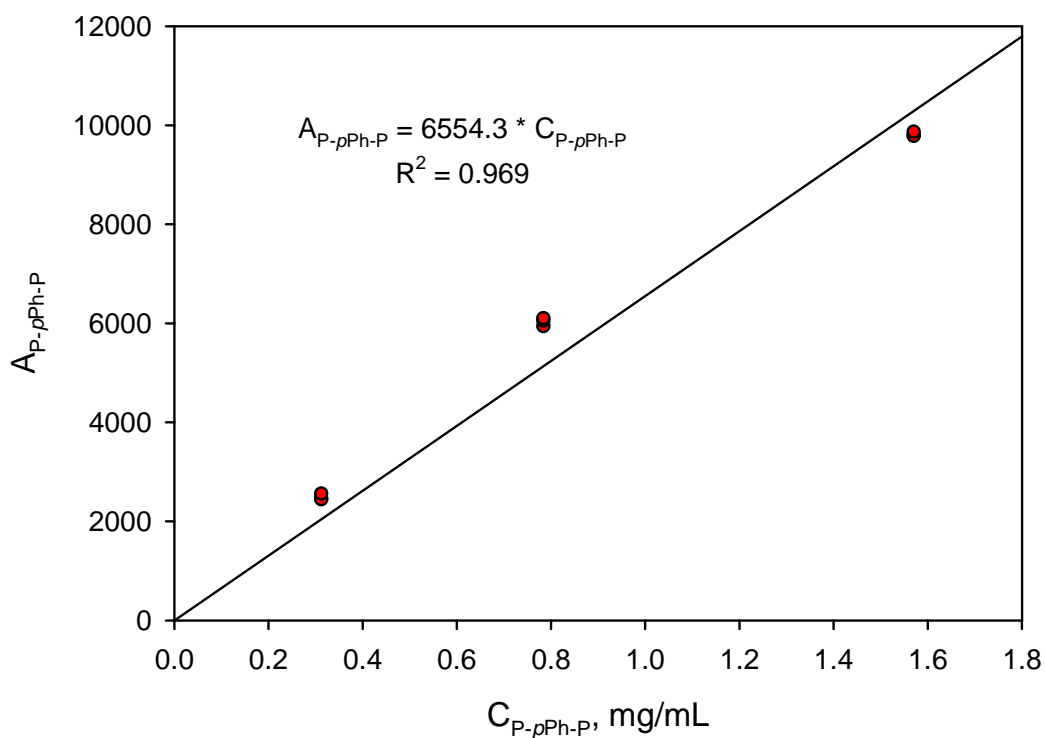


Figure A.28: Area of P-pPh-P in HPLC as a function of C.

A.4.2.6 Calibration for P-Th-P

Table A.13: HPLC calibration data for P-Th-P

C_{P-Th-P}	A_{P-Th-P}	C_{Phen}	A_{Phen}	A_{P-Th-P}/C_{P-Th-P}	A_{Phen}/C_{Phen}	F
2.063	15815.052	0.390	4157.779	7666.045	10674.657	0.718
2.063	15718.055	0.390	4169.500	7619.028	10704.750	0.712
2.063	15757.372	0.390	4241.139	7638.086	10888.674	0.701
2.063	15714.199	0.390	4180.368	7617.159	10732.653	0.710
1.032	8204.580	0.195	2172.578	7954.028	11155.730	0.713
1.032	8120.929	0.195	2178.963	7872.932	11188.514	0.704
1.032	8215.804	0.195	2194.120	7964.909	11266.343	0.707
1.032	8300.546	0.195	2188.252	8047.063	11236.210	0.716
0.413	3521.611	0.078	961.621	8535.170	12344.298	0.691
0.413	3489.923	0.078	989.874	8458.369	12706.979	0.666
0.413	3530.472	0.078	946.209	8556.645	12146.453	0.704
0.413	3529.291	0.078	939.563	8553.782	12061.140	0.709
Average F=						0.704

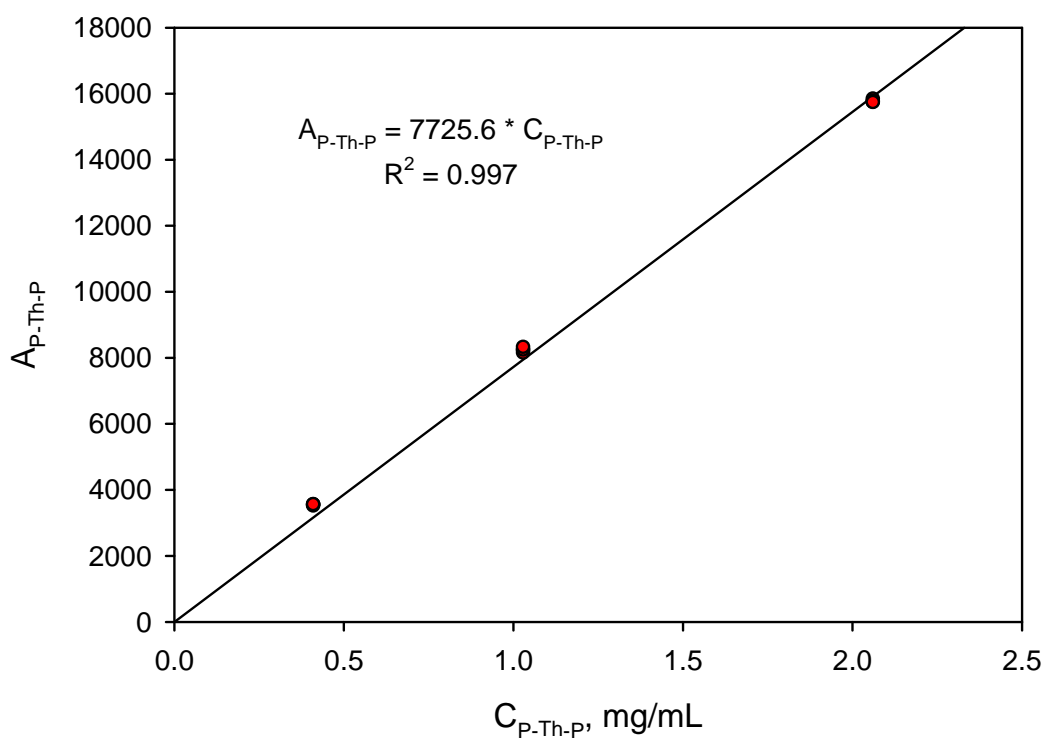


Figure A.29: Area of P-Th-P in HPLC as a function of C.

A.4.2.7 Calibration for BP

Table A.14: HPLC calibration data for Benzo[a]pyrene

C_{BP}	A_{BP}	C_{Phen}	A_{Phen}	A_{BP}/C_{BP}	A_{Phen}/C_{Phen}	F
3.270	5226.579	0.491	5339.380	1598.587	10885.587	0.147
3.270	5130.465	0.491	5226.694	1569.189	10655.850	0.147
3.270	4555.765	0.491	5211.644	1393.413	10625.165	0.131
1.635	2203.219	0.245	2406.106	1347.740	9810.832	0.137
1.635	2350.472	0.245	2536.039	1437.817	10340.627	0.139
1.635	2408.533	0.245	2512.200	1473.334	10243.426	0.144
0.654	966.931	0.098	1023.762	1478.713	10435.899	0.142
0.654	961.016	0.098	1018.949	1469.668	10386.838	0.141
0.654	1085.551	0.098	1052.808	1660.118	10731.991	0.155
Average F=						0.143

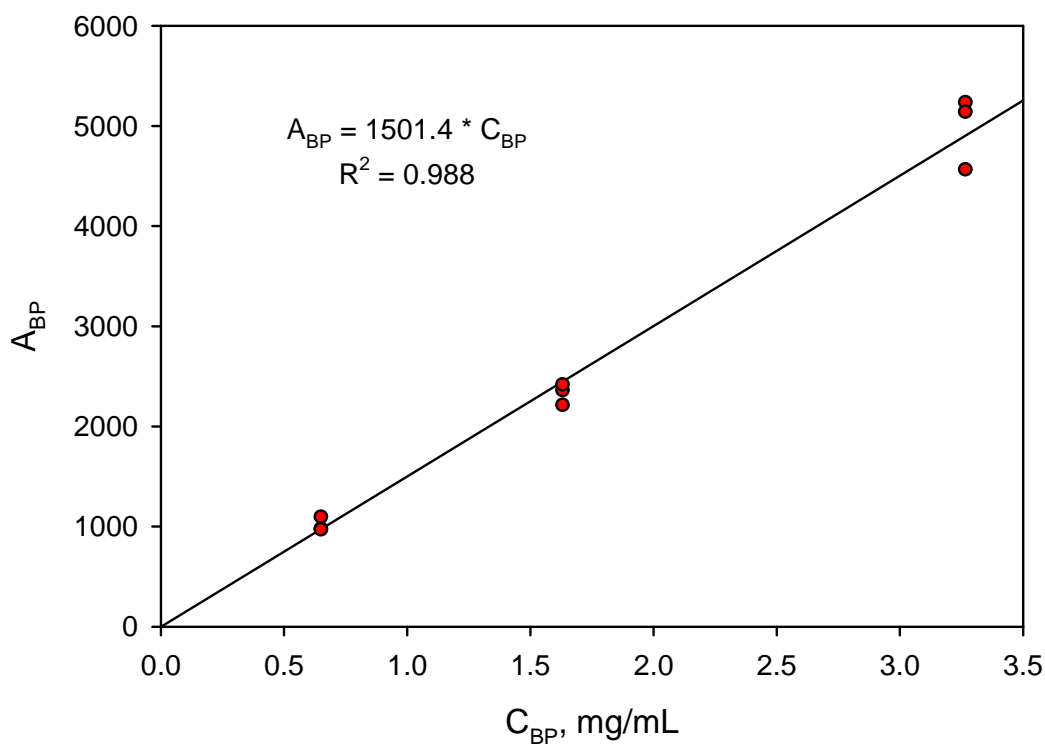


Figure A.30: Area of BP in HPLC as a function of its C in MC with Phen.

A.4.2.8 Calibration for TDP

Table A.15: HPLC calibration data for TDP

C_{TDP}	A_{TDP}	C_{Phen}	A_{Phen}	A_{TDP}/C_{TDP}	A_{Phen}/C_{Phen}	F
0.660	522.082	0.537	11638.732	791.033	21673.617	0.036
0.660	562.647	0.537	12342.300	852.495	22983.799	0.037
0.660	568.120	0.537	12512.764	860.788	23301.236	0.037
0.132	105.983	0.107	2437.859	802.902	22698.870	0.035
0.132	103.446	0.107	2423.087	783.684	22561.335	0.035
0.132	104.026	0.107	2466.564	788.078	22966.145	0.034
0.066	57.771	0.054	1411.582	875.319	26286.444	0.033
0.066	58.258	0.054	1410.493	882.698	26266.167	0.034
0.066	58.657	0.054	1401.184	888.736	26092.807	0.034
Average F=						0.035

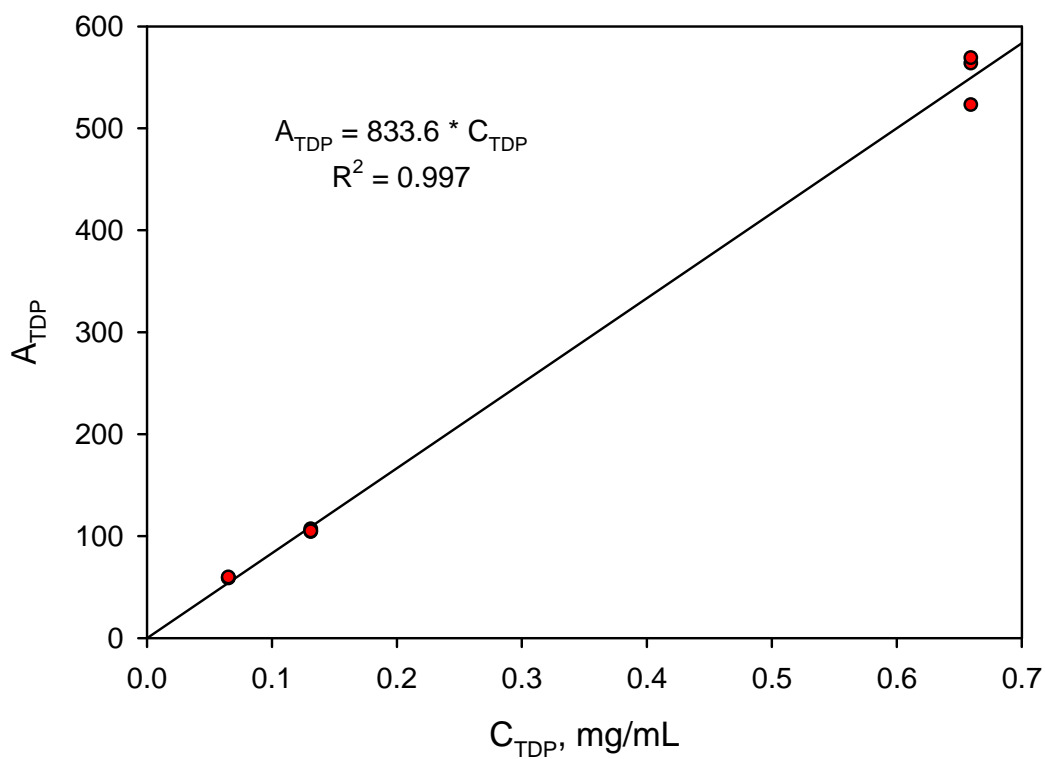


Figure A.31: Area of TDP in HPLC as a function of C.

A.4.2.9 Calibration for Chol-Ph

Table A.16: HPLC calibration data for Chol-Ph

$C_{\text{Chol-Ph}}$	$A_{\text{Chol-Ph}}$	C_{Phen}	A_{Phen}	$A_{\text{Chol-Ph}}/C_{\text{Chol-Ph}}$	$A_{\text{Phen}}/C_{\text{Phen}}$	F
2.132	5653.050	0.433	4323.115	2652.147	9984.100	0.266
2.132	5575.609	0.433	4281.704	2615.815	9888.461	0.265
1.066	2936.975	0.217	2277.444	2755.782	10519.371	0.262
1.066	2933.651	0.217	2286.602	2752.664	10561.673	0.261
0.426	1194.756	0.087	956.404	2802.617	11043.927	0.254
0.426	1199.885	0.087	962.535	2814.650	11114.725	0.253
Average F=						0.260

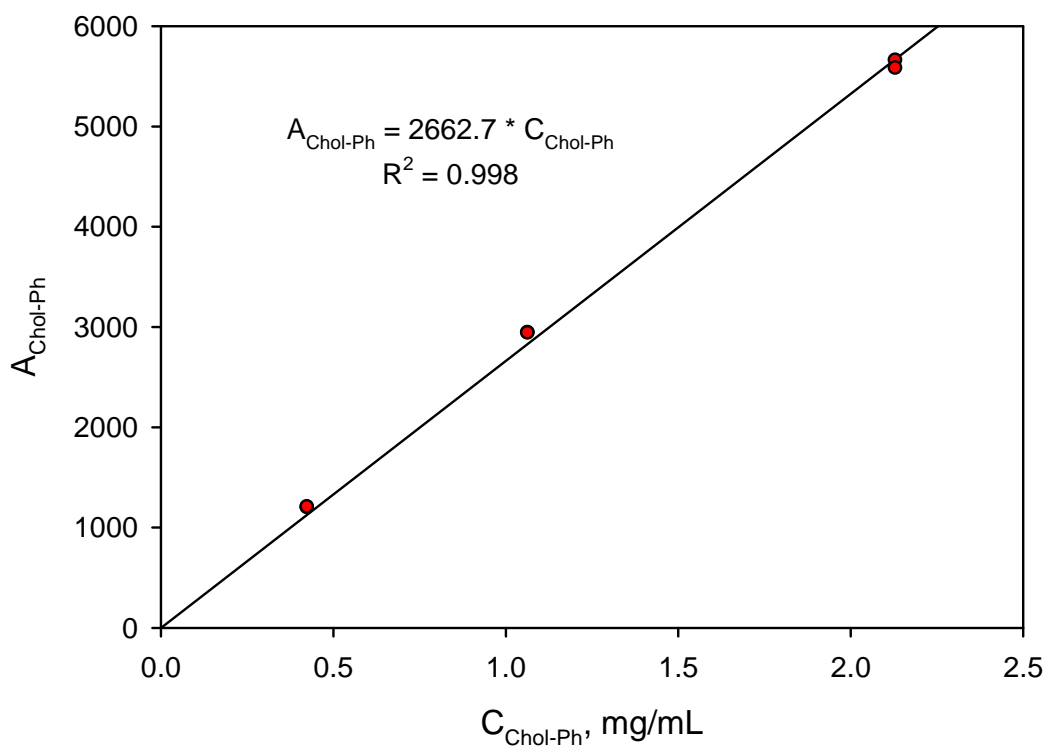


Figure A.32: Area of Chol-Ph in HPLC as a function of C.

A.4.2.10 Calibration for Chol-BB

Table A.17: HPLC calibration data for Chol-BB with pyrene (P) as standard

$C_{\text{Chol-BB}}$	$A_{\text{Chol-BB}}$	C_P	A_P	$A_{\text{Chol-BB}}/C_{\text{Chol-BB}}$	A_P/C_P	F
1.983	4326.733	0.697	5998.576	2181.913	8612.456	0.253
1.983	4179.266	0.697	6035.671	2107.547	8665.716	0.243
1.983	4273.464	0.697	6042.346	2155.050	8675.300	0.248
0.992	2087.646	0.348	3287.942	2105.543	9441.328	0.223
0.992	2094.118	0.348	3144.585	2112.071	9029.678	0.234
0.992	2126.898	0.348	3164.560	2145.132	9087.035	0.236
0.992	2106.733	0.348	3161.579	2124.794	9078.476	0.234
0.397	928.987	0.139	1418.059	2342.377	10179.892	0.230
0.397	968.419	0.139	1424.076	2441.803	10223.089	0.239
0.397	1005.911	0.139	1435.267	2536.337	10303.427	0.246
0.397	956.083	0.139	1408.391	2410.697	10110.491	0.238
Average F=						0.239

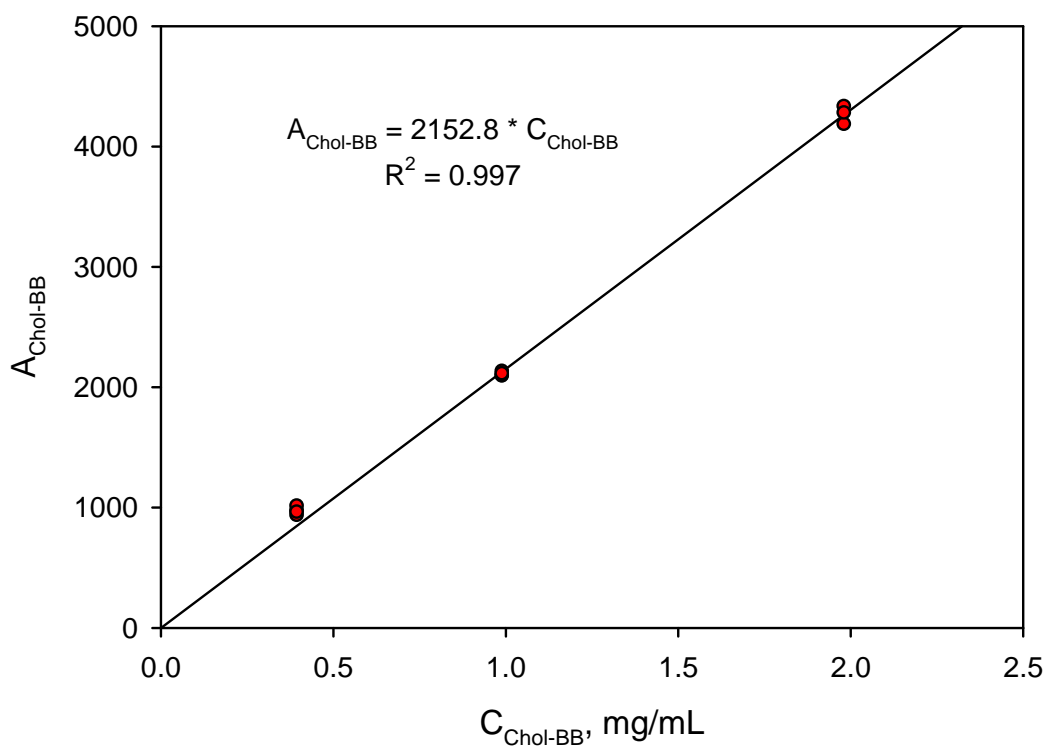


Figure A.33: Area of Chol-BB in HPLC as a function of C.

A.4.2.11 Calibration for Chol-Py

Table A.18: HPLC calibration data for Chol-Py

$C_{\text{Chol-Py}}$	$A_{\text{Chol-Py}}$	C_{Phen}	A_{Phen}	$A_{\text{Chol-Py}}/C_{\text{Chol-Py}}$	$A_{\text{Phen}}/C_{\text{Phen}}$	F
1.443	4452.948	0.507	4992.729	3086.966	9847.592	0.313
1.443	4565.923	0.507	5019.250	3165.285	9899.900	0.320
1.443	4490.666	0.507	5010.079	3113.113	9881.813	0.315
1.443	4532.437	0.507	5047.670	3142.071	9955.957	0.316
0.721	2296.812	0.254	2666.341	3184.487	10518.112	0.303
0.721	2342.291	0.254	2649.453	3247.544	10451.491	0.311
0.721	2349.010	0.254	2651.050	3256.859	10457.790	0.311
0.289	905.587	0.101	1057.625	3138.949	10430.223	0.301
0.289	920.834	0.101	1060.057	3191.798	10454.209	0.305
0.289	929.553	0.101	1064.092	3222.020	10494.000	0.307
0.289	920.150	0.101	1067.046	3189.428	10523.133	0.303
Average F=						0.310

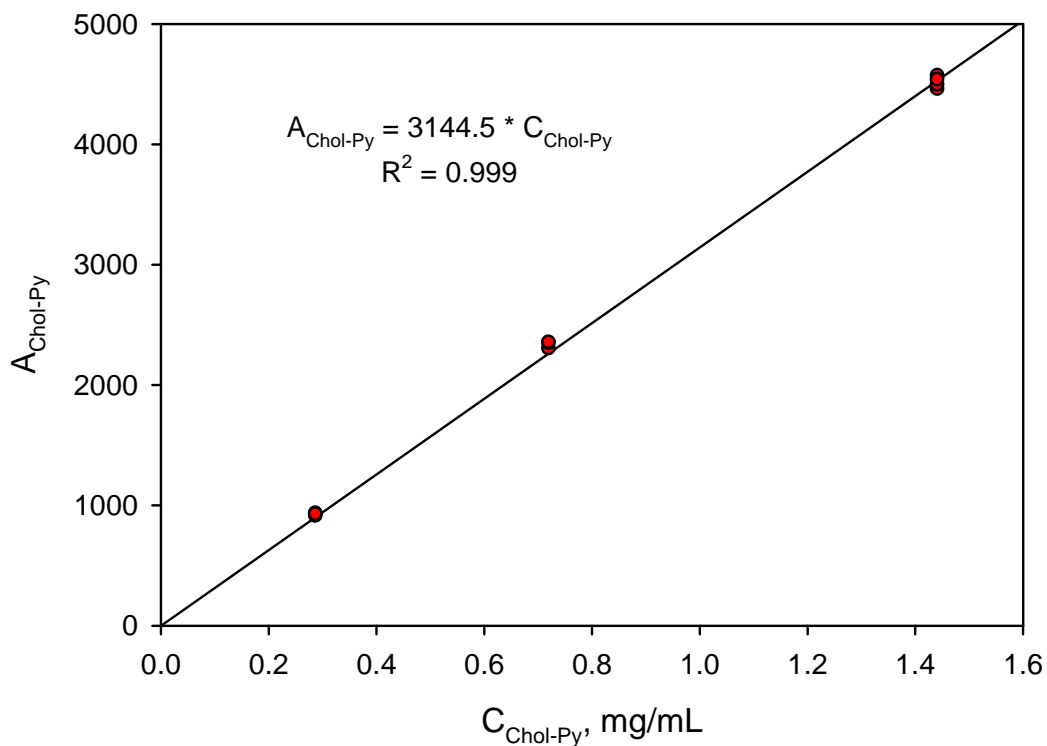


Figure A.34: Integrated area of Chol-Py in HPLC as a function of C.